

DESIGN AND CLINICAL  
VALIDATION OF NOVEL IMAGING  
STRATEGIES FOR ANALYSIS OF  
**ARRHYTHMOGENIC SUBSTRATE**

**PRANAV BHAGIRATH**

An electronic version of this thesis is accessible at:  
*<http://www.publicatie-online.nl/publicaties/p-bhagirath>*

Cover design and layout: Design Your Thesis ([www.designyourthesis.com](http://www.designyourthesis.com))  
Printing: Ridderprint ([www.ridderprint.nl](http://www.ridderprint.nl))  
ISBN: 978-946299-725-7

Copyright © 2017 by P. Bhagirath. All rights reserved. No parts of this thesis may be reproduced, stored or transmitted in any way without prior permission of the author.

**DESIGN AND CLINICAL VALIDATION OF NOVEL IMAGING  
STRATEGIES FOR ANALYSIS OF ARRHYTHMOGENIC SUBSTRATE**

ONTWERP EN KLINISCHE VALIDATIE VAN NIEUWE BEELDVORMENDE  
STRATEGIEËN TER ANALYSE VAN ARITMOGEEN SUBSTRAAT

PROEFSCHRIFT

ter verkrijging van de graad van doctor aan de  
Erasmus Universiteit Rotterdam  
op gezag van de  
rector magnificus  
Prof.dr. H.A.P. Pols  
en volgens besluit van het College voor Promoties.  
De openbare verdediging zal plaatsvinden op  
vrijdag, 20 oktober 2017 om 11:30 uur

door

**Pranav Bhagirath**

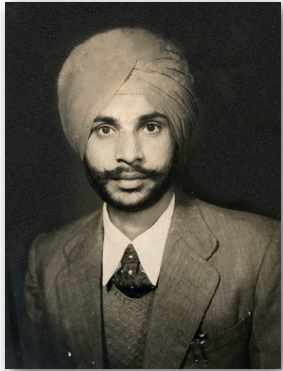
geboren op 9 november 1985 te New Delhi, India

## PROMOTIECOMMISSIE

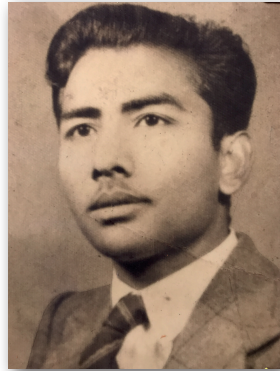
<b>Promotor:</b>	Prof.dr. F. Zijlstra
<b>Overige leden:</b>	Prof.dr. A.J.J.C. Bogers Prof.dr. F.E. Rademakers Dr. C.P. Allaart
<b>Copromotoren:</b>	Dr. M.J.W. Götte Dr. N.M.S. de Groot

Financial support by the Dutch Heart Foundation for the publication of this thesis is gratefully acknowledged.

*In honor of my loving grandparents who are watching from heaven*



Lt. Sardar Gurdial Singh Bhagirath



Lt. Sri. Shyam Lal Sharma



Lt. Smt. Dhian Kaur Bhagirath



Lt. Smt. Bimla Devi Sharma



## CONTENTS

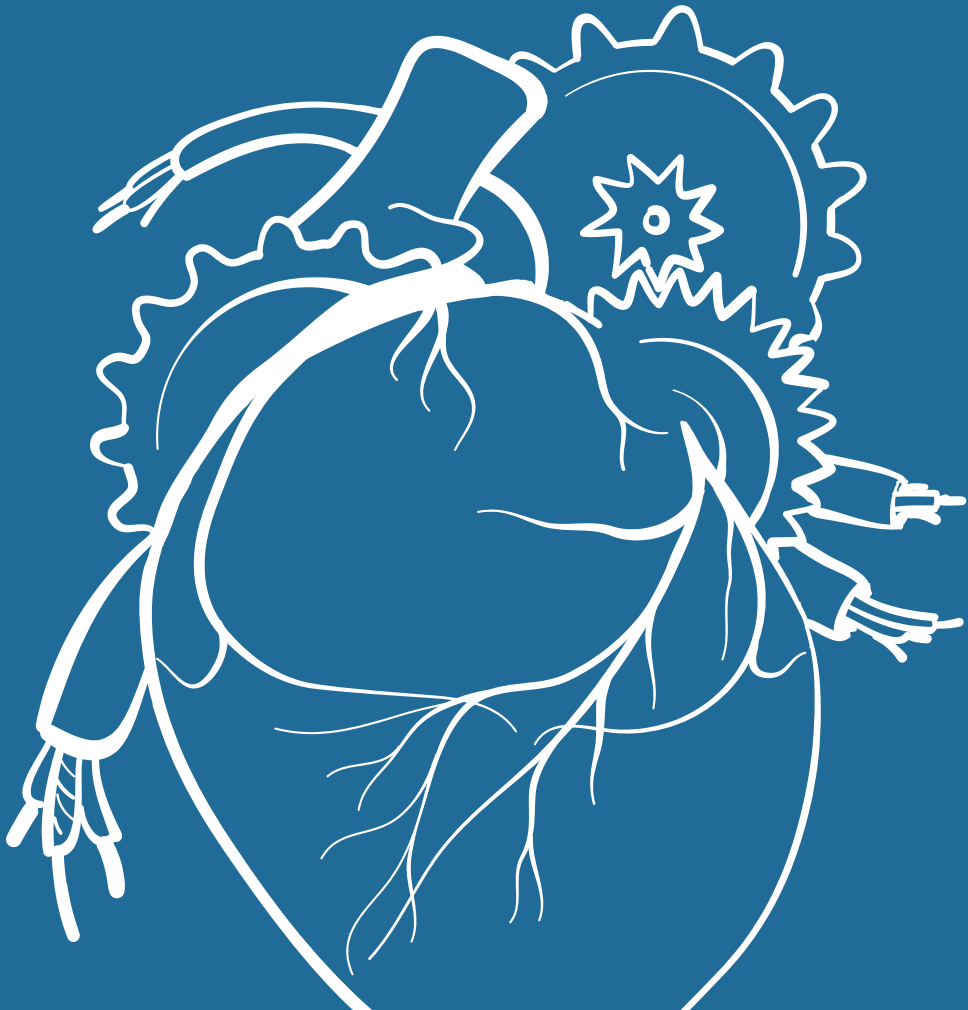
Chapter 1.	General Introduction	11
<b>SECTION 1. UTILITY OF CARDIAC IMAGING IN ELECTROPHYSIOLOGY</b>		
Chapter 2.	Multimodality imaging for patient evaluation and guidance of catheter ablation for atrial fibrillation - current status and future perspective. <i>Int J Cardiol. 2014 Aug 20;175(3):400-8.</i>	21
Chapter 3.	Evaluation of state-of-the-art segmentation algorithms for left ventricle infarct from late Gadolinium enhancement MR images. <i>Med Image Anal. 2016 May;30:95-107.</i>	41
Chapter 4.	Implementation of a standardized cardiac magnetic resonance based workflow for atrial fibrillation catheter ablation. <i>Submitted</i>	75
Chapter 5.	Left atrial sphericity: a promising parameter to predict response to ablation <i>Submitted</i>	91
Chapter 6.	Interventional cardiac magnetic resonance imaging in electrophysiology: advances toward clinical translation. <i>Circ Arrhythm Electrophysiol. 2015 Feb;8(1):203-11.</i>	107
<b>SECTION 2. ELECTRICAL ASSESSMENT OF ARRHYTHMOGENIC SUBSTRATE</b>		
Chapter 7.	Integrated whole-heart computational workflow for inverse potential mapping and personalized simulations. <i>J Transl Med. 2016 May 25;14(1):147.</i>	133
Chapter 8.	Computing volume potentials for noninvasive imaging of cardiac excitation. <i>Ann Noninvasive Electrocardiol. 2015 Mar;20(2):132-9.</i>	149
Chapter 9.	A priori model independent inverse potential mapping: the impact of electrode positioning. <i>Clin Res Cardiol. 2016 Jan;105(1):79-88.</i>	165
Chapter 10.	Feasibility and Accuracy of Cardiac Magnetic Resonance Imaging-Based Whole-Heart Inverse Potential Mapping of Sinus Rhythm and Idiopathic Ventricular Foci. <i>J Am Heart Assoc. 2015 Oct 14;4(10):e002222.</i>	189
Chapter 11.	General discussion	207

## **APPENDICES**

Summary	223
Samenvatting	227
List of publications	231
Curriculum vitae	233
Dankwoord	237



# 01



# GENERAL INTRODUCTION

---



## CURRENT CHALLENGES IN ELECTROPHYSIOLOGY

Technical advances in cardiovascular electrophysiology have resulted in an increasing number of catheter ablation procedures reaching 200 000 in Europe for the year 2013 <sup>1</sup>.

These advanced interventions are often complex and time consuming and may cause significant radiation exposure <sup>2</sup>. Furthermore, a substantial number of ablation procedures remain associated with poor (initial) outcomes and frequently require  $\geq 1$  redo procedures <sup>3</sup>. Innovations in modalities for substrate imaging could facilitate our understanding of the arrhythmogenic substrate, improve the design of patient-specific ablation strategies and improve the results of ablation procedures <sup>4</sup>.

## NOVEL SUBSTRATE IMAGING MODALITIES

### Cardiac magnetic resonance

Cardiac magnetic resonance imaging (CMR) can be considered the most comprehensive and suitable modality for the complete electrophysiology and catheter ablation workup (including patient selection, procedural guidance, and [procedural] follow-up) <sup>5</sup>.

Utilizing inversion recovery CMR, fibrotic myocardium can be visualized and quantified 10–15 min after intravenous administration of Gadolinium contrast. This imaging technique is known as late Gadolinium enhancement (LGE) imaging. Experimental models have shown excellent agreement between size and shape in LGE CMR and areas of myocardial infarction by histopathology <sup>6,7</sup>. Recent studies have also demonstrated how scar size, shape and location from pre-procedural LGE can be useful in guiding ventricular tachycardia's (VT) ablation <sup>8,9</sup> or atrial fibrillation (AF) ablation <sup>10</sup>. These procedures are often time-consuming due to the preceding electrophysiological mapping study required to identify slow conduction zones involved in re-entry circuits. Post-processed LGE images provide scar maps, which could be integrated with electroanatomic mapping systems to facilitate these procedures <sup>5,10</sup>.

### Inverse potential mapping

Through the years, various noninvasive electrocardiographic imaging techniques have emerged that estimate epicardial potentials or myocardial activation times from potentials recorded on the thorax <sup>11-13</sup>. Utilizing an inverse procedure, the potentials on the heart surface or activation times of the myocardium are estimated with the recorded body surface potentials as source data. Although this procedure only estimates the time course of unipolar epicardial electrograms, several studies have demonstrated

that the epicardial potentials and electrograms provide substantial information about intramyocardial activity and have great potential to facilitate risk-stratification<sup>14</sup> and generate personalized ablation strategies<sup>15</sup>.

### **Objectives of this thesis**

1. To evaluate the utility of cardiac magnetic resonance derived geometrical and tissue characteristic information for patient stratification and guidance of AF ablation.
2. To design and evaluate the performance of a finite element model based inverse potential mapping in predicting the arrhythmogenic focus in idiopathic ventricular tachycardia using invasive electro-anatomical activation mapping as a reference standard.

### **Outline of the thesis**

Section 1 is focused on methodology and clinical implementation of cardiac magnetic resonance in patients with atrial fibrillation.

- In chapter 2, the existing strategy for the workup and evaluation of atrial fibrillation catheter ablation is evaluated and potential improvements are proposed.
- In chapter 3, the current techniques to quantify the extent of late gadolinium enhancement are investigated.
- In chapter 4, the implementation of a standardized cardiac magnetic resonance based workflow for atrial fibrillation catheter ablation is evaluated.
- In chapter 5, the association of left atrial geometrical remodeling patterns with maintenance of sinus rhythm after repeat pulmonary vein isolation is investigated.
- In chapter 6, the technological requirements for performing interventional electrophysiological procedures in a magnetic resonance imaging environment are summarized.

Section 2 is focused on design and validation of an inverse potential mapping method in patients with idiopathic ventricular tachycardia.

- In chapter 7, a cardiac magnetic resonance based whole-heart computational workflow for inverse potential mapping and patient-specific cardiac activation simulation is implemented.
- In chapter 8, the feasibility and relevance of computing body volume potentials for inverse potential mapping is investigated.
- In chapter 9, the impact of electrode positioning on the solution of an inverse potential mapping computation is evaluated.

- In chapter 10, the inverse potential mapping workflow is clinically validated in patients undergoing catheter ablation of idiopathic ventricular tachycardia.
- In chapter 11, the key findings of this thesis are summarized and put in clinical perspective.



## REFERENCES

1. Arribas F, Auricchio A, Boriani G et al. Statistics on the use of cardiac electronic devices and electrophysiological procedures in 55 ESC countries: 2013 report from the European Heart Rhythm Association (EHRA). *Europace* 2014;16 Suppl 1:i1-78.
2. Heidbuchel H, Wittkampf FH, Vano E et al. Practical ways to reduce radiation dose for patients and staff during device implantations and electrophysiological procedures. *Europace* 2014;16:946-964.
3. Brooks AG, Stiles MK, Laborderie J et al. Outcomes of long-standing persistent atrial fibrillation ablation: a systematic review. *Heart Rhythm* 2010;7:835-846.
4. Blomstrom LC, Auricchio A, Brugada J et al. The use of imaging for electrophysiological and devices procedures: a report from the first European Heart Rhythm Association Policy Conference, jointly organized with the European Association of Cardiovascular Imaging (EACVI), the Council of Cardiovascular Imaging and the European Society of Cardiac Radiology. *Europace* 2013;15:927-936.
5. Bhagirath P, van der Graaf AW, Karim R et al. Multimodality imaging for patient evaluation and guidance of catheter ablation for atrial fibrillation - current status and future perspective. *Int J Cardiol* 2014;175:400-408.
6. Kim RJ, Fieno DS, Parrish TB et al. Relationship of MRI delayed contrast enhancement to irreversible injury, infarct age, and contractile function. *Circulation* 1999;100:1992-2002.
7. Wagner A, Mahrholdt H, Holly TA et al. Contrast-enhanced MRI and routine single photon emission computed tomography (SPECT) perfusion imaging for detection of subendocardial myocardial infarcts: an imaging study. *Lancet* 2003;361:374-379.
8. Estner HL, Zviman MM, Herzka D et al. The critical isthmus sites of ischemic ventricular tachycardia are in zones of tissue heterogeneity, visualized by magnetic resonance imaging. *Heart Rhythm* 2011;8:1942-1949.
9. Andreu D, Berruezo A, Ortiz-Perez JT et al. Integration of 3D electroanatomic maps and magnetic resonance scar characterization into the navigation system to guide ventricular tachycardia ablation. *Circ Arrhythm Electrophysiol* 2011;4:674-683.
10. Bisbal F, Guiu E, Cabanas-Grandio P et al. CMR-guided approach to localize and ablate gaps in repeat AF ablation procedure. *JACC Cardiovasc Imaging* 2014;7:653-663.
11. SippensGroenewegen A, Hauer RN, van Hemel NM, Janse MJ, Robles de Medina EO. Atlas of paced body surface QRS integral maps for localization of the site of origin of postinfarction ventricular tachycardia. *J Electrocardiol* 1994;27 Suppl:105-112.
12. Berger T, Fischer G, Pfeifer B et al. Single-beat noninvasive imaging of cardiac electrophysiology of ventricular pre-excitation. *J Am Coll Cardiol* 2006;48:2045-2052.
13. Ramanathan C, Ghanem RN, Jia P, Ryu K, Rudy Y. Noninvasive electrocardiographic imaging for cardiac electrophysiology and arrhythmia. *Nat Med* 2004;10:422-428.

14. Vijayakumar R, Silva JN, Desouza KA et al. Electrophysiologic substrate in congenital Long QT syndrome: noninvasive mapping with electrocardiographic imaging (ECGI). *Circulation* 2014;130:1936-1943.
15. Shah AJ, Hocini M, Xhaet O et al. Validation of novel 3-dimensional electrocardiographic mapping of atrial tachycardias by invasive mapping and ablation: a multicenter study. *J Am Coll Cardiol* 2013;62:889-897.

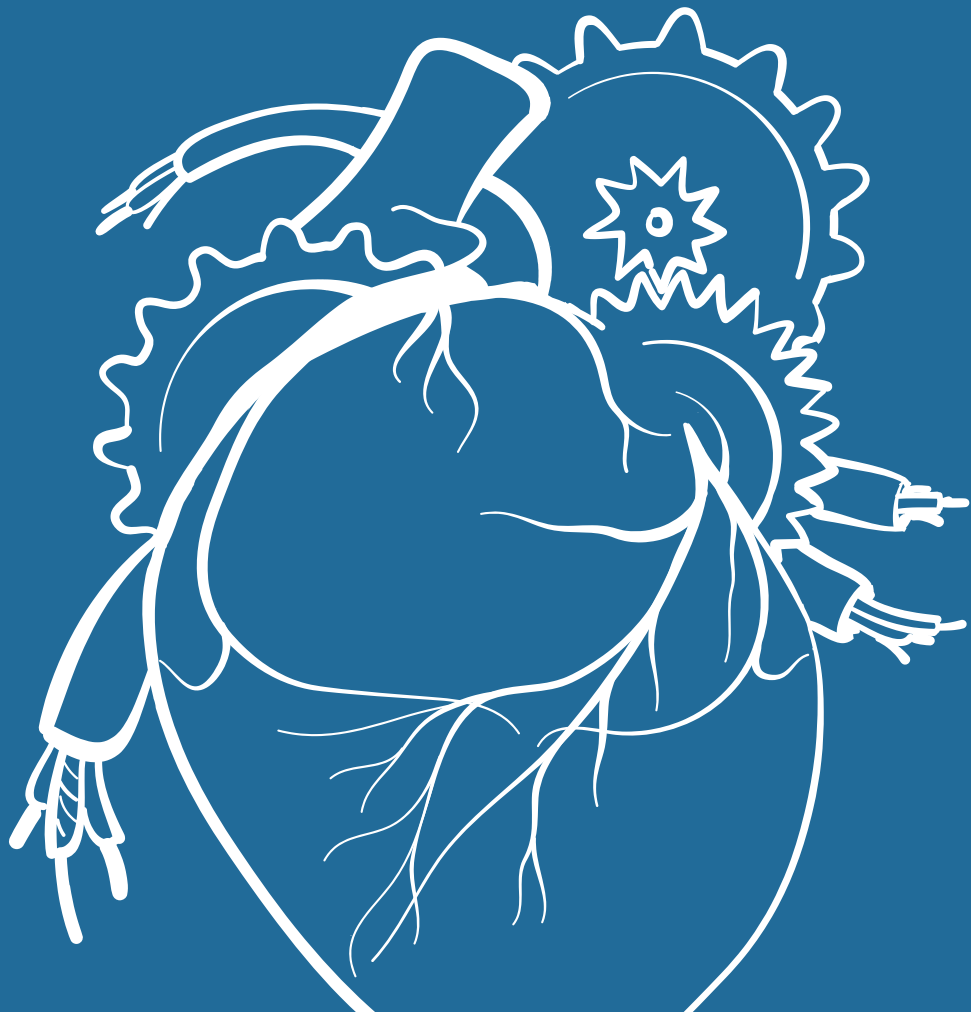




# **SECTION 1**

## UTILITY OF CARDIAC IMAGING IN ELECTROPHYSIOLOGY

# 02



# MULTIMODALITY IMAGING FOR PATIENT EVALUATION AND GUIDANCE OF CATHETER ABLATION FOR ATRIAL FIBRILLATION – CURRENT STATUS AND FUTURE PERSPECTIVE

---

P. Bhagirath MD; A.W.M. van der Graaf MD; R. Karim PhD; V.J.H.M. van Driel MD;  
H. Ramanna MD PhD; K. S. Rhode BSc PhD; N.M.S. de Groot MD PhD;  
M.J.W. Götte MD PhD  
*Int J Cardiol. 2014 Aug 20;175(3):400-8.*



## BACKGROUND

During the last decade, left atrium (LA) catheter ablation has emerged as an established non-pharmacological treatment of atrial fibrillation (AF), increasingly surpassing medicinal therapy<sup>(1-3)</sup>. Cardiac imaging plays a key role in patient selection and prediction of safety and efficacy for these LA procedures (**figure 1**)<sup>(3-6)</sup>.

The current guidelines advocate for an elaborate imaging approach and warrant a multimodality strategy<sup>(2;3;5;6)</sup>. In daily practice four different key, non-invasive modalities including transthoracic echocardiography (TTE), trans-esophageal echocardiography (TEE), computed tomography (CT) and cardiac magnetic resonance (CMR) are combined for assessment of underlying structural heart disease, exclusion of thrombus, identification of pulmonary vein (PV) anatomy and PV dimensions, and quantification of atrial function and dimensions<sup>(2;4)</sup>.

Recent technological development allow for non-invasive therapy stratification using pre-procedural tissue characterization maps<sup>(7)</sup>. The extent of fibrosis, a surrogate for the progression of disease, has been utilized to predict procedural outcome defined as post ablative recurrence of AF<sup>(7;8)</sup>. Furthermore, evaluating the circumferentiality of the induced PV antrum ablation lesions, might also be valuable for subsequent procedures<sup>(9)</sup>.

Onsite integration of electroanatomic maps (EAM) with CT or CMR can assist LA ablation procedures<sup>(4;5;10;11)</sup>. Peri-procedural use of previously acquired images, contributes towards improving therapeutic success<sup>(12;13)</sup> and reducing radiation exposure<sup>(14)</sup>.

In this overview, the advantages and limitations of the different cardiac imaging modalities facilitating LA ablation for AF will be examined on their merits. The primary objective is to explore the potential overlap and redundancy of these techniques and to advocate for an optimization and standardization of the multimodality approach.

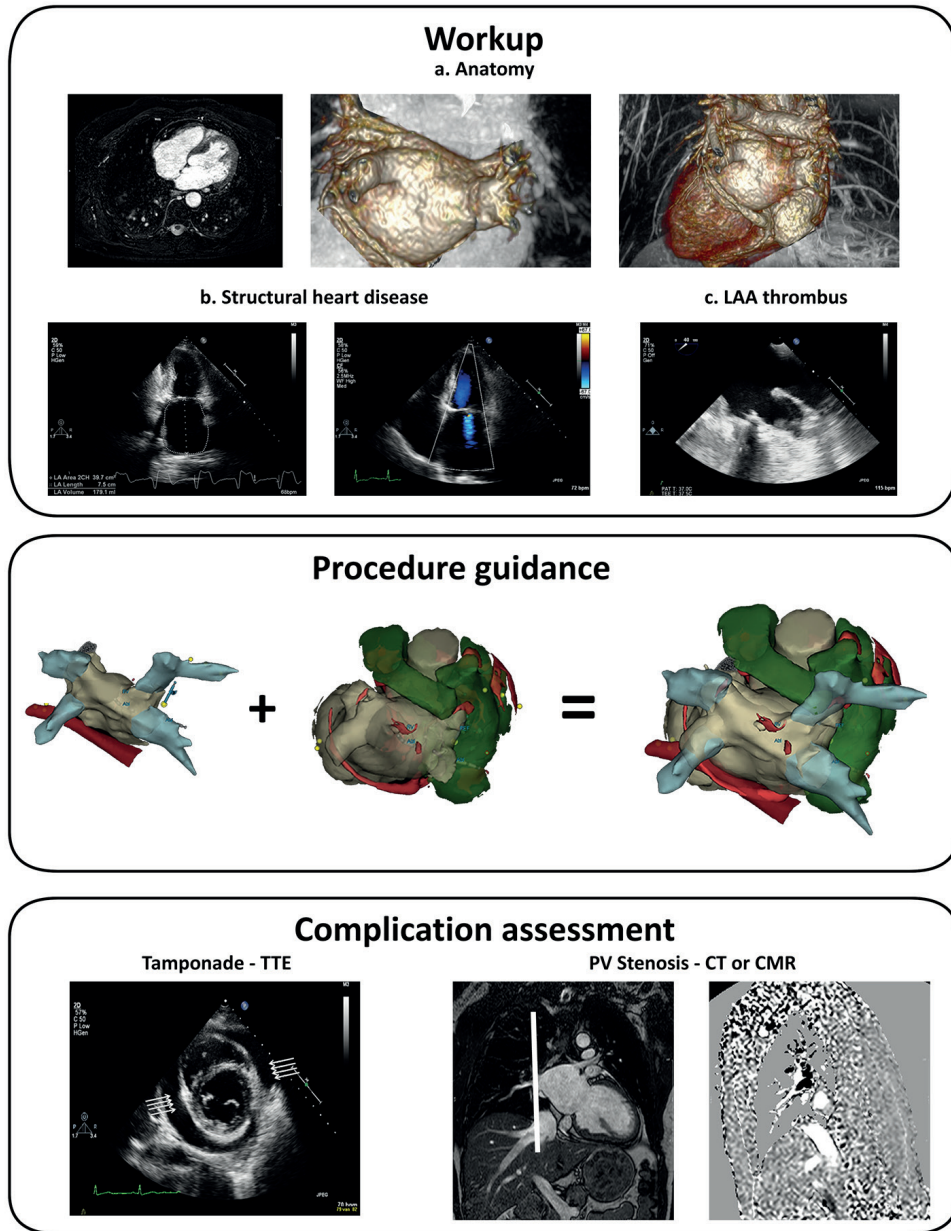


**Figure 1.** Current multimodality imaging strategy for ablation.

CT and/or CMR (a) and echocardiography (b and c) can be used to identify anatomy of the PVs and exclude structural heart disease and thrombus. The CT/CMR dataset acquired during the workup can be fused with the EAM for procedural guidance. Common complications arising from the procedure can be assessed with TTE and CT/CMR (arrows indicate pericardial effusion, white bar indicates planning view through right superior pulmonary vein).

## PRE-PROCEDURAL IMAGING

### LA structural remodeling - LA dimensions

LA dimensions are strongly related to adverse cardiovascular events and clinical outcome in patients ablated for AF<sup>(15;16)</sup>. Maintenance of sinus rhythm after ablation for AF is associated with a reduction of LA size<sup>(17)</sup>, and in return the LA volume is correlated to procedural success<sup>(18;19)</sup>. Therefore, accurate knowledge of these parameters is mandatory in order to correctly ascertain patient eligibility for ablation. Assessment of these parameters can be performed with various techniques including echocardiography, CMR and CT.

Despite its higher temporal resolution, TTE regularly underestimates the LA dimensions by 15-30 ml as a consequence of reduced image quality<sup>(20;21)</sup>. This modality also has a twice as high inter-observer variability ( $8.7 \pm 24\%$ ) when compared to CMR ( $3 \pm 10\%$ ) or CT ( $1 \pm 11\%$ )<sup>(20;21)</sup>. When measured with TEE, further underestimation of these parameters occurs by up to 10%<sup>(22;23)</sup>. This is caused due to incomplete visualization of the LA in the scan sector owing to its close proximity to the structure. Therefore, echocardiographic stratification may exert unjustified expectations on the ablation result.

CMR and CT show a good correlation for LA dimensions, with a correlation coefficient between 0.85 and 0.97<sup>(20;21;24)</sup>. CT makes a small yet significant overestimation of LA maximal volume when compared to CMR<sup>(20;24)</sup>. This difference is augmented in examinations performed during AF<sup>(21)</sup>.

Despite a lower spatial resolution than CT and a lower temporal resolution compared to echocardiography, CMR seems to be the most ideal modality for the assessment of LA dimensions.

### LA structural remodeling - LA geometry

Changes in dimensions cause alteration of the geometry. These geometrical changes have been marked as an independent predictor of AF recurrence post-ablation and can also be used for patient selection<sup>(25;26)</sup>. Results indicate that LA roof shapes can be considered a marker of atrial remodeling with flat and coved roof shape related to higher incidence of non-PV foci AF and AF inducibility after the ablative procedure<sup>(25)</sup>. LA sphericity, a new method for LA geometrical analysis, has recently been identified as a strong predictor of AF recurrence<sup>(26)</sup>.

### **LA structural remodeling - LA fibrosis**

Detection and quantification of fibrosis in the atrial wall prior to ablation as a part of patient stratification is a controversial topic. Oakes uses a well-documented approach to acquire the 3D LGE and perform the post-processing with the aim of utilizing the amount of fibrotic tissue to predict procedural outcome<sup>(7)</sup>. In another paper they describe tailored patient management based upon the pre-ablation LGE patterns (**figure 2**)<sup>(27)</sup>. Despite various attempts, other centers have so far been unable to reproduce these results<sup>(28;29)</sup>.

Results of the on-going DEECAP trial should provide new data on this topic.

### **Left atrial appendage thrombus**

Stroke is a feared complication of AF, associated with a severe reduction in the quality of life. The presence of thrombus in the left atrial appendage (LAA) is considered the most important risk factor for stroke<sup>(30;31)</sup>. Therefore, excluding an intracardiac thrombus is a pre-requisite in all patients selected for a left sided ablation procedure. Due to its high sensitivity and specificity (100% and 99% respectively), today TEE is considered the gold standard<sup>(32)</sup>. However, TEE without sedation usually causes great discomfort and, although uncommon, the examination may result in potentially serious complications<sup>(33)</sup>.

A recent meta-analysis of 19 retro- and prospective studies of patients undergoing both TEE and CT for exclusion of thrombus prior to an ablative procedure, revealed a high accuracy for these techniques in detecting LAA thrombus<sup>(34)</sup>. CT had a weighted mean sensitivity and specificity of 96% of 92% respectively. The positive predictive value and negative predictive value of CT was 41% and 99% respectively. The overall accuracy improved to 99% (PPV 92% and NPV 100%) when delayed phase imaging was used, making CT a non-invasive alternative for TEE under these terms.

Only 2 studies have compared CMR and TEE for detection of thrombus<sup>(35;36)</sup>. Both combined, examined 147 patients and demonstrated a 100% concordance between the two modalities for detection of LAA thrombus. This suggests that adding conventional MRA or early gadolinium enhancement pulse sequences to a standard CMR examination ensures adequate coverage of the LAA and may potentially substitute TEE in patients eligible for CMR, without a reduction in diagnostic yield (**figure 3**).

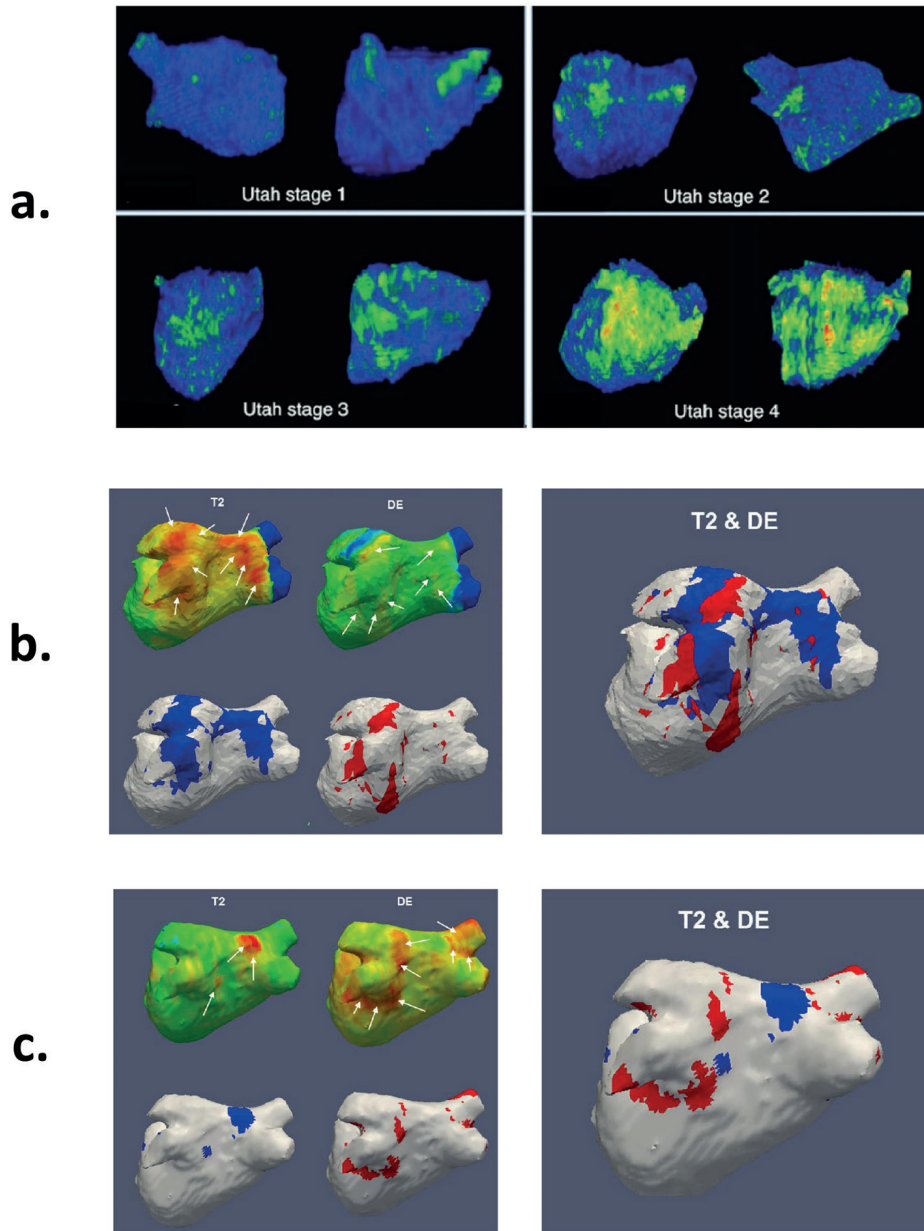


**Figure 2.** LA tissue characteristics: fibrosis, edema and necrosis.

Reconstructed 3D left atrial shells after post processing T2 and 3D LGE images of the left atrium. **a.** The 4 stages of fibrosis (bright green) used in the Utah classification to stratify ablation therapy. **b.** 18-24 hours post ablation. **c.** 3 months and beyond edema and scar. Reprinted with permission from (a.) Akoum et al<sup>14</sup> and (b. & c.) Arujuna et al<sup>16</sup>.

**TEE**

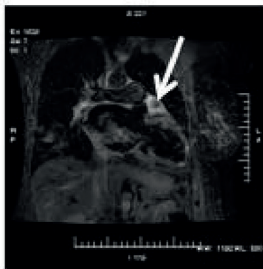


**CT**



**MRI**

**Double Inversion Recovery**



**Perfusion Imaging**



**Late Gadolinium Enhancement**



**Triple Inversion Recovery**



**Early Gadolinium Enhancement**



**MRA of the LAA/LA**



**Figure 3.** TEE, CT and MRI images depicting thrombus in the LAA.

TEE: Arrows indicate thrombus and arrowhead indicates LAA. CT: Arrow indicates thrombus in an axial view of the LAA. MRI: Multiple sequences depicting thrombus (arrow) in a coronal view of the LAA. Adapted and reprinted with permission from Rathi et al <sup>34</sup>.

## **Pulmonary vein anatomy evaluation**

Electrical isolation of the PV at the antrum level has long become the first step in ablative treatment of AF. Both myocardial sleeves (i.e. cardiac muscular fibers extending into the pulmonary veins) as an underlying trigger of AF and the adjacent disperse atrial substrate, surrounding the PV ostium containing triggers and rotors, must be electrically isolated <sup>(1)</sup>.

There is no uniform PV branching pattern and at least 1 accessory PV is present in 26% of the patients <sup>(11)</sup>. Therefore, detailed anatomical knowledge is desirable prior to the ablation procedure. TEE, CT and CMR can provide this information; however, only CT and CMR provide true 3 dimensional (3D) datasets that can be imported and fused with the EAM. This allows for detailed visualization of the anatomy thereby increasing catheter maneuvers and procedural efficacy <sup>(12;13)</sup>. CT and CMR have a high level of agreement in assessing PV anatomy and dimensions <sup>(10;37)</sup>.

## **PROCEDURAL IMAGING**

### **Anatomic guidance**

EAM systems can reconstruct 3D anatomy relative to a reference point and combine it with local electrical information to direct catheter ablation. Fusion of the EAM shell with a 3D anatomic dataset from CMR or CT provides a highly detailed anatomic projection. Besides the obvious benefits of improved visualization and simplified catheter guidance inside the complex LA anatomy, this approach significantly reduces fluoroscopic exposure <sup>(14)</sup>. Studies comparing ablation procedures using conventional fluoroscopy versus image integration report a lower arrhythmia recurrence rate for the image integration group, 19% image integration vs. 48% fluoroscopy only <sup>(12)</sup>. Another study showed similar values, 22.6% for EAM with image integration versus 41.7% using electroanatomic system only <sup>(13)</sup>.

Despite the limited number of patients studied, this data demonstrates the importance of EAM combined with 3D imaging. Fusion of these datasets contributes to reduced fluoroscopic exposure and may increase the efficacy of the ablative procedure.

### **MRI guidance**

Catheterization laboratories are successfully working towards performing ablation in an MR environment <sup>(38)</sup>. There are still hurdles to be won; catheter and tracking mechanism adjustments to function in a MRI scanner and training personnel to shift from fluoroscopy towards the MR suite, meanwhile maintaining cost-efficiency. The transition to an MRI

environment may prove to be a great advantage for electrophysiologists who can work outside the dangers of ionizing radiation. It also enables an enhanced visualization of anatomic structures and provides the unique ability to instantly adjust the ablation strategy based on tissue characteristics (edema and necrosis).

## POST-PROCEDURAL IMAGING

### Assessment of PV stenosis

PV stenosis is a complication which may occur after ablation and can be treated with balloon dilatation and stent placement <sup>(39)</sup>.

The requirement for intervention depends upon presence and severity of symptoms <sup>(1;39)</sup>. Evaluation of the PV anatomy at follow-up can be performed with CT or CMR. PV flow data can be acquired reliably and reproducibly using a CMR flow map study (**figure 4**) <sup>(40;41)</sup>. Comparison of flow before and after ablation allows a more functional assessment to be conducted regarding severity of the stenosis and interventional indication.

### Assessment of post-ablation scar

The ability to perform tissue characterization is restricted to CT and CMR. So far, CT has been used in a limited number of trials focused on scar in the ventricles and considering its low sensitivity, should be conceived as a developing technique <sup>(42;43)</sup>. CMR on the other hand is the gold standard for detection of infarcted myocardium and assessment of viability <sup>(44)</sup>.

Recent progress in 3D late gadolinium enhanced (LGE) imaging sequences enables identification and quantification of structural remodeling in cardiac tissue as thin as the atrial wall <sup>(7;45)</sup>.

### Acute atrial injury

Acute injury is characterized by presence of both necrosis (fibrosis) and edema. Cardiac MRI allows for discrimination between edema and fibrosis. A combination of LGE, defining necrosis, and Short Tau Inversion Recovery (STIR), targeted at edema, need to be performed. These images, once merged, show the distribution of edema and necrosis on an anatomic shell which can be used to predict arrhythmia recurrence and may guide redo ablation strategies (**figure 2**) <sup>(28)</sup>.

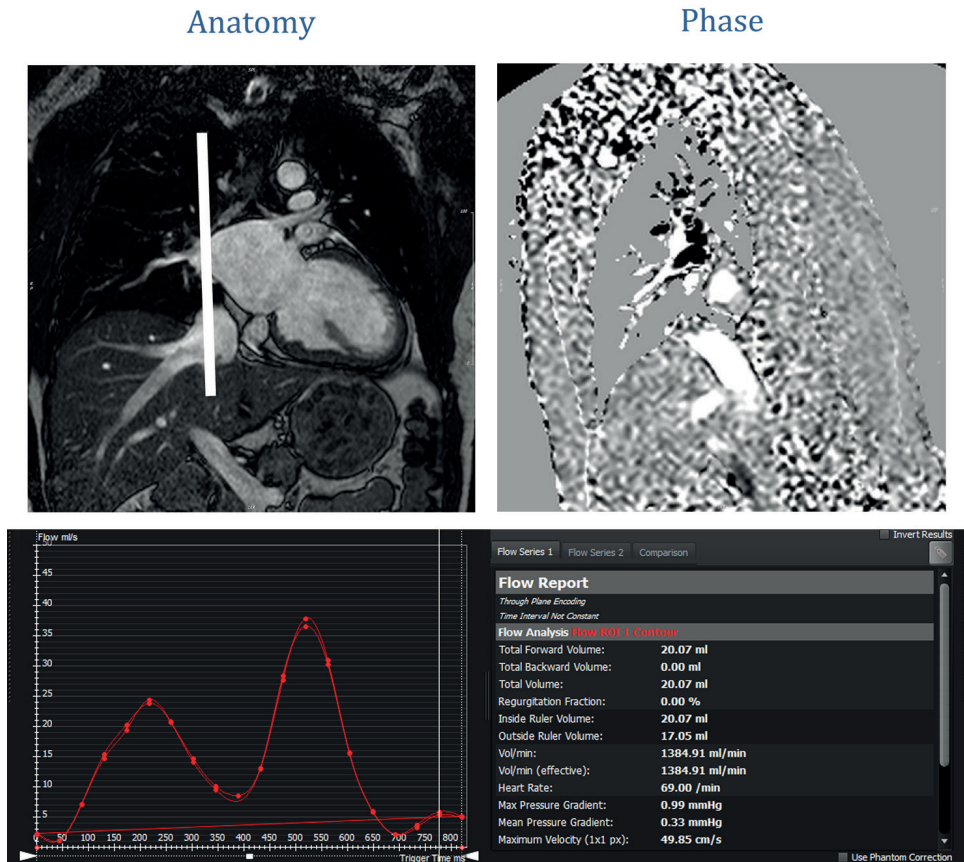


**Figure 4.** Planning view for PV flow map.

Left row; coronal view of the LA used to plan a flow map of the right superior PV. Right row; sagittal view with the phase component of the flow map.

### *Chronic atrial injury*

The extent of post-ablation scar is shown to stabilize after a period of 3 months <sup>(46)</sup>. Studies utilizing this information suggest a correlation between procedural outcome and location and volume of scar tissue post-ablation <sup>(47;48)</sup>. Results indicated absence of AF recurrence in the presence of circumferential scar around all PV's, whereas in patients with less than 2 PV's completely encircled, the chances of arrhythmia recurrence increased considerably <sup>(47)</sup>. Another study demonstrated that extensive scarring ( $\geq 1.98$  ml) especially around the inferior part of the right inferior pulmonary vein, is associated with a longer AF free survival <sup>(48)</sup>.

Recent work examining the correlation between the site of ablation and localization of the scar provides information about conduction gaps that could help in guiding redo procedures <sup>(9;28;48)</sup>. Reports listing an insufficient accuracy in determining these gaps after fusion of the EAM and LGE images <sup>(29;49)</sup> might have differences in patient selection, imaging protocol and post-processing tools. Technique inherent artifacts due to arrhythmias, motion or partial volume are also likely to play a role.

These results show that the amount of ablation induced LA structural remodeling may be used as a marker for procedural outcome. Furthermore, incorporation of 3D LGE sequences could play an important role during follow up examination and for devising patient specific redo ablative strategies. The inability of echocardiography and CT to perform atrial tissue characterization, make CMR the preferred modality for this purpose.

## DISCUSSION

Various non-invasive imaging modalities are currently employed in the treatment strategy of AF. All techniques have their advantages and limitations (**table 1**), and due to a different gold standard for each step in the workup, a multimodality approach is advocated in the daily practice.

Using multiple modalities is neither cost-efficient nor time-effective. An increasing demand for catheter ablation procedures has resulted in electrophysiology

**Table 1.** Comparison of imaging modalities for catheter ablation workup, guidance and evaluation.

		TTE	TEE	CT	CMR
Pre-procedural	LA dimension	+(*)	++	++	++
	LA fibrosis				+
	LA geometry			+	+
	LAA thrombus		+	+	+
	PV anatomy		+	+	+
Peri-procedural	Procedure guidance			+	+
Post-procedural	PV stenosis		+(**)	+	+
	PV flow				+
	Ablation scar				+

A summary of the elements encountered during the workup and follow up of a patient undergoing ablation. A '+' is given when the concerned modality can adequately perform the step. \*TTE significantly underestimates these parameters. \*\*TEE has difficulties to thoroughly examine all the PV's and underestimates the severity of obstruction.

centers with high volume practices, necessitating an optimization of the existing work-up. Moreover, on-going technological developments have increased the capability of the individual techniques and permit a single modality approach that can supply consistent and uniform imaging data, applicable during the workup, guidance and evaluation of ablation procedures.

A general problem for echocardiography is reproducibility. Varying anatomic planes during follow up exam may cause low inter-observer agreement. In addition TTE significantly underestimates atrial volumes and depends upon operator expertise and acoustic windows for image quality. TEE places a burden on the patient due to involvement of an invasive probe and usage of a sedative/anesthetic prior to the examination.

CT has the highest spatial resolution amongst the imaging techniques and is the fastest modality to perform. However, its use is largely limited by radiation exposure, which prohibits its use in routine follow-up. The efforts towards reducing this dosage over the last decade have caused a steep decline but still remain a significant load for the patient (**figure 5**)<sup>(50)</sup>. Tissue characterization serves an increasingly important role for ablation and although there is improvement, the current prospects of CT are extremely restricted.

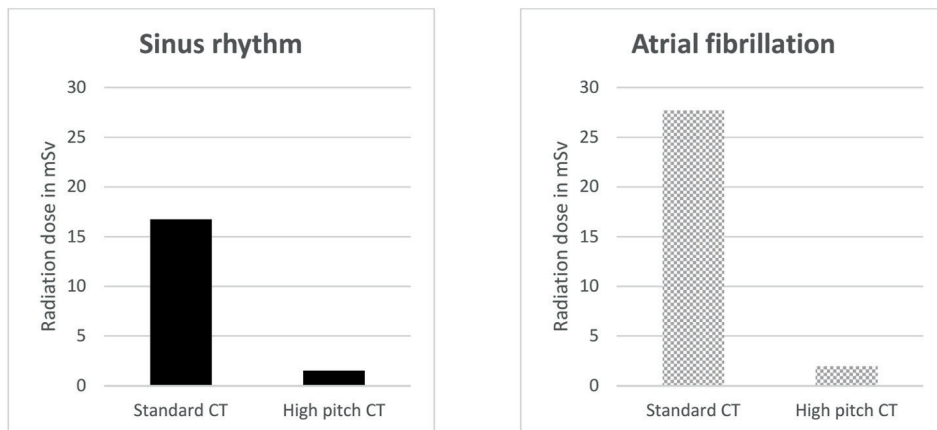


**Figure 5.** The evolution of CT: decreasing radiation dosage.

The radiation dosage is significantly reduced when using a 128 slice high pitch technique in comparison with a conventional 64 slice scan. This reduction is more prominent for patients suffering from an arrhythmia during the scan. (Adapted from Thai et al<sup>47</sup>)

Currently, the most promising modality seems to be CMR. Although it is the least frequently used due to time constraints and restrictions for some patient groups. Nevertheless, its ability to visualize anatomy combined with information about tissue characteristics enable a detailed workup to be performed. Using pre-procedurally acquired imaging data to guide ablation, results in lower radiation exposure and possible increase of therapeutic efficacy. A baseline for future follow-up examinations is established simultaneously.

Recent studies revealed the possibility for identifying potential interruptions of ablation lesions, so called electrical gaps which can be used to guide redo ablative procedures<sup>(9;28)</sup>. Gap identification, quantification of LA structural remodeling (volume, sphericity) and PV flow measurements allow for a thorough evaluation of procedural efficacy and related complications. Furthermore, CMR does not expose patients to radiation making it safe for (routine) follow-up.

Minor contraindications like claustrophobia can be counteracted with an anxiolytic. Free breathing and motion correction techniques are used to optimize image acquisition and reduce artifacts for challenging patients presenting with dyspnea and arrhythmia<sup>(51)</sup>.

## CONCLUSION

Multimodality imaging to guide catheter ablation therapy is not preferable for high volume institutes. Modern day healthcare demands a single technique, both cost- and time-efficient, that performs the complete workup of a patient for catheter ablation. CMR has shown to be comparable to the key imaging modalities, providing all the information during a single examination, in a safe and reproducible manner. In addition it seems to be more cost-effective. These conditions endorse this modality for a single technique approach.

## REFERENCES

1. Haissaguerre M, Jais P, Shah DC, Takahashi A, Hocini M, Quiniou G, et al. Spontaneous initiation of atrial fibrillation by ectopic beats originating in the pulmonary veins. *N Engl J Med* 1998 Sep 3;339(10):659-66.
2. Calkins H, Kuck KH, Cappato R, Brugada J, Camm AJ, Chen SA, et al. 2012 HRS/EHRA/ECAS Expert Consensus Statement on Catheter and Surgical Ablation of Atrial Fibrillation: recommendations for patient selection, procedural techniques, patient management and follow-up, definitions, endpoints, and research trial design. *Europace* 2012 Apr;14(4):528-606.
3. Camm AJ, Kirchhof P, Lip GY, Schotten U, Savelieva I, Ernst S, et al. Guidelines for the management of atrial fibrillation: the Task Force for the Management of Atrial Fibrillation of the European Society of Cardiology (ESC). *Eur Heart J* 2010 Oct;31(19):2369-429.
4. Tops LF, Schalij MJ, Bax JJ. Imaging and atrial fibrillation: the role of multimodality imaging in patient evaluation and management of atrial fibrillation. *Eur Heart J* 2010 Mar;31(5):542-51.
5. Blomstrom LC, Auricchio A, Brugada J, Boriani G, Bremerich J, Cabrera JA, et al. The use of imaging for electrophysiological and devices procedures: a report from the first European Heart Rhythm Association Policy Conference, jointly organized with the European Association of Cardiovascular Imaging (EACVI), the Council of Cardiovascular Imaging and the European Society of Cardiac Radiology. *Europace* 2013 Jul;15(7):927-36.
6. Fuster V, Ryden LE, Cannom DS, Crijns HJ, Curtis AB, Ellenbogen KA, et al. 2011 ACCF/AHA/HRS focused updates incorporated into the ACC/AHA/ESC 2006 guidelines for the management of patients with atrial fibrillation: a report of the American College of Cardiology Foundation/American Heart Association Task Force on practice guidelines. *Circulation* 2011 Mar 15;123(10):e269-e367.
7. Oakes RS, Badger TJ, Kholmovski EG, Akoum N, Burgon NS, Fish EN, et al. Detection and quantification of left atrial structural remodeling with delayed-enhancement magnetic resonance imaging in patients with atrial fibrillation. *Circulation* 2009 Apr 7;119(13):1758-67.
8. Akoum N, Daccarett M, McGann C, Segerson N, Vergara G, Kuppahally S, et al. Atrial fibrosis helps select the appropriate patient and strategy in catheter ablation of atrial fibrillation: a DE-MRI guided approach. *J Cardiovasc Electrophysiol* 2011 Jan;22(1):16-22.
9. Bisbal F, Guiu E, Berruezo A, Cabanas P, Prat-Gonzalez S, Garrido C, et al. MRI-GUIDED APPROACH TO LOCALIZE AND ABLATE GAPS IN REPEATED ATRIAL FIBRILLATION ABLATION PROCEDURE: A PILOT STUDY. *Journal of the American College of Cardiology* 2013 Mar 12;61(10\_S).
10. Hamdan A, Charalampos K, Roettgen R, Wellnhofer E, Gebker R, Paetsch I, et al. Magnetic resonance imaging versus computed tomography for characterization of pulmonary vein morphology before radiofrequency catheter ablation of atrial fibrillation. *Am J Cardiol* 2009 Dec 1;104(11):1540-6.

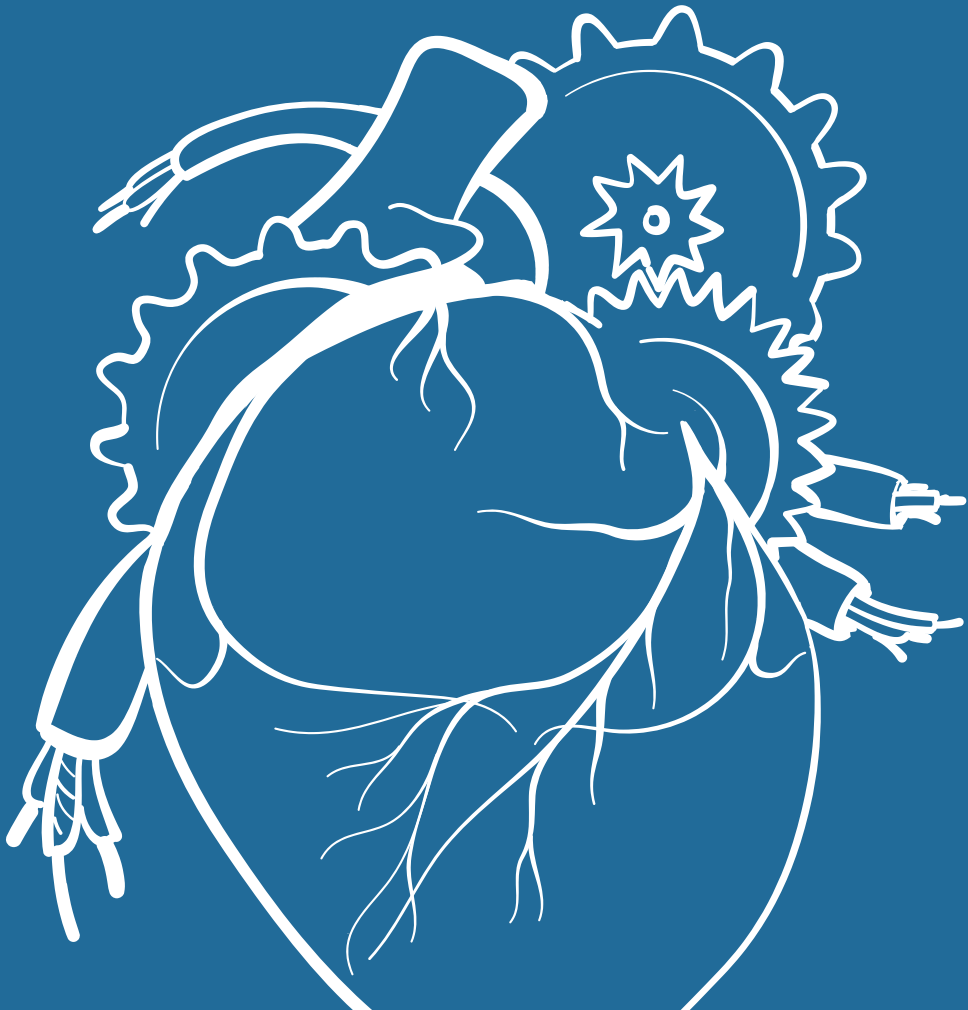
11. Anselmino M, Blandino A, Beninati S, Rovera C, Boffano C, Belletti M, et al. Morphologic analysis of left atrial anatomy by magnetic resonance angiography in patients with atrial fibrillation: a large single center experience. *J Cardiovasc Electrophysiol* 2011 Jan;22(1):1-7.
12. Della BP, Fassini G, Cireddu M, Riva S, Carbucicchio C, Giraldi F, et al. Image integration-guided catheter ablation of atrial fibrillation: a prospective randomized study. *J Cardiovasc Electrophysiol* 2009 Mar;20(3):258-65.
13. Bertaglia E, Bella PD, Tondo C, Proclemer A, Bottoni N, De Ponti R, et al. Image integration increases efficacy of paroxysmal atrial fibrillation catheter ablation: results from the CartoMerge Italian Registry. *Europace* 2009 Aug;11(8):1004-10.
14. Caponi D, Corleto A, Scaglione M, Blandino A, Biasco L, Cristoforetti Y, et al. Ablation of atrial fibrillation: does the addition of three-dimensional magnetic resonance imaging of the left atrium to electroanatomic mapping improve the clinical outcome?: a randomized comparison of Carto-Merge vs. Carto-XP three-dimensional mapping ablation in patients with paroxysmal and persistent atrial fibrillation. *Europace* 2010 Aug;12(8):1098-104.
15. Mitchell JH, Shapiro W. Atrial function and the hemodynamic consequences of atrial fibrillation in man. *Am J Cardiol* 1969 Apr;23(4):556-67.
16. Abhayaratna WP, Seward JB, Appleton CP, Douglas PS, Oh JK, Tajik AJ, et al. Left atrial size: physiologic determinants and clinical applications. *J Am Coll Cardiol* 2006 Jun 20;47(12):2357-63.
17. Lemola K, Sneider M, Desjardins B, Case I, Chugh A, Hall B, et al. Effects of left atrial ablation of atrial fibrillation on size of the left atrium and pulmonary veins. *Heart Rhythm* 2004 Nov;1(5):576-81.
18. von Bary C, Dornia C, Eissnert C, Nedios S, Roser M, Hamer OW, et al. Predictive value of left atrial volume measured by non-invasive cardiac imaging in the treatment of paroxysmal atrial fibrillation. *J Interv Card Electrophysiol* 2012 Aug;34(2):181-8.
19. Nedios S, Tang M, Roser M, Solowjowa N, Gerds-Li JH, Fleck E, et al. Characteristic changes of volume and three-dimensional structure of the left atrium in different forms of atrial fibrillation: predictive value after ablative treatment. *J Interv Card Electrophysiol* 2011 Nov;32(2):87-94.
20. Kuhl JT, Lonborg J, Fuchs A, Andersen MJ, Vejstrup N, Kelbaek H, et al. Assessment of left atrial volume and function: a comparative study between echocardiography, magnetic resonance imaging and multi slice computed tomography. *Int J Cardiovasc Imaging* 2012 Jun;28(5):1061-71.
21. Agner B, Kuhl J, Linde J, Kofoed K, Akeson P, Rasmussen B, et al. Assessment of left atrial volume and function in patients with permanent atrial fibrillation: comparison of cardiac magnetic resonance imaging, 320-slice multi-detector computed tomography, and transthoracic echocardiography. *Eur Heart J Cardiovasc Imaging* 2013 Nov 17.

22. Block M, Hourigan L, Bellows WH, Reeves J, Romson JL, Tran M, et al. Comparison of left atrial dimensions by transesophageal and transthoracic echocardiography. *J Am Soc Echocardiogr* 2002 Feb;15(2):143-9.
23. Singh H, Jain AC, Bhumbra DK, Failing C. Comparison of left atrial dimensions by transesophageal and transthoracic echocardiography. *Echocardiography* 2005 Nov;22(10):789-96.
24. Wen Z, Zhang Z, Yu W, Fan Z, Du J, Lv B. Assessing the left atrial phasic volume and function with dual-source CT: comparison with 3T MRI. *Int J Cardiovasc Imaging* 2010 Feb;26 Suppl 1:83-92.
25. Kurotobi T, Iwakura K, Inoue K, Kimura R, Toyoshima Y, Ito N, et al. The significance of the shape of the left atrial roof as a novel index for determining the electrophysiological and structural characteristics in patients with atrial fibrillation. *Europace* 2011 Jun;13(6):803-8.
26. Bisbal F, Guiu E, Calvo N, Marin D, Berruezo A, Arbelo E, et al. Left atrial sphericity: a new method to assess atrial remodeling. Impact on the outcome of atrial fibrillation ablation. *J Cardiovasc Electrophysiol* 2013 Jul;24(7):752-9.
27. Vergara GR, Marrouche NF. Tailored management of atrial fibrillation using a LGE-MRI based model: from the clinic to the electrophysiology laboratory. *J Cardiovasc Electrophysiol* 2011 Apr;22(4):481-7.
28. Arujuna A, Karim R, Caulfield D, Knowles B, Rhode K, Schaeffter T, et al. Acute pulmonary vein isolation is achieved by a combination of reversible and irreversible atrial injury after catheter ablation: evidence from magnetic resonance imaging. *Circ Arrhythm Electrophysiol* 2012 Aug 1;5(4):691-700.
29. Hunter RJ, Jones DA, Boubertakh R, Malcolme-Lawes LC, Kanagaratnam P, Juli CF, et al. Diagnostic accuracy of cardiac magnetic resonance imaging in the detection and characterization of left atrial catheter ablation lesions: a multicenter experience. *J Cardiovasc Electrophysiol* 2013 Apr;24(4):396-403.
30. Wazni O, Wilkoff B, Saliba W. Catheter ablation for atrial fibrillation. *N Engl J Med* 2011 Dec 15;365(24):2296-304.
31. Hoyt H, Bhonsale A, Chilukuri K, Alhumaid F, Needleman M, Edwards D, et al. Complications arising from catheter ablation of atrial fibrillation: temporal trends and predictors. *Heart Rhythm* 2011 Dec;8(12):1869-74.
32. Manning WJ, Weintraub RM, Waksmonski CA, Haering JM, Rooney PS, Maslow AD, et al. Accuracy of transesophageal echocardiography for identifying left atrial thrombi. A prospective, intraoperative study. *Ann Intern Med* 1995 Dec 1;123(11):817-22.
33. Hilberath JN, Oakes DA, Shernan SK, Bulwer BE, D'Ambra MN, Eltzhig HK. Safety of transesophageal echocardiography. *J Am Soc Echocardiogr* 2010 Nov;23(11):1115-27.
34. Romero J, Husain SA, Kelesidis I, Sanz J, Medina HM, Garcia MJ. Detection of left atrial appendage thrombus by cardiac computed tomography in patients with atrial fibrillation: a meta-analysis. *Circ Cardiovasc Imaging* 2013 Mar 1;6(2):185-94.

35. Ohyama H, Hosomi N, Takahashi T, Mizushige K, Osaka K, Kohno M, et al. Comparison of magnetic resonance imaging and transesophageal echocardiography in detection of thrombus in the left atrial appendage. *Stroke* 2003 Oct;34(10):2436-9.
36. Rathi VK, Reddy ST, Anreddy S, Belden W, Yamrozik JA, Williams RB, et al. Contrast-enhanced CMR is equally effective as TEE in the evaluation of left atrial appendage thrombus in patients with atrial fibrillation undergoing pulmonary vein isolation procedure. *Heart Rhythm* 2013 Jul;10(7):1021-7.
37. Fahlenkamp UL, Lembcke A, Roesler R, Schwenke C, Huppertz A, Streitparth F, et al. ECG-gated imaging of the left atrium and pulmonary veins: Intra-individual comparison of CTA and MRA. *Clin Radiol* 2013 Oct;68(10):1059-64.
38. Piorkowski C, Grothoff M, Gaspar T, Eitel C, Sommer P, Huo Y, et al. Cavotricuspid isthmus ablation guided by real-time magnetic resonance imaging. *Circ Arrhythm Electrophysiol* 2013 Feb;6(1):e7-10.
39. Prieto LR, Kawai Y, Worley SE. Total pulmonary vein occlusion complicating pulmonary vein isolation: diagnosis and treatment. *Heart Rhythm* 2010 Sep;7(9):1233-9.
40. Goo HW, Al Otay A, Grosse-Wortmann L, Wu S, Macgowan CK, Yoo SJ. Phase-contrast magnetic resonance quantification of normal pulmonary venous return. *J Magn Reson Imaging* 2009 Mar;29(3):588-94.
41. Ugander M, Jense E, Arheden H. Pulmonary intravascular blood volume changes through the cardiac cycle in healthy volunteers studied by cardiovascular magnetic resonance measurements of arterial and venous flow. *J Cardiovasc Magn Reson* 2009;11:42.
42. Schuleri KH, Centola M, George RT, Amado LC, Evers KS, Kitagawa K, et al. Characterization of peri-infarct zone heterogeneity by contrast-enhanced multidetector computed tomography: a comparison with magnetic resonance imaging. *J Am Coll Cardiol* 2009 May 5;53(18):1699-707.
43. Nacif MS, Kawel N, Lee JJ, Chen X, Yao J, Zavodni A, et al. Interstitial myocardial fibrosis assessed as extracellular volume fraction with low-radiation-dose cardiac CT. *Radiology* 2012 Sep;264(3):876-83.
44. Kim RJ, Wu E, Rafael A, Chen EL, Parker MA, Simonetti O, et al. The use of contrast-enhanced magnetic resonance imaging to identify reversible myocardial dysfunction. *N Engl J Med* 2000 Nov 16;343(20):1445-53.
45. Peters DC, Wylie JV, Hauser TH, Kissinger KV, Botnar RM, Essebag V, et al. Detection of pulmonary vein and left atrial scar after catheter ablation with three-dimensional navigator-gated delayed enhancement MR imaging: initial experience. *Radiology* 2007 Jun;243(3):690-5.
46. Badger TJ, Oakes RS, Daccarett M, Burgon NS, Akoum N, Fish EN, et al. Temporal left atrial lesion formation after ablation of atrial fibrillation. *Heart Rhythm* 2009 Feb;6(2):161-8.

47. Peters DC, Wylie JV, Hauser TH, Nezafat R, Han Y, Woo JJ, et al. Recurrence of atrial fibrillation correlates with the extent of post-procedural late gadolinium enhancement: a pilot study. *JACC Cardiovasc Imaging* 2009 Mar;2(3):308-16.
48. Badger TJ, Daccarett M, Akoum NW, Adjei-Poku YA, Burgon NS, Haslam TS, et al. Evaluation of left atrial lesions after initial and repeat atrial fibrillation ablation: lessons learned from delayed-enhancement MRI in repeat ablation procedures. *Circ Arrhythm Electrophysiol* 2010 Jun;3(3):249-59.
49. Spragg DD, Khurram I, Zimmerman SL, Yarmohammadi H, Barcelon B, Needleman M, et al. Initial experience with magnetic resonance imaging of atrial scar and co-registration with electroanatomic voltage mapping during atrial fibrillation: success and limitations. *Heart Rhythm* 2012 Dec;9(12):2003-9.
50. Thai WE, Wai B, Lin K, Cheng T, Heist EK, Hoffmann U, et al. Pulmonary venous anatomy imaging with low-dose, prospectively ECG-triggered, high-pitch 128-slice dual-source computed tomography. *Circ Arrhythm Electrophysiol* 2012 Jun 1;5(3):521-30.
51. Piehler KM, Wong TC, Punttil KS, Zareba KM, Lin K, Harris DM, et al. Free-breathing, motion-corrected late gadolinium enhancement is robust and extends risk stratification to vulnerable patients. *Circ Cardiovasc Imaging* 2013 May 1;6(3):423-32.

03



# EVALUATION OF STATE-OF-THE-ART SEGMENTATION ALGORITHMS FOR LEFT VENTRICLE INFARCT FROM LATE GADOLINIUM ENHANCEMENT MR IMAGES

---

Rashed Karim; Pranav Bhagirath; Piet Claus; R. James Housden; Zhong Chen; Zahra Karimaghloo; Hyon-Mok Sohn; Laura Lara Rodríguez; Sergio Vera; Xènia Albà; Anja Hennemuth; Heinz-Otto Peitgen; Tal Arbel; Miguel A. González Ballester; Alejandro F. Frangi; Marco Götte; Reza Razavi; Tobias Schaeffter; Kawal Rhode  
*Med Image Anal.* 2016 May;30:95-107.

## ABSTRACT

Studies have demonstrated the feasibility of late Gadolinium enhancement (LGE) cardiovascular magnetic resonance (CMR) imaging for guiding the management of patients with sequelae to myocardial infarction, such as ventricular tachycardia and heart failure. Clinical implementation of these developments necessitates a reproducible and reliable segmentation of the infarcted regions. It is challenging to compare new algorithms for infarct segmentation in the left ventricle (LV) with existing algorithms. Benchmarking datasets with evaluation strategies are much needed to facilitate comparison. This manuscript presents a benchmarking evaluation framework for future algorithms that segment infarct from LGE CMR of the LV. The image database consists of 30 LGE CMR images of both humans and pigs that were acquired from two separate imaging centers. A consensus ground truth was obtained for all data using maximum likelihood estimation.

Six widely-used fixed-thresholding methods and five recently developed algorithms are tested on the benchmarking framework. Results demonstrate that the algorithms have better overlap with the consensus ground truth than most of the  $n$ -SD fixed-thresholding methods, with the exception of the Full-Width-at-Half-Maximum (FWHM) fixed-thresholding method. Some of the pitfalls of fixed thresholding methods are demonstrated in this work. The benchmarking evaluation framework, which is a contribution of this work, can be used to test and benchmark future algorithms that detect and quantify infarct in LGE CMR images of the LV. The datasets, ground truth and evaluation code have been made publicly available through the website: <https://www.cardiacatlas.org/web/guest/challenges>.

## INTRODUCTION

In recent years, the translation of image analysis tools to the clinical environment has remained limited despite their rapid development. Although algorithms are extensively validated in-house following development, it is often not clear how they compare to other existing algorithms. Algorithm designers are faced with the challenging task of cross comparing their algorithm's performance. The absence of a common pool of data along with evaluation strategies has limited algorithm translation into the clinical workflow. Moreover, as larger cohort data sets become available, the need for reducing the manual labor involved in image analysis is becoming more important. Benchmarking of algorithms on common datasets provides a fair test-bed for comparison. It is thus a very important activity as we move from bench to the bedside in the medical image processing community.

In recent years, several conferences and meetings within the medical image processing community have provided a platform to benchmark algorithms from multiple research groups. These challenges invite participants to submit their algorithms and test them on common data. The results from the test are then evaluated and compared using common evaluation metrics. In the past, a few challenges have been organized, each with its own unique theme. There exists an index of past challenges within the medical image processing community and it can be found on the Cardiac Atlas project page on <https://www.cardiacatlas.org/web/guest/challenges>. In the cardiovascular imaging domain, some recent challenges include left atrial fibrosis and scar segmentation (Karim et al., 2013), left ventricle segmentation (Suinesiaputra et al., 2014), right ventricle segmentation (Petitjean et al., 2015), cardiac motion tracking (Tobon-Gomez et al., 2013) and coronary artery stenosis detection (Kirisli et al., 2013).

## MOTIVATION FOR LEFT VENTRICLE INFARCT SEGMENTATION

Cardiovascular magnetic resonance (CMR) imaging can be used to comprehensively assess the viability of myocardium in patients with ischemic heart disease. Myocardial infarction can be visualized and quantified using inversion recovery imaging 10–15 min after intravenous administration of Gadolinium contrast. This imaging technique is known as late Gadolinium enhancement (LGE) imaging. Experimental models have shown excellent agreement between size and shape in LGE CMR and areas of myocardial infarction by histopathology (Kim et al., 1999; Wagner et al., 2003). Infarct size from CMR is also a primary endpoint in many clinical trials (see Desch et al., 2011 for a complete list).

Recent studies have also demonstrated how infarct size, shape and location from pre-procedural LGE can be useful in guiding ventricular tachycardia's (VT) ablation (Estner et al., 2011; Andreu et al., 2011). These procedures are often time-consuming due to the preceding electrophysiological mapping study required to identify slow conduction zone involved in re-entry circuits. Post-processed LGE images provide scar maps, which can be integrated with electroanatomic mapping systems to facilitate these procedures (Andreu et al., 2011). Clinical implementation of these developments necessitates a reliable, fast, reproducible and accurate segmentation of the infarcted region. Moreover, as use of LGE-based infarct volume estimation becomes more clinically relevant, standardization will facilitate more consistent interpretation.

## STATE-OF-THE-ART FOR CARDIAC INFARCT SEGMENTATION

A short overview of previously published infarct detection algorithms for the left ventricle (LV) is presented here. **Table 1** lists the algorithms surveyed and highlights some of their important features. A common method for detecting infarct in the LV is the fixed-model approach, whereby intensities are thresholded to a fixed number of standard deviations (SD) from the mean intensity of nulled myocardium or blood pool (Flett et al., 2011). In the rest of the paper this will be known as the n-SD method, where  $n = 2, 3, 4, 5$  or  $6$ . A second common fixed-model approach is the full-width-at-half-maximum (FWHM) approach, where half of the maximum intensity within a user-selected hyper-enhanced region is selected as the fixed intensity threshold (Amado et al., 2004). Using this threshold, a region-growing process is employed from user-selected seeds. These seeds are selected to be within infarcted regions such that they can be segmented with region-growing.

As the aforementioned approaches require user input, making them prone to inter- and intra-observer variation, other approaches that are automatic have been developed. Hennemuth et al. (2008) modeled the intensities of homogeneous tissue in LGE CMR with a Rician distributions and an expectation-maximization (EM) algorithm was used for fitting the data. Pop et al. (2013) fitted Gaussian mixture models to myocardial tissue pixel intensities and correlated with histology. In Detsky et al. (2009), clustering in a feature space of steady-state and  $T^*1$  intensity values provided the segmentation which was shown to provide good correlation with FWHM. Tao et al. (2010) employed automatic thresholding using the Otsu method on bi-modal intensity histograms of myocardium and blood pool. More recently, the use of the graph-cut technique in image processing has been applied to segment infarct in several methods (Lu et al., 2012; Karim et al., 2014; Karimaghloo et al., 2012). An advantage of this technique is

**Table 1.** Overview of previously published methods for scar quantification and segmentation.

	Reference	Model	<i>n</i>	Algorithm	Highlight
LV	Kim et al. (1999)	Canine	26	2-SD	Correlation of MRI enhancement with scar
	Amado et al. (2004)	Animal	13	1-6 SD, FWHM	FWHM correlates to histology
	Kolipaka et al. (2005)	Human	23	2,3 SD	Manual correction is necessary despite algorithm
	Positano et al. (2005)	Human	15	Clustering	Fast clustering algorithm
	Schmidt et al. (2007)	Human	47	2-6 SD	Grey-zone and core quantification
	Hennemuth et al. (2008)	Human	21	EM fitting*	Model based on scanner acquisition and reconstruction parameters
	Detsky et al. (2009)	Human	15	Clustering*	Clustering in feature space
	Tao et al. (2010)	Human	20	Otsu thresholding	Dice overlap on chronic myocardial infarction with 2-observer manual segmentation
	Flett et al. (2011)	Human	60	2-6 SD, FWHM	Inter- and intra-observer reproducibility
	Rajchl et al. (2014)	Human	35	SD, FWHM, Max-flow	Inter- and intra-observer reproducibility on 3D CMR
	Andreu et al. (2011)	Human	12	50, 60, 70% FWHM	60% FWHM for good voltage correlation
	Lu et al. (2012)	Human	10	Graph-cuts*	Correlation with FWHM and manual segmentations on chronic myocardial infarction data
Pop et al. (2013)	Animal	9	Mixture model	ex-vivo histology and high-resolution MRI	
LA	Oakes et al. (2009)	Human	81	2-4 SD	LA fibrosis and correlation to recurrence
	Knowles et al. (2010)	Human	7	MIP	Necrosis and edema theory for reconnection, comparison with electroanatomical data
	Ravanelli et al. (2014)	Human	10	SD, Skeletonisation*	Comparison with electroanatomical data
	Karim et al. (2014)	Human	15	Graph-cuts*	Dice with 3-observer consensus delineation
	Harrison et al. (2014)	Animal	16	2-6 SD	ex-vivo histology infarct volume against MR

Methods are listed in chronological order, type of data they were evaluated with and the algorithm for: left ventricle (LV) or left atrium (LA). Methods which report on a segmentation algorithm developed are marked with an asterisk (\*). MIP, maximum intensity projection.

that constraints can be placed on the resulting segmentation, allowing segmentation boundary regularization with region-based properties. It also predicts which pixels are statistically most likely to be infarct based on prior probability distribution models.

## PROPOSED EVALUATION FRAMEWORK

In this paper we propose an evaluation framework for future algorithms that segment and quantify infarct from LGE CMR images of the LV. To demonstrate the framework, five algorithms were evaluated by comparing against a consensus segmentation of experienced observers. The algorithm and observers were both provided the myocardium segmentation. The algorithms were also provided with training data sets. Algorithms evaluated in this work were submitted as a response to the open challenge, put forth to the medical imaging community at the Medical Image Computing and Computer Assisted Intervention (MICCAI) annual meeting's workshop entitled as Delayed Enhancement MRI segmentation challenge. There were thirty LGE CMR data of the LV from both human and porcine cohorts used for the challenge. The data were divided into test ( $n = 20$ ) and training ( $n = 10$ ) sets. Each participant designed and implemented an algorithm which segmented the infarct in each dataset. The datasets are publicly available via the Cardiac Atlas project challenge website <https://www.cardiacatlas.org/web/guest/ventricular-infarction-challenge>

## MATERIAL AND METHODS

### Data acquisition database

LGE images were collected from two imaging centers: Imaging Sciences at King's College London (KCL-IM) and Universiteit Leuven (UL). A total of fifteen human and fifteen porcine datasets were collected, of which five in each cohort were used as a training set for the algorithms. For all datasets, a short-axis stack of DE-MRI images covering the LV were provided. The myocardial mask in each image was made available. This was delineated carefully by an expert observer using short-axis slices. A first step was to determine the basal, mid and apical slices based on the standard American Heart Association (AHA) guidelines (Cerqueira et al., 2002). The contours for epicardial and endocardial borders, excluding the papillary muscles, were carefully drawn on each slice before the enclosed region in between them was filled to produce the mask. The images in the database were limited to the above two different types but varied in their quality. Refer to **Table 2** for a summary of the two different types of data that were included in this study.

**Table 2.** Image acquisition parameters for the challenge LGE patient and porcine datasets.

	KCL-IM	UL
Scanner type	Philips Achieva 1.5T	Siemens Trio 3.0T
Sequence	Segmented 2D, inversion recovery gradient echo ECG triggered, breath-hold	Segmented 3D inversion recovery, gradient echo ECG triggered breath-hold
TI, TR, TE, FA	280 ms, 3.4 ms, 2.0 ms, 25 °	340-370 ms, 2.19 ms, 0.78 ms, 15 °
Resolution	1.8 × 1.8 × 8 mm	1.8 × 1.8 × 6 mm
Interleaving	Every R-R interval in ECG	Every other R-R interval in ECG
Subjects	Human	Porcine

TI, Inversion time; TR, Repetition time; TE, Echo time; FA, Flip angle; ECG, Electrocardiogram. Imaging centers: KCL-IM - Imaging Sciences, King's College London and UL - Universiteit Leuven. Note that the patient dataset was acquired at KCL-IM and porcine dataset was acquired at UL.

The human data (n=15) were from randomly selected patients who had a known history of ischemic cardiomyopathy and were under assessment for an implantable cardioverter defibrillator (ICD) device for primary or secondary prevention after infarction. In addition to this, the patients chosen had a history of myocardial infarction at least three months prior to their MRI scan. There was also evidence of significant coronary artery disease on angiography and evidence of left ventricular impaired systolic function on echocardiography. The images were acquired on a clinical 1.5T MRI unit (Philips Achieva, The Netherlands). All patients gave written informed consent.

The porcine data (n = 15) were randomly selected from an experimental database of a pre-clinical model of chronic myocardial ischemia (Wu et al., 2011), with induced lesions obtained by occluding either the left-anterior descending or left-circumflex artery. The data were acquired six weeks after the induction of the coronary lesion on a clinical 3T MRI unit (Siemens Healthcare, Germany). Representative images are shown in **figure 1**. Five research groups segmented the above datasets, leaving ten images aside, which were utilized for training. A brief summary of their algorithms is given in **Table 3**. They are described in greater detail in the sections below with a brief background on each technique implemented and details of their implementation.

**Table 3.** A brief summary of algorithms that were evaluated on the proposed framework.

Algorithm	Technique	Strengths and weaknesses	Key features	Interaction
<b>AIT:</b> Lara et al.	Otsu, support vector machines and level-sets	Post-processing improves results but increases running time	Otsu with two tissue classes. User selects seed in blood-pool	Semi-automatic
<b>UPF:</b> Albà et al.	Region-growing and morphology	Shapes uncharacteristic of scar are deleted but requires initialization for every slice	Two seeds, for healthy and scar, per slice. Region-labeling step ensures smoothness, filling gaps	Semi-automatic
<b>MCG:</b> Karimghaloo et al.	Conditional random fields	Hierarchical approach with two levels of processing, but uses statistics on a small neighborhood	Posterior distribution model estimated with a direct map and not Gaussian during training	Automatic
<b>MV:</b> Hennemuth et al.	EM-algorithm and Watershed Transformation	No fixed intensity model and the best-fit model is selected, but over-fitting can be an issue	Automated seed-selection in watershed process. Gaussian-mixture or Rician-Gaussian models for fitting intensities with EM algorithm	Semi-automatic
<b>KCL:</b> Karim et al.	Graph-cuts with EM-algorithm	Computes a globally optimal segmentation, but can sometimes reject good candidates.	Gaussian-mixture model fits intensities with EM algorithm using three tissue classes	Semi-automatic
<b>n-SD</b>	n standard deviations from healthy tissue (n = 2, 3, 4, 5, 6)	Simple to implement, but baseline is subjective	Only involves thresholding, no region-growing as FWHM	Semi-automatic
<b>FWHM</b>	50% of user-selected hyper-enhanced myocardium	Validated with histology in literature but was first used to describe a phenomenon in signal analysis	Computed threshold used for region-growing from user-selected seed locations in each slice	Semi-automatic

Institution abbreviations: AIT - Alma IT Systems, and - Universitat Pompeu Fabra, MCG - McGill University, MV - Mevis Fraunhofer, KCL - King's College London.

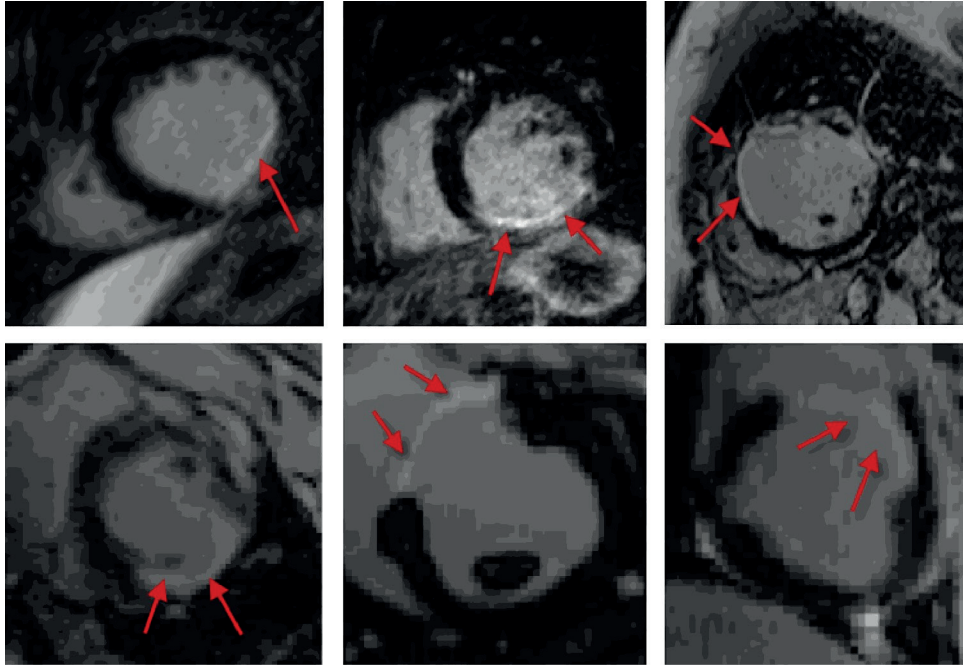


**Figure 1.** Sample datasets: a sample of LGE CMR data included in the challenge. The human (top-row) and porcine (bottom-row) images are shown.

### **Algorithm 1: Alma IT Systems - support vector machines and level sets (AIT)**

Background: Support vector machines (SVM) and level set methods were used to segment scar in this method. SVM is a machine learning technique which first computes the optimal hyperplane on a set of training data mapped to some feature space (Hearst et al., 1998). The hyperplane is a decision boundary which maximally separates the pre-labeled data. Once the hyperplane is obtained, the unseen data is mapped to the same feature space to see which side of the hyperplane it lies in. This labels and thus classifies the unseen data. Level-sets (Sethian, 1999) were also used in this method. In this technique a region evolves from an initial position within the region to be segmented. Level-sets have the added advantage of imposing shape constraints on the evolving region.

Implementation: A number of image processing techniques were employed. In the first stage, an Otsu-based thresholding was used. Here the threshold between healthy and scar tissue was computed by maximizing the intensity variance between the two labels in the intensity histogram (Otsu, 1975). However, as this method was subject to limitations, especially in instances where healthy and scar tissues had overlapping intensities, further steps were necessary. An ensuing connected-component analysis found groups of connected pixels. On these pixel groups, several features relevant to scar were extracted: area, bounding box, major and minor axes, eccentricity, convex-hull area and Euler number (Teague, 1980). This allowed pixel groups to be mapped to a feature space. Several classifiers were tested on the training data provided. These were namely SVM, K-nearest neighbors, linear Bayesian discriminant, and linear perceptron classifiers. SVM was chosen based on the best trade-off between error and sensitivity on the training data (Hearst et al., 1998).

Following classification using SVM, a further level-set-method step refined the segmentations obtained (Sethian, 1999). The contours obtained from the SVM classification step were used to initialize a level-set. The level-set was constrained by the search area obtained in the initial step of the algorithm. It evolved in a speed image  $P(x)$  derived from the SVM classified pixels:

$$P(x) = \begin{cases} I(x) - L, & \text{if } I(x) < \frac{U+L}{2} \\ U - I(x), & \text{otherwise} \end{cases}$$

The values  $U$  and  $L$  were obtained from grey-level intensity  $I(x)$  statistics of the SVM output, i.e.  $U = \mu + 5\sigma$  and  $L = \mu - 5\sigma$ . These parameters are in-line with the standard deviation approach for classifying scar (Karim et al., 2013).

### **Algorithm 2: Universitat Pompeu Fabra - Region growing and morphology (UPF)**

Background: Region-growing is a well-known image processing technique which finds a group of connected pixels with intensity homogeneity. It is an iterative process which starts from a seed point, and the region increases in size by including neighboring pixels that fit a certain pre-defined criteria. Region-growing can subsequently leak into neighboring areas, which is an important limitation of the technique.

Implementation: Seed selection for region-growing was automatic and repeated for each slice, making it essentially a 2D technique. A minimum of two seeds were selected for each tissue class: scar and healthy. The criteria for selecting seeds for the scar tissue class were the following:

$$I > \mu_k + 2 \sigma_k$$

where a pixel in the  $k$ th slice has intensity  $I$  and is subjected to the above test based on mean ( $\mu$ ) and variance ( $\sigma^2$ ) of myocardium intensity. Individual regions satisfying the above criteria were analyzed for their shape and size. Elongated and thin regions near the epicardium were deleted in an automated manner by computing the eccentricity and width (proportion to myocardial mask) of the region in question, on which a thresholding was performed based on empirical values obtained from the training set. The size of negligible regions was defined in proportion to the pixel size and size of the myocardial mask. The two largest and brightest regions were selected as the seeds. This selected seeds for the scar tissue class. For the healthy tissue class, a similar standard deviation approach was utilized (i.e.  $I < \mu_k + 2 \sigma_k$ ) and the two largest and darkest regions were selected as seeds. Region-growing was initiated from each seed region and these generated segmented regions for healthy or scar tissue classes. The choice of two seeds, per slice, for each tissue class is important as it generates two separate disconnected regions. However, this places a limit on the maximum number of scar or healthy regions possible (i.e. two) in each slice.

The region-growing process was followed by a region-labeling step in which pixels that were not labeled as scar or healthy tissue were analyzed; if they contained any adjacent neighbor belonging to either scar and healthy classes, they were labeled as such. This was followed by a post-processing step to fill holes or small gaps in the segmentations. Also, regions that were small islands containing a negligible number of pixels were removed from the segmentation. Finally, dark regions that lacked contrast, but were surrounded by scar pixels were re-labeled as scar. This is characteristic of a microvascular obstruction.

### **Algorithm 3: McGill - conditional random fields (MCG)**

Background: The previous methods described are geometrical in their nature; a region's intensity and its geometrical shape are used to determine its classification. The method described in this section is different from the above approaches in that a probabilistic classifier model was used. Based on the training dataset, the classifier can infer the posterior distribution of a pixel's label to be healthy or scar given the observation. There are two sets of observations made: (1) the pixel's intensity, and (2) the pixel's

neighborhood. Since labels of neighboring pixels are typically correlated, neighborhood information is incorporated by building a graphical model  $G(V, E)$ , where voxels are represented by a set of nodes ( $V$ ) and the relationships among them are represented by edges ( $E$ ). In the generative Markov random field (MRF) (see Boykov et al., 2001), the Bayes' relationship is used to determine the posterior distribution:

$$p(Y|X) = \frac{p(X|Y)p(Y)}{p(X)}$$

(3) where  $X$  is the unseen image to be segmented and  $Y$  is the labeling into healthy and scar. The likelihood  $p(X|Y)$  of the unseen image is estimated by assuming that the voxel intensities in  $X$  are independent given the labels. Also, a uni-modal Gaussian is often used. However, in the context of medical image segmentation, regions are not random collections of independent pixels. Instead, structures usually form coherent and continuous shapes. In this work, a conditional Markov random field (CRF) (Lafferty et al., 2001) is used which is a discriminative framework and the posterior  $p(Y|X)$  is estimated by learning a direct map from observations to the class labels (i.e. in training images). This is how it differs from other MRF approaches used in binary classification, where the posterior is estimated using Gaussian distributions.

Implementation: The CRF implemented in this work used a hierarchical approach and is described in Karimaghloo et al. (2012). There are two levels of CRF: in the first level image intensity information was used, and in the second level, a so called spin image feature vector derived from intensity information was used. In the first level CRF, the posterior distribution  $p(Y|X)$  was estimated as in a conventional CRF (Lafferty et al., 2001):

$$p(Y|X) = \frac{1}{Z} \exp \left[ \sum_{i=1}^n \phi(y_i|X) + \sum_{j \in N_i} \varphi(y_i, y_j|X) + \sum_{j, k \in N_i} \psi(y_i, y_j, y_k|X) \right]$$

where  $Z$  is a normalization term and  $\phi$ ,  $\varphi$  and  $\psi$  are unary, pair-wise and triplet potentials respectively. Pairwise and triplet potentials measure the interaction between pixels that are immediate neighbors (pairwise) and neighbor's neighbors (triplet). As regions in MRI images are not random collections of independent pixels but part of coherent and continuous shapes, the pairwise and triplet potentials reinforce this notion. The unary

potentials  $p(y_i | x_i)$  computed the inference on the healthy or scar labels ( $y_i$ ) from the MRI intensity observed at pixel  $i$ . This potential was modeled from labeled training data provided within the challenge using:

$$\phi(y_i | X) = \log p(y_i | x_i)$$

where  $y_i$  is the label and  $x_i$  is the observed intensity at voxel  $i$ . A binary classifier was employed for the purpose of distinguishing between healthy and scar. The decision boundary was learned from training data using a variant of support vector machines (SVM) known as relevance vector machines (RVM) (Tipping, 2001). The final classification of the first-level CRF was performed using a graph-cut optimization framework (Boykov et al., 2001).

In the second-level CRF, using infarction candidates from the first level, a two dimensional histogram encoding the distribution of image brightness values in the neighborhood of a particular reference point was constructed. This is the spin image which encoded local information around infarct candidates. Besides voxel intensity, these spin image features were also used for CRF. Similar to the first-level CRF, the final inference was performed using a graph-cut optimization framework.

#### **Algorithm 4: Mevis Fraunhofer - EM-algorithm and watershed transformation (MV)**

Background: The method presented in this work assumes that the voxel intensity distribution in MR images can be modeled using statistical distribution models. Depending on acquisition parameters and the reconstruction algorithm, it can either be modeled using a Gaussian, Rayleigh or non-central  $\chi$ -distribution (Dietrich et al., 2007). These distributions are also closely related to the Rician distribution, making it suitable for modeling healthy myocardium intensities. For diseased myocardium the Rician-Gaussian mixture was found to be appropriate, and for necrotic tissues, the non-central  $\chi$ -distribution was shown to be suitable (Hennemuth et al., 2008).

The watershed segmentation approach was used in this method (Hennemuth et al., 2008). Watershed is a classical image segmentation technique where the gradient image is considered as a topographic surface. Structures such as scar can be assumed to have high intensity gradients at edges and low gradients in the interior. This high-low-high intensity gradient profile creates basins in the image. Once points are located inside each basin they can be segmented by following paths of decreasing altitudes on the topography of the gradient image.

**Implementation:** In this work, three separate models were considered: Rician, Rician-Gaussian and Gaussian models. Each model was fitted to the myocardium intensity distribution in the unseen image. The model with the least mean fitting error was chosen. To achieve an optimal fit, the Expectation-Maximization (EM) algorithm was used. Two classes corresponding to healthy and scar were chosen to initialize the EM fit.

A threshold was then derived from the mixture distribution obtained from the EM-fitting process. This is the higher of the two means in the two-class mixture model. Using Euclidean distance in 3D and endocardial voxels computed from the myocardium segmentation, voxels with intensity higher than the threshold and closer to the endocardium were chosen as seeds for the watershed process. These seeds were used to define the basins and the watershed transformation determined the extent of each basin. The basins determined each location to be labeled as scar. An ensuing connected-components analysis step removed small noisy structures.

### **Algorithm 5: KCL - Graph-cuts with EM-algorithm (KCL)**

**Background:** The background of the method used in this work is in some ways similar to the method proposed by MCG in Section 2.4 except that it employs a non-conditional MRF solved using graph-cuts. The image to be segmented is modeled as a graph with paths or links between neighboring pixels. For each pixel there is also a link to two special nodes also known as source and sink nodes that correspond to scar and healthy myocardium. Each link is assigned a weight based on its intensity. The graph-cuts approach computes a partitioning to divide the graph into two sub-graphs, one containing the source node and the other the sink node. This partitioning assigns a label (source or sink) to each pixel solving the segmentation as an optimization problem. It searches for a globally-optimal solution.

**Implementation:** In the graph-cuts approach implemented in this work, each pixel in the myocardium was modeled as a node in the graph with links to source and sink nodes. These links were assigned weights representing the affinity to healthy (i.e. source) and scar (i.e. sink) nodes. The weights were derived from statistical distribution models developed from training images. There were separate intensity distribution models for healthy and scar tissue, both of which were derived from the training images. For scar, the ratio of delayed enhancement intensity to mean blood pool was modeled using a Gaussian distribution. For healthy tissue, a Gaussian mixture was used. The number of mixtures in the model was fixed at three. The standard EM-algorithm computed mean and variance for each mixture from the training images. In the graph-cuts framework there are also links between adjacent pixels and these were derived from a measure of intensity similarity of two pixels. Adjacent pixels with similar intensities attained a high

weight. This enforced coherence in the segmentation output. The final segmentation was obtained using global optimization over the entire image. This allowed for disjointed infarct regions to be identified in the image.

### **Algorithm evaluation**

Reference standard: consensus ground truth, a reference standard for scar in each case was obtained by combining volumetric segmentations from three separate observers. All observers were cardiologists with several years' experience in CMR assessment of LV function and tissue viability. They also had several years' experience working with patients suffering from ischemic heart diseases. For both datasets, they were blinded to the underlying clinical situation of patients and pigs. For pigs, lesions were obtained by occluding either the left-anterior descending or left-circumflex artery, and the observers were blinded to this fact. The observers were not instructed to look for areas of grey zones.

For regions affected by microvascular obstructions, they were instructed to avoid these by looking for regions of significant hypo-enhancement surrounded by enhanced regions.

Scars in the images were segmented as follows: (1) Each slice in the LGE CMR was analyzed separately in the short-axis view. The segmentation of the myocardium was loaded as an overlay. (2) The basal, mid and apical slices were identified along with the LV orientation, i.e. the posterior and anterior ends. (3) The short-axis slices were then analyzed one at a time sequentially from basal to apical or apical to basal. (4) The basal slices were then examined for non-scar related enhancements (see Turkbey et al., 2012) such as the right ventricle (RV) insertion point, and partial voluming in the basal slices due to the outflow tract and appendage. The mid and apical slices were also examined for coronary arteries carrying blood that could be enhanced, and microvascular obstructions. (5) Pixels enhanced within myocardium were labeled as scar and generally noisy pixels or regions were avoided. Noise observed in the lungs was used as a reference.

Each observer was provided with the same set of guidelines as above. However, their segmentations differed in some instances. This was generally due to differences in their opinion and experience. Such inter-observer variability is now widely accepted. It was thus important to merge the segmentations and obtain a consensus ground truth. A maximum likelihood estimation of ground truth was obtained using a published algorithm known as the STAPLE (Warfield et al., 2004). For every voxel, a probabilistic estimate of the true segmentation was computed using an optimal combination of

the observers' segmentations. The final consensus segmentation was then obtained by thresholding this probability above 0.7 or 70%. This is referred to in the rest of the text as the consensus ground truth.

### Common algorithms: n-SD and FWHM

Quantification of scar in LGE CMR images using a fixed model is often desirable and commonly used as it includes fewer image processing steps, with some studies advocating its reproducibility (Flett et al., 2011; Amado et al., 2004). In fixed models, scar is quantified by thresholding intensities at a fixed distance from a reference intensity value. Two types of fixed models were used, namely FWHM and the n-SD method. FWHM is a technique where half of the maximum intensity within a user-selected hyper-enhanced region is selected as the fixed intensity threshold for an ensuing region-growing step (Amado et al., 2004). In the region-growing step, infarcted regions are segmented based on user-selected seed points. These are used to initialize the region-growing step. The n-SD method (where  $n = 2, 3, 4, 5, 6$ ), uses a fixed number of standard deviations from mean signal within healthy myocardium. A manual region-of-interest (ROI) selection was required in both techniques. In FWHM, a ROI was delineated in hyper-intense myocardium. In n-SD, a ROI was delineated in remote myocardium. Remote myocardium was defined as a region with no enhancement and normal wall motion. Endocardial and epicardial surfaces were avoided in the delineation.

### Evaluation metrics

Segmentations from each algorithm were compared against the reference standard for scar. As no single metric is advocated as the best metric, two different types of metric were chosen for evaluating the segmentations. These were overlap and volumetric measures, and they are briefly described below: 1. Overlap metric: The Dice similarity is a metric for segmentation overlap measuring the proportion of true positives in the segmentation:

$$s = \frac{2|X \cap Y|}{|X| + |Y|}$$

where  $X$  is the segmented region in the ground-truth and  $Y$  is the region in the challenger's algorithm.

2. Volumetric-based metric: The total volume error between the algorithms's output and reference standard was found:

$$\delta V = |V_T - V_G|$$

where  $V_T$  is the volume of scar in the algorithm segmentation and  $V_G$  is the volume of scar in the consensus segmentation.

### Objective evaluation

In LGE CMR of the LV, hyper-enhanced areas not relating to scar are not uncommon (Turkbey et al., 2012). Unless the characteristic and geometry of these pseudo infarcts are explicitly modeled into the technique, it is challenging for an algorithm to distinguish them. Some common sources of pseudo infarcts seen in LGE CMR of the LV are: (1) the location of the RV insertion point, (2) partial voluming in basal slices due to the outflow tract and the appendage, and (3) hyper-enhanced areas due to epi- and pericardial fat. An experienced observer selected regions containing the aforementioned enhancements. These were identified using simple techniques such as checking for continuity of scar or artifact in the adjacent slices, i.e. if it continues then it is likely to be scar. Some instances of pseudo infarcts occurring in the patient dataset are shown in **figure 2**. To evaluate how the algorithms handled pseudo infarcts, each algorithm's output was evaluated separately on these regions. The percentage of voxels detected by each method in these spurious regions was determined.

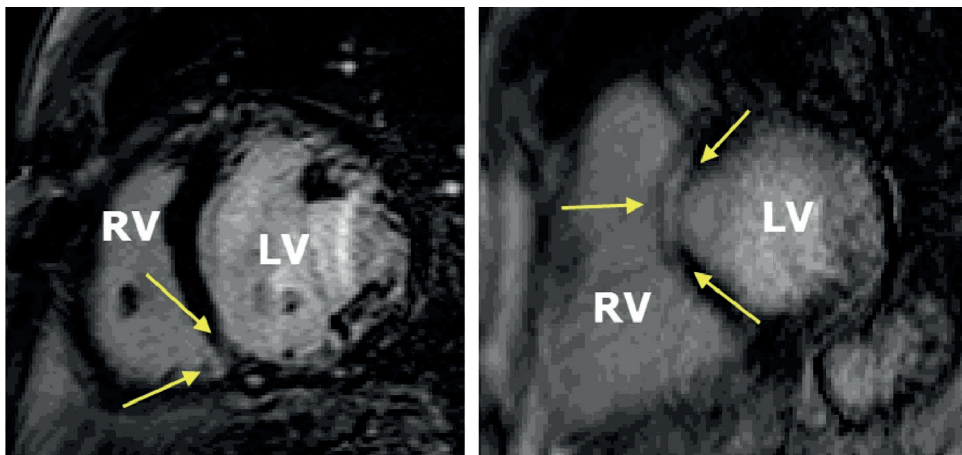


**Figure 2.** Examples of pseudo infarct in the patient database.

Arrows indicate enhancements due to the right ventricle insertion point (left) and outflow tract (right).

A good contrast between normal myocardium, blood pool and infarct is challenging and greatly depends on achieving the optimal inversion time. Each scan in the image database was scored by five raters experienced in LGE CMR images. The rating with maximum votes determined the scan's rating. Scans in the image database were ranked into three categories: good, average and poor. The Dice metric was computed separately in each category. This indicated how robust the algorithms were against contrast enhancement quality.

## RESULTS AND DISCUSSION

### Segmentation accuracy against consensus ground truth

On the patient and porcine LGE CMR scans, segmentations from the algorithms were compared to the consensus ground truth. A consensus was available by combining segmentations from three separate observers. Segmentation accuracies measured using the Dice metric are shown in **figure 3** for the patient dataset. The Dice overlaps between algorithm and consensus were determined on an automatically determined region-of-interest (ROI) enclosing each individual region of infarction labeled in the consensus. The medians of these individual Dice overlaps were as follows: AIT = 73, KCL = 74, MCG = 85, MV = 44, and UPF = 70. Fixed model approaches for segmenting scar (i.e. n-SD and FWHM) were also compared with the consensus ground-truth. The median Dice overlaps were: 2-SD = 47, 3-SD = 54, 4-SD = 55, 5-SD = 62, 6-SD = 64, FWHM = 78. An example of a single slice from the patient dataset is shown in **figure 5**.

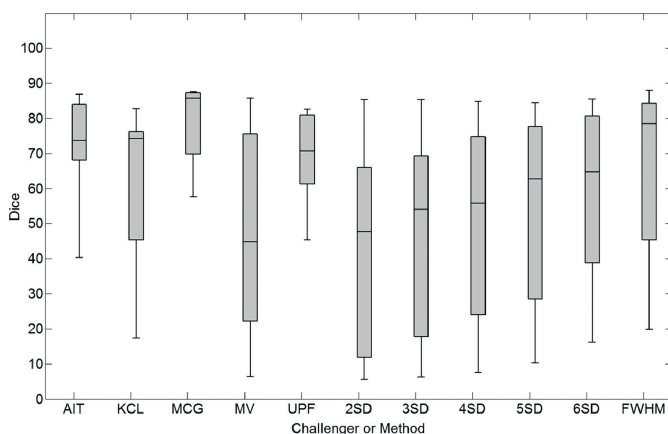


**Figure 3.** Performance on patient datasets: segmentation accuracy on the patient dataset. The figure also displays results from 2-SD, 3-SD, 4-SD, 5-SD, 6-SD and FWHM. Dice was computed on every individual region of scar found in the consensus segmentation.

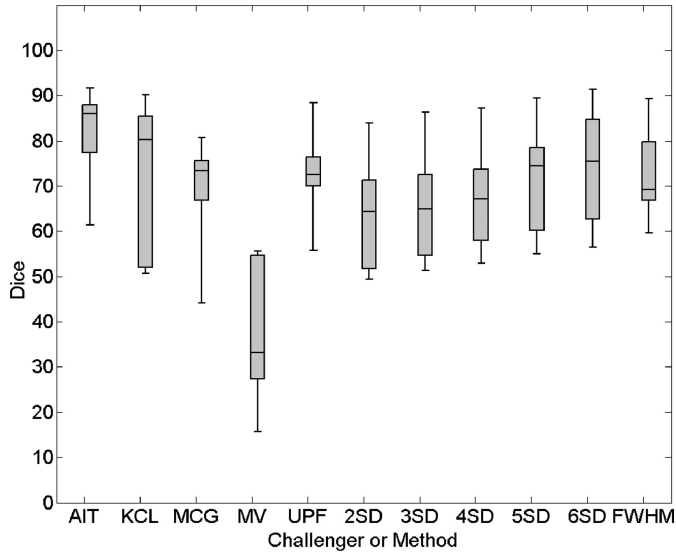


**Figure 4.** Performance on porcine datasets: segmentation accuracy on the porcine dataset. The figure also displays results from 2-SD, 3-SD, 4-SD, 5-SD, 6-SD and FWHM. Dice was computed on every individual region of scar found in the consensus segmentation.

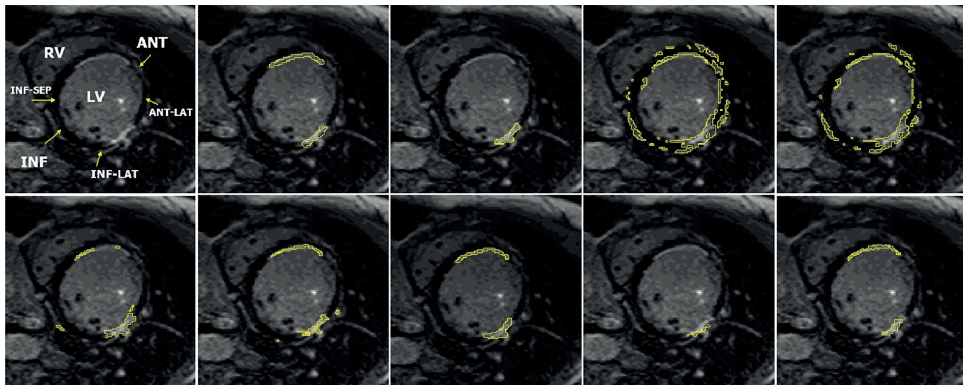


**Figure 5.** Example segmentation from the patient dataset.

Clockwise from top-left: original LGE CMR, consensus segmentation, FWHM, 5-SD, 6-SD, AIT, KCL, MCG, MV, UPF. Abbreviations: LV - left ventricle, RV - right ventricle, ANT - anterior, INF - inferior, INF-SEP - infero-septal, INF-LAT - infero-lateral, ANT-LAT - antero-lateral.

On the porcine LGE CMR scans segmentations from the algorithms and fixed-model approaches were compared in a similar way to the patient dataset. The Dice overlap metric is plotted in **figure 4** for each submitted algorithm and fixed model. The Dice overlaps were determined, as above, on ROIs enclosing each region of infarction labeled in the consensus. The medians of these individual Dice overlaps were as follows: AIT = 86, KCL = 80, MCG = 73, MV = 33, and UPF = 73. Standard methods using fixed models were also compared with the consensus ground-truth and the median Dice overlaps were: 2-SD = 64, 3-SD = 65, 4-SD = 67, 5-SD = 74, 6-SD = 76, FWHM = 69. An example of a single slice from the porcine dataset is given in **figure 6**.

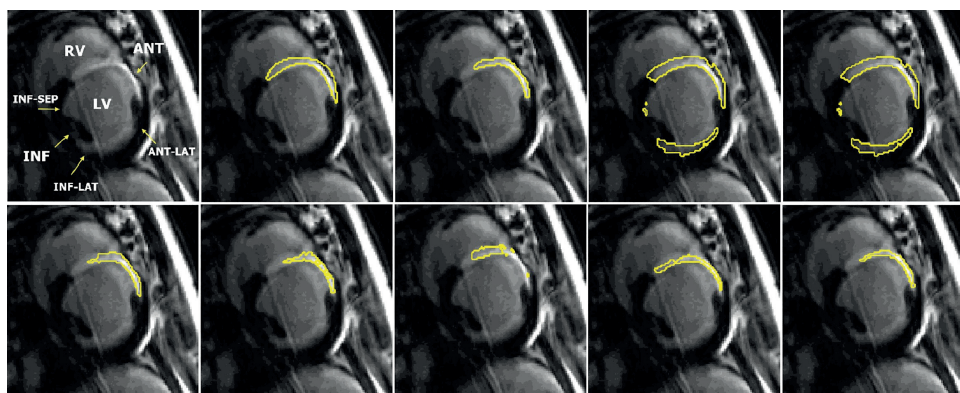


**Figure 6.** Example segmentation from the porcine dataset.

Clockwise from top-left: original LGE CMR, consensus segmentation, FWHM, 5-SD, 6-SD, AIT, KCL, MCG, MV, UPF. Abbreviations: LV - left ventricle, RV - right ventricle, ANT - anterior, INF - inferior, INF-SEP - infero-septal, INF-LAT - infero-lateral, ANT-LAT - antero-lateral.

The Dice scores, reported above, were evaluated within ROIs enclosing scar in the consensus segmentation. These areas can often be large sections within the image, especially if the scar is continuous and extends to several slices. This provided for a more objective evaluation. The algorithm's false positive outside the ROI is not accountable. To counteract this issue, segmentations were also compared by quantifying volume differences. This was determined by measuring the difference in total volume of scar between the consensus and algorithm segmentation. An algorithm could be deemed as accurate only when it yielded a good Dice together with a small volume difference. **Table 4** lists the mean volume differences and variance (as milliliters) over the entire image database for patient and porcine datasets.

**Table 4.** Segmentation accuracy with volume difference ( $\delta V$ ) on patient and porcine data for submitted algorithms and fixed-models. The standard deviation of each metric is quoted in brackets.

	<b>Patient data</b>   $\delta V$   (ml)	<b>Porcine data</b>   $\delta V$   (ml)
AIT	0.77 (0.7)	0.84 (0.5)
KCL	1.05 (1.0)	0.73 (0.5)
MCG	1.02 (0.5)	0.54 (0.1)
MV	1.70 (2.3)	0.75 (0.3)
UPF	0.70 (0.3)	0.97 (0.7)
2-SD	8.55 (0.4)	4.00 (0.2)
3-SD	6.71 (0.3)	3.52 (0.8)
4-SD	5.20 (0.2)	2.92 (0.8)
5-SD	3.92 (0.3)	2.44 (0.1)
6-SD	2.96 (0.3)	2.08 (0.1)
FWHM	3.10 (1.0)	2.20 (0.2)

To further evaluate more objectively, the Dice overlap of the algorithms' segmentations were compared to the consensus based on the slice position (basal, mid and apical). Short-axis slices were subdivided according to the standard guidelines (Cerqueira et al., 2002). The results are plotted in **figure 7**. It is not clear what should be a good Dice overlap for datasets of this type. To address this issue, the degree of agreement between observers and the computed consensus was analyzed and plotted in **figure 8**. It provided for an estimation of a reasonable target (i.e. good Dice score) for the evaluated algorithms.

### Pseudo infarct regions

The algorithms were evaluated on hyper-enhanced regions which mimic scar. These pseudo infarct regions occur for several aforementioned reasons and illustrated in **figure 2**. In each image, pseudo infarct was manually segmented by an experienced observer. These regions were either confirmed anatomically in the case of the outflow tract or by checking adjacent slices for scar continuity in the case of partial voluming. In each image, the total volume of pseudo infarct labeled by the observer was quantified. The total volume of these spurious infarct regions present in each algorithm and fixed model segmentation was also quantified. This was possible by comparing each segmentation to the manual labeling of pseudo infarcts. Results are represented in **figure 10**. KCL and MCG had a higher proportion of manually labeled pseudo infarct regions detected on

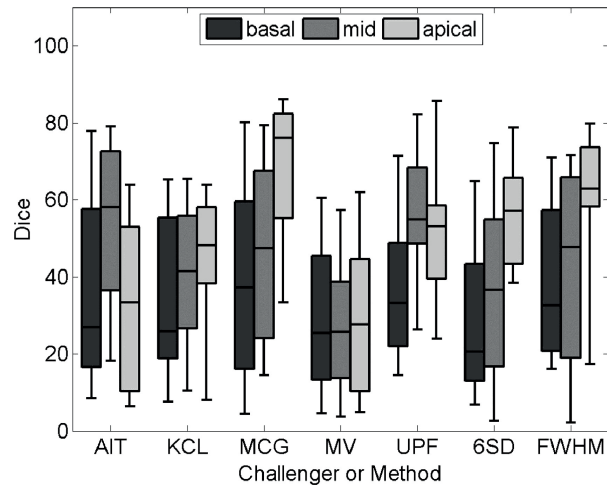


**Figure 7.** Plot showing the characterization of Dice by slice location (basal, mid and apical) by combining results from the patient and porcine datasets.

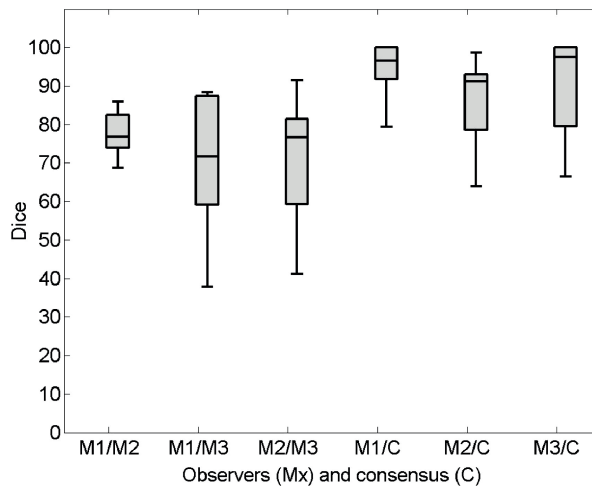


**Figure 8.** Plot showing agreement between observers' segmentations (M1, M2 and M3) and consensus segmentation (C) on the combined patient and porcine datasets. For example, M1/M2 is the Dice agreement between observer's M1 and M2.

average than other methods at 21 and 23%, respectively of pseudo infarct labeled by the observers. This is in comparison to MV, AIT and UPF with only 3, 9 and 3%, respectively. Fixed models 2, 3, 4, 5, 6-SD and FWHM contained 53, 44, 36, 30, 24 and 23% respectively of manually labeled pseudo infarct volume. Pseudo infarcts were most successfully avoided in the MV and UPF algorithms and least in the 2, 3, 4 and 5-SD methods.

### Image quality on segmentation

The LGE CMR images in the database were acquired at different imaging centers with differing protocols and scanners (see **Table 2**). The quality of enhancement is known to vary and it depends on a number of factors including optimal inversion times, signal-to-noise and contrast-to-noise (CNR) ratios. The images in the database were qualitatively rated by five observers experienced in LGE. Images were rated as poor, average or good depending on the overall quality of the image. The Dice overlap was measured separately in each category and these are given in **Table 5**. In both the good and average categories, there were 40%, 60% from the patient and porcine datasets respectively; in the poor category, there were 75%, 25% from the patient and porcine datasets, respectively. A representative set of images for each quality is shown in **figure 9**.

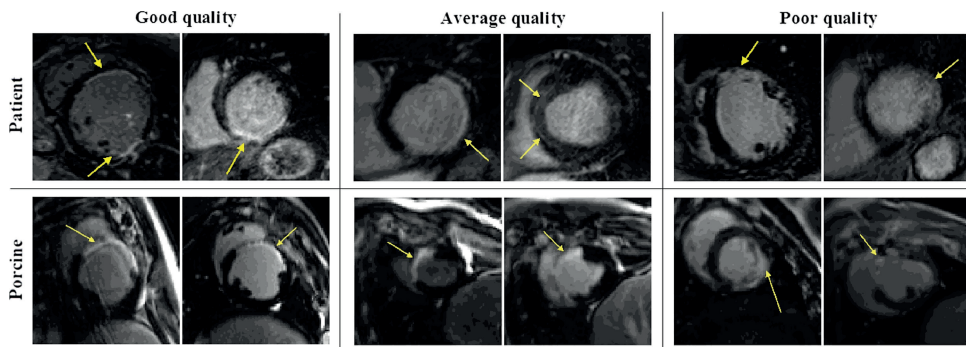


**Figure 9.** Images in the patient and porcine datasets that are representative of good, average and poor quality images. The arrow labels indicate sites of possible infarction as labeled by an observer. There are two images shown for every quality.

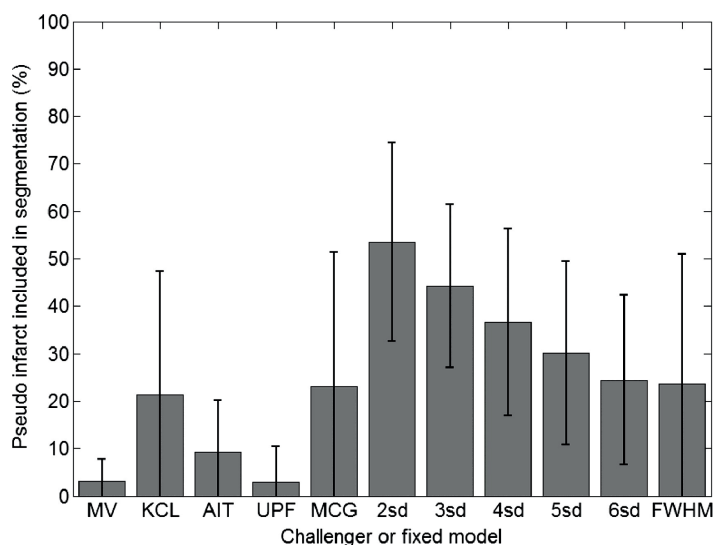


**Figure 10.** The proportion of pseudo infarct manually labeled by expert observer that was detected by each method. Pseudo infarcts included hyper-enhanced regions at the right ventricle insertion points, aortic outflow tract, epi- and pericardial fat.

**Table 5.** Analysis of segmentation accuracy based on image quality (good, average and bad) on human and porcine datasets combined. The mean, standard deviation (SD) and median of the Dice for each challenger (AIT to UPF) and fixed-model method (2-SD to FWHM) is quoted.

Challengers	Poor	Average	Good
	Mean (SD), Median		
AIT	48 (19), 47	68 (23), 69	89 (9), 89
KCL	47 (22), 47	60 (23), 57	66 (20), 65
MCG	42 (25), 42	58 (18), 59	53 (24), 33
MV	41 (25), 40	32 (22), 38	38 (25), 35
UPF	46 (22), 37	52 (20), 45	44 (21), 45
2-SD	53 (22), 56	46 (22), 37	52 (20), 52
3-SD	56 (27), 61	48 (21), 39	52 (23), 54
4-SD	60 (21), 69	52 (21), 44	56 (26), 56
5-SD	66 (21), 75	55 (21), 49	59 (29), 58
6-SD	69 (21), 76	57 (19), 55	61 (32), 61
FWHM	63 (24), 64	54 (23), 51	55 (28), 54

## DISCUSSION

We have presented a framework which standardizes evaluation of algorithms for segmenting scar in the LV. The framework was used to evaluate and compare five algorithms and six separate fixed model thresholding approaches (i.e.  $n$ -SD and FWHM). The algorithms were submitted as part of the STACOM challenge, a workshop organized at MICCAI in 2012. The data is publicly available via the website at: <https://www.cardiacatlas.org/web/guest/ventricular-infarction-challenge>.

### Evaluation framework

The presented evaluation framework comprises of both human and animal LV LGE CMR datasets and their respective myocardial segmentation masks. Human datasets were acquired from patients with a history of ischemic cardiomyopathy. The animal datasets were acquired in a pig model of myocardial infarction induced by coronary stenosis. Datasets were also acquired using different scanner vendors and resolutions. The human datasets were acquired with a 1.5T Philips scanner and the animal datasets were acquired with a 3T Siemens scanner. There were both 2D and 3D (non-isotropic) acquisitions. This ensured that algorithms evaluated on the framework were not biased to a specific acquisition protocol, scanner vendor or resolution. The proposed framework provides data acquisitions that are both commonly-used and modern, making it suitable for testing and evaluating state-of-the-art algorithms.

It is often challenging to establish ground truth on infarcted regions in LGE CMR. This makes algorithm evaluation difficult. The framework addresses this issue by proposing a reference standard against which the algorithms can be reliably evaluated. To achieve a reference standard, the human and animal datasets were manually segmented by three experienced observers provided with epi- and endocardial boundaries and a set of guidelines. Although, their delineations were consistent, some differences remained. The three expert delineations were combined to obtain a consensus segmentation of all three observers. The STAPLE algorithm (Warfield et al., 2004), which uses a probabilistic estimate of the true segmentation to derive the consensus, was used to obtain a consensus segmentation. The degree of agreement between observers and the computed consensus was analyzed in Fig. 8 and this not only allows the assessment of agreement but also quantitatively provides for an estimation of a good Dice score in such datasets. In addition to the reference standard for scar, six commonly-used and established fixed thresholding models were used to see how they compare with the algorithms. These were namely the  $n$ -SD (where  $n = 2, 3, 4, 5, 6$ ) and FWHM methods (Amado et al., 2004; Schmidt et al., 2007). The FWHM method is implemented as

described in Amado et al. (2004), where the user clicked on hyper-enhanced regions within myocardium and an ensuing multi-pass region growing algorithm segmented infarct using the FWHM criterion.

Algorithms are often evaluated on various different metrics. This makes comparison of algorithms challenging. Most of the methods surveyed in **Table 1** either use LGE volume or represent it as a percentage to evaluate detected enhancement (for example in Flett et al. (2011) ; Harrison et al. (2014) ), or compare the amount of overlap with manual segmentation using the Dice metric (for example in Tao et al. (2010) ; Ravanelli et al. (2014) ). The framework evaluated algorithms on both scales-volume and Dice metric. For the Dice metric, segmentations were evaluated on individual infarcted regions in the image. A Dice metric on the entire image has its pitfalls as it is difficult to ascertain within which local regions algorithms fail or succeed. This was addressed using a localized Dice evaluation strategy. Future algorithms tested on the framework will be subjected to the same metrics enabling algorithms and their segmentations to be compared in a reliable manner.

The presence of pseudo infarct, which mimics scar in LGE CMR images, poses various challenges for algorithms. Earlier algorithms have not addressed or incorporated this into its segmentation models. The framework provided delineations of pseudo infarct regions from an experienced observer. Algorithms were assessed on the proportion of false positives due to pseudo infarct regions. This has allowed a more objective evaluation within this framework. The n-SD and FHWM fixed models segmented a large proportion of pseudo infarct labeled by the observer. The algorithms segmented significantly less pseudo infarcts than fixed models (paired t-test  $p < 0.05$ ). Furthermore, images in the database were qualitatively rated for its quality by five different observers. Algorithms' segmentations were also evaluated separately based on the image's rating.

The proposed framework has several limitations. An important limitation is that the framework cannot be used to directly evaluate clinical utility or anatomic accuracy of the algorithms. This is since the reference standard does not include any information about outcomes (for the patient data set) or histology (for the pig data set). Another limitation is the image database size which is 30 images, of which 20 that can be used for testing and 10 usable for training. However, within this small sample, it provides a range of datasets from different scanner vendors, scanner resolution and cohorts.

A second limitation is the dimensionality of the dataset. The human datasets are 2D acquisitions with 8 mm slice thickness. 2D images are commonly employed clinically for treatment stratification. For example based on the infarct volume and ejection fraction

from 2D images, a patient could be subjected to certain therapeutic strategies, such as an implantable cardioverter defibrillator (ICD) implantation or ventricular ablation. 3D images provide more detailed quantification of infarct and only the porcine dataset within this framework are 3D non-isotropic acquisitions. A third limitation is the manner in which the Dice metric is computed individually on each region of infarction labeled by the consensus. The Dice is computed only within ROIs enclosing each consensus-labeled infarct. Outside these regions, the Dice is not accountable. Thus, algorithms which over-segment can still exhibit a good Dice but poor volume error. The Dice need to be combined with the volume error to give a clearer understanding.

Intensity variation across the images due to coil shading may have an impact on segmentation, especially for methods which process absolute signal intensities. A coil sensitivity scan is a routine part of the acquisition protocol used to acquire the datasets of this study. However, no further coil sensitivity correction was carried out. This was in-line with the principal of this study to use only routine MRI scans.

A final limitation is that only one observer was employed to segment the myocardial masks. The observer was a cardiologist with several years of experience in CMR assessment of LV function assessment and ischemic heart diseases. The issue of variability with different myocardial masks is counteracted by providing the human observers with these masks. The algorithms are also provided with the same masks. This ensures that infarct within the mask are labeled and computed. Thus, the evaluation is only carried out in the myocardial mask space.

## **Evaluated algorithms**

Quantifying infarct in the LV can have important clinical implications. A 3D rendering of the LV with infarct areas can be integrated into electro-anatomical systems for facilitating catheter ablation. As the resolution and SNR of LGE CMR continues to improve, detailed quantification of infarct is becoming possible. The pitfalls of fixed thresholding models advocated in past literature (Amado et al., 2004; Kim et al., 1999) have been highlighted in recent studies (Harrison et al., 2014). Fixed threshold model makes crude assumptions about the contrast levels between nulled blood pool and infarct, deeming a fixed cut-off threshold. However, as these contrast levels are directly dependent on the inversion time selected in LGE CMR, the preset threshold often requires user readjustments.

The algorithms were evaluated based on the slice position (basal, mid and apical) (see **figure 7**). In the analysis, there was no significant difference between the basal and mid slices. The apical slices showed better overlap for some algorithms. However, apical slices enclose a smaller myocardial area and thus the overlap assessments in these

regions can be biased. However, it is important to note that the Dice overlap used here was slice-based and not region-based as compared to the other results in this work. In general, with Dice scores, it is difficult to ascertain a good Dice for datasets of the nature included in this study. The analysis of agreement between the observers' segmentations (see **figure 8**) provide for a reasonable estimation and target for the algorithms.

The algorithm's comparison to common algorithms is important. The difference with FWHM remains small except for MCG, which was able to provide high accuracy in the patient dataset, and AIT providing the same in the porcine set. Both methods have considerable strengths, with the former using a state-of-the-art probabilistic technique for image segmentation, and the latter benefitting from post-processing steps which rectify the segmentation. The Dice results reflect the strengths of these methods. On the patient datasets, algorithms AIT, MCG and UPF performed similarly while KCL and MV also performed similarly but with a lower average Dice. This was due to greater variability in Dice for KCL and MV. However, AIT and UPF are both capable of rectifying errors in its segmentation with post-processing steps. AIT employs level-sets following SVM classification and UPF employs shape discriminants. Both KCL and MV rely heavily on its core segmentation process, with no post-processing. As a result, spurious regions are included. Models that are sub-optimal were able to benefit from post-processing.

The algorithms were also evaluated on the total infarct volume it segmented (see **Table 4**) and these volumes were compared to the consensus volumes. This is important as Dice computed in this work has the aforementioned limitations. Also, when evaluating the myocardium, quantification of infarct volume is an important step. The average volume error in challenger's algorithms were 1.04 ml and 0.76 ml for patient and porcine datasets respectively (from **Table 4**). This was low compared to the overall average infarct volume in the datasets (see **Table 6**).

**Table 6.** The mean infarct volume (in milliliters) and average number of regions (i.e. infarct) per slice in the consensus segmentation.

	Patient data	Porcine data
Mean infarct volume (ml)	5.38 (6.73)	13.81 (8.70)
Average regions per slice	1.2 (0.5)	1.0 (0.1)

The algorithms evaluated on the framework have common traits – most employ region-based image processing techniques, for example level-set (AIT), region-growing (UPF and FWHM) and watershed (MV). This is justifiable as the algorithms are meant to

segment infarct that has contiguous regions. However, key considerations such as the shape of candidate regions, are not always taken into account. UPF searches for regions that are elongated, as this is a strong characteristic of LV infarcts. A second important consideration is the seed selection step. If only a single seed is allowed per slice for capturing the infarct (for example UPF, see **Table 3**), other infarct areas on the same slice cannot be included. The average number of infarct regions per slice was computed for both patient and porcine datasets in **Table 6**. With the average number of regions found to be 1.2 in the patient dataset, more than a single seed may be necessary.

A second consideration is the spatial positioning of the scar candidate in relation to the image slices or 17-segment model of the AHA (Cerqueira et al., 2002). Enhancement in the basal slices due to the outflow tract or RV insertion point should be discriminated as a pseudo infarct. None of the algorithms or fixed models, have classified enhancement based on its location. Thus, pseudo infarcts have not been addressed in the evaluated methods.

A third consideration is the extent of scarring. Sub-classification of infarct as sub-endocardial, mid-wall and epicardial helps stratify treatment. But first and foremost, these formations are indicative of scar, one which the algorithms should be able to distinguish based on Euclidean distances measured on the myocardium segmentation. Equipped with this information, algorithms should be able to better distinguish scar, especially when enhancements arise due to partial voluming or a fat-related cause.

LGE CMR for the LV can be acquired either in 2D or 3D, with the former being more common as they can be obtained relatively quickly. However, 3D acquisitions are preferred over 2D when post-processing involves detailed quantification. As scanner engineering and technology continue to improve, 3D acquisitions will become more common. All algorithms, except UPF, evaluated within this framework and those surveyed in **Table 1** uses 3D techniques that also work on 2D datasets. The UPF technique performs region-growing with seed selection on a slice-by-slice basis. For the porcine 3D datasets, it chooses a particular slice orientation (x, y or z) to work on; and an increasing load on the operator for seed-selection in each 3D slice. The framework supplies with both types of acquisitions to enable future algorithms to be evaluated separately.

### Future algorithms

Infarct quantification in the LV is an important assessment criterion for many cardiac therapies. Furthermore, heterogeneity within infarct, especially in the peri-infarct regions, was shown to be a predictor of tachycardia and sudden cardiac death (Schmidt

et al., 2007). This work proposes an evaluation framework for future algorithms which segment and quantify LV infarct. To demonstrate its usability, five different algorithms were evaluated on the framework. Three of which have been published (Hennemuth et al., 2008; Karimaghaloo et al., 2012; Karim et al., 2014). Six different fixed-model approaches were also evaluated. The framework provides thirty datasets, of which ten are for algorithm training and the rest for testing. Although they represent a specific pulse sequence, some algorithms evaluated here could be re-trained on new sequences. The consensus ground truths are derived from manual segmentations of three separate observers. Future algorithms can be evaluated both objectively with overlap metrics or less objectively and conventionally with pixel volumes. Most importantly, they can be compared and benchmarked against existing algorithms. To our knowledge, this is the first proposed framework for evaluating LV infarct segmentation and quantification algorithms from LGE CMR images. For the left atrium, a benchmarking evaluation framework already exists (Karim et al., 2013).

## CONCLUSION

CMR continues to play an important role in imaging and quantifying infarct in the LV. Several algorithms have been proposed for its quantification but it is not clear how they compare or perform relative to one another. Furthermore, algorithms have only been tested on center- and vendor-specific images. The translation of such algorithms into the clinical environment thus remains challenging. Benchmarking frameworks, providing a common dataset and evaluation strategies, is important for clinical translation of these algorithms. The proposed benchmarking framework provides thirty datasets, with fifteen datasets in each cohort: patient and porcine. Datasets in the two separate cohorts were acquired using different scanner vendors and field strength (1.5T and 3T), resolutions and acquisition protocols (2D and 3D). The ground truth is often absent in such datasets, and to this end, the framework provides with a powerful expert observers' consensus ground truth. The proposed framework remains publicly available for accessing the image database, uploading segmentations for evaluation and contributing manual segmentations for improving the consensus ground truth on the datasets.

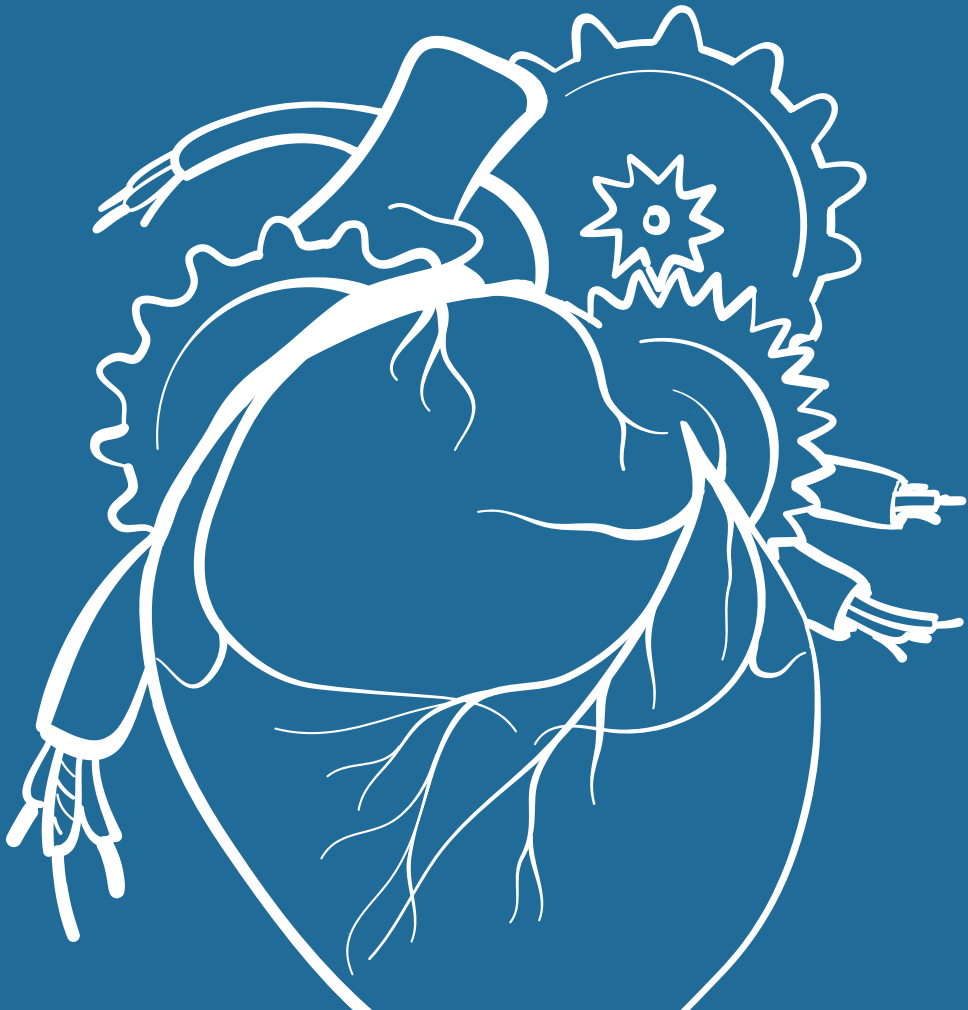
## REFERENCES

1. Amado L et al, 2004. Accurate and objective infarct sizing by contrast-enhanced magnetic resonance imaging in a canine myocardial infarction model. *J. Am. Coll. Cardiol.* 44 (12), 2383–2389.
2. Andreu D et al, 2011. Integration of 3d electroanatomic maps and magnetic resonance scar characterization into the navigation system to guide ventricular tachycardia ablation. *Circ.: Arrhythm. Electrophysiol.* 4 (5), 674–683.
3. Boykov Y et al, 2001. Fast approximate energy minimization via graph cuts. *IEEE Trans. Pattern Anal. Mach. Intell.* 23(2), 1222–1239.
4. Cerqueira MD et al, 2002. Standardized myocardial segmentation and nomenclature for tomographic imaging of the heart a statement for healthcare professionals from the cardiac imaging committee of the council on clinical cardiology of the american heart association. *Circulation* 105 (4), 539–542.
5. Desch S et al, 2011. Cardiac magnetic resonance imaging parameters as surrogate endpoints in clinical trials of acute myocardial infarction. *Trials* 12 (1), 204.
6. Detsky J et al, 2009. Reproducible classification of infarct heterogeneity using fuzzy clustering on multicontrast delayed enhancement magnetic resonance images. *IEEE Trans. Med. Imaging* 28 (10), 1606–1614.
7. Dietrich O et al, 2007. Measurement of signal-to-noise ratios in mr images: influence of multichannel coils, parallel imaging, and reconstruction filters. *J. Magn. Reson. Imaging* 26 (2), 375–385.
8. Estner HL et al, 2011. The critical isthmus sites of ischemic ventricular tachycardia are in zones of tissue heterogeneity, visualized by magnetic resonance imaging. *Heart Rhythm* 8 (12), 1942–1949.
9. Flett AS et al, 2011. Evaluation of techniques for the quantification of myocardial scar of differing etiology using cardiac magnetic resonance. *JACC: Cardiovasc. Imaging* 4 (2), 150–156.
10. Harrison JL et al, 2014. Cardiac magnetic resonance and electroanatomical mapping of acute and chronic atrial ablation injury: a histological validation study. *Eur. Heart J.* 35 (22), 1486–1495.
11. Hearst MA et al, 1998. Support vector machines. *Intell. Syst. Appl.* IEEE 13 (4), 18–28.
12. Hennemuth A et al, 2008. A comprehensive approach to the analysis of contrast enhanced cardiac mr images. *IEEE Trans. Med. Imaging* 27 (11), 1592–1610.
13. Karim R et al, 2014. A method to standardize quantification of left atrial scar from delayed-enhancement mr images. *J. Transl. Eng. Health Med.* 2.
14. Karim R et al, 2013. Evaluation of current algorithms for segmentation of scar tissue from late gadolinium enhancement cardiovascular magnetic resonance of the left atrium: an open-access grand challenge. *J. Cardiovasc. Magn. Reson.* 15 (105).

15. Karimaghloo Z et al, 2012. Automatic detection of gadolinium-enhancing multiple sclerosis lesions in brain mri using conditional random fields. *IEEE Trans. Med. Imaging* 31 (6), 1181–1194.
16. Kim RJ et al, 1999. Relationship of mri delayed contrast enhancement to irreversible injury, infarct age, and contractile function. *Circulation* 100 (19), 1992–2002.
17. Kirisli H et al 2013. Standardized evaluation framework for evaluating coronary artery stenosis detection, stenosis quantification and lumen segmentation algorithms in computed tomography angiography. *Med. Image Anal.* 8 (17), 856–876.
18. Knowles B et al, 2010. 3-D visualization of acute RF ablation lesions using MRI for the simultaneous determination of the patterns of necrosis and edema. *IEEE Trans. Biomed. Eng.* 57 (6), 1467–1475.
19. Kolipaka A et al, 2005. Segmentation of non-viable myocardium in delayed enhancement magnetic resonance images. *Int. J. Cardiovasc. Imaging* 21 (2-3), 303–311.
20. Lafferty J et al, 2001. Conditional random fields: probabilistic models for segmenting and labelling sequence data. In: *Proceedings of the 18th International Conference on Machine Learning*, pp. 282–289.
21. Lu Y et al, 2012. Automated quantification of myocardial infarction using graph cuts on contrast delayed enhanced magnetic resonance images. *Quant. Imaging Med. Surg.* 2 (2), 81.
22. Oakes R et al, 2009. Detection and quantification of left atrial structural remodelling with delayed-enhancement magnetic resonance imaging in patients with atrial fibrillation. *Circulation* 119 (13), 1758–1767.
23. Otsu N et al, 1975. A threshold selection method from gray-level histograms. *Automatica* 11 (285-296), 23–27.
24. Petitjean C et al, 2015. Right ventricle segmentation from cardiac mri: a collation study. *Med. Image Anal.* 19 (1), 187–202. <http://dx.doi.org/10.1016/j.media.2014.10.004>.
25. Pop M et al, 2013. Quantification of fibrosis in infarcted swine hearts by ex vivo late gadolinium-enhancement and diffusion-weighted mri methods. *Phys. Med. Biol.* 58 (15), 5009.
26. Positano V et al, 2005. A fast and effective method to assess myocardial necrosis by means of contrast magnetic resonance imaging. *J. Cardiovasc. Magn. Reson.* 7 (2), 487–494.
27. Rajchl M et al, 2014. Comparison of semi-automated scar quantification techniques using high-resolution, 3-dimensional late-gadolinium-enhancement magnetic resonance imaging. *Int. J. Cardiovasc. Imaging* 1–9.
28. Ravanelli D et al, 2014. A novel skeleton based quantification and 3d volumetric visualization of left atrium fibrosis using late gadolinium enhancement magnetic resonance imaging. *IEEE Trans. Med. Imaging* 33 (2).

29. Schmidt A et al, 2007. Infarct tissue heterogeneity by magnetic resonance imaging identifies enhanced cardiac arrhythmia susceptibility in patients with left ventricular dysfunction. *Circulation* 115 (15), 2006–2014.
30. Sethian JA et al, 1999. Level set methods and fast marching methods: evolving inter-faces in computational geometry, fluid mechanics, computer vision, and materials science. Cambridge university press.
31. Suinesiaputra A et al, 2014. A collaborative resource to build consensus for automated left ventricular segmentation of cardiac mr images. *Med. Image Anal.* 18 (1), 50–62.
32. Tao Q et al, 2010. Automated segmentation of myocardial scar in late enhancement mri using combined intensity and spatial information. *Magn. Reson. Med.* 64 (2), 586–594.
33. Teague MR et al, 1980. Image analysis via the general theory of moments \*. *JOSA* 70 (8), 920–930.
34. Tipping ME et al, 2001. Sparse Bayesian learning and the relevance vector machine. *J. Mach. Learn. Res.* 1, 211–244.
35. Tobon-Gomez C et al, 2013. Benchmarking framework for myocardial tracking and deformation algorithms: an open access database. *Med. Image Anal.* 17 (6), 632–648.
36. Turkbey E et al 2012. Differentiation of myocardial scar from potential pitfalls and artefacts in delayed enhancement mri. *Br. J. Radiol.* 85 (1019).
37. Wagner A et al, 2003. Contrast-enhanced mri and routine single photon emission computed tomography (spect) perfusion imaging for detection of subendocardial myocardial infarcts: an imaging study. *The Lancet* 361 (9355), 374–379.
38. Warfield S et al, 2004. Simultaneous truth and performance level estimation (staple): an algorithm for the validation of image segmentation. *IEEE Trans. Med. Imaging* 23 (7), 903–921.
39. Wu M et al, 2011. Non-invasive characterization of the area-at-risk using magnetic resonance imaging in chronic ischaemia. *Cardiovasc. Res.* 89 (1), 166–174.

04



# IMPLEMENTATION OF A STANDARDIZED CARDIAC MAGNETIC RESONANCE BASED WORKFLOW FOR ATRIAL FIBRILLATION CATHETER ABLATION

---

P. Bhagirath MD; M. van der Graaf MD; S. Ghoerbien MsC; V. van Driel MD;  
H. Ramanna MD PhD; K. Rhode PhD; R. Karim PhD; M. Götte MD PhD  
*Submitted*

## ABSTRACT

**Background:** Patient selection and procedural guidance of atrial fibrillation (AF) ablation is currently performed using multiple imaging modalities. Recent work suggests that a cardiac magnetic resonance (CMR) based approach can provide comparable information in a more integrated and cost-effective manner.

**Purpose:** This study investigated the clinical utility and feasibility of a CMR based imaging and post-processing workflow for patient selection and procedural guidance of AF ablation.

**Methods and results:** Eight patients scheduled for AF ablation underwent CMR examination using a 1.5T scanner. Images were post-processed using a combination of open-source and custom-written software. Acquisition and post-processing was performed in  $40 \pm 3.5$  minutes.

A left atrial (LA) shell was created in all patients ( $n=8$ ) to evaluate the LA volume and sphericity. The biplane area-length underestimated the average LA volume by 15 ml when compared to semi-automatic segmentation. Patients undergoing their index procedure had a lower sphericity of  $77 \pm 4$  whereas redo ablation patients had a high LA sphericity ( $85 \pm 3$ ).

In redo patients ( $n=5$ ), the LA shell containing information from the late gadolinium enhancement images correlated well with sites of ablation on the EAM of the index procedure. Not all gaps identified using the scar-map were of relevance for the ablation procedure.

**Conclusion:** A single modality, CMR based imaging workflow, is clinically relevant, feasible, and offers the prospect to perform patient selection as well as procedural guidance of AF ablation. In addition, catheter ablation procedures could benefit from targeted (patient-specific) ablation strategy using LGE-CMR derived scar-maps.

## BACKGROUND

Patient selection and procedural guidance of atrial fibrillation (AF) ablation is often performed using multiple imaging modalities such as echocardiography, computed tomography and cardiac magnetic resonance imaging (CMR) <sup>[1,2]</sup>. However, it has recently been suggested that a single modality, CMR based approach can provide a comparable diagnostic yield in a more time- and cost-efficient manner <sup>[3]</sup>.

Commercially available CMR pulse sequences have been applied to obtain detailed information about left atrial appendage (LAA) thrombus <sup>[4]</sup> and optional parameters such as pulmonary vein (PV) morphology <sup>[5]</sup>, and left atrial (LA) volume <sup>[6]</sup>.

Furthermore, CMR offers unmet capabilities for tissue characterization in the thin LA wall <sup>[7,8]</sup>. This tissue information may be used to identify potential electrical re-entry circuits <sup>[9]</sup> and to design patient specific ablation strategies <sup>[10]</sup>.

The current lack of uniformity for LA imaging however, poses significant limitations.

This study proposes a standardized CMR based imaging and post-processing workflow for patient selection and procedural guidance of AF ablation. Clinical utility and feasibility were examined by evaluating:

- (1) the ability to assess the following parameters: LAA thrombus, LA volume and sphericity,
- (2) the capability to facilitate procedural guidance by fusion of CMR-derived LA models with the electro-anatomical mapping (EAM) system, and
- (3) the correlation between sites of ablation and scar localization on the LA model.

## METHODS

### Patient Population

The study population consisted of 8 patients undergoing an index (n=3) or redo (n=5) catheter ablation procedure for paroxysmal or persistent AF. The study complied with the declaration of Helsinki and received approval from the local ethical committee and the institutional scientific board. Written informed consent was obtained from the study subjects.

According to the current standard of care, trans-esophageal echocardiography was performed within 2 days prior to the procedure to exclude LAA thrombus. Patients with persistent AF had undergone electrical cardio-version 2-4 weeks prior to the ablation procedure. In addition, a standard contrast-enhanced computed tomography (CT) examination was performed to evaluate the PV morphology in all patients.

## Imaging protocol

The complete workflow for image acquisition and post-processing is shown in **figure 1**.

The CMR examination was performed on a 1.5 Tesla Achieva (Philips Medical Systems, Best, Netherlands) using a sense cardiac phased-array receiver coil (Philips Medical Systems). The imaging protocol provided information about anatomical, functional and structural parameters.

Steady state free precession (SSFP) cine imaging was performed in the 4 chamber and 2 chamber orientations covering the entire LA. Subsequently 3 dimensional (3-D) magnetic resonance angiography (MRA) of the LA was performed after 0.2 mmol/kg Dotarem (Guerbet Group, Villepente, France) contrast agent injection. This was followed by acquisition of 3-D balanced SSFP (bSSFP) images in transversal orientation providing whole-heart coverage. Late gadolinium enhanced (LGE) imaging was performed 20-25 minutes after contrast injection using a free breathing 3-D ECG-triggered, inversion recovery gradient echo pulse sequence. Typical acquisition parameters are listed in **table 1**.

**Table 1.** Typical acquisition parameters.

Pulse sequence	Orientation	Acq. voxel size	TR/TE	Flip angle	Nav window
SSFP	4- and 2-chamber	1.2 x 1.2 x 5.0 mm	3.8/1.9 ms	60-70°	-
3-D MRA	Axial	0.8 x 0.8 x 1.5 mm	2.4/0.9 ms	25°	-
3-D bSSFP *	Axial	0.6 x 0.6 x 0.8 mm	4.5/2.3 ms	90°	5mm
3-D IR GRE **	Axial	1.3 x 1.3 x 2.5 mm	4.8/2.4 ms	25°	5mm

SSFP indicates steady state free precession; MRA, magnetic resonance angiography; bSSFP, balanced SSFP; IR GRE, inversion recovery gradient echo; TR, repetition time; TE, echo time; Nav, navigator.

\*ECG gating was used to acquire views during the diastolic phase of the LA cardiac cycle. \*\*The TI value for the scan was identified using a scout scan and was set at an intermediate between the optimal value to null blood and myocardium.

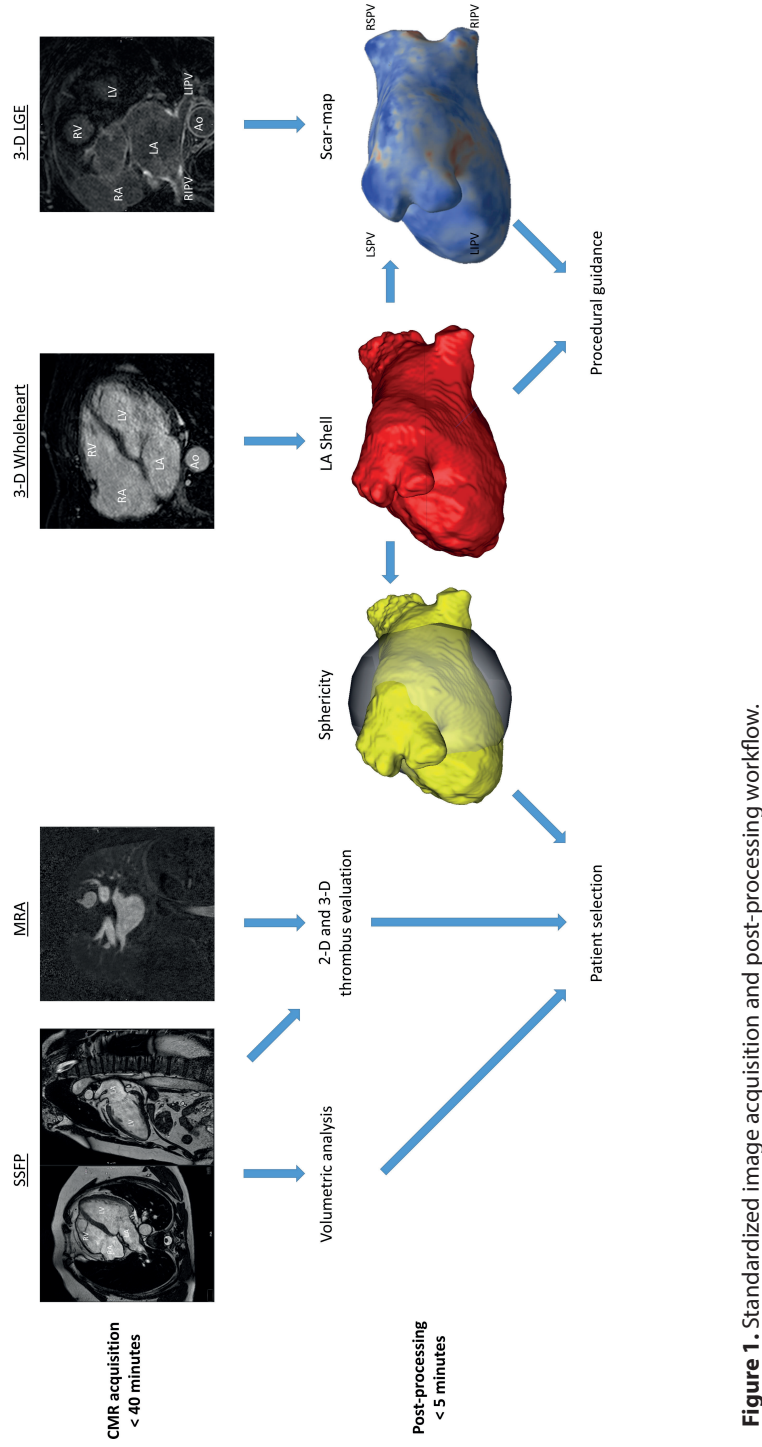


**Figure 1.** Standardized image acquisition and post-processing workflow. Top panel indicates the information acquired during the CMR examination. Bottom panel indicates the utility of the results from the post-processing and analysis workflow.

## Image analysis

### *Volume*

The LA volume was calculated using 2 methods:

1. Using the biplane area-length method <sup>[6]</sup> as given in equation 1:

$$LA \text{ volume} = \frac{(0.85 \times \text{four chamber area} \times \text{two chamber area})}{(\text{longest}) \text{ left atrial length}} \quad (1)$$

2. By segmenting the LA cavity from the CMR images using ITKSnap ([www.itk-snap.org](http://www.itk-snap.org)) and calculating the volume of the shell.

### *Thrombus*

The MRA was used to create 3-D reconstructions of the LAA to evaluate the presence of thrombus.

### *Sphericity and scar-map*

The LA sphericity, a measure of geometrical remodeling, was computed using custom-made software. The algorithm used for computing LA sphericity was recently introduced and validated by Bisbal et al <sup>[11]</sup>. The LA cavity segmentation for volumetric analysis was represented as a triangular mesh. The center-of-mass of LA was then computed from the area-weighted centers of each triangle in the mesh. The best-fit sphere for the LA could then be computed using the distances between the center-of-mass and each triangle in the mesh. The mean of these individual distances provided the radius ( $\mu$ ) of the sphere of best-fit. The standard deviation ( $\sigma$ ) of these distances was also calculated. LA sphericity was then simply calculated as a ratio:  $1 - \sigma / \mu$ .

A LA scar-map was generated in patients undergoing redo-ablation, using a semi-automated 3-D method which has been described in detail previously <sup>[12]</sup>. The LA reconstruction created for the volumetric analysis was fused with the LGE images. Vectors at a normal to the cardiac surface were created using the visual-toolkit libraries (VTK, Kitware, Inc., NY). A maximum intensity projection of the LGE images was performed at  $\pm 3$  mm along each normal vector.

The electrophysiologists were blinded to the sphericity and scar-map results.

## Ablation guidance

For navigation purposes, the anatomical shell and LA scar-map were converted into the proprietary format for the EAM (EnSite Verismo™, St. Jude Medical) and fused with the invasively acquired anatomy using a landmark based registration process (movie 1).

The fusion was performed by selecting landmarks (fiducials) on the invasively obtained anatomical shell and the LA shell. These fiducials usually consisted of the pulmonary veins and the mitral valve annulus.

## Comparison of scar-map and EAM

For patients undergoing a redo ablation, the location and distribution of scar on the generated scar-maps was compared with the ablation sites from the index procedure. The gaps identified on the scar-maps were compared with the ablation sites of the redo procedure.

## RESULTS

Five patients suffered from paroxysmal AF and three had long-standing persistent AF. There was a history of hypertension in 5 patients (63%). One patient suffered from systolic heart failure (LVEF 26%). Based on conventional imaging, all patients had LA dilatation and 5 patients (63%) suffered from mitral regurgitation (moderate). LAA thrombus was excluded in all patients using TEE and MRA. Additional patient characteristics are provided in **table 2**.

## Image acquisition and analysis

There were no patients with contra-indications for undergoing CMR. All scans were performed in sinus rhythm. Typical scan time for the CMR protocol was  $36 \pm 3$  minutes, depending on subject respiratory- and heart rate.

LA segmentations were constructed in  $2.8 \pm 0.8$  minutes. The biplane area-length method took  $52 \pm 7$  seconds to perform and underestimated the average LA volume ( $67 \pm 16$  ml) compared to ITK-Snap by 15 ml.

**Table 2.** Patient characteristics.

	Patient 1	Patient 2	Patient 3	Patient 4	Patient 5	Patient 6	Patient 7	Patient 8
Age (years)	66	60	49	60	62	54	56	63
Sex	Male	Female	Male	Female	Male	Male	Male	Female
Index-procedure	No	No	No	No	Yes	Yes	No	Yes
BMI	26	25	30	29	27	26	25	32
Hypertension	No	Yes	Yes	Yes	No	No	Yes	Yes
Mitral valve regurgitation	Yes	Yes	Yes	Yes	No	Yes	No	No
LVEF (%)	58%	63%	51%	26%	48%	62%	51%	57%
LA volume (ml)	93	52	53	78	76	180	45	73
Months to redo procedure	14	16	19	19	-	-	32	-
AF recurrence after redo	Yes	No	No	Yes	-	-	No	-

## Sphericity

Adaptation of the LA segmentation (removal of PV's and LAA) to perform sphericity analysis was achieved in  $1.5 \pm 0.5$  minutes. All patients undergoing a redo ablation had a high LA sphericity ( $85 \pm 3$ ) indicative of advanced structural remodeling and associated with a high AF recurrence rate (**figure 2**). Patients undergoing their index procedure had a lower sphericity of  $77 \pm 4$ . Median follow-up duration was 265 days (interquartile range: 142-874).

## Scar-map fusion with EAM

### *Index procedure*

After merging, a high visual correlation was observed between areas of scar on the scar-map and sites of ablation on the EAM (**figure 3**). Dense scar areas on the scar-map correlated with sites of multiple ablation applications on the EAM.

The left inferior pulmonary vein (LIPV) and right superior pulmonary vein (RSPV) demonstrated a higher presence of scar compared to the other areas (movie 2). The right inferior pulmonary vein (RIPV) showed the highest number of gaps (average 2) and the LIPV the fewest (average 0.8) (**table 3**).

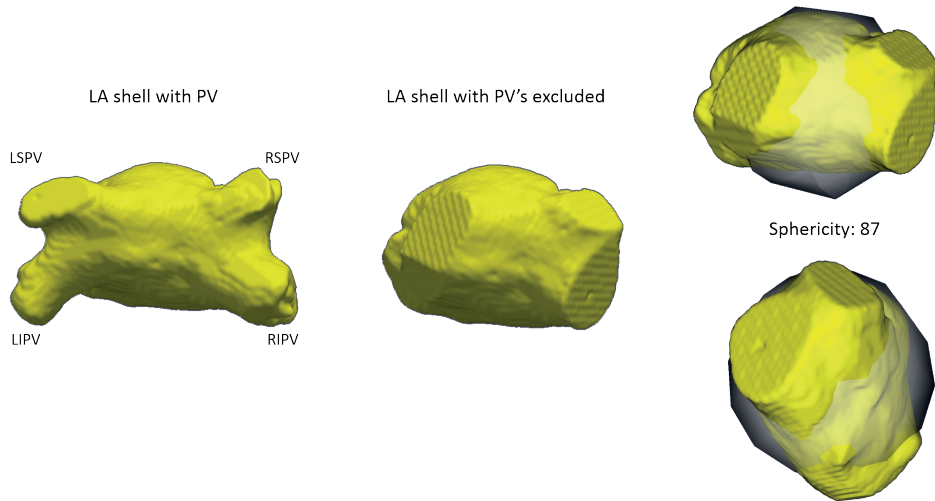


**Figure 2.** LA Sphericity analysis.

An example of the sphericity calculation using the segmented LA shell. The sphericity value of 87 indicates advanced structural remodeling and predicts a lower procedural success rate.

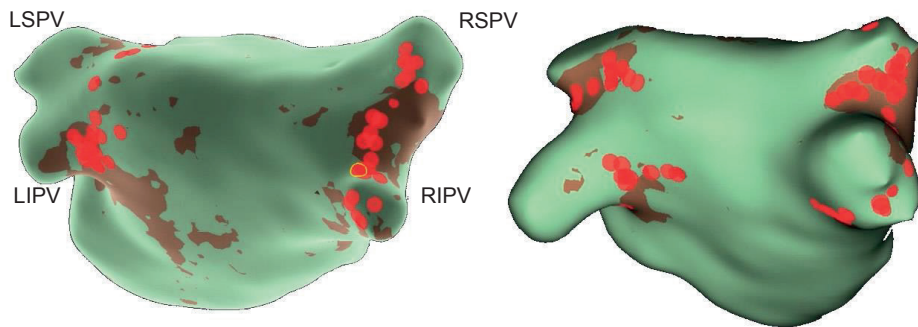


**Figure 3.** Comparison between scar-map and EAM of the index ablation procedure.

The scar-map is fused with the EAM of the index procedure. A good visual correlation is noted between regions of scar (brown) and ablation lesions (red dots).

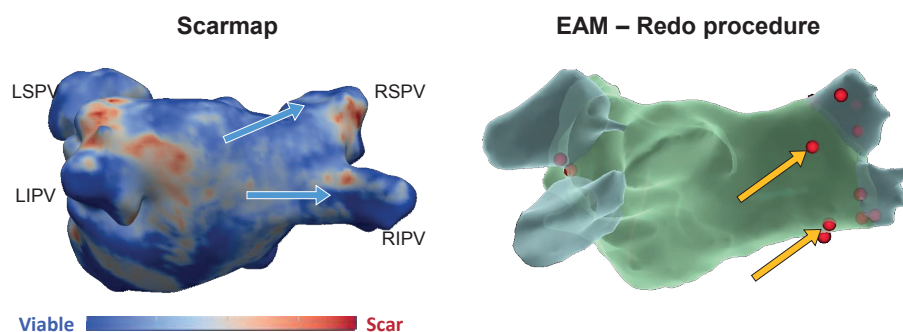
**Table 3.** Gap distribution among the pulmonary veins.

	RSPV	RIPV	LSPV	LIPV
Patient 1	3	2	1	1
Patient 2	1	2	1	0
Patient 3	1	2	0	1
Patient 4	2	2	2	1
Patient 7	1	2	1	1

RSPV indicates right superior pulmonary vein; RIPV, right inferior pulmonary vein; LSPV, left superior pulmonary vein; LIPV, left inferior pulmonary vein. Gaps on the scar-map were most frequently observed in the RIPV. The LIPV showed the lowest number of gaps on the scar-map.

### Redo procedure

The site of ablation during the redo procedure EAM was related to the gaps identified on the scar-map (**figure 4**). In addition, all scar-maps demonstrated gaps that correlated to electrically dormant and therefore unablated areas on the EAM. The posterior part of the left pulmonary veins was a predilection spot for such sites.

**Figure 4.** Example of a scar-map guided ablation.

The left panel demonstrates a scar-map and the right panel shows the redo-procedure EAM of the corresponding patient. There is a good visual correlation between the scar-map sites with gaps (blue arrows) and the redo-procedure ablation sites (orange arrows).

### Ablation outcome

The redo ablation was successful in two paroxysmal AF and one persistent AF patient. One of the patients with persistent AF underwent a third procedure aimed at performing substrate modification. The other patient with persistent AF underwent His bundle ablation with implantation of a permanent pacemaker.

## DISCUSSION

It is well established that imaging plays an important role in patient selection and procedural guidance of AF ablation procedures<sup>[3]</sup>. This study investigated the feasibility of using a standardized and integrated CMR based workflow for patient selection and procedural guidance for AF ablation. As the study population also consisted of patients undergoing a redo ablation, special emphasis was placed on examining the usefulness of LGE-CMR for procedural guidance.

The main findings are as follows: (1) A comprehensive CMR protocol targeted at acquiring relevant information for catheter ablation can be completed in less than 40 minutes; (2) Post-processing of this information can be completed in less than 5 minutes; (3) The ablation sites of the redo procedures correlate well with gaps detected in the scar-maps; and (4) Not all gaps are electrically active and could be considered as bystanders, not involved in the AF recurrence.

### **Clinical utility of the workflow**

Currently, patient assessment for AF ablation is often performed using multiple modalities. The findings of this study demonstrate the feasibility of the proposed protocol to perform assessment of LAA thrombus and LA geometry using a single CMR examination. This workflow can contribute to a potential reduction of procedural radiation exposure<sup>[13]</sup> by providing LA anatomical shells that can be quickly merged with the EAM for anatomical guidance of the procedure. Finally, the addition of LGE imaging further expands the utility of this workflow. The information about tissue-characteristics can be used to generate scar-maps and could potentially provide patient-specific (targeted) ablation strategies for redo procedures.

### **Correlation between LGE-CMR gaps and electrical reconnection**

The gaps identified using LGE-CMR demonstrated a high correlation with the invasively measured sites of reconnection. However, not all LGE-CMR gaps showed electrical reconnection. Although previous investigations have mentioned non-conducting gaps<sup>[14;15]</sup>, no study has yet characterized the temporal electrical course of these gaps.

Certain groups of patients develop AF recurrence long after the ablation procedure. Therefore, it may be hypothesized that such electrically dormant gaps may demonstrate reconnection in the long-term. In such case, these gaps should be considered a potential ablation site during the redo-procedure.

The outcome of the current investigation with regard to scar-maps, warrants further study towards the identification of a strategy to differentiate between electrically dormant gaps and gaps associated with the recurrence of AF.

### **Limitations**

Various studies have compared the accuracy and suitability of multiple imaging modalities to image the parameters required for patient selection or procedural guidance of catheter ablation [4;5;16;17]. However, this is the first study that performs a comprehensive, single modality workup of patients undergoing ablation. Although the 8 patients included in this study can be considered as a lower limit for statistical evaluation, the results indicate the clinical applicability and feasibility of the proposed workflow.

Although all scans were of diagnostic quality, factors such as irregular heart beat and inability to perform a breath-hold may cause artifacts that could limit the use of this technique. In addition, the CMR scanner field strength used in this study was 1.5 Tesla (T). It might be hypothesized that the increased magnet strength provided by a 3T scanner can be used to improve spatial resolution (image quality) or to reduce scan times.

### **Future perspectives**

The proposed CMR protocol and post-processing methods can be performed and completed within a limited time period. This offers the prospect to implement this single modality workflow in a straightforward manner for the daily clinical routine. In addition, the technical knowledge required for image analysis is comparable to basic CMR post-processing. Although these factors facilitate rapid implementation, a larger prospective study to investigate the cost-efficiency and clinical efficacy of this approach is currently being planned and would support the rationale for routine clinical use.

## **CONCLUSION**

A single modality, CMR based imaging workflow is clinically feasible, and suitable to perform patient selection and procedural guidance of AF ablation. Especially redo ablation procedures may benefit from a scar-map guided, targeted (patient-specific) ablation strategy. Future studies should investigate the cost-efficiency and efficacy of this workflow.

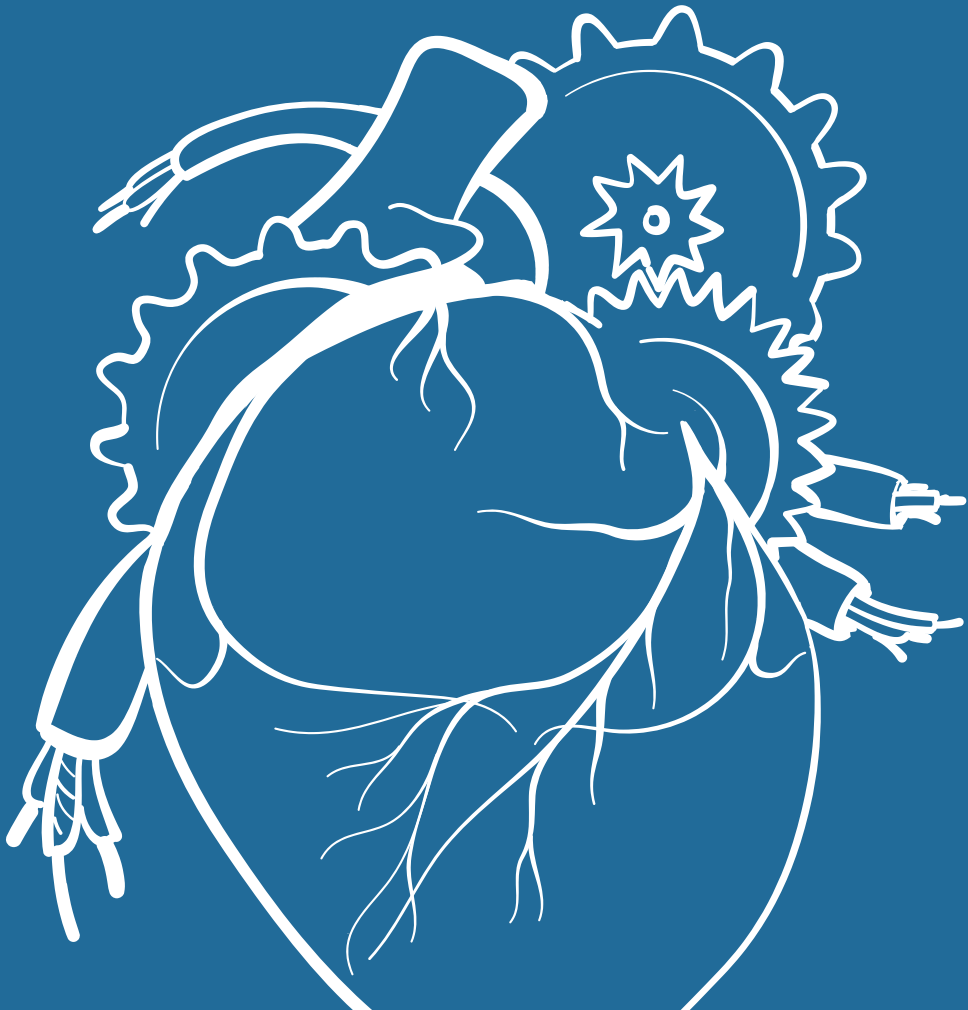
## REFERENCES

- 1 Blomstrom Lundqvist C, Auricchio A, Brugada J, et al. The use of imaging for electrophysiological and devices procedures: a report from the first European Heart Rhythm Association Policy Conference, jointly organized with the European Association of Cardiovascular Imaging (EACVI), the Council of Cardiovascular Imaging and the European Society of Cardiac Radiology. *Europace* 2013;15(7):927-36.
- 2 Tops LF, Schalij MJ, Bax JJ. Imaging and atrial fibrillation: the role of multimodality imaging in patient evaluation and management of atrial fibrillation. *Eur Heart J* 2010;31(5):542-51.
- 3 Bhagirath P, van der Graaf AWM, Karim R, et al. Multimodality imaging for patient evaluation and guidance of catheter ablation for atrial fibrillation - current status and future perspective. *Int J Cardiol* 2014;175(3):400-8.
- 4 Rathi VK, Reddy ST, Anreddy S, et al. Contrast-enhanced CMR is equally effective as TEE in the evaluation of left atrial appendage thrombus in patients with atrial fibrillation undergoing pulmonary vein isolation procedure. *Heart Rhythm* 2013;10(7):1021-7.
- 5 Hamdan A, Charalampos K, Roettgen R, et al. Magnetic resonance imaging versus computed tomography for characterization of pulmonary vein morphology before radiofrequency catheter ablation of atrial fibrillation. *Am J Cardiol* 2009;104(11):1540-6.
- 6 Hof IE, Velthuis BK, Van Driel VJ, et al. Left atrial volume and function assessment by magnetic resonance imaging. *J Cardiovasc Electrophysiol* 2010;21(11):1247-50.
- 7 Peters DC, Wylie JV, Hauser TH, et al. Detection of pulmonary vein and left atrial scar after catheter ablation with three-dimensional navigator-gated delayed enhancement MR imaging: initial experience. *Radiology* 2007;243(3):690-5.
- 8 Oakes RS, Badger TJ, Kholmovski EG, et al. Detection and quantification of left atrial structural remodeling with delayed-enhancement magnetic resonance imaging in patients with atrial fibrillation. *Circulation* 2009;119(13):1758-67.
- 9 Ranjan R, Kato R, Zviman MM, et al. Gaps in the ablation line as a potential cause of recovery from electrical isolation and their visualization using MRI. *Circ Arrhythm Electrophysiol* 2011;4(3):279-86.
- 10 Bisbal F, Guiu E, Cabanas-Grandio P, et al. CMR-guided approach to localize and ablate gaps in repeat AF ablation procedure. *JACC Cardiovasc Imaging* 2014;7(7):653-63.
- 11 Bisbal F, Guiu E, Calvo N, et al. Left atrial sphericity: a new method to assess atrial remodeling. Impact on the outcome of atrial fibrillation ablation. *J Cardiovasc Electrophysiol* 2013;24(7):752-9.
- 12 Knowles BR, Caulfield D, Cooklin M, et al. 3-D visualization of acute RF ablation lesions using MRI for the simultaneous determination of the patterns of necrosis and edema. *IEEE Trans Biomed Eng* 2010;57(6):1467-75.

- 13 Caponi D, Corleto A, Scaglione M, et al. Ablation of atrial fibrillation: does the addition of three-dimensional magnetic resonance imaging of the left atrium to electroanatomic mapping improve the clinical outcome?: a randomized comparison of Carto-Merge vs. Carto-XP three-dimensional mapping ablation in patients with paroxysmal and persistent atrial fibrillation. *Europace* 2010;12(8):1098-104.
- 14 Spragg DD, Khurram I, Zimmerman SL, et al. Initial experience with magnetic resonance imaging of atrial scar and co-registration with electroanatomic voltage mapping during atrial fibrillation: success and limitations. *Heart Rhythm* 2012;9(12):2003-9.
- 15 Hunter RJ, Jones DA, Boubertakh R, et al. Diagnostic accuracy of cardiac magnetic resonance imaging in the detection and characterization of left atrial catheter ablation lesions: a multicenter experience. *J Cardiovasc Electrophysiol* 2013;24(4):396-403.
- 16 Agner BFR, Kuhl JT, Linde JJ, et al. Assessment of left atrial volume and function in patients with permanent atrial fibrillation: comparison of cardiac magnetic resonance imaging, 320-slice multi-detector computed tomography, and transthoracic echocardiography. *Eur Heart J Cardiovasc Imaging* 2014;15(5):532-40.
- 17 von Bary C, Dornia C, Eissnert C, et al. Predictive value of left atrial volume measured by non-invasive cardiac imaging in the treatment of paroxysmal atrial fibrillation. *J Interv Card Electrophysiol* 2012;34(2):181-8.



05



# LEFT ATRIAL SPHERICITY: A PROMISING PARAMETER TO PREDICT RESPONSE TO ABLATION

---

Pranav Bhagirath MD; Maurits van der Graaf MD; Hemanth Ramanna MD PhD;  
Natasja de Groot MD PhD; Rashed Karim PhD; Marco Götte MD PhD  
*Submitted*

## ABSTRACT

**Background:** Patient selection for atrial fibrillation (AF) ablation remains challenging as the currently used parameters, such as left atrial volume, are often poorly correlated with post-procedural AF recurrence. This is especially the case in patients undergoing repeat ablation. Recent investigations have reported left atrial sphericity (LASP) as an independent and strong predictor of success for index AF ablation procedures.

**Objective:** This study investigated the utility of LASP in predicting AF recurrence following a repeat ablation.

**Methods:** Patients undergoing repeat ablation for AF were included. Contrast enhanced computed tomography, acquired prior to and following the index ablation procedure, was used for creating a left atrial segmentation. LASP was computed using custom-made software.

**Results:** 25 patients ( $61 \pm 8.4$  years, 80% male) with paroxysmal (40%) and persistent (60%) AF were included. Fourteen patients (56%) had AF recurrence after the repeat procedure. No relation was observed between recurrence and the nature ( $p=0.62$ ) or duration of AF ( $p=0.51$ ).

There was no significant correlation between LA volumetric changes and AF recurrence ( $p=0.17$ ). Only the change in LASP was significantly related with AF recurrence ( $p<0.001$ ). All patients with a positive change in LASP were free from AF recurrence during the follow-up ( $664 \pm 245$  days).

**Conclusion:** Changes in LASP following the index ablation correlate with outcome of repeat catheter ablation procedures. Positive changes in the LASP (reverse remodeling) are strongly related to a higher success rate of the repeat procedure.

Patient selection for repeat ablation could be improved by including geometrical remodeling as a stratification factor.

## BACKGROUND

Patient selection for catheter ablation of atrial fibrillation (AF) is a challenging task <sup>(1)</sup>, in particular for repeat ablation procedures <sup>(2)</sup>. Studies evaluating adverse remodeling of the left atrium (LA), measured using size and function, as a predictor for post ablation AF recurrence have reported conflicting results <sup>(3-8)</sup>.

Although these discrepancies could be due to technique inherent limitations of the imaging modality used, it can also be hypothesized that the use of LA dimensions and volume provides only an indirect and inaccurate reflection of structural (tissue based) remodeling.

Recent observations in patients undergoing index AF ablation, emphasize the importance of distinguishing between volumetric and geometrical remodeling <sup>(9 10)</sup>. Bisbal et al. have observed that volumetric changes are not necessarily related to remodeling of the geometry <sup>(11)</sup>. Furthermore, they have also reported that patients *without* AF recurrence are found to have favorable geometrical remodeling when compared to those *with* recurrence <sup>(12)</sup>.

However, to date there is no description of long-term remodeling effects in the patient group *with* recurrence of AF, especially with regard to their impact on the efficacy of a repeat ablation procedure.

This study evaluated the impact of LA geometrical and volumetrical remodeling on repeat catheter ablation outcome. To this extent, long-term remodeling was only evaluated in patients with AF recurrence following an index catheter ablation. These parameters were correlated to the outcome of the repeat ablation procedure.

## METHODS

### Patient Population

A total of 54 patients who had undergone a first repeat catheter ablation for AF between January 2012 and June 2013 were retrospectively screened for inclusion. In total 25 patients with a contrast enhanced computed tomography (CT) examination pre- and post-index ablation were identified and included in the study. The terms pre- and post-ablation are used with respect to the index procedure (supplemental material). The study complied with the declaration of Helsinki and received approval from the local ethical committee and the institutional scientific board.

The standard definitions for paroxysmal (self-terminating episodes of AF lasting 7 days) and persistent AF (AF sustained 7 days and/or requiring electrical or pharmacological cardioversion) were used.

### **Imaging protocol**

All patients had undergone an electrocardiogram (ECG) gated contrast enhanced computed tomography (CT) examination (Siemens Somatom Flash Definition) 24-48 hours prior to the index ablation procedure to identify pulmonary vein (PV) anatomy and to exclude left atrial appendage (LAA) thrombus. A second CT exam was performed 6 months following the index procedure to evaluate PV stenosis. Scanning was prospectively triggered at 25% of the R-R interval on ECG. Images were acquired from the supra-aortic region till upper abdomen. Seventy five ml of contrast agent (Xenetix 350, Guerbet, France) was injected in all patients.

### **Image post-processing and analysis**

#### ***Volume***

The LA volume was obtained from the CT images using the volume and statistics module of ITK-Snap ([www.itk-snap.org](http://www.itk-snap.org)) and indexed to the BSA, calculated according to the Mosteller formula <sup>(13)</sup>. Prior to using this volume module, a semi-automatic segmentation of the LA cavity was performed.

Briefly, the CT images were loaded in ITK-Snap and the region of interest (ROI) was defined, ensuring that the PV's and LAA were completely encompassed. Seed points were then selected within the LA and PV allowing a built-in region-growing algorithm to segment the LA cavity.

The generated segmentation was sub-classified manually by labeling the right and left PV's. The LAA was grouped as part of the left PV's. The resulting LA cavity segmentation was exported for further analysis.

A visual representation of the segmentation process is provided in video 1 (supplemental material).

#### ***Sphericity***

The LASP, represented as a percentage, was computed using custom-made software. The applied algorithm used for computing LASP is recently proposed and validated by Bisbal et al <sup>(12)</sup>. Briefly, the LA cavity segmentation for volumetric analysis was represented as a triangular mesh. The center-of-mass of LA was then computed from

the area-weighted centers of each triangle in the mesh. The best-fit sphere for the LA could then be computed using the distances between the center-of-mass and each triangle in the mesh. The mean of these individual distances provided the radius ( $\mu$ ) of the sphere of best-fit. The standard deviation ( $\sigma$ ) of these distances was also calculated. LASP was then calculated as a ratio:  $1 - \sigma / \mu$  (**figure 1**).

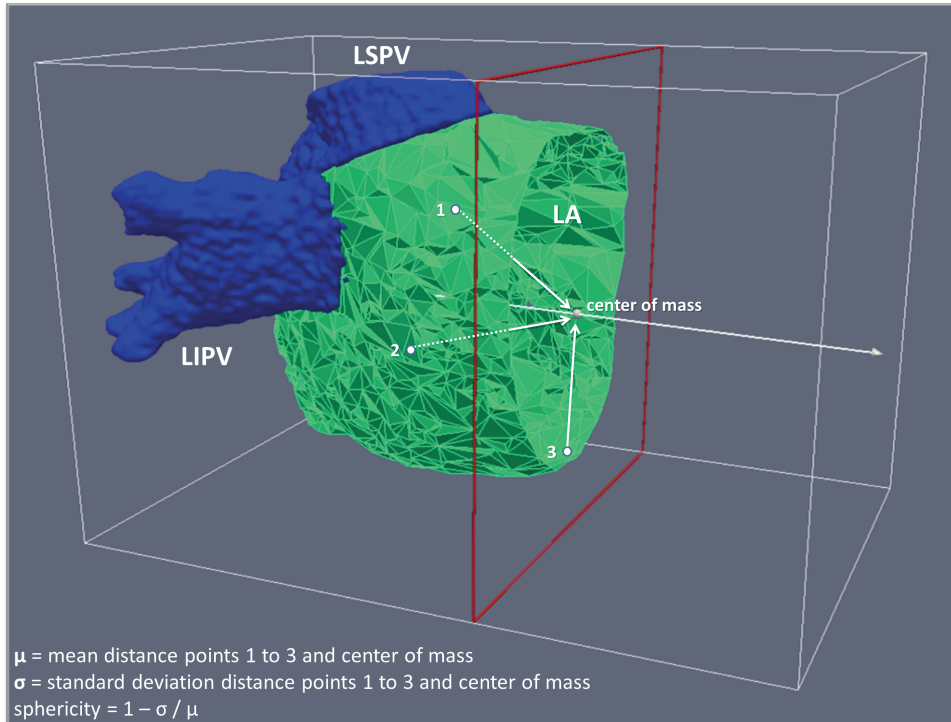


**Figure 1.** Calculation of LA sphericity.

Posterior view of the left atrial (LA) triangular mesh, right side cropped for illustration purpose. The LA center-of-mass (white dot) can be computed using the area-weighted centers of each triangle in the mesh, example point 1 to 3. The mean and standard deviation of the individual distances between these points and the center-of-mass can then be used to calculate the LA sphericity. LSPV indicates left superior pulmonary vein; LIPV, left inferior pulmonary vein; LA, left atrium.

## Statistical analysis

Statistical analysis was performed using PASW Statistics (Version 17.0). Continuous variables were expressed as mean  $\pm$  standard deviation. Normality testing was performed using the Shapiro-Wilk test. Normally distributed data were compared using the independent Student's t-test. The  $\chi^2$  test was used to compare the proportions between the groups. Pearson's r was used to perform correlation analysis. A  $p < 0.05$  was considered to be statistically significant.

## RESULTS

### Patient population

A total of 25 patients were included in the study. The majority of the patients were male ( $n=20$ ) and had persistent AF ( $n=15$ ). There were no significant differences in the total AF duration amongst the paroxysmal AF group ( $2333 \pm 1817$  days) and the persistent AF group ( $1853 \pm 1333$  days) ( $p=0.48$ ).

Average patient follow-up after the repeat procedure was  $664 \pm 245$  days. Additional baseline characteristics are summarized in **table 1**.

### Catheter ablation outcome

Electro-anatomic mapping during the repeat procedure demonstrated that none of the patients had complete circumferential isolation of all PV's. The majority of the repeat ablations (61%) were caused by electrical reconnection of the right inferior PV (RIPV).

Fourteen patients (56%) had AF recurrence after the first repeat procedure. From these patients, eight (57%) underwent a third ablation procedure. The other six patients were treated with anti-arrhythmic drugs. There was no relation between the duration ( $p=0.51$ ) and nature (paroxysmal or persistent) ( $p=0.62$ ) of AF on the probability of AF recurrence.

### Left atrial remodeling

There was no correlation between the pre-(index)procedural LA volume index (LAVi) and LASP (Pearson's  $r=0.107$ ,  $p=0.61$ ). Furthermore, post-(index)procedural LAVi and LASP also did not show a correlation (Pearson's  $r=0.266$ ,  $p=0.20$ ). Nine cases showed discordance between volumetric and geometric remodeling (**figure 2**).

**Table 1.** Patient characteristics.

N = 25			
Nature of AF	Paroxysmal (n=10)	Persistent (n=15)	
Total duration of AF (days)	2333 ± 1817	1853 ± 1333	p = 0.48
Age (years)	64 ± 6.8	58 ± 8.3	
Male (%)	70%	87%	
Hypertension (%)	40%	47%	
Body mass index	27 ± 5.5	29 ± 5.2	
Body surface area	2 ± 0.2	2 ± 0.3	
Anti-arrhythmic drugs			
- Sotalol or beta-blocker	80%	93%	
- Amiodarone	10%	13%	
- Flecainide	10%	7%	
Pre- (index) procedural LA sphericity	81.5 ± 3.3	84.7 ± 3	p = 0.02*
Post-(index) procedural LA sphericity	81.2 ± 4.6	84.8 ± 2.6	p = 0.04*

LA, left atrium.

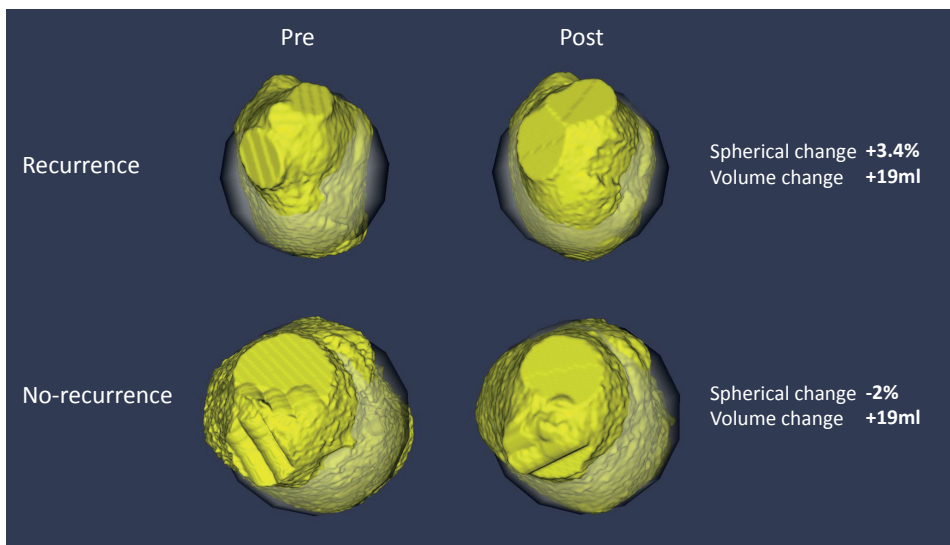


**Figure 2.** Comparison between structural and geometrical remodeling.

A right sided view of the left atrial cavity depicting the discrepancy between changes in left atrial sphericity and volume following a repeat procedure. Top panel; a patient with recurrence of AF after repeat ablation with increased LASP (negative remodeling) and increased LA volume. Bottom panel; a patient without recurrence of AF after repeat ablation with decreased LASP (positive remodeling) and increased LA volume.

### ***Geometric remodeling***

Pre- and post-procedural LASP were significantly lower in patients with paroxysmal AF compared to persistent AF ( $p=0.02$  and  $p=0.04$ , respectively) (**table 1**).

The post-procedural *change* in the left atrial geometry, calculated as the difference between pre-procedural LASP and post-procedural LASP, was significantly related to AF recurrence ( $p<0.001$ ) (**figure 3** and **table 2**). Patients with AF recurrence following the repeat ablation ( $n=14$ ) showed an increase of the LASP (negative remodeling) after the index procedure. Eleven patients had a reduction of LASP (positive remodeling) after the index ablation and were free from AF recurrence following the repeat ablation (**table 2**).

The nature of AF was not correlated with changes in the LASP as both negative and positive geometrical changes were observed in paroxysmal as well as persistent AF patient groups (**figure 4**).

### ***Volumetric remodeling***

Both pre- and post-index procedural LAVi demonstrated no correlation with post-procedural AF recurrence (**table 2**). Change in the LAVi, calculated as the difference between pre-procedural LAVi and post-procedural LAVi, was also not correlated with AF recurrence ( $p=0.17$ ).

No significant difference was found in the pre-procedural LAVi between paroxysmal AF ( $61 \pm 16$  ml/m<sup>2</sup>) and persistent AF ( $74 \pm 15$  ml/m<sup>2</sup>) ( $p=0.06$ ). A significant difference was observed in the post-procedural LAVi between paroxysmal AF ( $57 \pm 19$  ml/m<sup>2</sup>) and persistent AF ( $77 \pm 21$  ml/m<sup>2</sup>) ( $p=0.02$ ).

### **Left atrial remodeling and PV isolation**

No significant correlation was observed between the volumetric indices and total number of isolated PV's (**table 3**). An inverse relation was found between pre-procedural LASP and total number of isolated PV's (Pearson's  $r=-0.528$ ,  $p=0.007$ ) (**table 3**). Post-procedural LASP was not correlated with the total number of isolated PV's (Pearson's  $r=-0.352$ ,  $p=0.08$ ) (**table 3**).

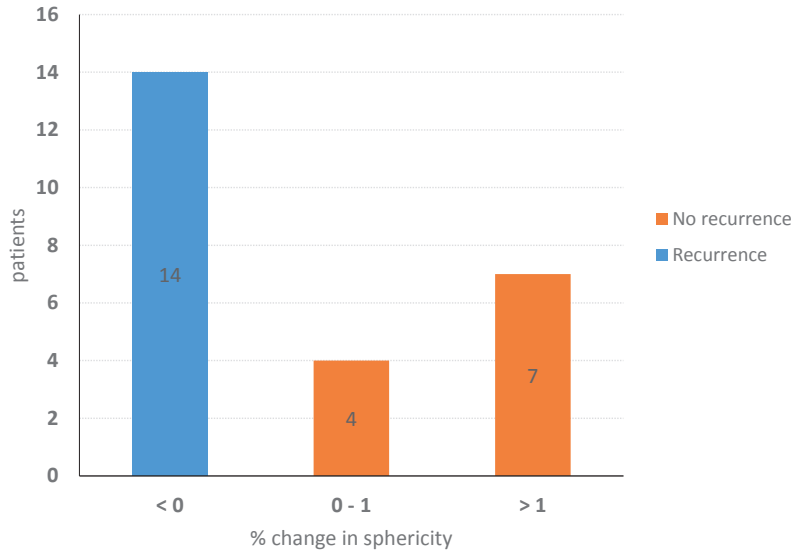


**Figure 3.** Correlation between post-index PVI change in sphericity and AF recurrence.

Changes in LASP following the index ablation demonstrated a strong correlation with the probability of AF recurrence. All patients with increased LASP (negative remodeling) (blue bar) had AF-recurrence during the follow-up. Patients with a reduction in the LASP (positive remodeling) (orange bars) had no episodes of AF during the follow-up.

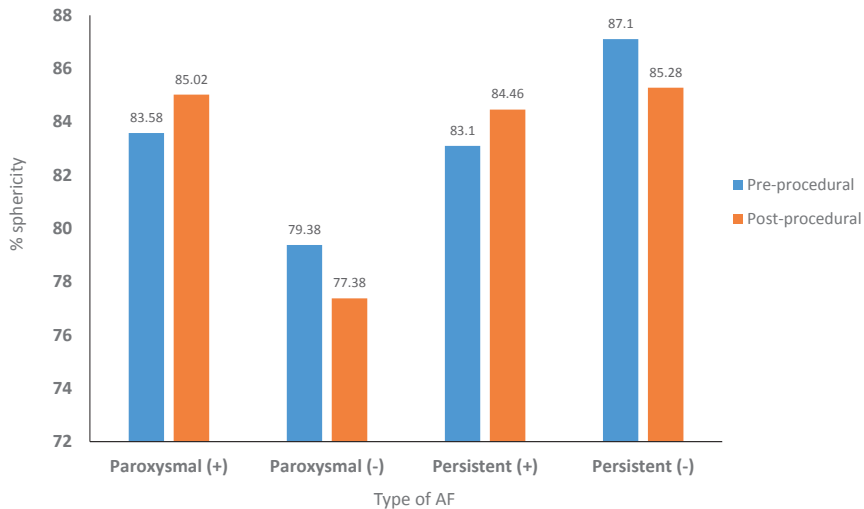


**Figure 4.** Differences in LASP for paroxysmal and persistent AF.

The nature of AF compared to the left atrial sphericity (LASP). (-) indicates no AF recurrence; (+), recurrence. Patients with recurrence showed an increase of the LASP after the index procedure.

**Table 2.** Comparison of geometric remodeling after index procedure to AF recurrence after repeat ablation.

	No recurrence	Recurrence*	P value
N	11 (44%)	14 (56%)	
Age (years)	60 ± 1	61 ± 7	0.76
Male (%)	82%	79%	0.84
Paroxysmal AF (%)	45%	36%	0.62
Duration of complaints (days)	2289 ± 1776	1853 ± 1337	0.51
LASP (%)			
Pre-procedural	83.6 ± 4.4	83.3 ± 2.7	0.84
Post-procedural	81.7 ± 4.8	84.7 ± 2.4	0.05
Change	-1.9 ± 1.7	+1.4 ± 1.7	< 0.001

LASP, left atrial sphericity; \* third episode of AF.

**Table 3.** Correlation between LA remodeling parameters and number of isolated PV's.

Remodeling parameter	Correlation with number of isolated PV's (Pearson's R)	P value
LA volume index (ml/m <sup>2</sup> )		
Pre-procedural	0.05	0.81
Post-procedural	0.099	0.64
Change	-0.114	0.59
LASP (%)		
Pre-procedural	-0.528	0.007*
Post-procedural	-0.352	0.08
Change	-0.196	0.347

LA, left atrium; LASP, left atrial sphericity.

## DISCUSSION

This study investigated the relation of LA geometrical remodeling, expressed as sphericity, and maintenance of sinus rhythm after repeat pulmonary vein isolation. The results indicate that LA sphericity is a clinically useful parameter to predict the outcome of a repeat ablation procedure. The pattern of LA geometrical remodeling (positive versus negative) was found to be an independent predictor of procedural outcome in contrast to volumetric remodeling and conventional clinical parameters.

To the best of our knowledge, this is the first study to report the time-course of LA geometrical remodeling following pulmonary vein isolation and its predictive value with respect to the outcome of a repeat ablation.

### **Post-ablation remodeling of the left atrium**

The impact of arrhythmias on the LA remodeling process and vice versa is well described<sup>(14-16)</sup>. Sotomi et al<sup>(3)</sup> demonstrated a reduction of LA volume and improvement of LA ejection fraction irrespective of AF recurrence whereas Marsan et al<sup>(5)</sup> reported an increase of LA volume and deterioration of LA ejection fraction in patients with recurrence of AF.

Besides these controversies, estimating the extent of remodeling by analyzing size and function still remains a challenging task despite all (advanced) imaging modalities available. The results from this study demonstrated that a conventional remodeling parameter such as LA volume failed to predict the outcome of the repeat procedure. Furthermore, the observed discordance between volumetric and geometric remodeling in nine cases (36%) suggests that volumetric changes are not necessarily correlated with geometrical changes. In line with recent observations, it may be concluded that changes in LA geometry are of clinical relevance and could provide a more *direct* measure of the remodeling process<sup>(11)</sup>.

More importantly, the current results indicated a strong correlation between AF recurrence and changes in LASP following the index ablation. Patients with a reduction in the LASP following index PVI had a 100% success rate of the repeat procedure. Furthermore, all cases with an increase in the LASP had recurrence of AF during follow-up. These findings, although in a relatively small patient group, suggest that therapy stratification for repeat ablation may benefit by incorporating LASP.

### **Recurrence of atrial fibrillation after catheter ablation**

Patients with a lower LASP demonstrated a higher number of isolated PV's during the repeat procedure as indicated by the inverse relation between pre-procedural LASP and total number of isolated PV's (Pearson's  $r=-0.528$ ,  $p=0.007$ ).

A potential cause for this effect could be that higher LA sphericity leads to continuous volume overload and results in an increased level of wall stress and myocardial stretch. As described in a recent animal study, excessive elevation of left atrial wall stress leads to a loss of cardiomyocyte structure, calcium homeostasis and contractile function<sup>(17)</sup>, and could eventually result in a persisting, non-reversible structural dilatation of the LA cavity, susceptible for arrhythmia recurrence. This theory is further supported

by a recent simulation study on the effects of mechanical deformation on cardiac bioelectrical activity where myocardial stretch resulted in an increased dispersion of repolarization time and action potential duration <sup>(18)</sup>. In addition, clinical observations have also described a relation between increased arrhythmogenicity of the LA with increasing stretch between the LA and PV junction <sup>(19)</sup>.

In line with these findings it can also be hypothesized that larger positive remodeling (reduction in LASP) leads to better connectivity between the applied ablation lesions ('closing of the remaining gaps'). Due to more complete and gap free isolation lines, the ectopic foci localized in the pulmonary veins are unable to initiate and maintain AF (**figure 5**). This is supported by the observation that pulmonary vein isolation during the acute phase is caused due to a combination of necrosis and edema <sup>(20)</sup>. The resolution of edema may lead to reconnection of the PV's and could result in recurrence of AF.

The results of the current study underline the importance of including the LASP as a parameter for selection of candidates suitable for a repeat ablation procedure.

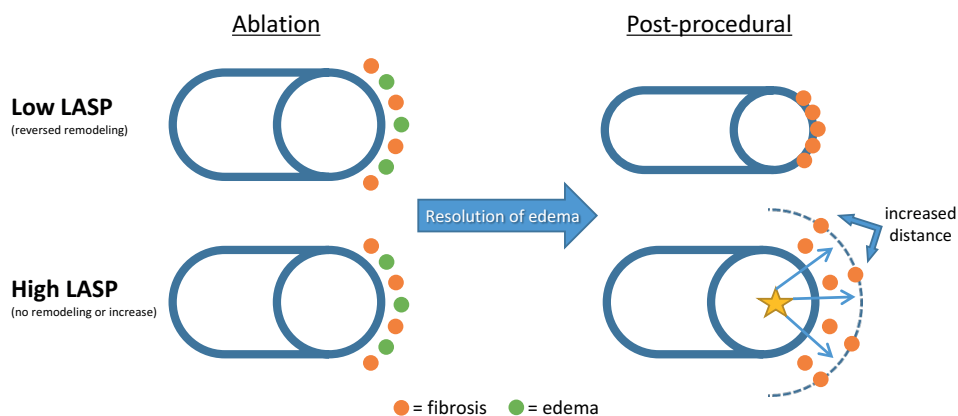


**Figure 5.** Schematic representation of the potential mechanism related to LASP and successfully isolated PV's.

The left panel of figures depicts the sites of ablation lesions (orange and green dots) on the pulmonary vein (blue cylinder). The right panel depicts the change in PV size due to reverse remodeling and its impact on the proximity of ablation lesions following the resolution of ablation induced edema. The PV's of patients with a higher LASP retain their original size or may undergo an increase in size (dotted semi-circle) which, due to increased distance between ablation lesions, may be an additional factor that contributes to incomplete electrical isolation (gaps) (star indicates PV ectopy; arrows indicate electrical leaks).

## Limitations

The percentage of LASP is obtained after segmentation of the LA cavity. Although the segmentation process is mostly automated, the sub-classification of the PV's and LAA is performed manually and is therefore susceptible to inter-observer variations. The impact of manual sub-classification has been evaluated by Bisbal et al. <sup>(12)</sup>. Their results showed a high concordance correlation coefficient of 0.96 and 0.94 for intra- and inter-observer variability. These results indicate that despite the manual nature of the segmentation process, it is a highly reproducible and clinically applicable technique.

The sample size of 25 patients is a lower limit for statistical evaluation. However, the purpose of the study was to indicate the feasibility of using left atrial geometrical remodeling as a predictor of repeat ablation success (proof of concept). To this extent, the current sample size is considered sufficient.

## Future perspectives

The study results indicate that geometrical changes of the LA following index ablation, reflected by the LASP, can predict the success rate of a repeat procedure. Comparative studies should further investigate the long-term clinical impact of these results for patient selection and procedural outcome.

## CONCLUSION

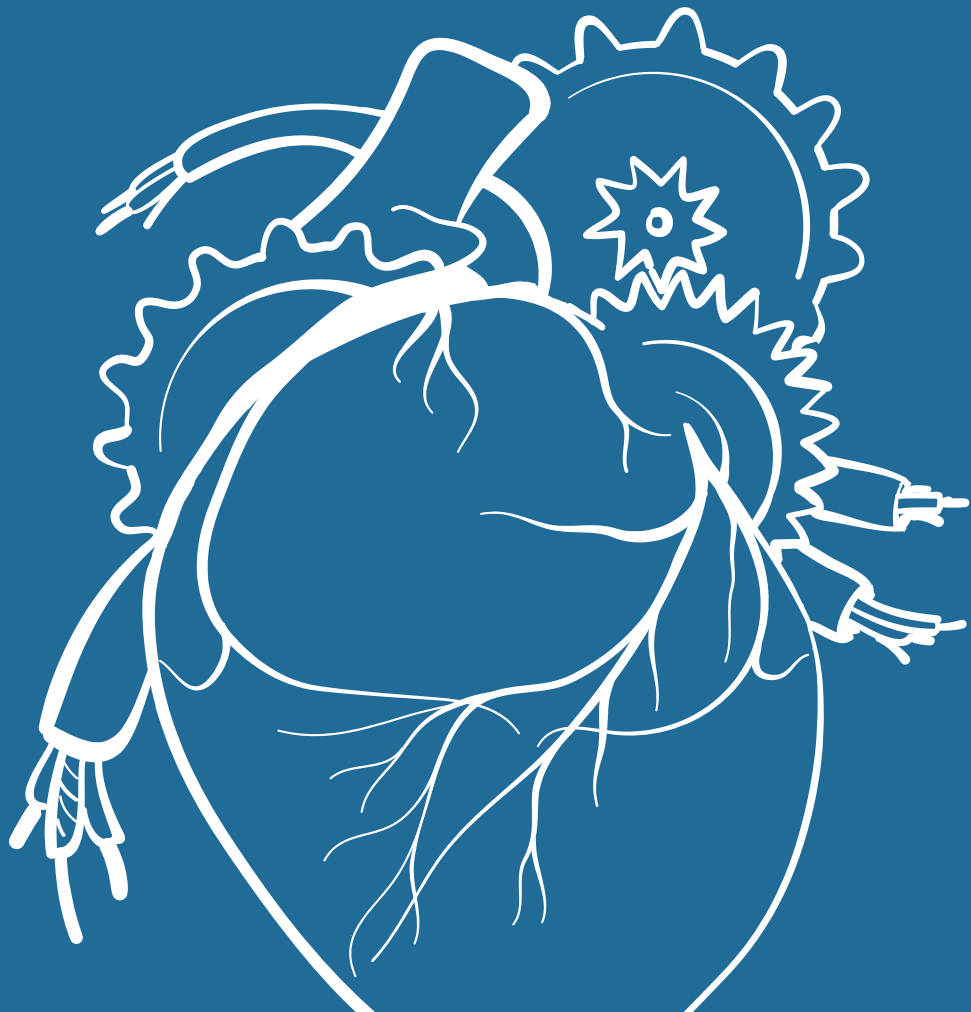
Changes in LASP following index PVI can reliably predict the procedural success rate (probability of AF recurrence) for patients undergoing repeat catheter ablation for AF. A reduction of the LASP is strongly correlated with a higher success rate of the repeat procedure. Applying geometrical remodeling as a selection criterion could improve the procedural efficacy of repeat AF ablation.

## REFERENCES

- 1 Calkins H, Kuck KH, Cappato R, et al. 2012 HRS/EHRA/ECAS expert consensus statement on catheter and surgical ablation of atrial fibrillation: recommendations for patient selection, procedural techniques, patient management and follow-up, definitions, endpoints, and research trial design: a report of the Heart Rhythm Society (HRS) Task Force on Catheter and Surgical Ablation of Atrial Fibrillation. Developed in partnership with the European Heart Rhythm Association (EHRA), a registered branch of the European Society of Cardiology (ESC) and the European Cardiac Arrhythmia Society (ECAS); and in collaboration with the American College of Cardiology (ACC), American Heart Association (AHA), the Asia Pacific Heart Rhythm Society (APHRS), and the Society of Thoracic Surgeons (STS). Endorsed by the governing bodies of the American College of Cardiology Foundation, the American Heart Association, the European Cardiac Arrhythmia Society, the European Heart Rhythm Association, the Society of Thoracic Surgeons, the Asia Pacific Heart Rhythm Society, and the Heart Rhythm Society. *Heart Rhythm* 2012;9:632-96.
- 2 Pokushalov E, Romanov A, De Melis M, Artyomenko S, Baranova V, Losik D, Bairamova S, Karaskov A, Mittal S, Steinberg JS. Progression of atrial fibrillation after a failed initial ablation procedure in patients with paroxysmal atrial fibrillation: a randomized comparison of drug therapy versus reablation. *Circ Arrhythm Electrophysiol* 2013;6:754-60.
- 3 Sotomi Y, Inoue K, Tanaka K, et al. Persistent left atrial remodeling after catheter ablation for non-paroxysmal atrial fibrillation is associated with very late recurrence. *J Cardiol* 2015.
- 4 Helms AS, West JJ, Patel A, Lipinski MJ, Mangrum JM, Mounsey JP, Dimarco JP, Ferguson JD. Relation of left atrial volume from three-dimensional computed tomography to atrial fibrillation recurrence following ablation. *Am J Cardiol* 2009;103:989-93.
- 5 Marsan NA, Tops LF, Holman ER, Van de Veire NR, Zeppenfeld K, Boersma E, van der Wall EE, Schalij MJ, Bax JJ. Comparison of left atrial volumes and function by real-time three-dimensional echocardiography in patients having catheter ablation for atrial fibrillation with persistence of sinus rhythm versus recurrent atrial fibrillation three months later. *Am J Cardiol* 2008;102:847-53.
- 6 Akutsu Y, Kaneko K, Kodama Y, Suyama J, Li HL, Hamazaki Y, Tanno K, Gokan T, Kobayashi Y. Association between left and right atrial remodeling with atrial fibrillation recurrence after pulmonary vein catheter ablation in patients with paroxysmal atrial fibrillation: a pilot study. *Circ Cardiovasc Imaging* 2011;4:524-31.
- 7 Pump A, Di BL, Price J, et al. Efficacy of catheter ablation in nonparoxysmal atrial fibrillation patients with severe enlarged left atrium and its impact on left atrial structural remodeling. *J Cardiovasc Electrophysiol* 2013;24:1224-31.
- 8 Hof IE, Vonken EJ, Velthuis BK, Wittkampfh FH, van der Heijden JF, Neven KG, Kassenberg W, Meine M, Cramer MJ, Hauer RN, Loh P. Impact of pulmonary vein antrum isolation on left atrial size and function in patients with atrial fibrillation. *J Interv Card Electrophysiol* 2014;39:201-9.

- 9 Kurotobi T, Iwakura K, Inoue K, Kimura R, Toyoshima Y, Ito N, Mizuno H, Shimada Y, Fujii K, Nanto S, Komuro I. The significance of the shape of the left atrial roof as a novel index for determining the electrophysiological and structural characteristics in patients with atrial fibrillation. *Europace* 2011;13:803-8.
- 10 Nedios S, Tang M, Roser M, Solowjowa N, Gerds-Li JH, Fleck E, Kriatselis C. Characteristic changes of volume and three-dimensional structure of the left atrium in different forms of atrial fibrillation: predictive value after ablative treatment. *J Interv Card Electrophysiol* 2011;32:87-94.
- 11 Bisbal F, Guiu E, Cabanas P, et al. Reversal of spherical remodelling of the left atrium after pulmonary vein isolation: incidence and predictors. *Europace* 2014;16:840-7.
- 12 Bisbal F, Guiu E, Calvo N, et al. Left atrial sphericity: a new method to assess atrial remodeling. Impact on the outcome of atrial fibrillation ablation. *J Cardiovasc Electrophysiol* 2013;24:752-9.
- 13 Mosteller RD. Simplified calculation of body-surface area. *N Engl J Med* 1987;317:1098.
- 14 Casacang-Verzosa G, Gersh BJ, Tsang TS. Structural and functional remodeling of the left atrium: clinical and therapeutic implications for atrial fibrillation. *J Am Coll Cardiol* 2008;51:1-11.
- 15 Hoit BD. Left atrial size and function: role in prognosis. *J Am Coll Cardiol* 2014;63:493-505.
- 16 Kottkamp H. Catheter ablation of atrial fibrillation: on the pathophysiology of the arrhythmia and the impact of cardiac risk factor management. *J Am Coll Cardiol* 2014;64:2232-4.
- 17 Frisk M, Ruud M, Espe EK, Aronsen JM, Roe AT, Zhang L, Norseng PA, Sejersted OM, Christensen GA, Sjaastad I, Louch WE. Elevated ventricular wall stress disrupts cardiomyocyte t-tubule structure and calcium homeostasis. *Cardiovasc Res* 2016;112:443-51.
- 18 Colli FP, Pavarino LF, Scacchi S. Joint influence of transmural heterogeneities and wall deformation on cardiac bioelectrical activity: A simulation study. *Math Biosci* 2016;280:71-86.
- 19 Walters TE, Lee G, Spence S, Larobina M, Atkinson V, Antippa P, Goldblatt J, O'Keefe M, Sanders P, Kistler PM, Kalman JM. Acute atrial stretch results in conduction slowing and complex signals at the pulmonary vein to left atrial junction: insights into the mechanism of pulmonary vein arrhythmogenesis. *Circ Arrhythm Electrophysiol* 2014;7:1189-97.
- 20 Arujuna A, Karim R, Caulfield D, et al. Acute pulmonary vein isolation is achieved by a combination of reversible and irreversible atrial injury after catheter ablation: evidence from magnetic resonance imaging. *Circ Arrhythm Electrophysiol* 2012;5:691-700.

06



# INTERVENTIONAL CARDIAC MAGNETIC RESONANCE IMAGING IN ELECTROPHYSIOLOGY: ADVANCES TOWARD CLINICAL TRANSLATION

---

Pranav Bhagirath MD; Maurits van der Graaf MD; Rashed Karim PhD; Kawal Rhode BSc PhD; Christopher Piorkowski MD; Reza Razavi MD FRCP; Juerg Schwitter MD PhD; Marco Götte MD PhD

*Circ Arrhythm Electrophysiol.* 2015 Feb;8(1):203-11



## INTRODUCTION

Technical advances in cardiovascular electrophysiology (EP) have resulted in an increasing number of catheter ablation procedures reaching 200,000 in Europe for the year 2013<sup>1</sup>. These advanced interventions are often complex and time-consuming, and may cause significant radiation exposure<sup>2</sup>. Furthermore, a substantial number of ablation procedures remain associated with poor (initial) outcomes and frequently require one or more redo procedures<sup>3</sup>.

Innovations in cardiac imaging and image guidance could help improve the results of ablation procedures<sup>4</sup>. Amongst the available imaging modalities, Cardiac Magnetic Resonance Imaging (CMR) can be considered the most comprehensive and suitable modality for the complete EP and catheter ablation process (including patient selection, procedural guidance and (procedural) follow-up)<sup>5</sup>. The unique ability of CMR including tissue characterization (e.g. T2 weighted imaging for edema visualization, Late Gadolinium Enhancement (LGE for necrosis quantification)) may be of advantage for the evaluation of lesion formation and therapeutic efficacy<sup>6-9</sup>. These benefits and the lack of radiation exposure inspired the development of hybrid fluoroscopy and CMR (XMR) suites<sup>10</sup> and dedicated interventional CMR (iCMR) units<sup>11</sup>.

This review examines the requirements and clinical feasibility of a dedicated iCMR suite for EP procedures. First, the limitations of current EP procedures and ablation strategies are analyzed and the advantages of an iCMR suite for this purpose are discussed. Second, the clinical feasibility is examined by presenting the current challenges of working in an MRI environment. Safety, imaging and device related aspects are also reviewed. Finally, the requirements for implementing an iCMR suite and the current state of their developments is addressed.

## CURRENT CHALLENGES IN ELECTROPHYSIOLOGY

There are different phases during the workup and follow-up of a diagnostic or ablative EP procedure. The limitation of the current strategy, including the role of fluoroscopy, in diagnosis and treatment of arrhythmias are discussed in the following paragraphs.

### **Patient identification and procedure planning**

Imaging is considered a cornerstone of patient selection for ablation therapy<sup>4</sup>. Information about arrhythmic substrate can be acquired prior to the procedure using CMR. However, despite the proven usefulness<sup>12, 13</sup>, pre-procedurally acquired

data is usually not merged with the Electrical Anatomical Mapping (EAM) systems. The integration of pre-procedurally (non-invasively) acquired data (i.e. MRI-based anatomical and pre-existing scar road map) may result in shorter durations of the invasive, X-ray-based conventional procedures. The use of iCMR would allow these advantages although reduced procedure times might not be seen initially because of the learning curve of doing the procedures in a new environment.

### **Procedural radiation**

The use of electro-anatomical mapping systems has led to some reduction in radiation exposure from the historically high doses seen in electrophysiology procedures. There are in addition several new developments that focus on further reduction of radiation exposure. A recent example is the MediGuide™ (St. Jude Medical Inc., St. Paul, MN, USA) system, a novel 4-dimensional electromagnetic catheter tracking technology. It allows visualization of catheters inside angiographically derived left atrium models and pre-recorded cine-loops. The system is aimed to reduce radiation exposure by limiting fluoroscopy duration. Although, studies illustrate that EP procedures significantly benefit from this technology<sup>14, 15</sup>, it still awaits widespread clinical implementation. However, iCMR would completely eliminated radiation exposure even in long complex cases.

### **Therapeutic efficacy**

Particular ablation procedures such as atrial fibrillation and ventricular tachycardia ablations are often associated with one or more redo procedures. Recent studies, based on MRI techniques including T2 and LGE have proposed an explanation for this phenomenon<sup>9, 12</sup>. During radio-frequency ablation there is formation of edema and necrosis<sup>9, 16</sup>. Post-ablation, edema gradually disappears and gaps between adjacent ablation lesions become apparent. These gaps or areas with incomplete isolation result in recurrence of arrhythmia. Identification of gaps in advance may facilitate redo procedures substantially (**figure 1**)<sup>12</sup>. However, this requires a robust imaging strategy for gap identification. Furthermore, the integration of the generated gap information needs to be easily integrated into the EAM system. Current EAM systems unfortunately do not offer this functionality.

It is safe to conclude that despite various technological advances, there is substantial need for further improvements in the current EP and ablation treatment and evaluation strategy. To a large extent, these developments (e.g. improved procedural guidance, reduction of radiation exposure and evaluation of procedural efficacy) could theoretically be achieved by operating in an iCMR environment.

## Post-ablation gaps

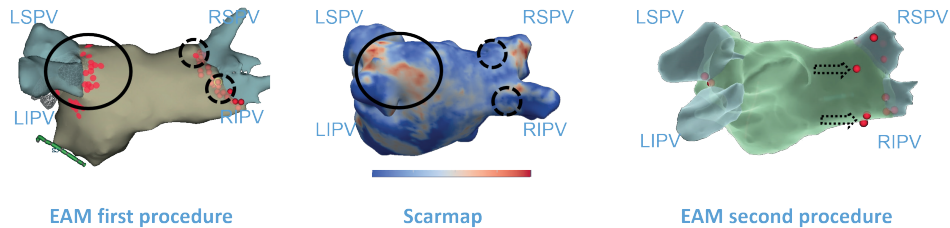


**Figure 1.** Isolation gaps detected using LGE and used for redo ablation guidance.

Left panel depicts the first pulmonary vein isolation EAM. Certain gaps are visible between the RF application points (red dots). Center panel demonstrates the scar-map generated using LGE images acquired 3 months post-procedure. Tissue characteristics are color coded; blue is healthy myocardium whereas red defines scar/fibrosis. The black circle demonstrates a good visual correlation between the extent of ablation on the EAM and presence of scar on the LGE. Two major gaps are visible on the scar-map (dashed black circle). During the redo procedure (right panel) these gaps were targeted (dashed black arrow).

## iCMR IN EP

iCMR allows for integrated use of pre-procedural 3D anatomical scans to help guidance of active tracked catheters, peri-procedural interactive multi-planar visualization of relevant anatomy and visualization of the extent of ablation lesion as well as evaluation of complications. The therapeutic strategy incorporating these information could potentially improve the EP procedure by reducing procedural time and increasing (therapeutic) efficacy, including less redo procedures.

A limited number of centers have explored the (clinical) possibilities towards performing EP procedures (diagnostic and ablation) in an MRI environment (the vast majority at 1.5 Tesla (T)) (**table 1**). The majority of these studies have been performed in animals.

So far, the limited number of (safety) studies conducted in humans have been successful and uncomplicated. However, each research group concludes that prior to performing iCMR guided ablation procedures on a routine basis, the following challenges need to be overcome; 1) Equipment (e.g. communication headsets, catheters and mapping systems) needs to be modified to ensure MR-compatibility and allow active tracking

possibilities, 2) Image acquisition protocols and reconstruction frameworks need to be standardized, and, 3) Existing operational and safety workflow requires considerable modification.

**Table 1.** Real-time MRI guided electrophysiology studies.

		Population	Procedure	Magnet (T)	Catheter tracking
2008	Nazarian et al <sup>11</sup>	10 dogs / 2 humans	Diagnostic study	1.5	Passive and Active
2008	Dukkipati et al <sup>17</sup>	14 swine	Diagnostic study	1.5	Active
2009	Schmidt et al <sup>18</sup>	8 pigs	Diagnostic and ablation study	1.5	Active
2009	Nordbeck et al <sup>19</sup>	8 pigs	Diagnostic and ablation study	1.5	Passive
2009	Hoffmann et al <sup>20</sup>	20 pigs	Diagnostic and ablation study	1.5	Passive
2011	Nordbeck et al <sup>21</sup>	9 mini pigs	Ablation study	1.5	Passive
2011	Eitel et al <sup>22</sup>	1 human	Diagnostic study	1.5	Passive
2011	Vergara et al <sup>23</sup>	6 pigs	Diagnostic and ablation study	3.0	Active
2012	Ranjan et al <sup>24</sup>	12 swine	Diagnostic and ablation study	3.0	Active
2012	Ganesan et al <sup>25</sup>	12 sheep	Diagnostic and ablation study	1.5	Passive
2012	Nordbeck et al <sup>26</sup>	1 human	Diagnostic and ablation study	1.5	Passive
2012	Sommer et al <sup>27</sup>	5 humans	Diagnostic study	1.5	Passive
2013	Nordbeck et al <sup>28</sup>	1 mini pig	Diagnostic study	1.5	Passive
2013	Gaspar et al <sup>29</sup>	1 swine	Diagnostic and ablation study	1.5	Active
2013	Piorkowski et al <sup>30</sup>	1 human	Diagnostic and ablation study	1.5	Passive
2013	Grothoff et al <sup>31</sup>	10 humans	Diagnostic and ablation study	1.5	Passive

## EQUIPMENT

### Device Tracking

There are two approaches to track devices in an MRI environment; Passive and Active. Both techniques have their unique advantages and shortcomings.

#### Passive

Passive tracking utilizes the signal void and susceptibility artifact caused by the device due to local inhomogeneity of the magnetic field <sup>32</sup>. The passive approach requires continuous tracking of the artifact during in-plane device movement. This requires on-

going adjustments to the imaging plane by the operator. This is a difficult and time consuming task that requires skilled operators. Furthermore, incorrect imaging plane selection during in-plane manipulation can result in loss of device visualization and may increase procedural duration. In addition, loss of anatomical information might occur in the area surrounding the artifact, reducing differentiation between various tissues and may hamper precise navigation.

Despite these disadvantages, both diagnostic EP procedures and ablations have been successfully performed in patients using passive tracking (**figure 2a**)<sup>27,31</sup>.

### Active

Active tracking is performed using small radio-frequency receiver coils built into the device. Imaging sequences can interrogate the location of these coils and allow for real-time, device only navigation<sup>33</sup>. The current EP procedures often require multiple different (multi-electrode) catheters. To get accurate orientation of a catheter and be able to use pre-determined models of the shape of the distal end of the catheter where the electrodes are placed, at least 2 active coils are needed. These coils have a hypothetical danger of heating due to RF coupling<sup>34</sup>. There have however been a number of strategies developed to address this<sup>35</sup>. However, due to this safety concern, active tracking has so far only been studied in animal models (**figure 2b**)<sup>11,23,24,29</sup>. Initial reports did not encounter any adverse events.

## Differences between device tracking

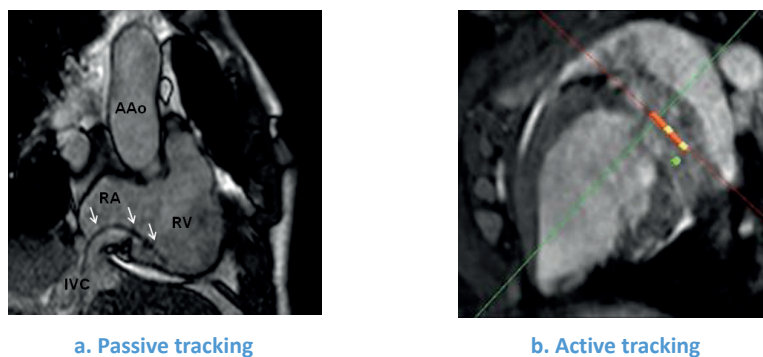


**Figure 2.** Different device tracking strategies.

Left panel depicts passive tracking, an approach utilizing the susceptibility artifact (white arrows) for device visualization. Right panel depicts the active tracking approach using micro-coils on the device resulting in multiple benefits including improved visualization update (achievable within a few milliseconds) and device guided navigation.

### **Devices**

The availability of MR-compatible devices is currently extremely limited. The majority of the devices are used for investigative purposes and are yet to obtain regulatory approval.

### **Instrumentation EP study**

A conventional EP study requires a recording and mapping system, stimulator and an RF generator. Currently there is no MRI-compatible equipment available commercially. As a result, every center has their customized solution. Several centers are investigating devices from Imricor Medical Systems (Burnsville, MN) and MRI Interventions (Irvine, CA). These companies are in the process of developing a range of MRI compatible devices with regulatory approval<sup>24,25,31</sup>.

### **EAM**

An important component of the conventional EP studies is the EAM system that allow for catheter navigation inside realistic anatomical heart models. Recent studies have proposed modifications to create MRI compatible EAM systems<sup>36</sup>. The introduction of such an EAM system will offer the prospect of a fully integrated approach, suitable for MRI-based navigation, deployment of specific, targeted ablation, and immediate evaluation of therapy.

### **Catheters**

Essential components in performing EP procedures are the diagnostic and ablation catheters. Both passive and active catheters have been used for investigational purposes in animals. However, due to safety concerns (heating) all human trials have been conducted using passive tracking only (**table 1**). Although active tracking is not a prerequisite for iCMR guided EP, active catheters can be used for device guided navigation. This feature eliminates operator interaction for manual scanning plane adjustment. In addition, the improved visibility of active catheters may contribute towards reducing procedural duration.

### **Guidewire**

Performing interventional EP procedures may require the use of guidewires to facilitate the insertion of multiple sheaths and guidance of some catheters required during ablation. Passive guidewires have been successfully applied during cardiac interventions and are being investigated in larger trials<sup>37</sup>. The major limitation of using active guidewires is the potential of RF coupling due to the substantial length of these devices. This restriction has recently been addressed by the development of an

active guidewire with embedded fiberoptic temperature probe<sup>38</sup>. Although this new feature does not eliminate the risk of heating, the temperature probe allows accurate monitoring of device heating and contributes towards safer usage of guidewires.

### ***Pericardial needles***

Both passive and active needles have been studied in animals<sup>39, 40</sup>. A comparison between these needles demonstrates favorable results for active tracking. Active needles needed shorter access time (88 vs. 244 sec,  $P = 0.022$ ), and required significantly fewer needle passes (4.5 vs. 9.1,  $P = 0.028$ )<sup>40</sup>.

To summarize, recent technical improvements have resulted in the advent of MRI conditional (active trackable) EP tools, including needles, guidewires and (multi-electrode) catheters.

## **IMAGE ACQUISITION**

Image acquisition for procedural guidance can be divided in three stages; 1) catheter navigation, 2) catheter tip localization prior to ablation, and 3) visualization and evaluation of lesions immediately after ablation. Mandatory sequences for this workflow (e.g. Steady State Free Precession (SSFP), T2 and LGE) are available for both 1.5 T and 3T scanners. Although the various stages require different strategies (e.g. high-quality low temporal resolution procedural roadmap versus high temporal (low-quality) resolution catheter navigation), a standardization of applied sequences and scanning approach is still lacking (**table 2**).

### **Procedural roadmap**

The majority of studies conducted so far, do not implement pre-procedurally acquired roadmaps for EP and ablation procedures. This might be due to the limited number of studies investigating redo procedures or evaluating the substrate-based ablation of arrhythmias. A study in a porcine myocardial infarction model reported a good correlation of infarct location on LGE images compared to a MRI-compatible EAM system-based voltage map<sup>17</sup>. Pre-procedural planning (anatomy and substrate imaging) is essential for complex arrhythmias and integration of this data in iCMR suites should be further investigated.

**Table 2.** Ablation stages and utilized CMR sequences.

Procedural stage	Type sequence	Availability	References
Pre-procedural			
Substrate identification	T1-weighted PSIR turbo-GRE		
Roadmap	MRA (3D respiratory navigated and ECG-gated GRE)	Commercial	24
	3D self-navigation strategies	Experimental	41
Catheter guidance			
Catheter navigation	Real-time balanced SSFP (8 fps)	Commercial	31
Catheter tip at ablation site	T1-weighted FLASH (5-6 fps)	Experimental	21, 23
	Real-time balanced SSFP (8 fps)	Commercial	31
Ablation lesion			
Edema	T2-weighted HASTE	Commercial	23
	T2-weighted TSE	Commercial	31
	High-resolution quantitative 2D and 3D T <sub>2</sub> -mapping strategies	Experimental	42, 43
Necrosis	3D respiratory-navigated IR-GRE	Experimental	24
	T1-weighted PSIR turbo-GRE	Commercial	31

### Catheter navigation and tip localization

It has been observed that a frame-rate of approximately 5 frames per second (fps) is acceptable for catheter guidance in EP procedures<sup>11</sup>. Currently, commercially available, real-time SSFP sequences provide frame rates ranging between 5-8 fps<sup>31</sup>. The easy availability of these sequences facilitates passive tracking in every center with a diagnostic CMR scanner. This encourages clinical translation without a demand for major device modifications.

However, due to its inherent advantages and despite the current pre-clinical state of development, active tracking features are considered to be the method of choice for clinical EP and ablation in the near future.

### Lesion evaluation

A unique strength of CMR, compared to other imaging modalities, is the ability to perform tissue characterization. This can be used to identify and distinguish between the two cellular reactions that occur during an ablation; 1) Acute (Edema) and 2) Permanent (Necrosis). Both edema and necrosis can be evaluated using commercially available sequences<sup>6, 31</sup>. T2-weighted Ultrafast Spin Echo sequences<sup>6, 23, 31</sup> and quantitative high-

resolution  $T_2$ -mapping techniques in 2D<sup>42</sup> and even in 3D<sup>43</sup> can be used to visualize edema. Necrosis can be visualized using the commercially available T1-weighted PSIR turbo-GRE<sup>31</sup> or using the experimental 3D respiratory-navigated IR-GRE sequence<sup>24</sup>. Direct feedback during the ablation procedure may contribute to a complete isolation during the first attempt. In case there is reoccurrence of arrhythmia's due to incomplete isolation, this information can be utilized to perform targeted gap ablation. Detailed MRI-derived information with respect to lesion formation has therefore the potential to improve single procedure success rates<sup>12</sup>.

## IMAGE RECONSTRUCTION

Implementing an iCMR suite is significantly different from the conventional diagnostic imaging set-up and requires an optimization of the imaging workflow. Performing an interventional study requires 1) real-time acquisition and near real-time reconstruction, 2) rapid sequence changes and 3) integration with device hardware for tracking purpose (**figure 3**). It has been shown that standard sequences, present on every diagnostic scanner, can be used for performing and evaluating interventions<sup>31</sup>. However, there are three specifically designed visualization frameworks targeted at the EP community (i.e. Gadgetron, Vurtigo and RTHawk), that are user-friendly and can facilitate procedural guidance. An overview of these frameworks and their respective functionalities is provided below.

### Gadgetron

Gadgetron is an open source, modular framework designed to facilitate rapid development and easier sharing of image analysis and reconstruction algorithms<sup>44</sup>. Modules (gadgets) can be developed using standard toolkits present in the framework. These gadgets are programmed to perform specific post-processing tasks and can be configured as part of the scanner data pipeline. Multiple gadgets can be used for simultaneous processing. Furthermore, the individual gadgets can be re-used in different workflows thereby enabling thorough evaluation of consistency and performance.

However, this dynamic framework does have a major limitation. There are no possibilities to control the MRI scanner directly using the tools provided. Therefore, image acquisition can only be performed using the existing scanner front-end. Due to the restrictions of the in-built interfaces, this will require deployment of third-party solutions.

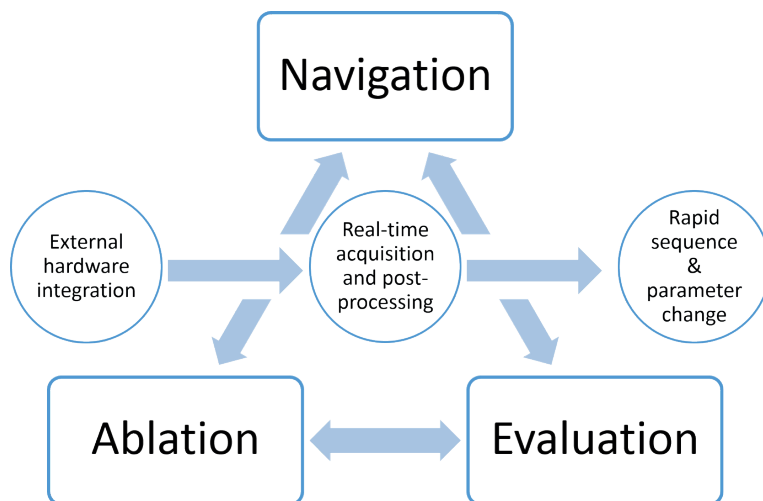


**Figure 3.** Key components during an iCMR EP procedure.

The key components of every iCMR EP procedure. Blocks depict the needs of the interventionalist. Circles indicate the requirements from the scanner and imaging interface.

### Vurtigo

The visualization Platform for Real-time, MRI-guided Cardiac Electroanatomic Mapping (Vurtigo) is another open source platform-independent application that provides useful features for interventional EP<sup>45</sup>.

The core of Vurtigo is the Geometry server, a storage space containing images, plane orientations and catheter information. Vurtigo can communicate directly with the scanner through a plugin (OpenIGTLink), allowing direct manipulation of the scan plane. In addition, this software tool also offers the possibility to integrate pre-existing electro-anatomical maps (EAM) with acquired volume and tissue-characterization images. This can facilitate the ablation by generating procedural roadmaps, incorporating anatomical information and tissue substrate.

### RTHawk

RTHawk is an advanced development platform to design, simulate and run MRI applications (sequences, reconstruction pipelines).<sup>46</sup> In addition, there are possibilities for rapidly switching between different pulse sequences and performing real-time post-processing. Furthermore, it also enables integration of the designed applications with external hardware e.g. interventional devices. Unfortunately, sparse information with respect to this platform is currently available.

## **SAFETY AND WORKFLOW IN THE IMR**

The transition from conventional fluoroscopic procedures towards an iCMR suite requires revision of the existing workflow. Cath-lab personnel used to work in a fluoroscopic environment need education about operating in a magnetic field. Furthermore, patient monitoring and safety protocols require thorough revision and scenario training.

### **Architectural layout**

In contrast to conventional fluoroscopy guided procedures, an intervention in the iCMR suite is bound to more strict rules. The procedures are performed in an environment that is less accessible for personnel since each step closer to the magnet increases the risk of ferro-magnetic interaction. The design of an iCMR suite needs to incorporate various aspects considered daily practice for conventional interventions. This includes but is not limited to 1) patient preparation, 2) access to device storage, 3) sterility and air treatment, and 4) evacuation possibilities in case of an emergency. Each of these aspects needs to be carefully considered and adequately addressed.

### **Personnel**

During the EP and ablation procedures, an experienced technician, radiologist, or imaging cardiologist needs to be present for image acquisition. During the development phase of an iCMR suite, it is advisable (if not mandatory) to have a knowledgeable physicist present for optimization of imaging sequences used during the procedures.

During the initial another potential role during interventions could be that of a safety officer. This person could be appointed as coordinator in case of emergency situations. Once a routine procedural workflow is achieved, a dedicated coordinator may become redundant.

### **Communication**

An essential part of the ablation procedure is the communication between the electrophysiologists and the technician. The development over the past years has progressed rapidly with commercially available MR-compatible solutions (Opto-acoustics, Clear-com, Gaven).

### ***Headsets***

Initial MR-headsets used fiber optic cables and limited the working radius of the interventionalist. More recent technology offers wireless communication and supports multiple headsets. Opto-acoustics uses infra-red (IR) technology to full wireless coverage in both the scanning room and the control room.

### ***Projection systems***

High definition beamers can be shielded and installed in the iCMR. These commercially available systems offer a resolution of 1080p and can be configured to display multiple data streams.

## **Patient safety**

### ***Telemetry***

Conventional ablations rely on both intracardiac and surface electrocardiograms (ECG) recorded during the intervention. However, surface electrocardiograms get distorted in the MRI due to the magneto-hydrodynamic effect caused by the static magnetic field ( $B_0$ ). Additional interference is caused due to the switching gradients and results in further deformation of the ECG signal. Such ECG artifacts can also lead to trigger problems and consequently suboptimal image quality.

There are currently no commercial solutions for 12-lead ECG monitoring in the MRI. Recent human studies have successfully demonstrated the feasibility of a custom made 12-lead ECG acquisition during a CMR study<sup>47</sup>. This is accomplished using custom made filtering hardware and provides reliable ECG signals with a SNR loss <5%. No adverse events e.g. electrode heating or surface burns were reported.

### ***Sedation***

Recent studies advocate the importance of sedation during complex ablative procedures (e.g. atrial fibrillation, ventricular tachycardia)<sup>48</sup>. Sedation reduces patient discomfort and can result in shorter and more effective procedures. In order to operate under sedation, the intervention room set up requires basic anesthesia equipment e.g. ventilator, vital signs recorders (PO<sub>2</sub>, blood-pressure, respiration) and ECG monitors.

Advanced MRI-compatible anesthesia equipment is available (Aestiva/5 MRI, Datex-Ohmeda, Madison, WI), and can be easily transferred into the iCMR environment.

### ***Tamponade***

Cardiac tamponade is a potentially life threatening complication associated with ablative therapy. The incidence varies for the different interventions with numbers reported up to 6%. Current guidelines advise immediate echocardiography in case hypotension develops. Confirmation of this diagnosis is followed by pericardiocentesis to drain the excessive fluid from the pericardial space. Due to variations in the anatomy, this sometimes results in a complex procedure.

In conventional fluoroscopic rooms, this is best performed using echocardiography. In case of iCMR, there are various sequences that can diagnose and potentially locate the lesion. In addition, a recent animal study demonstrated the feasibility of performing pericardiocentesis inside the scanner room using commercially available needles<sup>39</sup>. In total 12 successful procedures (no complications) were performed using a real-time imaging approach and passive tracking of the needle. This development increases the practicability of complex ablative therapy in the scanner and significantly expands the emergency solving capacity of iCMR.

### ***SAR***

The specific absorption rate (SAR) indicates the amount of radio-frequency energy deposited in the tissue. The safety limit, as indicated by the Food and Drug Administration, for whole body SAR is 4W/Kg/15 minutes exposure and should be monitored during the procedure. In case this limit is exceeded, scanning should be stopped to allow recovery of the tissue. In general, this situation can also be prevented by increasing the repetition time (TR) or reducing the flip angle.

### ***Defibrillation***

Performing EP procedures in an iCMR suite requires a meticulously constructed evacuation plan. This is especially required for patients on respiratory support and with a multitude of monitors attached. A possible solution could be integrating monitoring and ventilation with the scanner table. This would allow emergency cases to be rapidly shifted towards a room where defibrillation and other resuscitative actions can be performed without any restrictions.

Electrical mapping of arrhythmias is performed by inducing the tachycardia by means of stimulation protocols. Especially in case of ventricular tachyarrhythmias this can cause hemodynamic instability in patients and forces cardioversion to be performed. Currently, there is no solution allowing defibrillation to be performed inside an iCMR suite. In case of diagnostic scans, this has not been a limiting factor, as a patient can be transported out of the magnet within few seconds. This changes when a patient is

instrumented with catheters and undergoing an ablation. In this particular scenario, even with the correct protocols in place, it is a challenging task to safely bring the patient outside the MR suite<sup>31</sup>. Therefore, defibrillation should be considered as a major issue which needs to be addressed prior to performing complex (ventricular) ablative procedures.

## CLINICAL PERSPECTIVE

The benefits of iCMR including 3-dimensional guidance, tissue characterization and lack of radiation exposure over conventional fluoroscopic procedural guidance are the underlying rationale for researchers investigating the feasibility of iCMR (**Table 1**). Despite the growing number of centers experimenting with iCMR, the clinical translation remains a challenge.

An important reason is the limited availability of MRI compatible devices (e.g. needles, guidewires, catheters, recording system) and they are currently available for investigational purposes, only.

In the recent years, both active and passive devices have been developed and tested (**table 1**). Although active devices might be prone to heating issues, they offer multiple benefits over passive devices, including 1) real time, device guided navigation 2) no artifact and loss of anatomical information in the surrounding tissue and 3) easy distinction (using color coding) between electrodes and different devices. Future trials should focus at the design and heating aspects to enable active device usage in human studies.

Another major reason delaying clinical implementation is the comprehensive technical know-how required on both, the imaging and EP level. However, the fact that basic (human) ablation studies can already be performed successfully inside the MRI using passive devices, indicates that the initial (difficult) pioneering phase has come to an end<sup>31</sup>. The workflow (using commercial imaging sequences) and setup (MRI-compatible catheters and EP system) as described in this review has resulted in an increased interest from multiple institutions to explore iCMR for EP and ablation purposes.

A well thought out implementation strategy is essential prior to considering a transition towards iCMR. It appears obvious to start with relatively simple procedures like right sided heart catheterization<sup>49, 50</sup>. This serves three important goals; 1) familiarizing and educating the assisting personnel about the safety issues of working in an MRI environment, 2) training the radiographer to better understand the requirements

(visualization planes) of the operating physician and 3) allowing the interventionalist to get used to the benefits (no heavy lead protection) and limitations associated with procedures in the iCMR. Once the necessary experience is acquired, these procedures can be replaced by electrophysiological interventions with simple catheter setups e.g. atrial flutter ablation. Prior to applying iCMR in complex ablations (atrial fibrillation and ventricular tachycardia) fundamental obstacles e.g. commercial 12 lead ECG system and defibrillation need to be resolved.

### New challenges - competitive methods

Besides the tissue characteristic based road-map, non-invasively obtained inverse potential maps (IPM) generated from body surface potential mapping (BSPM) may reduce procedural duration and improve outcome<sup>51</sup>. IPM is already being applied to analyze complex arrhythmias and has great potential to generate personalized ablation strategies<sup>52</sup>. The anatomical volume conductor models required to perform IPM can also be used for preparing a patient-specific procedural roadmap (**figure 4**).

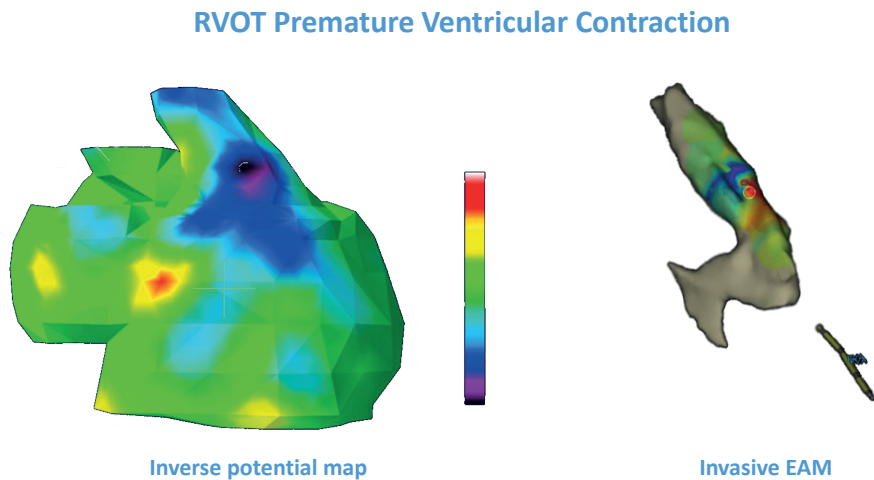


**Figure 4.** Inverse potential map of an RVOT premature ventricular contraction.

Left panel indicates the first point of activation (black) during a PVC. Right panel shows the focus of activation as measured during invasive EP study. There is significant visual agreement between the two images. This indicates the potential of IPM as a pre-procedural diagnostic modality.

Not only the required technical advances for the devices needed to conduct an EP or ablation procedures safely in an MRI environment will be crucial, but also improved patient selection and therapy stratification. Integrating non-invasively obtained anatomical information with tissue characteristics *and* electrical properties will remain a challenging field of research and development.

## **CONCLUSION**

iCMR is an emerging technology and may play an important role in the future for the treatment of complex arrhythmias. The last decade has seen tremendous progress made in this field with relatively simple EP procedures being performed successfully in humans. However, there are still a few major challenges to overcome prior to performing complex ablation procedures in the MRI environment; 1) MRI compatible equipment (12 lead ECG, catheters and ablation systems) with regulatory approval is needed, and 2) emergency strategies especially regarding defibrillation inside the MRI have to be established. The coming years should be targeted at resolving these issues in order to expedite the clinical transition of ablation procedures towards iCMR. Finally, the complete integration of non-invasively obtained anatomical data with tissue characteristics and its electrical behavior will demonstrate the full strength of such an iCMR approach.

## REFERENCES

- 1 Arribas F, Auricchio A, Boriani G, Brugada J, Deharo JC, Hindriks G, Kuck KH, Merino JL, Vardas P, Wolpert C, Zeppenfeld K. Statistics on the use of cardiac electronic devices and electrophysiological procedures in 55 ESC countries: 2013 report from the European Heart Rhythm Association (EHRA). *Europace* 2014;16:i1-i78.
- 2 Heidbuchel H, Wittkamp FHM, Vano E, Ernst S, Schilling R, Picano E, Mont L, Reviewers; Jais P, de Bono J, Piorkowski C, Saad E, Femenia F. Practical ways to reduce radiation dose for patients and staff during device implantations and electrophysiological procedures. *Europace* 2014.
- 3 Brooks AG, Stiles MK, Laborderie J, Lau DH, Kuklik P, Shipp NJ, Hsu LF, Sanders P. Outcomes of long-standing persistent atrial fibrillation ablation: a systematic review. *Heart Rhythm* 2010;7:835-46.
- 4 Blomström Lundqvist C, Auricchio A, Brugada J, Boriani G, Bremerich J, Cabrera JA, Frank H, Gutberlet M, Heidbuchel H, Kuck KH, Lancellotti P, Rademakers F, Winkels G, Wolpert C, Vardas PE. The use of imaging for electrophysiological and devices procedures: a report from the first European Heart Rhythm Association Policy Conference, jointly organized with the European Association of Cardiovascular Imaging (EACVI), the Council of Cardiovascular Imaging and the European Society of Cardiac Radiology. *Europace* 2013;15:927-36.
- 5 Bhagirath P, van der Graaf AWM, Karim R, van Driel VJHM, Ramanna H, Rhode KS, de Groot NMS, Götte MJW. Multimodality imaging for patient evaluation and guidance of catheter ablation for atrial fibrillation: current status and future perspective. *International Journal of Cardiology*.
- 6 Lardo AC, McVeigh ER, Jumrussirikul P, Berger RD, Calkins H, Lima J, Halperin HR. Visualization and temporal/spatial characterization of cardiac radiofrequency ablation lesions using magnetic resonance imaging. *Circulation* 2000;102:698-705.
- 7 Peters DC, Wylie JV, Hauser TH, Nezafat R, Han Y, Woo JJ, Taclas J, Kissinger KV, Goddu B, Josephson ME, Manning WJ. Recurrence of atrial fibrillation correlates with the extent of post-procedural late gadolinium enhancement: a pilot study. *JACC Cardiovasc Imaging* 2009;2:308-16.
- 8 Harrison JL, Jensen HK, Peel SA, Chiribiri A, Grondal AK, Bloch LO, Pedersen SF, Bentzon JF, Kolbitsch C, Karim R, Williams SE, Linton NW, Rhode KS, Gill J, Cooklin M, Rinaldi CA, Wright M, Kim WY, Schaeffter T, Razavi RS, O'Neill MD. Cardiac magnetic resonance and electroanatomical mapping of acute and chronic atrial ablation injury: a histological validation study. *Eur Heart J* 2014;35:1486-95.
- 9 Arujuna A, Karim R, Caulfield D, Knowles B, Rhode K, Schaeffter T, Kato B, Rinaldi CA, Cooklin M, Razavi R, O'Neill MD, Gill J. Acute pulmonary vein isolation is achieved by a combination of reversible and irreversible atrial injury after catheter ablation: evidence from magnetic resonance imaging. *Circ Arrhythm Electrophysiol* 2012;5:691-700.

- 10 Rhode KS, Sermesant M, Brogan D, Hegde S, Hipwell J, Lambiase P, Rosenthal E, Bucknall C, Qureshi SA, Gill JS, Razavi R, Hill DLG. A system for real-time XMR guided cardiovascular intervention. *IEEE Trans Med Imaging* 2005;24:1428-40.
- 11 Nazarian S, Kolandaivelu A, Zviman MM, Meininger GR, Kato R, Susil RC, Roguin A, Dickfeld TL, Ashikaga H, Calkins H, Berger RD, Bluemke DA, Lardo AC, Halperin HR. Feasibility of real-time magnetic resonance imaging for catheter guidance in electrophysiology studies. *Circulation* 2008;118:223-9.
- 12 Bisbal F, Guiu E, Cabanas-Grandio P, Berruezo A, Prat-Gonzalez S, Vidal B, Garrido C, Andreu D, Fernandez-Armenta J, Tolosana J, Arbelo E, de Caralt T, Perea R, Brugada J, Mont L. MRI-Guided Approach to Localize and Ablate Gaps in Repeat AF Ablation Procedure. *JACC Cardiovasc Imaging* 2014.
- 13 Fernandez-Armenta J, Berruezo A, Andreu D, Camara O, Silva E, Serra L, Barbarito V, Carotenutto L, Evertz R, Ortiz-Perez JT, De Caralt TM, Perea RJ, Sitges M, Mont L, Frangi A, Brugada J. Three-dimensional architecture of scar and conducting channels based on high resolution ce-CMR: insights for ventricular tachycardia ablation. *Circ Arrhythm Electrophysiol* 2013;6:528-37.
- 14 Sommer P, Richter S, Hindricks G, Rolf S. Non-fluoroscopic catheter visualization using MediGuide technology: experience from the first 600 procedures. *J Interv Card Electrophysiol* 2014.
- 15 Vallakati A, Reddy YM, Emert M, Janga P, Mansour MC, Heist EK, Pimentel R, Dendi R, Atkins D, Bommana S, Mahapatra S, Heard M, Ruskin J, Berenbom L, Dawn B, Lakkireddy D. Impact of nonfluoroscopic MediGuide tracking system on radiation exposure in radiofrequency ablation procedures (LESS-RADS registry)-an initial experience. *J Interv Card Electrophysiol* 2013;38:95-100.
- 16 Ranjan R, Kato R, Zviman MM, Dickfeld TM, Roguin A, Berger RD, Tomaselli GF, Halperin HR. Gaps in the ablation line as a potential cause of recovery from electrical isolation and their visualization using MRI. *Circ Arrhythm Electrophysiol* 2011;4:279-86.
- 17 Dukkupati SR, Mallozzi R, Schmidt EJ, Holmvang G, d'Avila A, Guhde R, Darrow RD, Slavin G, Fung M, Malchano Z, Kampa G, Dando JD, McPherson C, Foo TK, Ruskin JN, Dumoulin CL, Reddy VY. Electroanatomic mapping of the left ventricle in a porcine model of chronic myocardial infarction with magnetic resonance-based catheter tracking. *Circulation* 2008;118:853-62.
- 18 Schmidt EJ, Mallozzi RP, Thiagalingam A, Holmvang G, d'Avila A, Guhde R, Darrow R, Slavin GS, Fung MM, Dando J, Foley L, Dumoulin CL, Reddy VY. Electroanatomic mapping and radiofrequency ablation of porcine left atria and atrioventricular nodes using magnetic resonance catheter tracking. *Circ Arrhythm Electrophysiol* 2009;2:695-704.
- 19 Nordbeck P, Bauer WR, Fidler F, Warmuth M, Hiller KH, Nahrendorf M, Maxfield M, Wurtz S, Geistert W, Broscheit J, Jakob PM, Ritter O. Feasibility of real-time MRI with a novel carbon catheter for interventional electrophysiology. *Circ Arrhythm Electrophysiol* 2009;2:258-67.

- 20 Hoffmann BA, Koops A, Rostock T, Mullerleile K, Steven D, Karst R, Steinke MU, Drewitz I, Lund G, Koops S, Adam G, Willems S. Interactive real-time mapping and catheter ablation of the cavotricuspid isthmus guided by magnetic resonance imaging in a porcine model. *Eur Heart J* 2010;31:450-6.
- 21 Nordbeck P, Hiller KH, Fidler F, Warmuth M, Burkard N, Nahrendorf M, Jakob PM, Quick HH, Ertl G, Bauer WR, Ritter O. Feasibility of contrast-enhanced and nonenhanced MRI for intraprocedural and postprocedural lesion visualization in interventional electrophysiology: animal studies and early delineation of isthmus ablation lesions in patients with typical atrial flutter. *Circ Cardiovasc Imaging* 2011;4:282-94.
- 22 Eitel C, Piorkowski C, Hindricks G, Gutberlet M. Electrophysiology study guided by real-time magnetic resonance imaging. *Eur Heart J* 2012;33:1975.
- 23 Vergara GR, Vijayakumar S, Kholmovski EG, Blauer JJE, Guttman MA, Gloschat C, Payne G, Vij K, Akoum NW, Daccarett M, McGann CJ, Macleod RS, Marrouche NF. Real-time magnetic resonance imaging-guided radiofrequency atrial ablation and visualization of lesion formation at 3 Tesla. *Heart Rhythm* 2011;8:295-303.
- 24 Ranjan R, Kholmovski EG, Blauer J, Vijayakumar S, Volland NA, Salama ME, Parker DL, MacLeod R, Marrouche NF. Identification and acute targeting of gaps in atrial ablation lesion sets using a real-time magnetic resonance imaging system. *Circ Arrhythm Electrophysiol* 2012;5:1130-5.
- 25 Ganesan AN, Selvanayagam JB, Mahajan R, Grover S, Nayyar S, Brooks AG, Finnie J, Sunnarborg D, Lloyd T, Chakrabarty A, Abed HS, Sanders P. Mapping and ablation of the pulmonary veins and cavo-tricuspid isthmus with a magnetic resonance imaging-compatible externally irrigated ablation catheter and integrated electrophysiology system. *Circ Arrhythm Electrophysiol* 2012;5:1136-42.
- 26 Nordbeck P, Beer M, Kostler H, Ladd ME, Quick HH, Bauer WR, Ritter O. Cardiac catheter ablation under real-time magnetic resonance guidance. *Eur Heart J* 2012;33:1977.
- 27 Sommer P, Grothoff M, Eitel C, Gaspar T, Piorkowski C, Gutberlet M, Hindricks G. Feasibility of real-time magnetic resonance imaging-guided electrophysiology studies in humans. *Europace* 2013;15:101-8.
- 28 Nordbeck P, Quick HH, Ladd ME, Ritter O. Real-time magnetic resonance guidance of interventional electrophysiology procedures with passive catheter visualization and tracking. *Heart Rhythm* 2013;10:938-9.
- 29 Gaspar T, Piorkowski C, Gutberlet M, Hindricks G. Three-dimensional real-time MRI-guided intracardiac catheter navigation. *European Heart Journal* 2014;35:589.
- 30 Piorkowski C, Grothoff M, Gaspar T, Eitel C, Sommer P, Huo Y, John S, Gutberlet M, Hindricks G. Cavotricuspid isthmus ablation guided by real-time magnetic resonance imaging. *Circ Arrhythm Electrophysiol* 2013;6:e7-10.

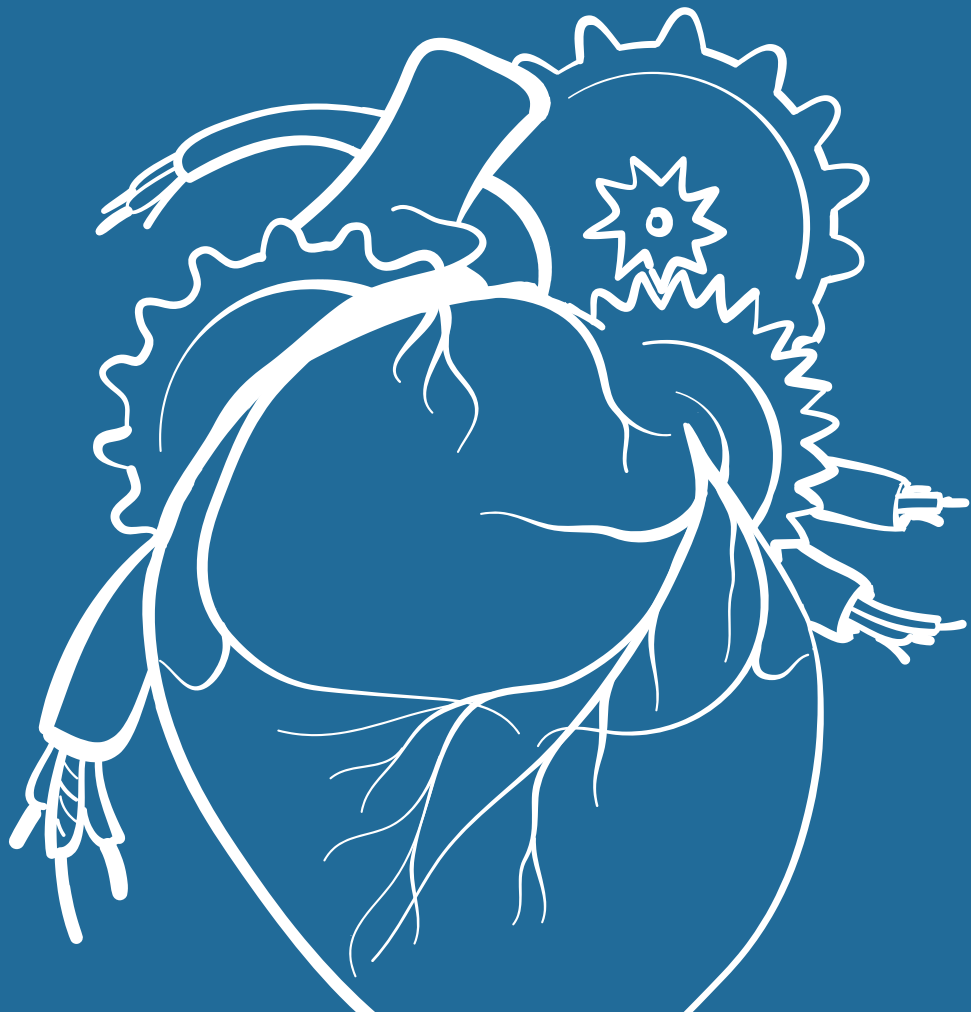
- 31 Grothoff M, Piorkowski C, Eitel C, Gaspar T, Lehmkuhl L, Lucke C, Hoffmann J, Hildebrand L, Wedan S, Lloyd T, Sunnarborg D, Schnackenburg B, Hindricks G, Sommer P, Gutberlet M. MR Imaging-guided Electrophysiological Ablation Studies in Humans with Passive Catheter Tracking: Initial Results. *Radiology* 2014;271:695-702.
- 32 Rubin DL, Ratner AV, Young SW. Magnetic susceptibility effects and their application in the development of new ferromagnetic catheters for magnetic resonance imaging. *Invest Radiol* 1990;25:1325-32.
- 33 Dumoulin CL, Souza SP, Darrow RD. Real-time position monitoring of invasive devices using magnetic resonance. *Magn Reson Med* 1993;29:411-5.
- 34 Konings MK, Bartels LW, Smits HF, Bakker CJ. Heating around intravascular guidewires by resonating RF waves. *J Magn Reson Imaging* 2000;12:79-85.
- 35 Weiss S, Wirtz D, David B, Krueger S, Lips O, Caulfield D, Pedersen SF, Bostock J, Razavi R, Schaeffter T. In vivo evaluation and proof of radiofrequency safety of a novel diagnostic MR-electrophysiology catheter. *Magn Reson Med* 2011;65:770-7.
- 36 Tse Z, Dumoulin C, Watkins R, Byrd I, Schweitzer J, Kwong R, Michaud G, Schmidt E. MRI guided electrophysiological intervention with a voltage-based electro-anatomic mapping system. *Journal of Cardiovascular Magnetic Resonance* 2012;14:206.
- 37 Tzifa A, Krombach GA, Kramer N, Kruger S, Schutte A, von Walter M, Schaeffter T, Qureshi S, Krasemann T, Rosenthal E, Schwartz CA, Varma G, Buhl A, Kohlmeier A, Bucker A, Gunther RW, Razavi R. Magnetic resonance-guided cardiac interventions using magnetic resonance-compatible devices: a preclinical study and first-in-man congenital interventions. *Circ Cardiovasc Interv* 2010;3:585-92.
- 38 Sonmez M, Saikus CE, Bell JA, Franson DN, Halabi M, Faranesh AZ, Ozturk C, Lederman RJ, Kocaturk O. MRI active guidewire with an embedded temperature probe and providing a distinct tip signal to enhance clinical safety. *J Cardiovasc Magn Reson* 2012;14:38.
- 39 Halabi M, Faranesh A, Schenke W, Wright V, Hansen M, Saikus C, Kocaturk O, Lederman R, Ratnayaka K. Real-time cardiovascular magnetic resonance subxiphoid pericardial access and pericardiocentesis using off-the-shelf devices in swine. *J Cardiovasc Magn Reson* 2013;15:61.
- 40 Saikus CE, Ratnayaka K, Barbash IM, Colyer JH, Kocaturk O, Faranesh AZ, Lederman RJ. MRI-guided vascular access with an active visualization needle. *J Magn Reson Imaging* 2011;34:1159-66.
- 41 Piccini D, Monney P, Siero C, Coppo S, Bonanno G, van Heeswijk RB, Chaptinel J, Vincenti G, de Blois J, Koestner SC, Rutz T, Littmann A, Zenge MO, Schwitter J, Stuber M. Respiratory self-navigated postcontrast whole-heart coronary MR angiography: initial experience in patients. *Radiology* 2014;270:378-86.
- 42 van Heeswijk RB, Feliciano H, Bongard C, Bonanno G, Coppo S, Lauriers N, Locca D, Schwitter J, Stuber M. Free-breathing 3 T magnetic resonance T2-mapping of the heart. *JACC Cardiovasc Imaging* 2012;5:1231-9.

- 43 van Heeswijk R, Piccini D, Feliciano H, Hullin R, Schwitter J, Stuber M. Self-navigated isotropic three-dimensional cardiac T mapping. *Magn Reson Med* 2014.
- 44 Hansen MS, Sorensen TS. Gadgetron: an open source framework for medical image reconstruction. *Magn Reson Med* 2013;69:1768-76.
- 45 Radau P, Pintilie S, Flor R, Biswas L, Oduneye S, Ramanan V, Anderson K, Wright G. VURTIGO: Visualization Platform for Real-Time, MRI-Guided Cardiac Electroanatomic Mapping. In: Camara O, Konukoglu E, Pop M, Rhode K, Sermesant M, Young A, eds. *Statistical Atlases and Computational Models of the Heart. Imaging and Modelling Challenges*. 7085 Ed. Springer Berlin Heidelberg; 2012:244-253.
- 46 Santos JM, Wright GA, Pauly JM. Flexible real-time magnetic resonance imaging framework. *Conf Proc IEEE Eng Med Biol Soc* 2004;2:1048-51.
- 47 Tse Z, Dumoulin C, Clifford G, Schweitzer J, Qin I, Oster J, Jerosch-Herold M, Kwong R, Michaud G, Stevenson W, Schmidt E. A 1.5T MRI-conditional 12-lead electrocardiogram for MRI and intra-MR intervention. *Magn Reson Med* 2013.
- 48 Cho JS, Shim JK, Na S, Park I, Kwak YL. Improved sedation with dexmedetomidine-remifentanil compared with midazolam-remifentanil during catheter ablation of atrial fibrillation: a randomized, controlled trial. *Europace* 2014;16:1000-6.
- 49 Razavi R, Hill DLG, Keevil SF, Miquel ME, Muthurangu V, Hegde S, Rhode K, Barnett M, van Vaals J, Hawkes DJ, Baker E. Cardiac catheterisation guided by MRI in children and adults with congenital heart disease. *Lancet* 2003;362:1877-82.
- 50 Ratnayaka K, Faranesh AZ, Hansen MS, Stine AM, Halabi M, Barbash IM, Schenke WH, Wright VJ, Grant LP, Kellman P, Kocaturk O, Lederman RJ. Real-time MRI-guided right heart catheterization in adults using passive catheters. *Eur Heart J* 2013;34:380-9.
- 51 van der Graaf AWM, Bhagirath P, Ramanna H, van Driel VJHM, de Hooge J, de Groot NMS, Gotte MJW. Noninvasive imaging of cardiac excitation: current status and future perspective. *Ann Noninvasive Electrocardiol* 2014;19:105-13.
- 52 Shah AJ, Hocini M, Xhaet O, Pascale P, Roten L, Wilton SB, Linton N, Scherr D, Miyazaki S, Jadidi AS, Liu X, Forclaz A, Nault I, Rivard L, Pedersen MEF, Derval N, Sacher F, Knecht S, Jais P, Dubois R, Eliautou S, Bokan R, Strom M, Ramanathan C, Cakulev I, Sahadevan J, Lindsay B, Waldo AL, Haissaguerre M. Validation of novel 3-dimensional electrocardiographic mapping of atrial tachycardias by invasive mapping and ablation: a multicenter study. *J Am Coll Cardiol* 2013;62:889-97.



**SECTION 2**  
ELECTRICAL  
ASSESSMENT OF  
ARRHYTHMOGENIC  
SUBSTRATE

07



# INTEGRATED WHOLE-HEART COMPUTATIONAL WORKFLOW FOR INVERSE POTENTIAL MAPPING AND PERSONALIZED SIMULATIONS

---

P. Bhagirath MD; A.W.M. van der Graaf MD; J. de Hooge MSc;  
N.M.S. de Groot MD PhD; M.J.W. Götte MD PhD  
*J Transl Med. 2016 May 25;14(1):147*

## ABSTRACT

**Background:** Integration of whole-heart activation simulations and inverse potential mapping (IPM) could benefit the guidance and planning of electrophysiological procedures. Routine clinical application requires a fast and adaptable workflow. These requirements limit clinical translation of existing simulation models.

This study proposes a comprehensive FEM based whole-heart computational workflow suitable for IPM and simulations.

**Methods:** Three volunteers underwent body surface potential (BSP) acquisition followed by a cardiac MRI (CMR) scan. The cardiac volumes were segmented from the CMR images using custom written software. The feasibility to integrate tissue-characteristics was assessed by generating meshes with virtual edema and scar. Isochronal activation maps were constructed by identifying the fastest route through the cardiac volume using the Möller-Trumbore and Floyd-Warshall algorithms. IPM's were reconstructed from the BSP's.

**Results:** Whole-heart computational meshes were generated within seconds. The first point of atrial activation on IPM was located near the crista terminalis of the superior vena cave into the right atrium. The IPM demonstrated the ventricular epicardial breakthrough at the attachment of the moderator band with the right ventricular free wall. Simulations of sinus rhythm were successfully performed. The conduction through the virtual edema and scar meshes demonstrated delayed activation or a complete conduction block respectively.

**Conclusion:** The proposed FEM based whole-heart computational workflow offers an integrated platform for cardiac electrical assessment using simulations and IPM. This workflow can incorporate patient-specific electrical parameters, perform whole-heart cardiac activation simulations and accurately reconstruct cardiac activation sequences from BSP's.

## BACKGROUND

Inverse potential mapping (IPM) and simulations of cardiac activation are promising computational techniques for non-invasive assessment of rhythm disorders <sup>[1,2]</sup>. Recent studies have examined the role of simulation models for personalizing catheter ablation strategies <sup>[3,4]</sup>. Furthermore, catheter ablation guidance by IPM shows a higher accuracy when compared to conventional mapping procedures <sup>[5,6]</sup>.

In general, IPM requires a (computational) mesh representing the thoracic and cardiac volumes to reconstruct cardiac activation sequences from body surface potentials (BSP). Similarly, realistic simulations demand for a patient-specific mesh, incorporating functional information about tissue characteristics such as electrical conductivity, mechanical deformation and fiber orientation <sup>[3,4,7]</sup>. In contrast to meshes used solely for visualization (shells), the computational meshes for these purposes require topologically correct segmentations.

Although the currently available models are useful, they are very time consuming <sup>[4]</sup>, or too comprehensive (multiple parameters) <sup>[7]</sup>, and therefore not ready for use on a routine basis in the clinical arena.

In addition, none of the currently available methods provide an integrated whole-heart (topologically correct) mesh, incorporating both the atria and ventricles. This limits a comprehensive and integrated study of whole-heart electrical interaction.

This article proposes a comprehensive finite element model based whole-heart computational workflow suitable for IPM and efficient personalized simulations. The clinical feasibility of reconstructing IPM was explored using BSP's of healthy volunteers.

Subsequently, the simulation features were explored by generating activation maps (isochrones) in different models of human hearts, both normal and with structural heart disease.

## METHODS

The computational workflow for whole-heart electrical assessment consists of four steps (**figure 1**). These steps involve (1) acquisition of BSP, (2) acquisition of subject specific geometry using cardiac magnetic resonance imaging (MRI), (3) topologically correct segmentation and generation of the computational mesh and (4) utilizing the mesh for reconstructing cardiac surface potentials or conducting simulations.

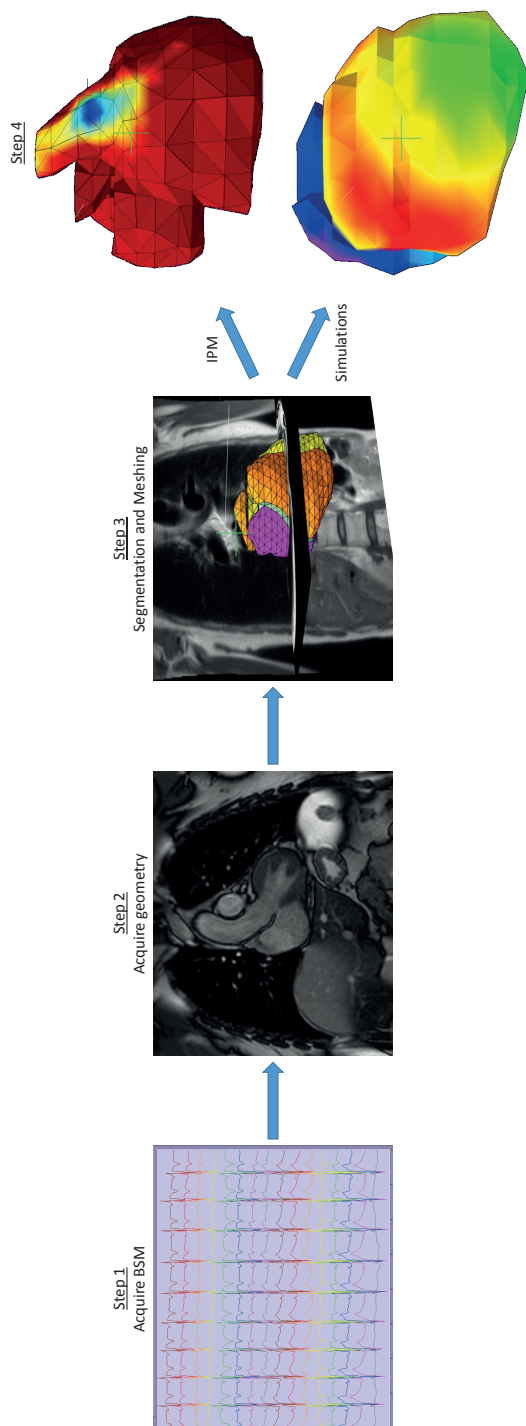


**Figure 1.** Workflow of the integrated whole-heart computational models. Step 1 represents the acquisition of the multichannel body surface potentials; Step 2 acquisition of geometry in 3D (1D shown); Step 3 depicts the topologically correct whole-heart segmentation in the transversal and coronal plane of a volunteer; Step 4 the workflow can generate both inverse potential maps (top) and simulations (bottom) using the information supplied in the previous steps.

## **Study population**

Three healthy volunteers participated in this investigation. The study complied with the declaration of Helsinki and received approval from the local ethical committee (METC Zuidwest Holland study number NL38156.098.11) and the institutional scientific board. Written informed consent was obtained from the volunteers.

## **Body surface potential acquisition**

An MRI scout scan was performed to approximate the position of the heart with respect to the thorax. Subsequently, 62 (+3 limb) electrodes were applied to the subject's torso, centralized over the heart. Body surface potentials (BSP) were acquired using a 65 channel ActiveTwo system (BioSemi B.V., Amsterdam, The Netherlands). Once the acquisition was completed, the electrode locations were marked with MRI markers enabling accurate identification of the electrode positions.

## **Image acquisition**

MRI studies were obtained on a 1.5 Tesla Aera scanner (Siemens Healthcare, Erlangen, Germany). Blackblood imaging was performed using a Half-Fourier Acquisition Single Shot Turbo Spin Echo (HASTE) pulse-sequence to acquire three perpendicular stacks (axial, coronal and sagittal). The scan provides coverage from the neck till lower abdomen.

Images were acquired during free breathing using navigator gating (diaphragm) with 1 mm window. ECG gating was used to acquire views during the diastolic phase of the cardiac cycle. Typical imaging parameters were: a spatial resolution of  $1.2 \times 1.2 \times 6$  mm, TR/TE 744/42 ms and flip angle=  $160^\circ$ .

## **Whole-heart computational model**

### ***Anatomical and electrical components***

A topologically correct description of the whole-heart anatomy was constructed using the different cardiac structures such as atrial and ventricular endocard and epicard, the inter-ventricular septum (IVS) and inter-atrial septum (IAS), and tricuspid and mitral valvular plane (video 1). These different structures were used to generate the cardiac volumes required to represent a whole-heart.

In order to incorporate the electrical pathways and to account for the differences in conductivity, the conduction system of the heart was also modeled. The origin of activation for sinus rhythm was defined at the lateral border of the superior vena cava and right atrium junction, approximating the location of the sinus node. The right and left bundle branches were also defined.

### ***Image segmentation and mesh generation***

The three perpendicular stacks of MRI images were loaded in a custom developed software tool. Subsequently, the pre-defined anatomical and electrical components were segmented. The extra-cardiac thoracic volumes (lungs and thorax) were assigned conductivity values ( $\Sigma$ ) described in the literature; lungs (0.04 S/m) and thorax (0.2 S/m) <sup>[8]</sup>.

To investigate the feasibility of incorporating tissue properties, two segmentations were created containing pre-defined regions of edema (speed 0.2 m/s and  $\Sigma$  0.0325 S/m) and scar tissue (speed 0 m/s and  $\Sigma$  0 S/m) respectively.

The software tool was used to generate a script containing the geometrical description of the topologically correct segmentation result. The script generated by the segmentation tool was used as input to the GMSH mesh generator to construct the computational mesh <sup>[9]</sup>.

### **Inverse potential mapping and simulation of cardiac activation**

In the healthy volunteers, the IPM's were reconstructed by multiplication of the BSP's with

$$(T^T T + \lambda^2 I)^{-1} T^T$$

where T is the transfer matrix and  $\lambda = 0.01$ . This provided the cardiac surface potentials from which the IPM was derived.

Simulations were performed using a fixed conduction velocity model. In concordance with the literature, an effective conduction velocity of 0.6 m/s was defined for both atrial and ventricular myocardium <sup>[10]</sup>. Based on the same literature the bundle branches were assigned a speed (2 m/s) and delay (0 m/s).

The simulations were performed (1) computing direct connections between all mesh nodes using the Möller-Trumbore algorithm <sup>[11]</sup> followed by (2) solving the shortest path problem amongst the computed paths using the Floyd-Warshall algorithm <sup>[12]</sup>. The mesh

nodes were assigned a potential versus time activation curve. A standard potential curve was chosen for this purpose. For each individual node, this curve was offset by the local activation time which was computed by the first come first serve principle. Based upon the results of the simulations an isochronal activation map was generated.

## RESULTS

All volunteers underwent the MRI examination in  $12 \pm 2$  minutes; there were no complications.

**Table 1.** Clinical characteristics of study patients.

	Volunteers	Patients
n	3	8
Age (years)	$28 \pm 3$	$46 \pm 13$
BMI	$22.1 \pm 1.4$	$25.2 \pm 6.7$
Female (%)	1 (33%)	7 (88%)
LVEF (%)	$55 \pm 2$	$50 \pm 3$

### Whole-heart computational model

For each volunteer, five different volumes were defined at the atrial level consisting of the left and right atrium, IAS and the mitral and tricuspid valvular planes. The ventricular volumes were defined as the left and right ventricle and IVS (video 1). Limited interaction (<5 minutes) was required to create the meshes with (virtual) structural heart disease.

Mesh generation was typically completed in seconds and required no further post-processing.

### IPM in sinus rhythm

During sinus rhythm, the first point of activation on the potential map of all healthy volunteers was located near the crista terminalis of the superior vena cava into the right atrium (**figure 2a**).

The first point of ventricular epicardial breakthrough was located at the right ventricular free wall. This corresponds to the location where the moderator band was attached to the ventricular myocardium (**figure 2b**). During this time, a high potential distribution is observed at the right atrial wall, indicating the atrial repolarization (**figure 2a**).

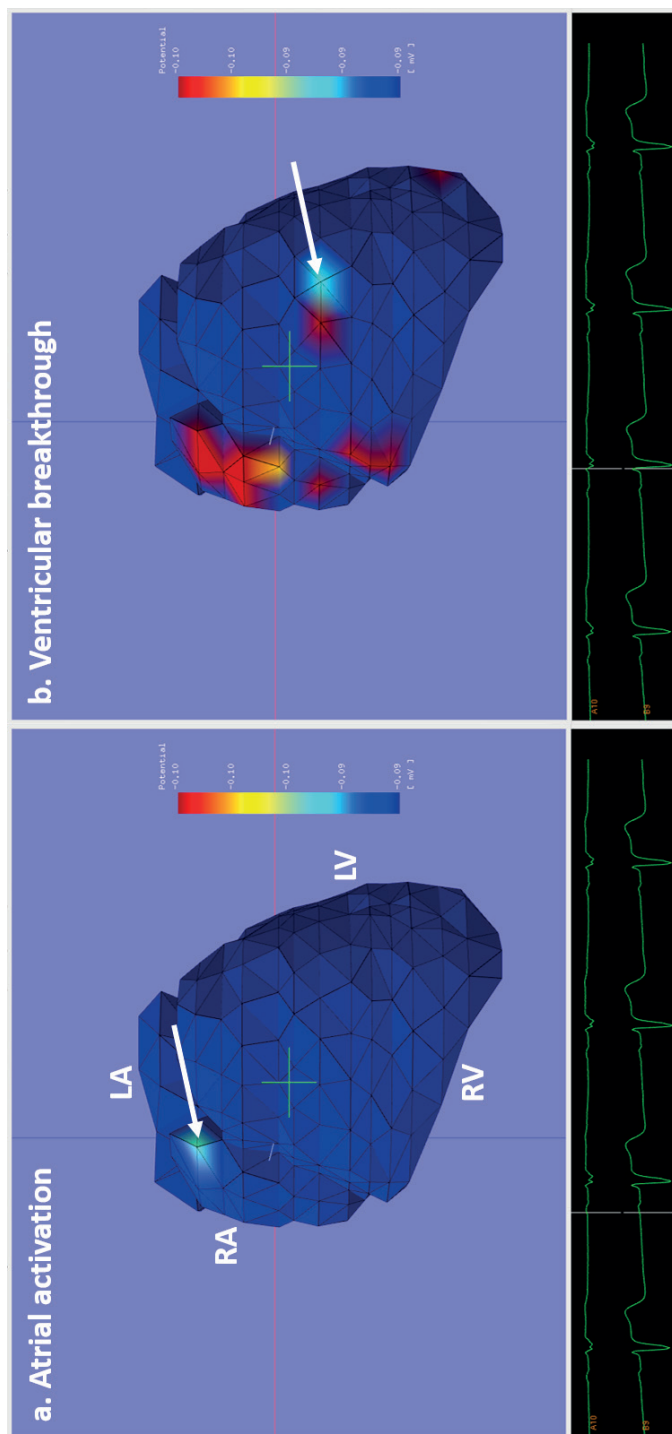


**Figure 2.** IPM in a healthy volunteer during sinus rhythm. The left panel depicts the IPM at the start of the atrial depolarization (P wave) and the right panel depicts the IPM at the start of the ventricular depolarization (QRS). The first point of atrial activation is observed near the entrance of the Superior Vena Cave (white arrow) into the Right Atrium. The first point of ventricular epicardial breakthrough is observed at the RV free wall (white arrow) at the site of the moderator band

## Simulations

The cardiac activation cycle (sinus rhythm) was successfully simulated on all healthy computational meshes of the healthy volunteers. The generated virtual isochrones maps depicted cardiac activation patterns in accordance with the literature (**figure 3** and video 2) <sup>[13]</sup>.

The simulations for computational meshes with structural abnormalities (edema and scar), were also completed successfully. The mesh with a pre-defined virtual edema region demonstrated a delayed activation pattern (**figure 4**), whereas, a complete conduction block was observed for the computational mesh containing virtual transmural scar (**figure 4**).

## DISCUSSION

To our knowledge, this is the first study to integrate and evaluate IPM and cardiac activation simulations within a clinically applicable whole-heart workflow. The proposed computational workflow provided accurate IPM reconstructions and enabled patient-specific simulations to be performed.

The use of MRI enables visualization and incorporation of tissue-characteristics in computational meshes. In addition, an integrated IPM and simulation based approach facilitates a comprehensive assessment of arrhythmias and underlying substrate. These two factors significantly contribute towards the clinical applicability of this workflow and offer a unique environment for the development and evaluation of patient tailored therapeutic strategies.

## IPM

The IPM localized the origin of atrial activity to the anatomically known location of the sinus node <sup>[14]</sup>, suggesting the correctness of the model. These results imply that sinus node function and also dysfunction may be non-invasively characterized and assessed using IPM.

The ability to reconstruct atrial depolarization and repolarization can also contribute to novel clinical insights in the electrical substrate of complex supra-ventricular tachycardia's such as left atrial flutter and atrial fibrillation.

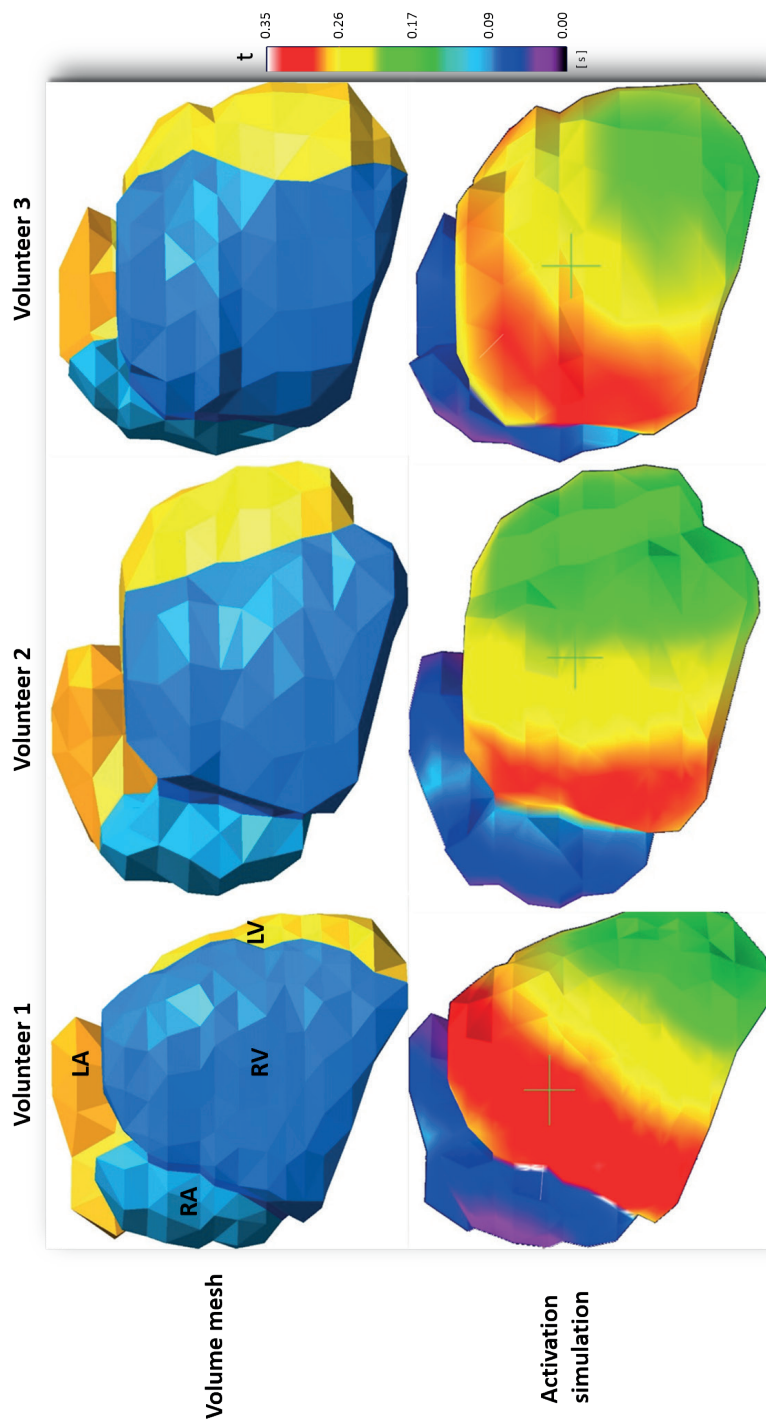


**Figure 3.** Simulation of normal cardiac activation on whole-heart computational meshes. Top row depicts computational volume meshes generated from the three different segmentations. Bottom row depicts isochrone maps generated after performing a cardiac activation simulation on the computational mesh.

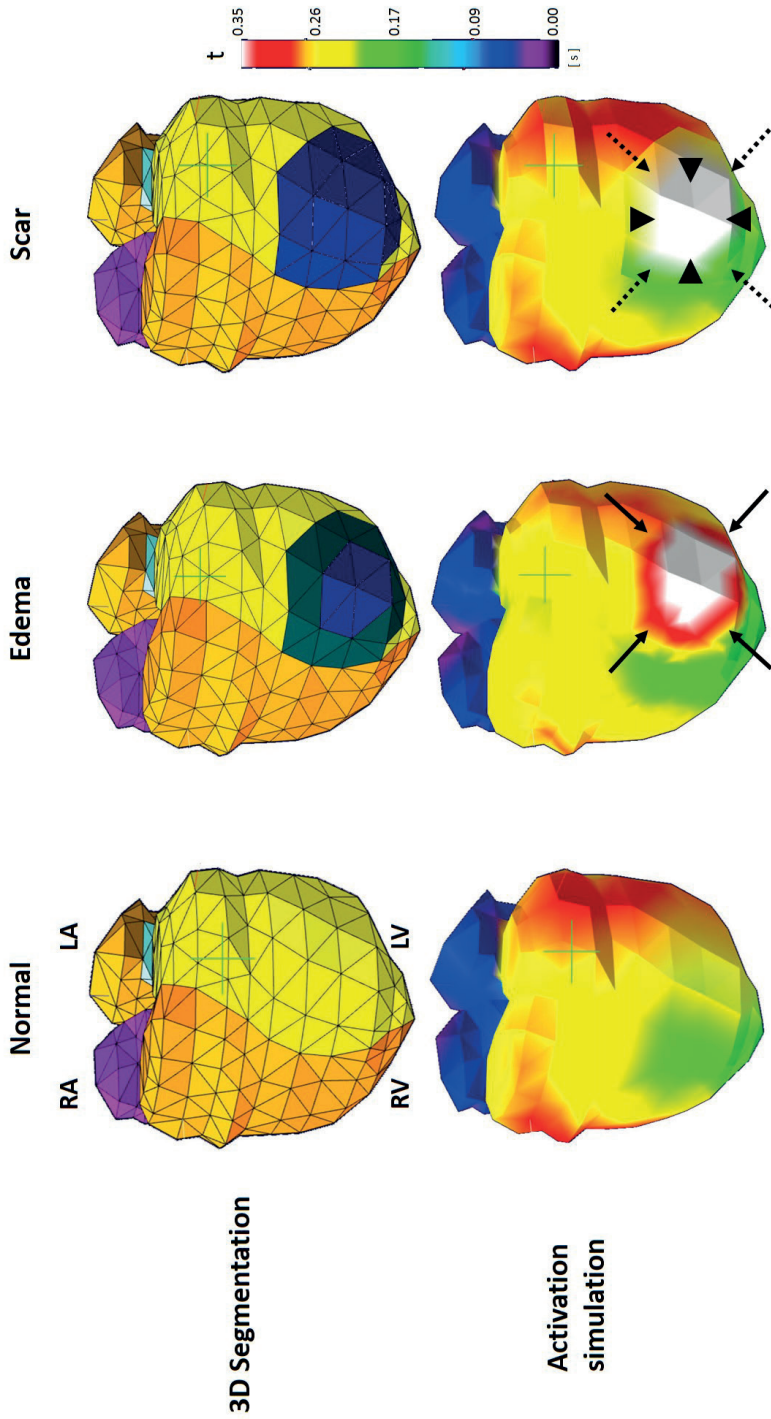


**Figure 4.** Feasibility of cardiac activation simulation on customized meshes with pre-defined structural abnormalities. Top row depicts the segmentations created using the custom made tool. The middle and right column segmentations have a pre-defined structural abnormality. The impact of these abnormalities is visible on the corresponding simulations. A delayed activation can be observed in the isochrone map for regions with edema (solid black arrows). The computational mesh containing a transmural scar (black arrowheads and dotted black arrows), demonstrates a total conduction block.

## **Simulations**

The simulations of sinus rhythm performed on the computational meshes generated reliable results when compared to measurements reported in the literature <sup>[13]</sup>. Simulations performed on the personalized meshes incorporating virtual edema and scar resulted in a different activation pattern with delayed conduction and conduction block respectively.

These observations illustrate the wide range of simulations which can be obtained utilizing this simulation model. This can be clinically relevant for patients presenting with arrhythmias with a history of a disease associated with fibrosis such as myocardial infarction and myocarditis.

## **Whole-heart computational model**

Although only a few pathologies involve the atria and ventricles simultaneously, a combined assessment remains relevant for a comprehensive study of atrio-ventricular electro-mechanical coupling and electrical interaction.

The atrial contraction presents such an example. It has been reported that pressure modulation due to atrial contractions can remotely alter the electrical behavior and activation pattern of the ventricular myocytes <sup>[15,16]</sup>. A whole-heart model is required to incorporate such complex relations and to provide physiologically accurate simulations.

## **Limitations**

The simulations performed in this study used a standardized set of epicardial potentials recorded in a structurally normal human heart. Furthermore, the currently used simulation algorithm applied fixed conduction velocities for the cardiac volumes.

However, the aim of the current study was to develop a clinically applicable and reliable method for isochrones generation. The evaluation of this algorithm could be successfully performed using one set (atrial and ventricular) of epicardial potentials. The generated simulation results were accurate for all subjects when compared to previous descriptions in the literature. Therefore, the absence of patient specific epicardial potentials and usage of a fixed conduction model was not considered as a limitation.

The customized meshes were constructed to test the feasibility of incorporating tissue properties. The conductivity and speed values for edema and scar tissue were based on estimates. Although, this can be considered as a substantial limitation, the simulations with patient-specific geometries (incorporating scar and edema) demonstrated realistic results, and underline the feasibility of the simulation algorithm.

A next step would be combining simulations with reconstructed IPM in order to non-invasively characterize tissue.

### **Future directions**

Future research will focus on evaluating the IPM algorithm for patients undergoing catheter ablation for ectopic ventricular beats. The simulation algorithm will be further evaluated and optimized in patients with structural heart disease and arrhythmias.

### **CONCLUSION**

The proposed FEM based whole-heart computational workflow offers an integrated platform for cardiac electrical assessment using IPM and simulations. The IPM algorithm can accurately reconstruct reliable cardiac activation sequences from BSP's. The simulation model was able to incorporate patient-specific electrical parameters and rapidly perform whole-heart cardiac activation simulations. The use of MRI substantially contributes towards the clinical applicability.

This workflow offers the prospect to improve patient selection and personalize therapeutic strategies for interventional electrophysiological procedures. Future studies should investigate the role of this innovative approach for analysis of complex atrial and ventricular arrhythmias.



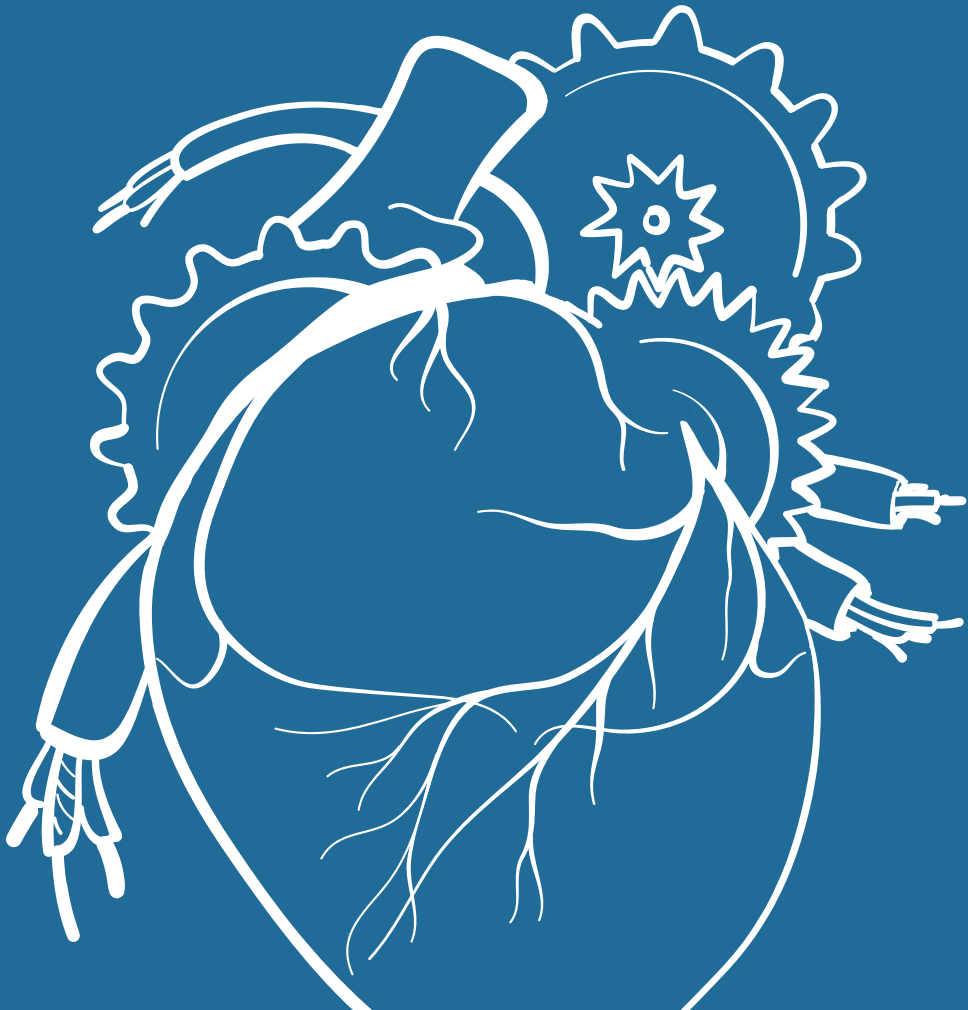
## REFERENCES

- 1 Ramanathan C, Ghanem RN, Jia P, Ryu K, Rudy Y. Noninvasive electrocardiographic imaging for cardiac electrophysiology and arrhythmia. *Nat Med* 2004;10:422-428.
- 2 Keldermann RH, ten Tusscher KHWJ, Nash MP, Bradley CP, Hren R, Taggart P *et al.*. A computational study of mother rotor VF in the human ventricles. *Am J Physiol Heart Circ Physiol* 2009;296:H370-H379.
- 3 Krueger MW, Seemann G, Rhode K, Keller DUJ, Schilling C, Arujuna A *et al.*. Personalization of atrial anatomy and electrophysiology as a basis for clinical modeling of radio-frequency ablation of atrial fibrillation. *IEEE Trans Med Imaging* 2013;32:73-84.
- 4 Ashikaga H, Arevalo H, Vadakkumpadan F, Blake RC, Bayer JD, Nazarian S *et al.*. Feasibility of image-based simulation to estimate ablation target in human ventricular arrhythmia. *Heart Rhythm* 2013;10:1109-1116.
- 5 Erkapic D, Greiss H, Pajitnev D, Zaltsberg S, Deubner N, Berkowitsch A *et al.*. Clinical impact of a novel three-dimensional electrocardiographic imaging for non-invasive mapping of ventricular arrhythmias-a prospective randomized trial. *Europace* 2014.
- 6 Jamil-Copley S, Bokan R, Kojodjojo P, Qureshi N, Koa-Wing M, Hayat S *et al.*. Noninvasive electrocardiographic mapping to guide ablation of outflow tract ventricular arrhythmias. *Heart Rhythm* 2014;11:587-594.
- 7 Sermesant M, Chabiniok R, Chinchapatnam P, Mansi T, Billet F, Moireau P *et al.*. Patient-specific electromechanical models of the heart for the prediction of pacing acute effects in CRT: a preliminary clinical validation. *Med Image Anal* 2012;16:201-215.
- 8 Oostendorp T, Nenonen J, Korhonen P. Noninvasive determination of the activation sequence of the heart: application to patients with previous myocardial infarctions. *J Electrocardiol* 2002;35 Suppl:75-80.
- 9 C.Geuzaine, J.F.Remacle. Gmsh: a three-dimensional finite element mesh generator with built-in pre- and post-processing facilities. *International Journal for Numerical Methods in Engineering* 79(11), 1309-1331. 2009.
- 10 Kleber AG, M.J.Janse, V.G.Fast: Fast, Normal and abnormal conduction in the heart. In *Handbook of Physiology. Section 2 The Cardiovascular System, vol. 1 The Heart*. Oxford: Oxford University Press; 2001:455-530.
- 11 Tomas Möller, Ben Trumbore. Fast, Minimum Storage Ray/Triangle Intersection. *Journal of Graphics Tools* 1997.
- 12 R.W.Floyd. Algorithm 97: shortest path. *Communications of the ACM* 1962.
- 13 Durrer D, van Dam RT, Freud GE, Janse MJ, Meijler FL, Arzbaecher RC. Total excitation of the isolated human heart. *Circulation* 1970;41:899-912.
- 14 Sanchez-Quintana D, Cabrera JA, Farre J, Climent V, Anderson RH, Ho SY. Sinus node revisited in the era of electroanatomical mapping and catheter ablation. *Heart* 2005;91:189-194.

- 15 ter Keurs HE, Rijnsburger WH, van Heuningen R, Nagelsmit MJ. Tension development and sarcomere length in rat cardiac trabeculae. Evidence of length-dependent activation. *Circ Res* 1980;46:703-714.
- 16 Zwanenburg JJM, Gotte MJW, Kuijjer JPA, Hofman MBM, Knaapen P, Heethaar RM *et al.*. Regional timing of myocardial shortening is related to prestretch from atrial contraction: assessment by high temporal resolution MRI tagging in humans. *Am J Physiol Heart Circ Physiol* 2005;288:H787-H794.



08



# COMPUTING VOLUME POTENTIALS FOR NONINVASIVE IMAGING OF CARDIAC EXCITATION

---

van der Graaf AW, Bhagirath P, van Driel VJ, Ramanna  
H, de Hooge J, de Groot NM, Götte MJ  
*Ann Noninvasive Electrocardiol.* 2015 Mar;20(2):132-9

## ABSTRACT

**Background:** In non-invasive imaging of cardiac excitation, the use of body surface potentials (BSP) rather than body volume potentials (BVP) has been favoured due to enhanced computational efficiency and reduced modelling effort. Nowadays, increased computational power and the availability of open source software enable the calculation of BVP for clinical purposes. In order to illustrate the possible advantages of this approach, the explanatory power of BVP is investigated using a rectangular tank filled with an electrolytic conductor and a patient specific three-dimensional model.

**Methods:** MRI images of the tank and of a patient were obtained in three orthogonal directions using a turbo spin echo MRI sequence. MRI images were segmented in three-dimensional using custom written software. Gmsh software was used for mesh generation. BVP were computed using a transfer matrix and FEniCS software.

**Results:** The solution for 240,000 nodes, corresponding to a resolution of 5 mm throughout the thorax volume, was computed in 3 minutes. The tank experiment revealed that an increased electrode surface renders the position of the 4V equipotential plane insensitive to mesh cell size and reduces simulated deviations. In the patient-specific model, the impact of assigning a different conductivity to lung tissue on the distribution of volume potentials could be visualised.

**Conclusion:** Generation of high quality volume meshes and computation of BVP with a resolution of 5 mm is feasible using generally available software and hardware. Estimation of BVP may lead to an improved understanding of the genesis of BSP and sources of local inaccuracies.

## INTRODUCTION

Non-invasive imaging of cardiac excitation using recorded body surface potentials (BSP) and mathematical inverse procedures is an active field of research that has yielded some clinical applications [1-4]. In an inverse procedure, local epicardial potentials or myocardial activation times are computed from recorded BSP. In contrast, a forward procedure estimates BSP from potentials measured on the surface of the heart [5-6].

The Boundary Element Method (BEM) has been favoured for electrocardiographic forward procedures due to enhanced computational efficiency and reduced modelling effort [7-9]. In contrast to the BEM, which yields potential information on predefined surfaces, the Finite Element Method (FEM) provides body volume potentials (BVP) (**figure 1**) [10].

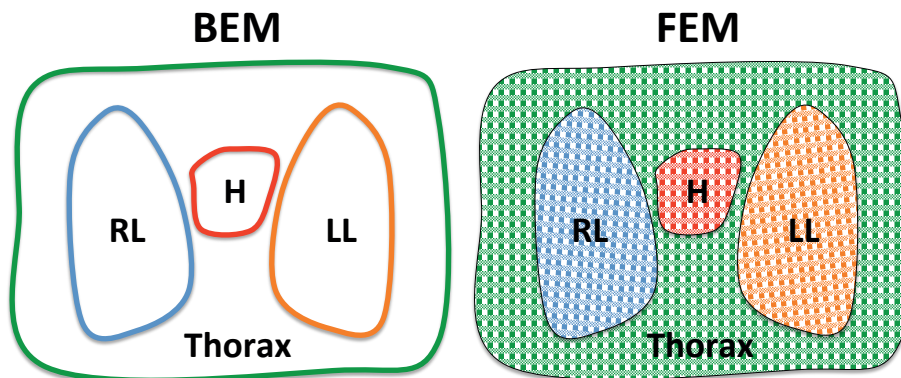


**Figure 1.** The Boundary Element Method (BEM) yields potential information on predefined *surfaces* only. Hence, no information on the areas between the compartments can be derived when using the BEM. The Finite Element Method (FEM) on the contrary, provides body *volume* potentials (BVP). Volume potentials can be computed as well using the BEM, by increasing the number of model compartments. However, the FEM is typically more efficient, especially when the number of model compartments is high or when anisotropic conductivity is modelled. (RL right lung; LL left lung; H heart; L liver)

Utilizing knowledge on the spatial potential field may lead to improved insight in the potential distribution throughout the thorax. Although potentials can be computed everywhere in a volume as well using the BEM by creating multiple surfaces inside the

volume, the FEM is typically more efficient for this purpose. Especially when the number of model compartments is high or when anisotropic conductivity is modelled, the FEM is recommended [11].

Although the application of BVP has been studied previously [12-13], it has never advanced into clinical practice due to its time consuming and elaborative nature. Increased computational power and the introduction of open source software enable the calculation of BVP for clinical purposes. In this study the explanatory power of BVP is illustrated by experiments performed in a simple rectangular tank. In addition, simulations in a 3D patient specific model demonstrate the possible advantage of using BVP.

## METHODS

### Rectangular tank

A rectangular tank of 33 x 25 x 25 cm filled with an electrolytic conductor was used. Electrodes with a surface of 2 x 2 cm were positioned in the middle of opposing sides. To block interference from nearby power sources, a 1000 Hz 8 V peak-to-peak sinusoidal power source was used. Measurements were performed using a dual beam oscilloscope, enabling monitoring the source voltage while measuring the resulting potential in the tank. The accuracy of the measurements approximated 2%, which was considered sufficient for validation purposes.

### MRI images

MRI images of the rectangular tank and the patient were acquired using a Turbo Spin Echo (Black Blood) sequence in three orthogonal directions (slice thickness 8mm). Electrode positions in the tank and on the body surface were marked using liquid-filled vitamin D capsules, appearing hyper intense on MRI. The MRI scan was performed on a Siemens Aera 1.5 Tesla MRI scanner (Siemens Healthcare, Erlangen, Germany).

The study complied with the declaration of Helsinki and received approval from the local ethical committee and the institutional scientific board. Written informed consent was obtained from the patient.

### Meshing

In order to achieve topological propriety, MRI images were segmented in 3D using bounding planes. No spatial smoothing was applied. The Gmsh tool [14], freely available on the Internet for non-commercial use, was used for mesh generation.

## Computing BVP

Given the source potential distribution on the epicardial surface, the resulting volume potential distribution is governed by the equations below.

The current density  $J$  as a function of conductivity  $s$  and field strength  $E$  is given by ohms law:

$$J = s E = s \text{ grad}(P), \text{ where } P \text{ is the potential} \quad [1]$$

Apart from the heart there are no current sources in the thorax so:

$$\text{div}(J) == 0 \quad [2]$$

From [1] and [2] follows Laplace's equation:

$$\text{div}(s \text{ grad}(P)) == 0 \quad [3]$$

Multiplying by a test function  $T$  leads to the following variational form:

$$\int \text{div}(s \text{ grad}(P)) T \, dV == \int 0 * T \, dV == 0 \quad [4]$$

Partial integration yields ( $n$  is the unit surface normal):

$$\int \text{div}(s \text{ grad}(P)) T \, dV == \int s \text{ grad}(P) \cdot \text{grad}(T) \, dV - \int s \text{ grad}(P) \cdot n \, T \, dS \quad [5]$$

From [4] and [5] follows:

$$\int s \text{ grad}(P) \cdot \text{grad}(T) \, dV == \int s \text{ grad}(P) \cdot n \, T \, dS \quad [6]$$

With  $J \cdot n = 0$  and [1] at the skin this becomes:

$$\int s \text{ grad}(P) \cdot \text{grad}(T) \, dV = 0 \quad [7]$$

To yield a non-trivial solution, the source potentials at the heart surface are applied as boundary conditions. There are many general-purpose FEM tools available to solve these equations. FEniCS [15], freely available for research purposes, was selected.

This software package allowed the aforementioned equation to be specified in a very natural form. All work is done by the following lines of code:

$$\text{RHS} = \text{sigma} * \text{inner}(\text{grad}(\text{trialFunction}), \text{grad}(\text{testFunction})) * \text{dx} \quad [1]$$

$$\text{LHS} = \text{Constant}(0) * \text{testFunction} * \text{dx} \quad [2]$$

$$A, b = \text{assemble\_system}(\text{LHS}, \text{RHS}, \text{boundaryCond}, \text{keep\_diagonal} = \text{True}) \quad [3]$$

$$\text{solve}(A, \text{potential.vector}(), b, \text{'gmres'}, \text{'default'}) \quad [4]$$

Note the close correspondence between lines [1] and [2] of the code and equation [6] by substituting them in equation  $LHS = RHS$ .

### Computing platform

All analyses were performed on a 2.4 GHz quadcore laptop running Windows 8 OS. Solving the potential equations was delegated to an Ubuntu 12.10 virtual machine running on this laptop, communicating with the activation modelling software by the use of synchronised message file sharing. Reference times were computed using a single core.

## RESULTS

### Rectangular tank

**Figure 2** shows the 3D mesh of the tank. A potential of 4V peak to peak was observed in the middle of the tank. The computations using a tetrahedral mesh with 1.5 cm edge length, demonstrated a deviation of the 4V plane from the middle by about one grid cell. By refining the mesh to an edge length of 0.5 cm, this deviation was expected to diminish. Paradoxically, the deviation from the middle actually increased by about 2.5 cm, to a total deviation about 10 times larger than the mesh size (**figure 2a**).

**Figure 2b** and c reveal the potential gradients to increase near to the electrode. This is caused by the small contact area between the fluid and the electrodes introducing a high resistivity:  $R = 1 / (\text{area} \times \sigma)$  [Ohm/m]. Because R is large, the potential drop U is large according to Ohms law. Moreover, a relative misrepresentation of the electrode area by 5% leads to a relative error in this potential drop in the same order of magnitude.

**Figure 2d** illustrates that minor errors in the potential drop near the electrodes yield large deviations in the 4V equipotential plane. In the middle of the tank the x coordinate varies rapidly with small potential changes. By using volume information, the counterintuitive effect shown in **figure 2a** can be understood. For large electrodes, misrepresentations of their area by the mesh are relatively small. This should render the position of the 4V equipotential plane insensitive to the mesh cell size (**figure 2e**).

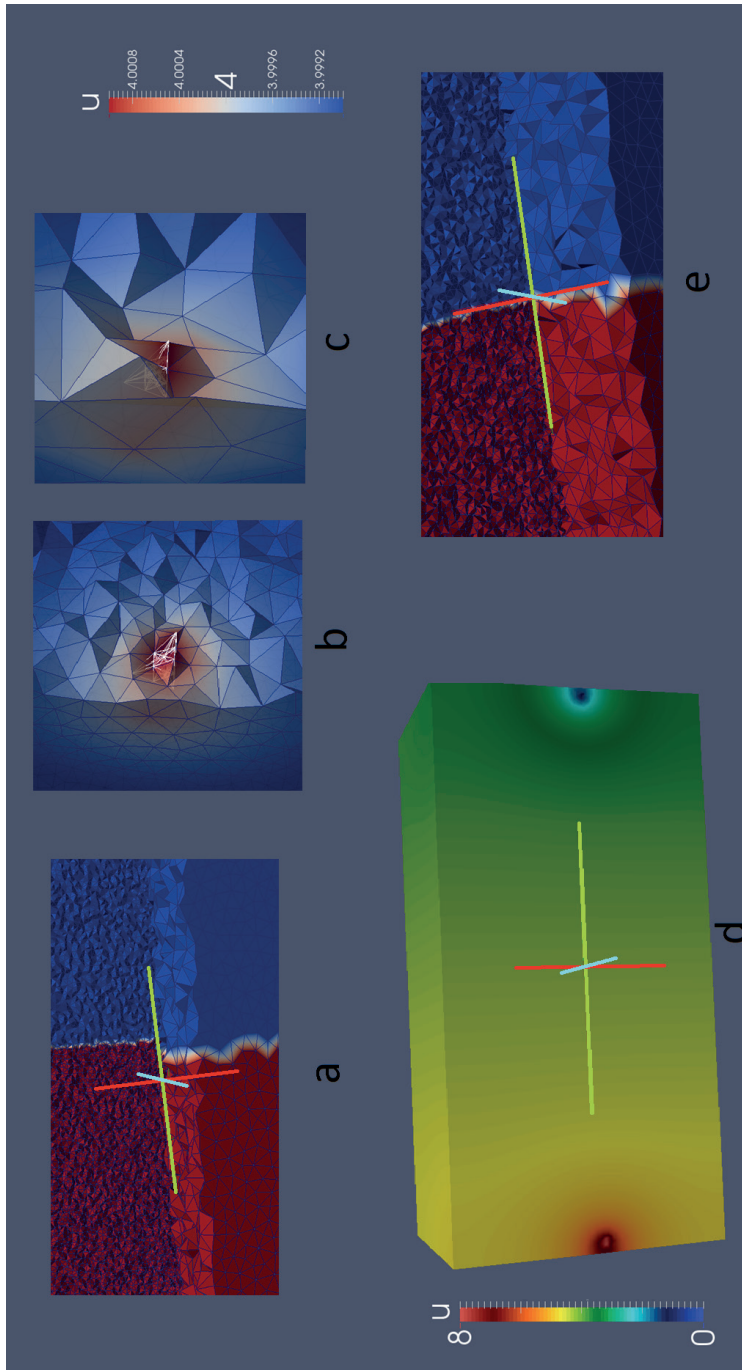


**Figure 2.** (a) Using a tetrahedral mesh with an edge length of 1.5 cm computed position of the 4V equipotential plane (white) deviates from the measured position that was in the middle of the tank. Refining the mesh to an edge length of 0.5 cm increases the deviation. A large potential drop was observed in the vicinity of positive electrode, which is indicated by the white wireframe, both for the fine (b) and the crude (c) grid. Artifacts depend on the exact location of the grid cells with respect to the electrodes, which may be coincidentally more asymmetric with the fine grid. (d). In the middle of the tank, the x coordinate (green axis) varies rapidly as a function of the potential. (e). Large electrodes render the position of the 4V equipotential plane insensitive to the mesh cell size at the same time decreasing the deviation from the middle.

### Patient torso

**Figure 3** shows a multi compartment 3D computer model of a human thorax. The positions of the electrodes on the body surface were derived from the anatomic markers on MRI. **Figure 4** demonstrates the resulting 3D mesh. As can be observed the mesh is highly regular and is locally refined in the vicinity of details.

### Shortest Paths of Activation

The computation of all possible shortest paths of the activation wavefront through the cardiac wall resulted in a set of epicardial isochrones yielding a time dependent epicardial potential as shown in **figure 5**.

### Computing BVP

Potential equations for 13,000 mesh nodes were solved in 3 seconds utilizing a 2.4 GHz single core. Solving these equations for a mesh consisting of 240,000 nodes, corresponding to a resolution of 5 mm throughout the thorax volume, lasted 3 minutes. Two sequences of computed BVP are shown in **figure 6**, one using a mesh edge size of 0.5cm (a-j) and one using a mesh edge size of 1.5cm (k-t). The potential field permeates the lungs without visual deformation, even if their sigma is only half that of their environment.

### Impact of lung tissue on BVP

The impact of variable organ conductivity on BVP was investigated using forward simulations in the human torso model. **Figure 7** illustrates the impact on the electric field when a smaller sigma (conductivity) is assigned to lung tissue (**A**). The BVP field is compared to simulations in a homogeneous torso model (**B**). A smaller sigma of the lung tissue leads to an increased breakthrough of the potential field.

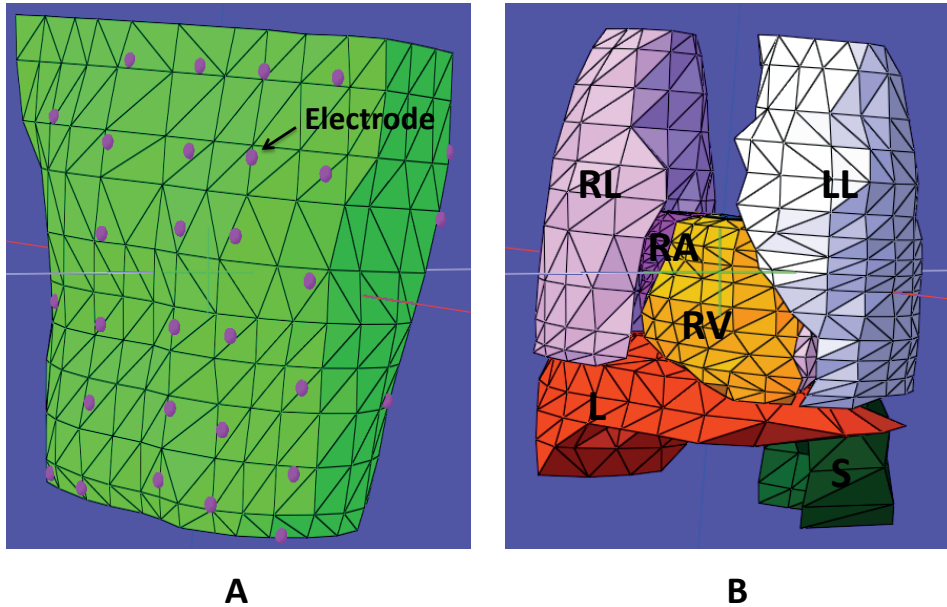


**Figure 3.** A 3D computer model of the human thorax with the positions of the body surface electrodes **(A)**. The electrode positions were derived from the positions of the liquid-filled vitamin D capsules, appearing hyper intense on MRI. The thorax model contains multiple compartments **(B)**. (RA right atrium; RV right ventricle; S spleen)

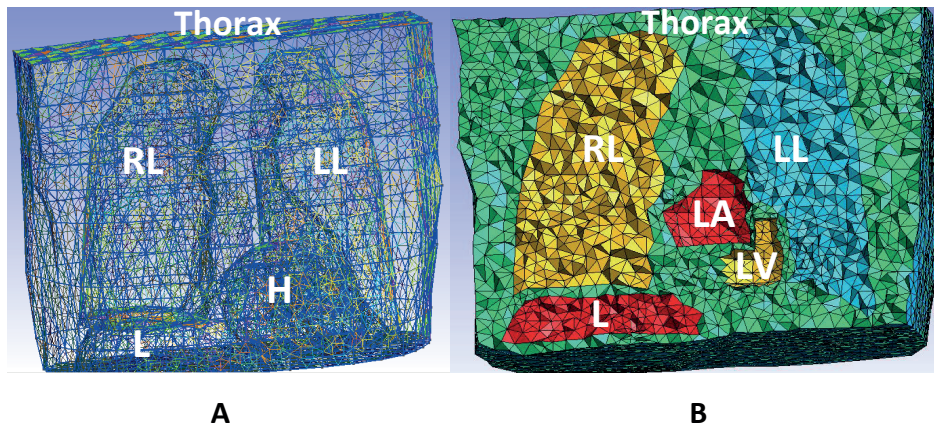


**Figure 4.** Locally refined multi compartment thorax 3D mesh **(A)** and volume mesh **(B)**. The mesh is error free and was generated in 25 seconds using freely available software on a 2.4 GHz single core on a laptop. No spatial smoothing was applied. (LA left atrium; LV left ventricle)

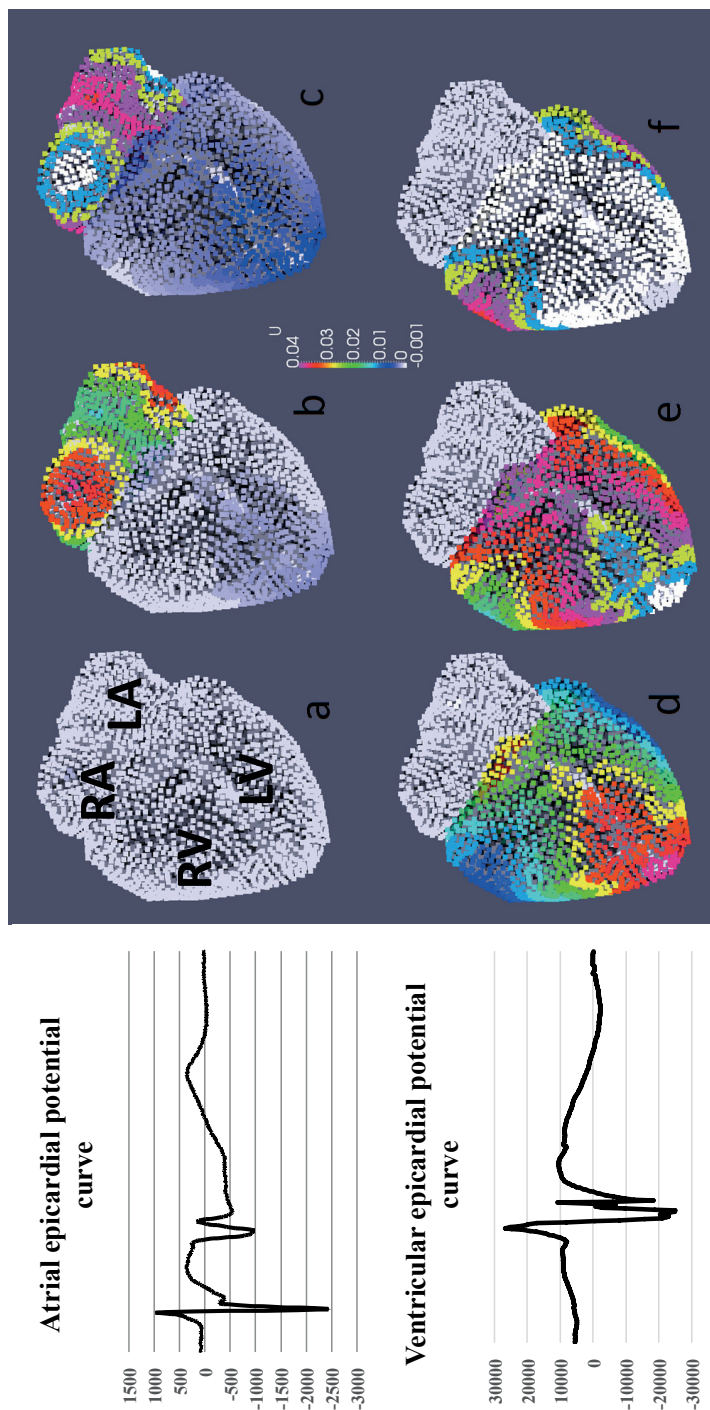


**Figure 5a-f.** Snapshots of the time dependent epicardial potential, taken from a sequence of 50 time steps. On the left, an example of atrial (top) and ventricular (bottom) epicardial potentials is displayed.

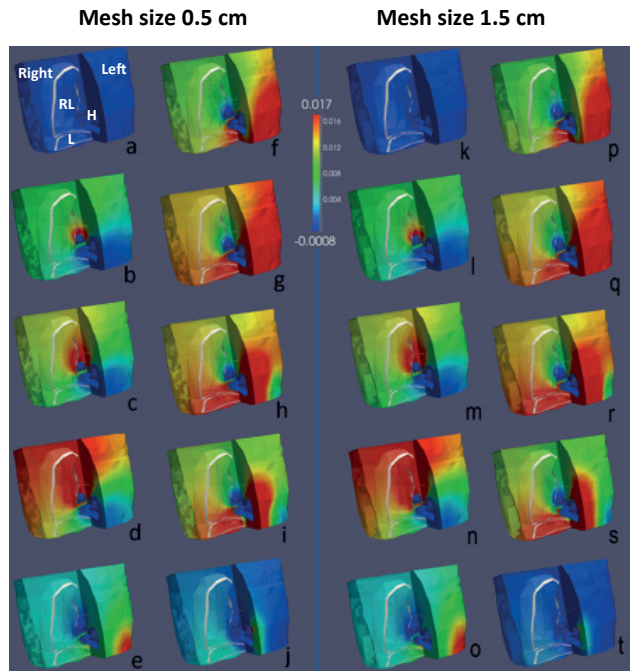


**Figure 6.** Anterior view of the thorax. Shown are the computed BVP during one heartbeat. **(a-j)** Mesh edge size is 0.5 cm. **(k-t)** Mesh edge size is 1.5 cm. The crude edges are artifacts from segmentation, performed in 3D. Since topology had to be preserved, no spatial smoothing was applied.

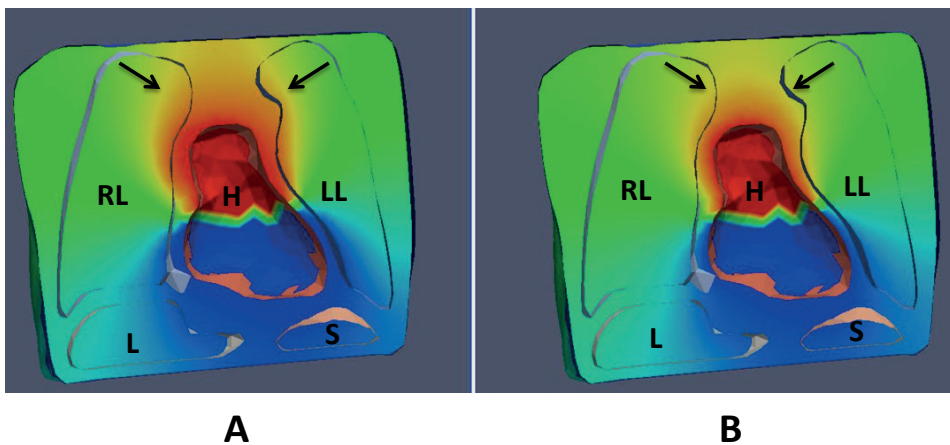


**Figure 7.** The impact of variable organ conductivity on BVP. A smaller sigma of the lung tissue leads to an increased breakthrough of the potential field **(A)**, compared to simulations in a homogeneous torso model **(B)**.

## DISCUSSION

In this study the feasibility of computing BVP for non-invasive imaging of cardiac excitation is illustrated. So far, volume potentials have been considered to be of limited value. However, computing BVP using the FEM is efficient if the number of bounding surfaces between organs taken into account is high. In addition, using the FEM rather than the BEM enables the incorporation of different anisotropies, local tissue characteristics and sigma gradients over different regions. BVP may be used to gain a better insight in the genesis of BSP and sources of local inaccuracies.

**Figure 6** suggests that the computed BVP hardly depend on the mesh cell characteristic length for a ratio as big as 1:3. However, the tank experiment indicates that there are geometries where the mesh size does have a significant influence on the outcome. The FEM could be used to understand which aspects of the geometry caused the large misrepresentation of the 4V equipotential plane. By visualizing the large potential gradient near the electrodes and the small potential gradient in the middle of the box, the FEM contributed to understanding the inaccuracy of the computed position of the 4V equipotential plane.

### Computation of BVP

From a computational standpoint, computing a potential field by means of the FEM is not a problem. The computation time of a 240,000 points potential field was approximately 3 minutes. Graphics processors with hundreds of computation units combined with quadcore main CPU's are becoming available at consumer prices. Generally available FEM packages are able to benefit from this just by setting some parameters and no custom coding. While the performance gain by computing the FEM in parallel may easily be tenfold. The FEniCS package has been selected because this tool has a lot of mindshare, a vivid user community and excellent documentation.

### Meshing

Generating high quality meshes and solving differential equations have been part of engineering disciplines for decades. In many articles on biomedical computing, generation of a computational mesh is taken for granted. Early experiments revealed that generation of a surface mesh from a labelled voxel set often leads to irregular meshes with topological errors that are hard to repair. Several groups have developed their own meshing software and others have proposed to do away with meshing altogether [16-18]. However, the meshing itself does not appear to be the problem.

General-purpose mesh generation tools can generate high quality volume meshes in a matter of seconds for an arbitrarily complex segmentation result, provided that the segmentation contains no topological errors.

Fast generation of volume meshes and FEM solutions with generally available means has brought computation of BVP as part of non-invasive imaging of cardiac excitation within practical clinical reach. This route will further be explored, hoping to gain direct and visual insight in the sources of inaccuracies, including the so called “ill conditioning” of the inverse problem, in the required number of electrodes, numbers of less than 20 to more than 200 currently being advocated in literature [19-20], and in the optimal placement of these electrodes in individual patients.

## **CONCLUSION**

This study illustrates that efficient generation of high quality volume meshes and computation of BVP with a resolution of 5 mm is feasible using generally available software and hardware. With the computational effort decreasing dramatically, estimation of BVP may be reasonable when the number of model compartments is high or when anisotropic conductivity is modelled. Observing the potential field everywhere in the thorax may lead to an improved understanding of the genesis of BSP and sources of local inaccuracies. In the near future, computation of BVP for non-invasive imaging of cardiac excitation may evolve towards clinical application.



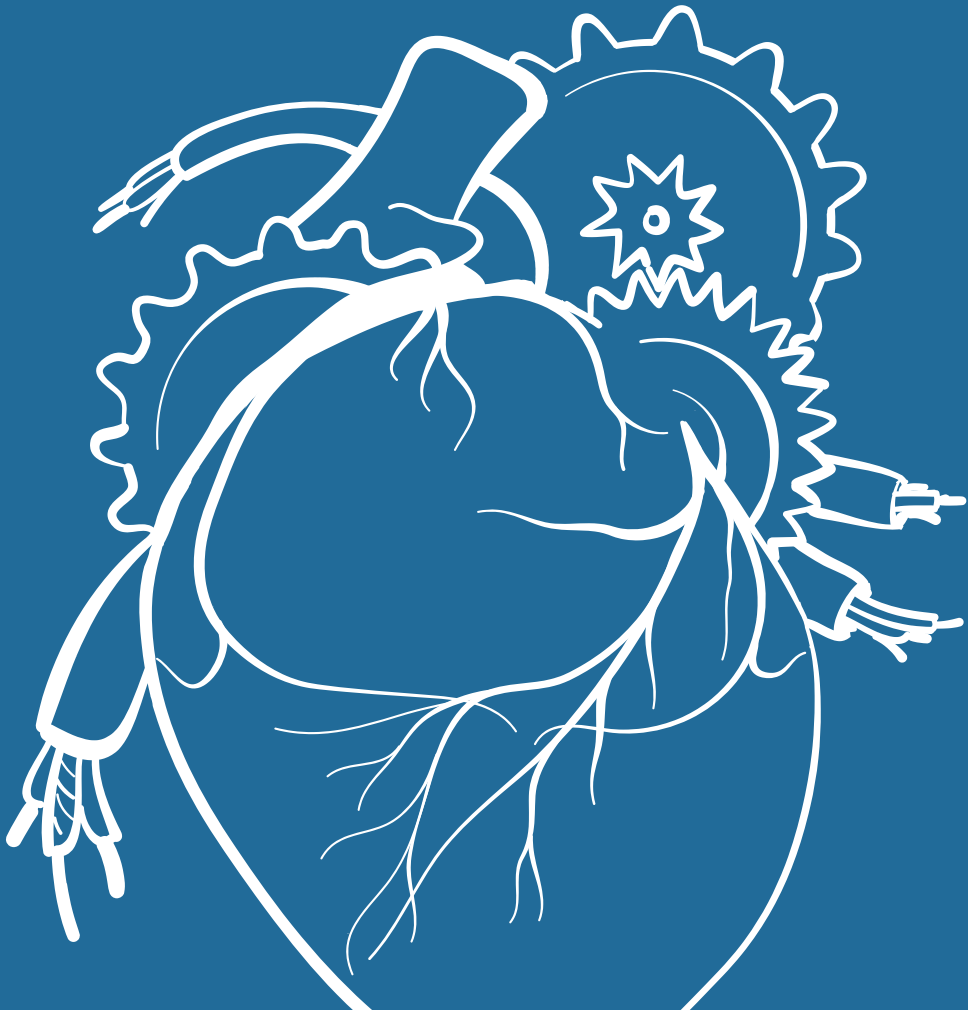
## REFERENCES

1. Desouza KA, Joseph SM, Cuculich PS, Ewald GA, Rudy Y. Non-invasive mapping of ventricular activation in patients with transplanted hearts. *J Electrocardiol.* 2013;46(6):698-701.
2. Sapp JL, Dawoud F, Clements JC, Horáček BM. Inverse solution mapping of epicardial potentials: quantitative comparison with epicardial contact mapping. *Circ Arrhythm Electrophysiol.* 2012;5(5):1001-9.
3. Galeotti L, van Dam PM, Loring Z, Chan D, Strauss DG. Evaluating strict and conventional left bundle branch block criteria using electrocardiographic simulations. *Europace* 2013;15(12):1816-1821.
4. Berger T, Pfeifer B, Hanser FF, Hintringer F, Fischer G, Netzer M, Trieb T, Stuehlinger M, Dichtl W, Baumgartner C, Pachinger O, Seger M. Single-beat non-invasive imaging of ventricular endocardial and epicardial activation in patients undergoing CRT. *PLoS One* 2011;27;6(1):e16255.
5. Gulrajani RM. The forward and inverse problems of electrocardiography. *IEEE Eng Med Biol Mag.* 1998;17(5):84-101.
6. van der Graaf AW, Bhagirath P, Ramanna H, van Driel VJ, de Hooge J, de Groot NM, Götte MJ. Noninvasive imaging of cardiac excitation: current status and future perspective. *Ann Noninvasive Electrocardiol.* 2014 Mar;19(2):105-13.
7. Stenroos M, Haueisen J. Boundary element computations in the forward and inverse problems of electrocardiography: comparison of collocation and Galerkin weightings. *IEEE Trans Biomed Eng.* 2008;55(9):2124-33.
8. Wang Y, Rudy Y. Application of the method of fundamental solutions to potential-based inverse electrocardiography. *Ann Biomed Eng.* 2006;34(8):1272-88.
9. Van Dam PM, Oostendorp TF, Linnenbank AC, Oosterom A van. Non-invasive imaging of cardiac activation and recovery. *Ann Biomed Eng.* 2009;37(9):1739-56.
10. Hunter P. FEM/BEM notes. CMISS Auckland Bioengineering Institute and Engineering Science, The University of Auckland, New Zealand. October 8, 2008:1-140.
11. Shahidi AV, Savard P, Nadeau R. Forward and inverse problems of electrocardiography: modeling and recovery of epicardial potentials in humans. *IEEE Trans Biomed Eng.* 1994;41(3):249-56.
12. Klepfer RN, Johnson CR, Macleod RS. The effects of inhomogeneities and anisotropies on electrocardiographic fields: a 3-D finite-element study. *IEEE Trans Biomed Eng.* 1997;44(8):706-19.
13. Wang D, Kirby RM, Macleod RS, Johnson CR. Inverse Electrocardiographic Source Localisation of Ischemia: An Optimisation Framework and Finite Element Solution. *J Comput Phys.* 2013;1;250:403-424.
14. Marchandise E, Geuzaine C, Remacle JF. Cardiovascular and lung mesh generation based on centerlines. *Int J Numer Method Biomed Eng.* 2013;29(6):665-82.

15. Mortensen M, Langtangen HP, Wells GN. A FEniCS-based programming framework for modeling turbulent flow by the Reynolds-averaged Navier-Stokes equations. *Advances in Water Resources*. 2011. DOI: 10.1016/j.advwatres.2011.02.013.
16. Wang Y, Rudy Y. Meshless methods in potential inverse electrocardiography. *Conf Proc IEEE Eng Med Biol Soc*. 2006;1:2558-9.
17. Li ZS, Zhu SA, He B. Solving the ECG forward problem by means of a meshless finite element method. *Phys Med Biol*. 2007;7;52(13):N287-96.
18. Chinchapatnam P, Rhode K, Ginks M, Nair PB, Razavi R, Arridge SR, Sermesant M. Voxel Based Adaptive Meshless Method for Cardiac Electrophysiology Simulation. *Lecture Notes in Computer Science* 2009;5528:182-190.
19. Rudy Y. Noninvasive electrocardiographic imaging of arrhythmogenic substrates in humans. *Circ Res*. 2013;1;112(5):863-74.
20. Van Dam PM, Tung R, Shivkumar K, Laks M. Quantitative localisation of premature ventricular contractions using myocardial activation ECGI from the standard 12-lead electrocardiogram. *J Electrocardiol*. 2013;46(6):574-9.



09



# A PRIORI MODEL INDEPENDENT INVERSE POTENTIAL MAPPING: THE IMPACT OF ELECTRODE POSITIONING

---

A. W. Maurits van der Graaf; Pranav Bhagirath; Jacques de  
Hooge; Natasja M. S. de Groot; Marco J. W. Götte  
*Clin Res Cardiol. 2016 Jan;105(1):79-88*

## ABSTRACT

**Introduction:** In inverse potential mapping, local epicardial potentials are computed from recorded body surface potentials (BSP). When BSP are recorded with only a limited number of electrodes, in general biophysical a priori models are applied to facilitate the inverse computation. This study investigated the possibility of deriving epicardial potential information using only 62 torso electrodes in the absence of an a priori model.

**Methods:** Computer simulations were used to determine the optimal in vivo positioning of 62 torso electrodes. Subsequently, three different electrode configurations, i.e., surrounding the thorax, concentrated precordial (30 mm inter-electrode distance) and super-concentrated precordial (20 mm inter-electrode distance) were used to record BSP from three healthy volunteers. Magnetic resonance imaging (MRI) was performed to register the electrode positions with respect to the anatomy of the patient. Epicardial potentials were inversely computed from the recorded BSP. In order to determine the reconstruction quality, the super-concentrated electrode configuration was applied in four patients with an implanted MRI-conditional pacemaker system. The distance between the position of the ventricular lead tip on MRI and the inversely reconstructed pacing site was determined.

**Results:** The epicardial potential distribution reconstructed using the super-concentrated electrode configuration demonstrated the highest correlation ( $R = 0.98$ ;  $p < 0.01$ ) with the original epicardial source model. A mean localisation error of 5.3 mm was found in the pacemaker patients.

**Conclusion:** This study demonstrated the feasibility of deriving detailed anterior epicardial potential information using only 62 torso electrodes without the use of an a priori model.

## INTRODUCTION

Inverse potential mapping (IPM) is a promising technique that may complement conventional invasive electrophysiological (EP) studies [1-2]. In IPM, local epicardial potentials are inversely computed from recorded body surface potentials (BSP) [3]. Typically, 252 electrodes surrounding the thorax are used to record BSP [4-5].

When a smaller number of recording electrodes is used, optimal electrode positioning is important. In the past, several studies have addressed this topic. Early studies focused on the detection and elimination of redundant information in the recorded BSP [6–10]. Later, biophysical a priori models, i.e., computer models that enable the in silico mimicking of in vivo conditions by using pre-programmed settings relating to physical properties, e.g., conduction velocity, fiber orientation, anisotropy, activation pathways, were introduced to compensate for the limited BSP data actually recorded [11]. In general, inverse procedures involving 64 or fewer electrodes always apply an a priori activation model.

The purpose of this study was to investigate the feasibility of IPM using only 62 torso electrodes in the absence of an a priori model. A simulation using 252 electrodes served as a reference for desired image quality. Simulations were performed using various electrode configurations. Three different electrode positions using 62 electrodes were subsequently applied on healthy volunteers to record BSP. From the recorded BSP, epicardial potentials were reconstructed. The amount of detail and the correlation with the original source model were assessed. To evaluate the localisation error and size of the smallest visible detail, this mapping technique was applied in four patients with an implanted MRI-conditional DDD pacemaker system.

## METHODS

### Computer simulations

#### *3D model*

Simulations were performed using a 3D thorax model. This model was constructed after manual segmentation of different structures and organs on anatomic magnetic resonance imaging (MRI) images using custom written software. The model incorporated the whole-heart (including atria, ventricles, septum), liver, lungs, spleen, and torso surface. To each of these tissue elements conductivities were assigned as reported in



literature (thorax: 0.2 S/m, lungs: 0.04 S/m, liver: 0.03 S/m and spleen: 0.04 S/m) [12]. Gmsh software [13] was used for the generation of a volume mesh, required for the simulations (**figure 1**).

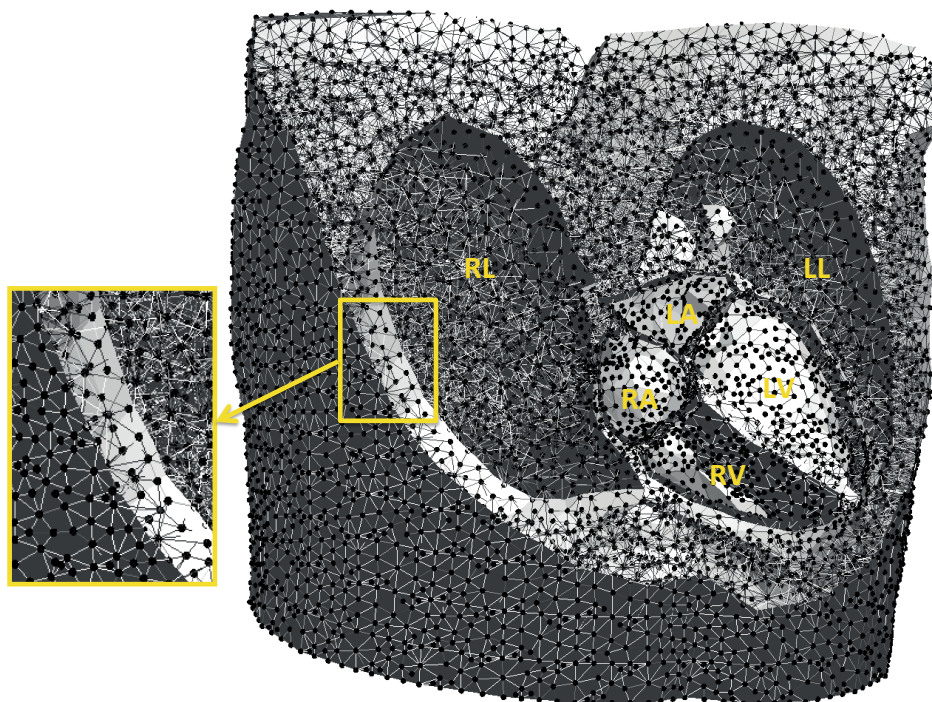


**Figure 1.** Example of a 3D volume mesh used for the simulations. This volume mesh was generated after segmentation of the thoracic organs on the MRI images. RL right lung, LL left lung, RA right atrium, LA left atrium, RV, right ventricle, LV left ventricle.

### *Forward simulation*

**Figure 2** provides a complete overview of the forward and inverse procedures used in this research, as described previously [14].

Propagation of electrical activity through the tissue elements of the whole-heart model was simulated using Moller-Trumbore [15] and Floyd-Warshall algorithms [16], yielding isochrones. From these isochrones, time dependent epicardial source potentials were computed by applying location specific activation curves. From the source potentials and in conjunction with the different tissue conductivities, BSP were computed by

multiplication with the transfer matrix  $T$ . From these BSP, ECG potentials were computed by spatial sampling. In order to approximate real-life conditions, noise was added to the simulated ECG potentials with a signal-to-noise ratio (SNR) of 21 dB.

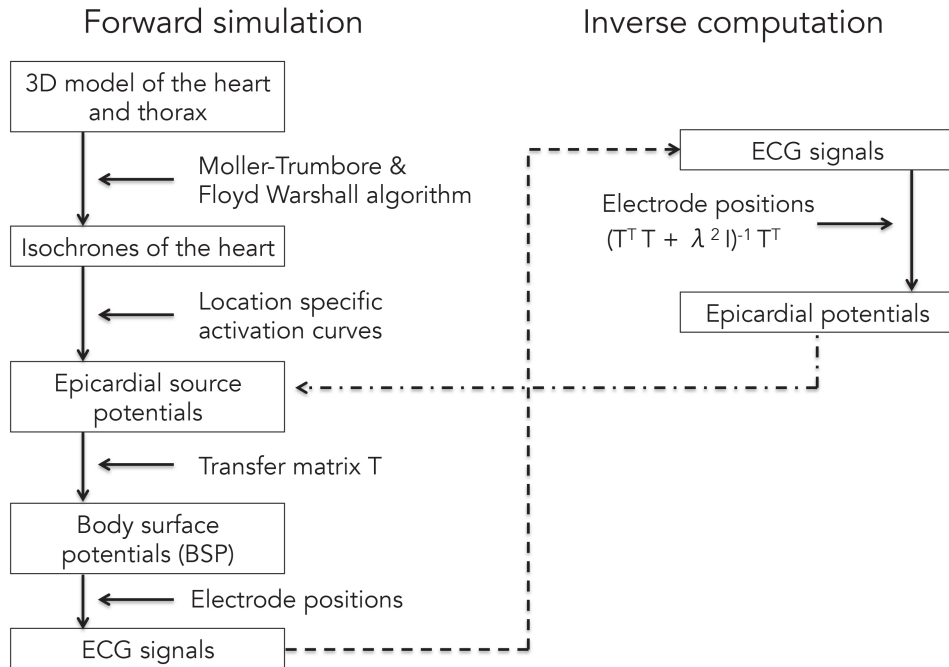


**Figure 2.** Flowchart visualizing the processes associated with forward simulations and inverse computations.

### ***Inverse reconstruction of epicardial potentials from simulated ECG potentials***

Epicardial potentials ( $P_{epi}$ ) were calculated from the ECG potentials ( $P_{bs}$ ) using  $P_{epi} = (T^T T + \lambda^2 I)^{-1} T^T P_{bs}$  where  $T$  is the forward transfer matrix and  $\lambda$  is the regularisation strength, initially determined by simulation with patient-specific geometries. For all electrode configurations, the correlation between the initial source epicardial potentials (used for the simulation of ECG potentials) and the reconstructed epicardial potentials was computed. In addition, for all electrode configurations, correlation was calculated for 16 identical points on the anterior epicardium. These values were plotted in a graph to visualise correlation trends. To exclude systematic errors due to grid artifacts, all computations were performed on different grids. Four different electrode configurations were used in the simulations (**figure 3**).

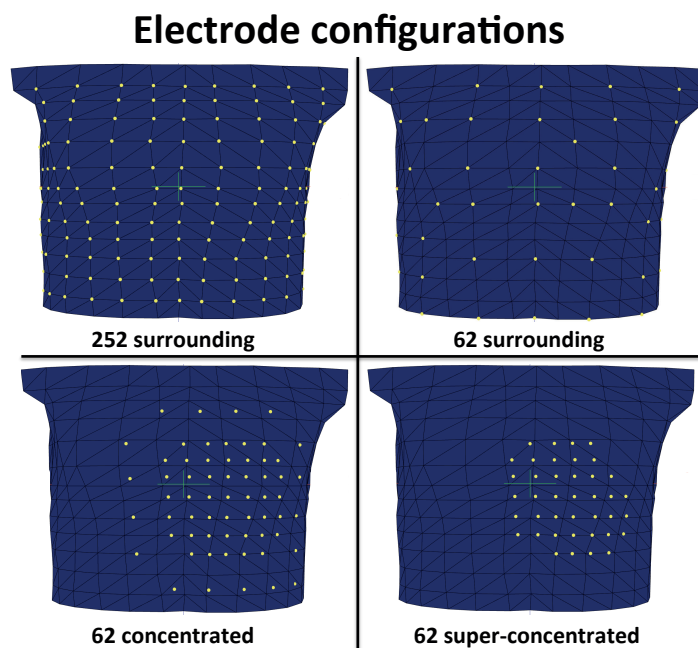


**Figure 3.** Anterior view of the thorax. Four different electrode configurations were used for the simulation part of the study: 252 electrodes surrounding the thorax, 62 surrounding the thorax, 62 concentrated (inter-electrode distance 30mm) and super-concentrated (inter-electrode distance 20mm). The yellow markers on the 3D thorax model represent the electrodes.

*Reference configuration* 252 electrodes surrounding the thorax. This configuration served as a reference, since this number of electrodes is the current standard in body surface potential mapping (BSPM).

- *Configuration I* 62 electrodes surrounding the thorax.
- *Configuration II* 62 concentrated (30 mm inter-electrode distance) electrodes directly overlaying the heart.
- *Configuration III* 62 super-concentrated (20 mm inter-electrode distance) electrodes directly overlaying the heart.

### Inverse reconstruction of recorded human data

#### *Study population*

Three different electrode layouts were subsequently used to record data in three healthy volunteers (mean age  $28 \pm 1$  year).

To evaluate the localisation error and size of the smallest visible detail, four male patients (mean age  $58 \pm 12$  years old) with an implanted MRI-conditional DDD pacemaker system (Advisa MRI™ Surescan®, Medtronic Inc., Minneapolis, MN, USA) and a structurally normal heart were enrolled. Patient characteristics are provided in **table 1**. The RV lead tip was positioned either in the RV apex (2 patients), or in the right ventricular outflow tract (RVOT) (2 patients).

**Table 1.** Patient characteristics.

Patient	Age (yrs)	Sex	RV lead tip location	Pacing indication	Relevant comorbidity
1	66	M	Apex	Asystole	Hypertension
2	42	M	Apex	Asystole	Hemochromatosis
3	69	M	RVOT	AV-block	-
4	54	M	RVOT	Chronotropic Incompetence	-

Written informed consent was obtained from all participants. This study complied with the declaration of Helsinki and received approval from the local ethical committee and the institutional scientific board.

### **Body Surface Potential Mapping**

Three different electrode layouts were used to record data in the healthy volunteers.

- *Configuration I* 62 electrodes surrounding the thorax.
- *Configuration II* 62 concentrated (30 mm inter-electrode distance) electrodes directly overlaying the heart.
- *Configuration III* 62 super-concentrated (20 mm inter-electrode distance) electrodes directly overlaying the heart.

BSP were recorded using a 65-channel (62 thorax electrodes) ActiveTwo BSPM system with passive electrodes and shielded cables (BioSemi BV, Amsterdam, The Netherlands). A sampling rate of 2048 Hz was selected and every data acquisition was performed for 60 s.

In the pacemaker patients, BSP were recorded using the 62 super-concentrated electrode configuration (configuration III). Potentials were recording during right ventricular (RV) pacing at a rate exceeding the intrinsic rate with at least 15 beats/min (paced AV-delay 70 ms).

Every BSP recording was immediately followed by an MRI scan in order to register the electrode positions to the anatomy of the volunteer.

### ***Magnetic Resonance Imaging***

After each BSPM recording, MRI markers were applied to replace all torso electrodes. These markers were used to locate the electrode positions on the MRI images, thereby minimizing the systematic error in the inverse procedure.

Axial, coronal and sagittal anatomical images were obtained using a Turbo Spin Echo (black blood) sequence during breath hold (slice thickness 6 mm, no gap between slices).

MRI was performed on a Siemens Aera 1.5 Tesla MRI scanner (Siemens Healthcare, Erlangen, Germany).

For patients with an implanted pacemaker, pacing thresholds, P- and R-wave amplitude and lead impedance were determined before entering the MRI room and the pacemaker system was programmed into MRI SureScan® mode [17]. These parameters were again determined after the examination and compared to the initial values. Finally, original programming of the pacemaker was restored.

### ***Inverse reconstruction of recorded ECG data***

From the MRI images, a 3D thorax model was constructed comprising the epicardial surface and the thorax volume conductor, accounting for lungs, liver and spleen. Epicardial potentials were calculated from the recorded BSP ( $P_{bs}$ ) using  $P_{epi} = (T^T T + \lambda^2 I)^{-1} T^T P_{bs}$ , where  $T$  is the forward transfer matrix and  $\lambda$  is the regularisation strength. Following each BSP recording, epicardial activation sequences were inversely reconstructed and visualised

### **Evaluation of the quality of the inverse results**

To evaluate the quality of the results, ECGs were reconstructed from the inverse by forward transformation. The correlation between the recorded ECG potentials and the computed ECG potentials was subsequently determined.

Note that while an a priori activation model was used for simulations to optimise the electrode positioning, no such model was used to perform the inverse reconstruction from recorded human BSP.

## **Patients with an implanted pacemaker system**

### ***Localisation error***

An investigator blinded to the actual ventricular lead tip position, identified the site of earliest depolarisation on the colour-coded epicardial potential map. Subsequently, the distance between this site and the position of the ventricular lead tip on the MRI images was determined. Hence, the localisation error was quantified as the distance between the true pacing location and the pacing location projected from the inverse.

### ***Amount of true detail***

The amount of detail was evaluated by performing a threshold-test on the epicardial potential peak induced by a pacing stimulus at a well-known electrode location. When the threshold was set too high, the potential peak would split, suggesting false detail.

The minimum size of the inversely mapped potential peak induced by pacing is determined by the highest threshold value that does not cause the peak to split. The detail shown in this case is true, rather than false (**figure 4**).

The smallest visible detail was quantified as the maximum point spread cross-section in mm of the potential peak due to pacing.

## **Computing platform**

All analyses were performed on a 2.4 GHz quadcore laptop running the Windows 8 OS. Solving the potential equations was delegated to an Ubuntu 12.10 virtual machine running on this laptop. Correlation coefficients were determined using Pearson's product moment correlation coefficients as computed by the NumPy library.



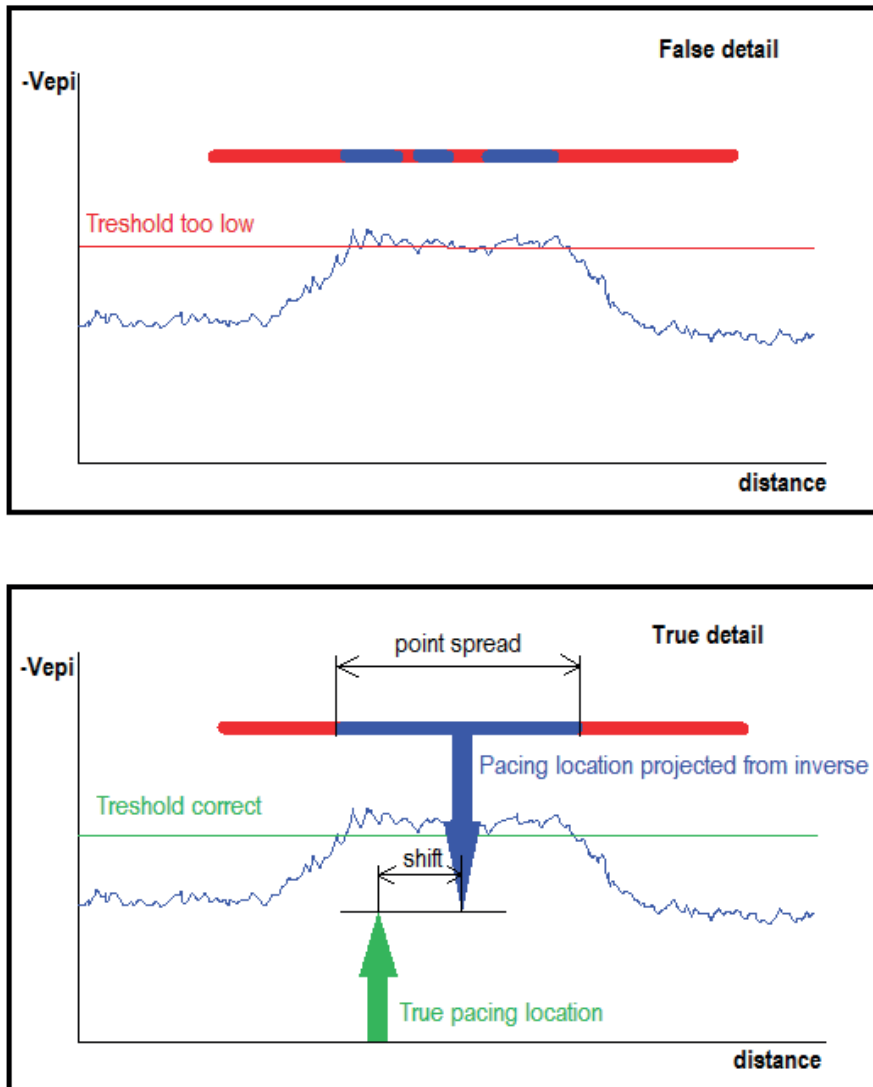


**Figure 4.** The amount of detail was evaluated by performing a threshold-test on an epicardial potential peak induced by a pacing stimulus. When the threshold is set too high, the potential peak will split, suggesting false detail (upper panel). The highest threshold value that does not cause the potential peak to split, reflects the minimum amount of true detail in the inversely reconstructed potential (lower panel).

## RESULTS

### Computer simulations

#### *252 electrodes surrounding the thorax*

This electrode layout provided a high image quality (**figure 5a**, video 1). Right ventricular breakthrough could be easily discerned. An overall high correlation ( $R = 0.96$ ;  $p < 0.01$ ) with the source model was found. The correlation map (**figure 5b**) clearly demonstrated a reduced correlation in areas with increased electrode spacing.

#### *62 electrodes surrounding the thorax*

This electrode configuration resulted in a poor image quality (**figure 5d**, video 2). Several gaps appeared in the epicardial potential map, indicating loss of information in these areas. A reduced overall correlation compared to the source model was found ( $R = 0.92$ ;  $p < 0.01$ ) (**figure 5e**).

#### *62 electrodes concentrated (30mm inter-electrode distance)*

When concentrating all available electrodes on the anterior part of the thorax in the region directly overlaying the heart, a clinical relevant image of the potentials on the anterior epicardium was obtained (**figure 5g**, video 3). **Figure 5h** shows that the correlation with the source model greatly improved ( $R = 0.97$ ;  $p < 0.01$ ), compared to the configuration using 62 electrodes surrounding the thorax.

#### *62 electrodes super-concentrated (20mm inter-electrode distance)*

By reducing the inter-electrode distance to 20 mm, image quality improved. The depolarisation front appeared to be more homogeneous (**figure 5j**, video 4). This was confirmed by a slightly higher correlation with the source model ( $R = 0.98$ ;  $p < 0.01$ ), compared to that obtained using the 30 mm electrode spacing configuration. As can be observed in **figure 5k**, IPM using the super-concentrated electrode configuration provided the highest correlation with the source model.

### Inverse reconstruction of recorded human data

The BSP recording and MRI examination lasted approximately 60 min. Segmentation and data processing lasted approximately 150 min. Correlation coefficients between measured and reconstructed ECGs were  $>0.94$  for all leads used in the inversion and  $>0.97$  for 85 % of those leads.



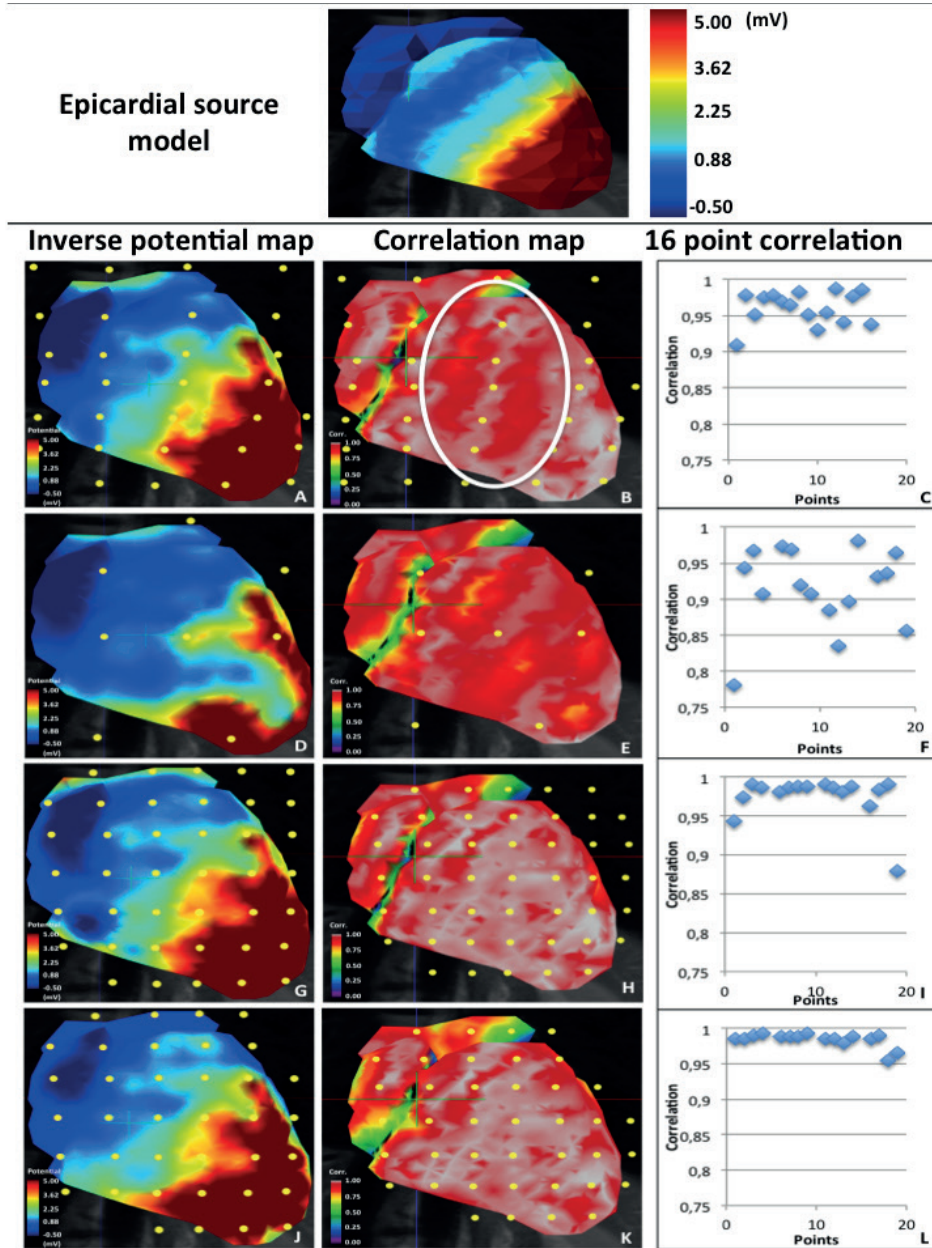


**Figure 5.** Epicardial source model at 30ms into the QRS (upper panel). Epicardial potential map at 30ms into the QRS, temporal correlation map and correlation plot of 16 sampling points for every simulated electrode layout (lower panel). A-C: 252 electrodes surrounding the thorax, D-F: 62 surrounding the thorax, G-I: 62 concentrated, J-L: super-concentrated. A reduced correlation was observed in areas between two electrodes (encircled in 4B). The highest correlation with the epicardial source model was obtained with the super-concentrated electrode placement.

### ***62 electrodes surrounding the thorax***

The 62 electrodes surrounding the thorax did not provide clinical sufficient information (video 5). Only ventricular epicardial activation could be reconstructed using this configuration. Regions with no or low signal variance were observed as gaps in the reconstructed epicardial potentials.

### ***62 electrodes concentrated (30mm inter-electrode distance)***

Concentrated positioning of the 62 available electrodes, directly above the heart, improved the overall resolution (video 6). Although reduced in size and number, areas of low signal were still present when using this electrode configuration.

### ***62 electrodes super-concentrated (20mm inter-electrode distance)***

Higher concentration of the electrode configuration (20 mm inter-electrode distance) resulted in a substantial increase of image resolution (video 7). Atrial and ventricular activation could be clearly distinguished and spatially localised in the reconstructed epicardial activation sequence. **Figure 6** shows epicardial potential maps for six instants of time during the QRST interval. In all three volunteers, similar results were obtained.

## **Reconstruction of pacing sites**

None of the patients reported any complaints during or after the MRI examination. Pacing thresholds and leads impedances remained unaffected by the MRI scan in all patients.

For all patients, the site of earliest ventricular depolarisation could be identified. In two patients, depolarisation started in the superior part of the right ventricular septum. In remaining patients, the site of earliest depolarisation was located in the apical region of the right ventricle.

## **In vivo evaluation of localisation error and amount of detail**

A mean localisation error of 5.3 mm was found. The mean size of the smallest visible detail during pacing, determined by a threshold test, was 7 mm. Individual values are listed in **table 2**.



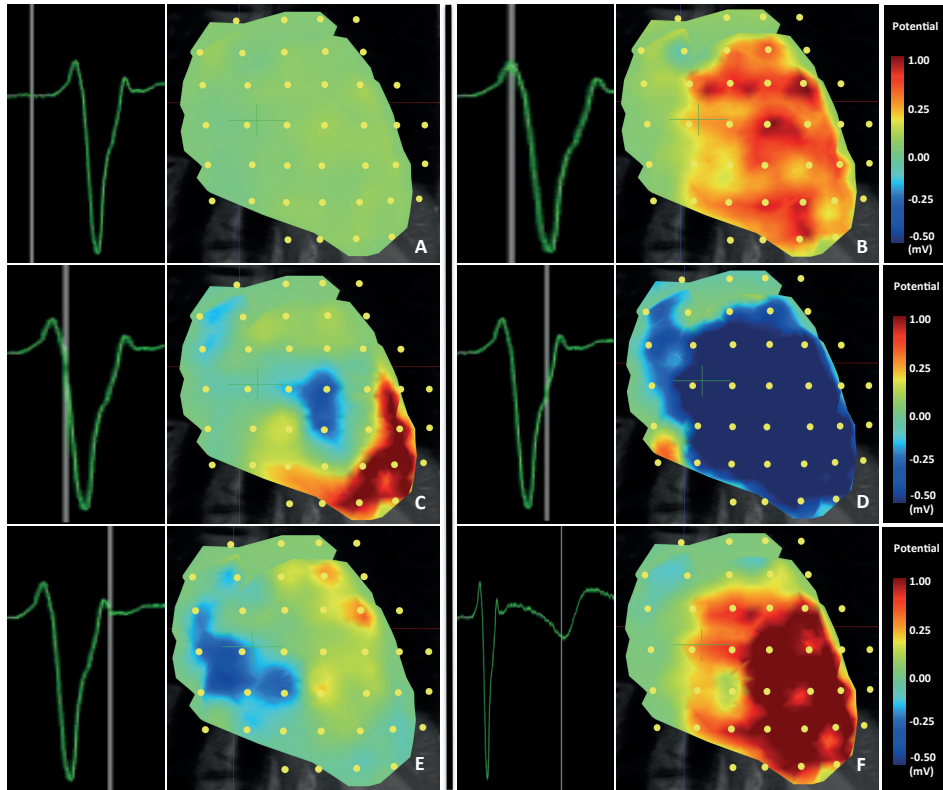


**Figure 6.** Epicardial potentials during a QRST interval inversely estimated from human BSP recorded using the super-concentrated (20mm inter-electrode distance) electrode configuration. Right ventricular breakthrough can be observed in panel C.

**Table 2.** Localisation errors and amount of detail in pacemaker patients.

	Localisation error (mm)	Max point spread (mm)
Patient 1 (RV apex)	5	7
Patient 2 (RV apex)	5	8
Patient 3 (RVOT)	5	7
Patient 4 (RVOT)	6	6

## DISCUSSION

This study investigated the optimal positioning of only 62 torso electrodes for IPM in the absence of an a priori model. Computer simulations were used to improve insight and predict image quality of different electrode configurations. A configuration of 62 electrodes positioned on the anterior part of the thorax, with a 20 mm inter-electrode distance, provided the highest amount of detail in the epicardial potential maps of the anterior side of the heart.

In addition, the epicardial potential distribution reconstructed using this configuration demonstrated the highest correlation ( $R = 0.98$ ;  $p < 0.01$ ) with the original epicardial source model. Using this configuration, a minimum occurring at 10 ms into the QRS near V1, reflecting right ventricular breakthrough could be discerned. This finding is in accordance with previous observations reported by Taccardi in 1963 [18] and Okamoto et al. in 1990 [19].

The results of application of this method in patients with implanted pacemakers indicated a clinically relevant reconstruction quality. A mean localisation error of 5.3 mm was found in the pacemaker patients.

### Clinical relevance of this study

Inverse potential mapping is a promising but also challenging modality to gain further insight into cardiac substrates and arrhythmia mechanisms in a non-invasive fashion. This study focused on simplification of the procedure by applying a reduced number of recording electrodes. The ventricular paced beats analysed in this study served as ectopic ventricular foci. The mapping approach presented in this paper may help to tailor the invasive electrophysiological procedure to the individual patient. The concentrated electrode configuration may make it an attractive clinical alternative in situations where this specific view is required.

### Importance of simulations

The possibility to simulate epicardial potentials from random electrode configurations facilitated a stepwise approach towards optimal electrode positioning. In this way, the simulations guided the placement of the electrodes. In addition, the validity of the simulations could be determined by application of the selected configurations in vivo. The validity of the simulations was subsequently confirmed by the results obtained in patients with implanted pacemaker systems.

### A-priori model

In literature [20–22], inverse procedures involving 64 or fewer electrodes always apply an a priori activation model. Although detailed images may be obtained using even <20 electrodes, the number of degrees of freedom in this situation fundamentally limits the number of pathology related activation patterns that can be represented. This is further elaborated upon in appendix and in **figure 7**.

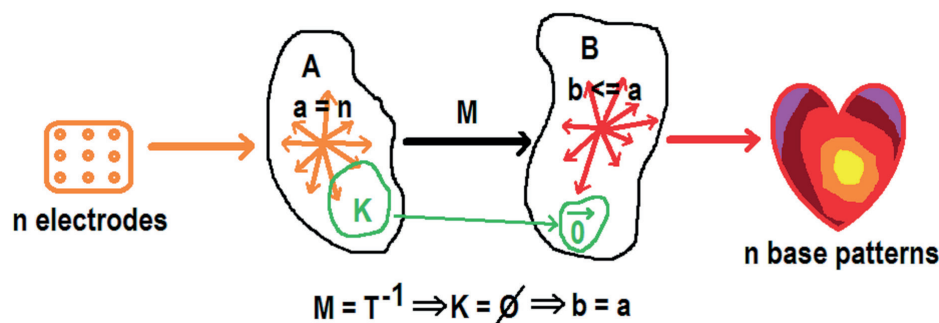


**Figure 7.** Linear mapping  $M$  denotes the ideal reconstruction, reflecting the unknown but exact linear quasi-stationary field equations.  $M$  maps  $n$  independent electrode signals onto at most  $n$  independent epicardial base vectors. Note that, by definition of  $M$ , no reconstruction method can do better. In practice, ill conditioning will render certain subsets of epicardial patterns indistinguishable, reducing the dimension of the solution space.

Obtaining detailed images of cardiac surface potentials using a limited number of electrodes, without excluding a wide variety of pathological activation patterns by constraining the solutions using an a priori activation model derived from healthy myocardial tissue, requires focusing all degrees of freedom on a limited region of interest on the cardiac surface.

### MRI

Although computed tomography (CT) is frequently preferred due to the speed of the acquisition process, MRI allows reliable function analysis, assessment of wall motion abnormalities and highly detailed characterisation of tissue [23–26]. Unlike CT, MRI does not use radiation. Hence, MRI is the preferred imaging modality to be repeatedly used in patients. In recent years, the safe performance of MRI in patients with non-MRI-conditional pacing devices has been demonstrated [27–29]. In addition, MRI-conditional devices have been introduced, decreasing the risk of potential hardware or software interactions [30].

### **Limitations of this study**

Application of 62 anterior electrodes with an inter-electrode distance of 20 mm enables detailed reconstruction of an anterior view of the epicardial potentials in the absence of an a priori model. Information on the posterior area of the heart could not be reconstructed from the BSP recorded using the anterior positioned super-concentrated electrode configuration. By increasing the total number of recording electrodes and by positioning electrodes on the back of the thorax this can be resolved. But since the application of a large number of electrodes is time consuming, implementation in the clinical arena may still be challenging. Hence, an optimal balance between information content and clinical utility is pursued. Parallel computation of the inverse solution will further reduce the post-processing time.

In the presence of a limited number of electrodes, electrode positioning is crucial. In order to achieve a high resolution, it is very important to position the electrodes directly overlaying the heart. Because this may be difficult to determine, a rapid exploratory MRI scan (scout anatomical images) prior to BSPM may help to optimise electrode positioning. Regarding the small number of patients in this study, further research is needed to further evaluate the clinical benefits of this non-invasive mapping strategy.

### **Future perspective**

Although IPM is considered a promising technique to complement conventional invasive electrophysiological procedures, it has not yet advanced to routine clinical application. This is mainly due to the time consuming nature of the acquisition and post-processing of the data. The possibility to derive detailed information on cardiac excitation from a rapid and simplified BSPM procedure may facilitate clinical implementation. The ability to perform detailed simulations using patient data may provide clinicians valuable insight into the potential impact of their treatment. Non-invasive characterisation of arrhythmogenic foci or substrates, prior to invasive electrophysiological or device implant procedures, may help to increase therapeutic outcome. Further research is required to provide evidence of the effectiveness and accuracy of this approach to IPM.

## **CONCLUSION**

The purpose of this study was to investigate the feasibility of IPM using only 62 torso electrodes without the aid of an a priori model. By concentrating the available electrodes in the area directly overlaying the heart, a high-resolution anterior view of the epicardial potentials can be obtained. Application of this mapping approach in patients with

implanted MRI-conditional pacemakers demonstrated a clinically relevant inverse reconstruction accuracy. Further research needs to be performed to further evaluate the clinical benefits of this technique.

## REFERENCES

1. Jamil-Copley S, Bokan R, Kojodjojo P, Qureshi N, Koa-Wing M, Hayat S, Kyriacou A, Sandler B, Sohaib B, Wright I, Davies DW, Whinnett Z, S Peters N, Kanagaratnam P, Lim PB. Noninvasive electrocardiographic mapping to guide ablation of outflow tract ventricular arrhythmias. *Heart Rhythm* 2014;11(4):587-94.
2. Sapp JL, Dawoud F, Clements JC, Horáček BM. Inverse solution mapping of epicardial potentials: quantitative comparison with epicardial contact mapping. *Circ Arrhythm Electrophysiol.* 2012;5(5):1001-9.
3. Gulrajani RM. The forward and inverse problems of electrocardiography. *IEEE Eng Med Biol Mag.* 1998;17(5):84-101, 122.
4. Ramanathan C, Ghanem RN, Jia P, Ryu K, Rudy Y. Noninvasive electrocardiographic imaging for cardiac electrophysiology and arrhythmia. *Nat Med.* 2004;10(4):422-8.
5. Rudy Y. Noninvasive electrocardiographic imaging of arrhythmogenic substrates in humans. *Circ Res.* 2013;112(5):863-74.
6. Lux RL, Evans AK, Burgess MJ, Wyatt RF, Abildskov JA. Redundancy reduction for improved display and analysis of body surface potential maps. I. Spatial compression. *Circ Res.* 1981;49(1):186-96.
7. Hoekema R, Uijen GJ, van Oosterom A. On selecting a body surface mapping procedure. *J Electrocardiol.* 1999;32(2):93-101.
8. Lux RL, Smith RF, Abildskov JA. Limited lead selection for estimating body surface potentials in electrocardiography. *IEEE Biomed Eng.* 1978;25:270-6.
9. Finlay DD, Nugent CD, Donnelly MP, Black ND. Selection of optimal recording sites for limited lead body surface potential mapping in myocardial infarction and left ventricular hypertrophy. *J Electrocardiol.* 2008;41(3):264-71.
10. Messenger-Rapport BJ, Rudy Y. Noninvasive recovery of epicardial potentials in a realistic heart-torso geometry. Normal sinus rhythm. *Circ Res.* 1990;66(4):1023-39.
11. van Oosterom A. The dominant T wave and its significance. *J Cardiovasc Electrophysiol.* 2003;14(10 Suppl):S180-7.
12. Oostendorp T, Nenonen J, Korhonen P. Noninvasive determination of the activation sequence of the heart: application to patients with previous myocardial infarctions. *J Electrocardiol.* 2002;35 Suppl:75-80.
13. Marchandise E, Geuzaine C, Remacle JF. Cardiovascular and lung mesh generation based on centerlines. *Int J Numer Method Biomed Eng.* 2013;29(6):665-82.
14. van der Graaf AW, Bhagirath P, van Driel VJ, Ramanna H, de Hooge J, de Groot NM, Götte MJ. Computing Volume Potentials for Noninvasive Imaging of Cardiac Excitation. *Ann Noninvasive Electrocardiol.* 2014 Jul 17.

15. Möller T and Trumbore B. Fast, Minimum Storage Ray/Triangle Intersection. *J Graph Tools*. 1997;2;1:21-28.
16. Floyd RW. Algorithm 97: Shortest Path. *Communications of the ACM* 1962;5;(6):345.
17. Wollmann CG, Thudt K, Kaiser B, Salomonowitz E, Mayr H, Globits S. Safe performance of magnetic resonance of the heart in patients with magnetic resonance conditional pacemaker systems: the safety issue of the ESTIMATE study. *J Cardiovasc Magn Reson*. 2014;6;16;30:1-8.
18. Taccardi B. Distribution of heart potentials on the thoracic surface of normal human subjects. *Circ Res*. 1963;12:341-52.
19. Okamoto Y, Musha T, Harumi K. Reduction of the number of electrodes in the measurement of body surface potential distribution. *Front Med Biol Eng*. 1990;2(4):283-92.
20. van Dam PM, Tung R, Shivkumar K, Laks M. Quantitative localisation of premature ventricular contractions using myocardial activation ECGI from the standard 12-lead electrocardiogram. *J Electrocardiol*. 2013;46(6):574-9.
21. Seger M, Hanser F, Dichtl W, Stuehlinger M, Hintringer F, Trieb T, Pfeifer B, Berger T. Non-invasive imaging of cardiac electrophysiology in a cardiac resynchronisation therapy defibrillator patient with a quadripolar left ventricular lead. *Europace* 2014;16(5): 743-749.
22. Bokeriia LA, Revishvili ASH, Kalinin AV, Kalinin VV, Liadzhina OA, Fetisova EA. Hardware-software system for noninvasive electrocardiographic examination of heart based on inverse problem of electrocardiography. *Med Tekh*. 2008;(6):1-7.
23. Abbasi SA, Ertel A, Shah RV, Dandekar V, Chung J, Bhat G, Desai AA, Kwong RY, Farzaneh-Far A. Impact of cardiovascular magnetic resonance on management and clinical decision-making in heart failure patients. *J Cardiovasc Magn Reson*. 2013;1;15:89.
24. Petrov G, Kelle S, Fleck E, Wellnhofer E. Incremental cost-effectiveness of dobutamine stress cardiac magnetic resonance imaging in patients at intermediate risk for coronary artery disease. *Clin Res Cardiol*. 2015;104(5):401-9.
25. Schuster A, Ishida M, Morton G, Bigalke B, Moonim MT, Nagel E. Value of cardiovascular magnetic resonance imaging in myocardial hypertrophy. *Clin Res Cardiol*. 2012;101(3):237-8.
26. Schumm J, Greulich S, Sechtem U, Mahrholdt H. T1 mapping as new diagnostic technique in a case of acute onset of biopsy-proven viral myocarditis. *Clin Res Cardiol*. 2014;103(5):405-8.
27. Nazarian S, Hansford R, Roguin A, Goldsher D, Zviman MM, Lardo AC, Caffo BS, Frick KD, Kraut MA, Kamel IR, Calkins H, Berger RD, Bluemke DA, Halperin HR. A Prospective Evaluation of a Protocol for Magnetic Resonance Imaging of Patients With Implanted Cardiac Devices. *Ann Intern Med*. 2011;155:415-24.
28. Jilek C, Lennerz C, Stracke B, Badran H, Semmler V, Reents T, Ammar S, Fichtner S, Haller B, Hessling G, Deisenhofer I, Kolb C. Forces on cardiac implantable electronic devices during remote magnetic navigation. *Clin Res Cardiol*. 2013;102(3):185-92.

29. Boilson BA, Wokhlu A, Acker NG, Felmler JP, Watson RE Jr, Julsrud PR, Friedman PA, Cha YM, Rea RF, Hayes DL, Shen WK. Safety of magnetic resonance imaging in patients with permanent pacemakers: a collaborative clinical approach. *J Interv Card Electrophysiol.* 2012;33:59–67.
30. Ferreira AM, Costa F, Tralhão A, Marques H, Cardim N, Adragão P. MRI-conditional pacemakers: current perspectives. *Med Devices (Auckl).* 2014;7:7:115-24.

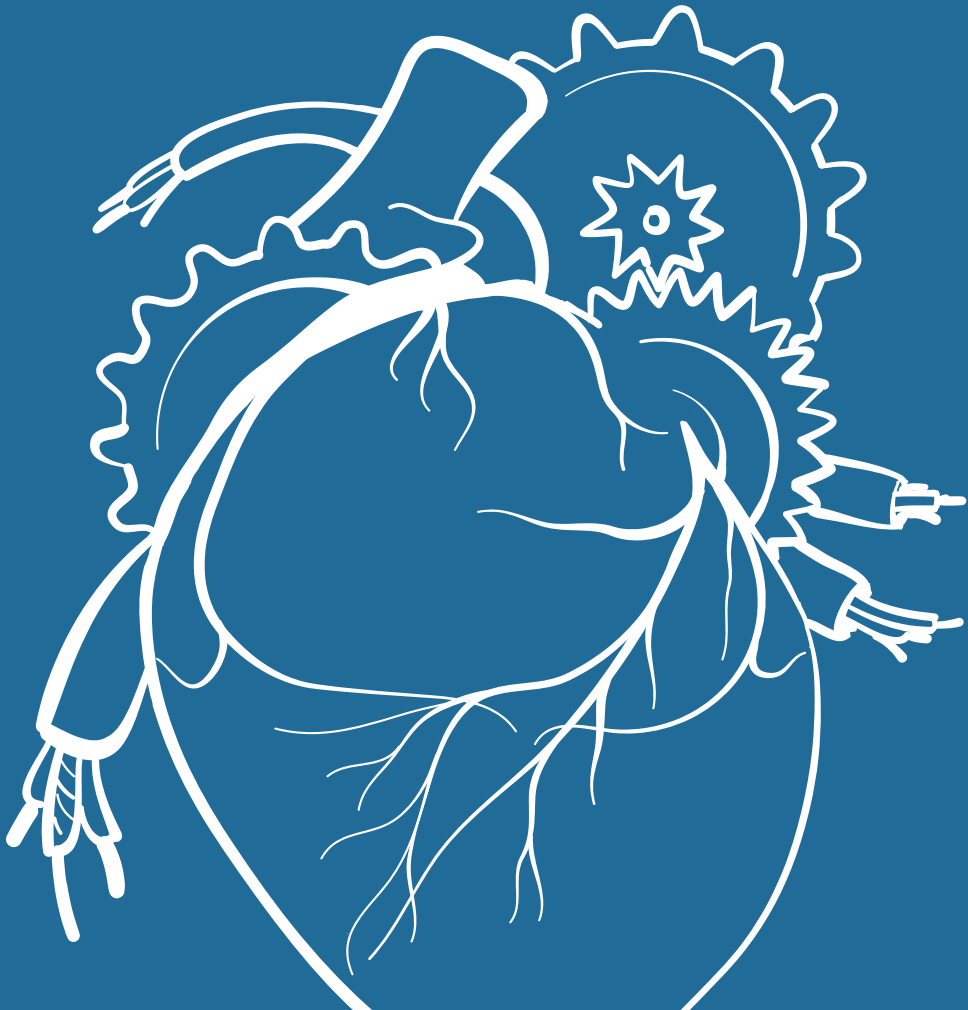


## APPENDIX I

Let  $n$  be the number of electrodes, let  $a$  be the dimension of the linear span  $A$  of the electrode potential vectors and let  $b$  be the dimension of the linear span  $B$  of the reconstructed epicardial potential vectors. Then  $a = n$  and  $b \leq a$ , since the base vectors of  $B$  are, by linearity of the quasi stationary electrical field equations, obtained by a linear mapping  $M$  from the base vectors of  $A$ , that may have a kernel  $K$  of dimension  $k > 0$ . In general  $b = a$ , since  $M$  will be non-degenerate as is illustrated in **figure 7**. Note that the exact nature of the parameter estimation procedure plays no role in this fundamental relationship.



# 10



# FEASIBILITY AND ACCURACY OF CARDIAC MAGNETIC RESONANCE IMAGING-BASED WHOLE-HEART INVERSE POTENTIAL MAPPING OF SINUS RHYTHM AND IDIOPATHIC VENTRICULAR FOCI

---

Pranav Bhagirath MD; Maurits van der Graaf MD; Elise van Dongen  
MD; Jacques de Hooge MSc; Vincent van Driel MD; Hemanth Ramanna  
MD PhD; Natasja de Groot MD PhD; Marco Götte MD PhD  
*J Am Heart Assoc. 2015 Oct 14;4(10):e002222*

## ABSTRACT

**Background:** Inverse potential mapping (IPM) non-invasively reconstructs cardiac surface potentials (CSP) using body surface potentials (BSP). This requires a volume conductor model (VCM), usually constructed from computed tomography (CT).

CT however, exposes the patient to harmful radiation and lacks information about tissue structure. Magnetic resonance imaging (MRI), in contrast, is not associated with this limitation, and might be of advantage for mapping purposes.

This feasibility study investigated an MRI-based IPM approach. In addition, the impact of incorporating the lungs and their particular resistivity values was explored.

**Methods and Results:** Three volunteers and eight patients with premature ventricular contractions (PVC) scheduled for ablation underwent 65 electrodes BSP mapping. VCM was created using MRI. CSP were estimated from BSP and used to determine the origin of electrical activation.

The IPM defined origin of sinus rhythm corresponded well with the anatomical position of the sinus node as described in the literature. In patients, the IPM derived PVC focus was 3-dimensionally located within  $8.3 \pm 2.7$  mm to the invasively determined focus using electro-anatomical mapping (EAM).

The impact of lungs on the IPM was investigated using homogeneous and inhomogeneous VCM's. The inhomogeneous VCM, incorporating lung specific conductivity, provided more accurate results compared to homogeneous VCM ( $8.3 \pm 2.7$  mm and  $10.3 \pm 3.1$  mm respectively ( $p=0.043$ ). The inter-observer agreement was high for homogeneous ( $ICC=0.862, p=0.003$ ) and inhomogeneous ( $ICC=0.812, p=0.004$ ) VCM.

**Conclusion:** MRI based whole-heart inverse potential mapping enables accurate spatial localization of sinus rhythm and PVC, comparable to EAM. An inhomogeneous volume conductor model improved inverse potential mapping accuracy.

## INTRODUCTION

Inverse potential mapping (IPM) allows for non-invasive reconstruction of epicardial activation patterns. The most frequently used IPM method is based on a homogeneous volume conductor model (VCM) constructed from computed tomography (CT) images<sup>(1)</sup>. This technique is increasingly being applied for analysis of idiopathic ventricular foci and guidance of catheter ablation<sup>(2,3)</sup>.

Although clinically useful, there are important limitations of this CT based approach. The most important limitation besides the exposure to radiation and associated risk of malignancies<sup>(4)</sup>, is the inability to characterize tissue in detail. Magnetic resonance imaging (MRI) does not have these limitations and is considered the gold standard for tissue characterization, in particular for edema and fibrosis. Although most publications underscore the fact that both CT and MRI can be used, MRI is less frequently utilized for IPM<sup>(5-7)</sup>.

In addition, the use of a *homogeneous* VCM could also be considered a limitation since it may not appropriately incorporate the effects of specific tissue conductivity characteristics such as from the lungs (i.e. inhomogeneous conditions)<sup>(8)</sup>.

This study investigated the feasibility of whole-heart IPM using a VCM derived from MRI. The clinical applicability of this approach was evaluated in healthy volunteers and patients with idiopathic ventricular foci. In addition, the influence of tissue impedance on the results of IPM was studied using two different VCM's. A homogeneous thoracic VCM (Model 1) was compared to an inhomogeneous VCM where in addition to thoracic impedance, the resistance value of the lungs was included (Model 2).

## METHODS

### Patient Population

The study population consisted of 3 healthy volunteers and 8 patients with symptomatic or therapy resistant premature ventricular contractions (PVC). The study complied with the declaration of Helsinki and received approval from the local ethical committee (METC Zuidwest Holland study number NL38156.098.11) and the institutional scientific board. Written informed consent was obtained from the study subjects.

### Body surface potential acquisition

An MRI scout scan was performed to approximate the position of the heart with respect to the thorax. Subsequently, 62 (+3 limb) electrodes were applied to the subject's torso, centralized over the heart. Body surface potentials (BSP) were acquired using a 65 channel ActiveTwo system (BioSemi B.V., Amsterdam, The Netherlands). Once the acquisition was completed, the electrode locations were marked with MRI markers enabling accurate identification of the electrode positions.

### Image acquisition

MRI studies were obtained using a 1.5 Tesla Aera scanner (Siemens Healthcare, Erlangen, Germany). Blackblood imaging was performed using a Half-Fourier Acquisition Single Shot Turbo Spin Echo (HASTE) pulse-sequence to acquire three perpendicular stacks (axial, coronal and sagittal) from the neck till lower abdomen.

Images were acquired during free breathing using navigator gating (diaphragm) with 1 mm window. ECG gating was used to acquire images during the diastolic phase of the cardiac cycle. Typical imaging parameters were: a spatial resolution of  $1.2 \times 1.2 \times 6$  mm, TR/TE 744/42 ms and flip angle=  $160^\circ$ .

### Volume conductor model and computational algorithm

The MRI images were segmented using a custom developed tool. This tool generates a script containing the geometrical description (points, lines and planes and directed line loops) of the segmentation. Subsequently, the script was meshed using GMSH<sup>(9)</sup>. The  $\Sigma$  for the homogeneous VCM (Model 1) was specified at 0.2 S/m<sup>(10)</sup>. The inhomogeneous VCM (Model 2) had a similar  $\Sigma$ , but also contained specific conductivity values of the lungs, specified at 0.04 S/m<sup>(10)</sup>.

Cardiac surface potentials (CSP) were calculated from BSP using

$$\text{CSP} = (\mathbf{T}^T \mathbf{T} + \lambda^2 \mathbf{I})^{-1} \mathbf{T}^T \text{BSP}$$

where  $\mathbf{T}$  is the transfer matrix and  $\lambda$  is the regularization strength.

### Electrophysiological study and catheter ablation

The electrophysiologists (HR and VD) were blinded for the IPM results. During the electrophysiological study (EPS), femoral venous and arterial access was established. In all cases, a hexapolar catheter (Supreme™, St. Jude Medical) was placed in the right atrial appendage, the proximal electrode located in the inferior vena cava served as the unipolar indifferent electrode. Additionally, a screw-in temporary pacing lead (Medtronic) was placed in the right ventricle as a positional reference for the electro

anatomical mapping (EAM) system (Ensite Velocity 3.0, St. Jude Medical). An EAM was created using the roving catheter. Respiratory compensation was set to automatic. No field scaling was performed.

If no spontaneous PVC's were present, isoproterenol and/or pacing maneuvers were used to provoke PVC's. After the focus location was identified, targeted ablation was performed using a standard 4-mm non irrigated ablation catheter with power delivery up to 50W and a temperature limitation of 50°C. Subsequently, the site of ablation was marked on the EAM system.

### **Comparison of focus localization**

Following the ablation procedure, the ectopic PVC focus location, as identified on the IPM, was compared with the site of ablation, as specified on the EAM (gold-standard). For this purpose, two experienced operators (PB and HR) independently identified the foci on IPM and EAM to provide a measure of inter-observer variability.

This resulted in three different datasets describing the focus localization as the x, y and z coordinate: 1) IPM utilizing the homogeneous model (dataset 1), 2) IPM utilizing the inhomogeneous model (dataset 2) and 3) EAM (dataset 3). Subsequently, the Pythagoras theorem for 3-dimensional coordinate vectors, where the distance between two points is equal to the square root of the sum of the squared coordinate differences, was used to calculate the differences between coordinate dataset 1 and 3, and coordinate dataset 2 and 3.

### **Statistical analysis**

Statistical analysis was performed using IBM SPSS Statistics (Version 22.0). Continuous variables were expressed as mean  $\pm$  standard deviation or using median and interquartile range. Localization errors between the two VCM were compared using the Wilcoxon Signed-Rank test. The intra-class correlation coefficient (ICC) was used to analyze the inter-observer agreement. A  $p < 0.05$  was considered to be statistically significant.

## **RESULTS**

### **Study population**

Baseline characteristics of the 3 volunteers and 8 patients (N=11) are provided in **table 1**. All volunteers had normal electrocardiograms. In both volunteers and patients, structural heart disease was excluded based on the MRI examination.

**Table 1.** Characteristics of subjects undergoing inverse potential mapping.

	Volunteers	Patients
n	3	8
Age (years)	28 ± 3	46 ± 13
BMI	22.1 ± 1.4	25.2 ± 6.7
Female (%)	1 (33%)	7 (88%)
LVEF (%)	55 ± 2	50 ± 3
RVOT PVC's	-	6 (75%)
Duration of PVC's (months)	-	18 ± 12
PVC burden pre procedure	-	14,121 (IQR: 10432-22373)
PVC burden post procedure	-	17 (IQR: 1-24)

Age, BMI, LVEF and PVC duration are expressed in mean ± standard deviation. PVC burden pre- and post-procedure is expressed using median and IQR. IQR indicates interquartile range. PVC burden is expressed in ectopic beats/24 hours.

### Ablation procedure

The pre-procedural median PVC burden was 14,121 (interquartile range: 10432-22373) ectopic beats/24 hours. Average procedural time, including mapping and ablation, was 129±53 minutes. An average of 4468 points were acquired to construct the EAM. No peri-procedural displacements of the EAM were observed.

After catheter ablation, the PVC burden was reduced to a median of 17 (interquartile range:1-24) ectopic beats/24 hours, a reduction of more than 99%.

### IPM in sinus rhythm

During sinus rhythm, the first point of activation on the potential map of healthy volunteers was anatomically located near the transition of the superior vena cave (crista terminalis) (white arrow) into the right atrium (**figure 1a**). Ventricular breakthrough initiated at the right ventricular free wall (**figure 1b**) at the site where the moderator band was attached to the ventricular myocardium.

### Comparison between IPM focus and actual ablation site

No pacing maneuvers were required for PVC induction. Five patients required isoproterenol to induce PVC. Based on invasive mapping, six patients had the ablation site in the right ventricular outflow tract (RVOT) and two in the left ventricular outflow tract (LVOT) (**table 2**). One of the patients had a right bundle branch block (RBBB) which was reconstructed correctly by IPM (movie 1).

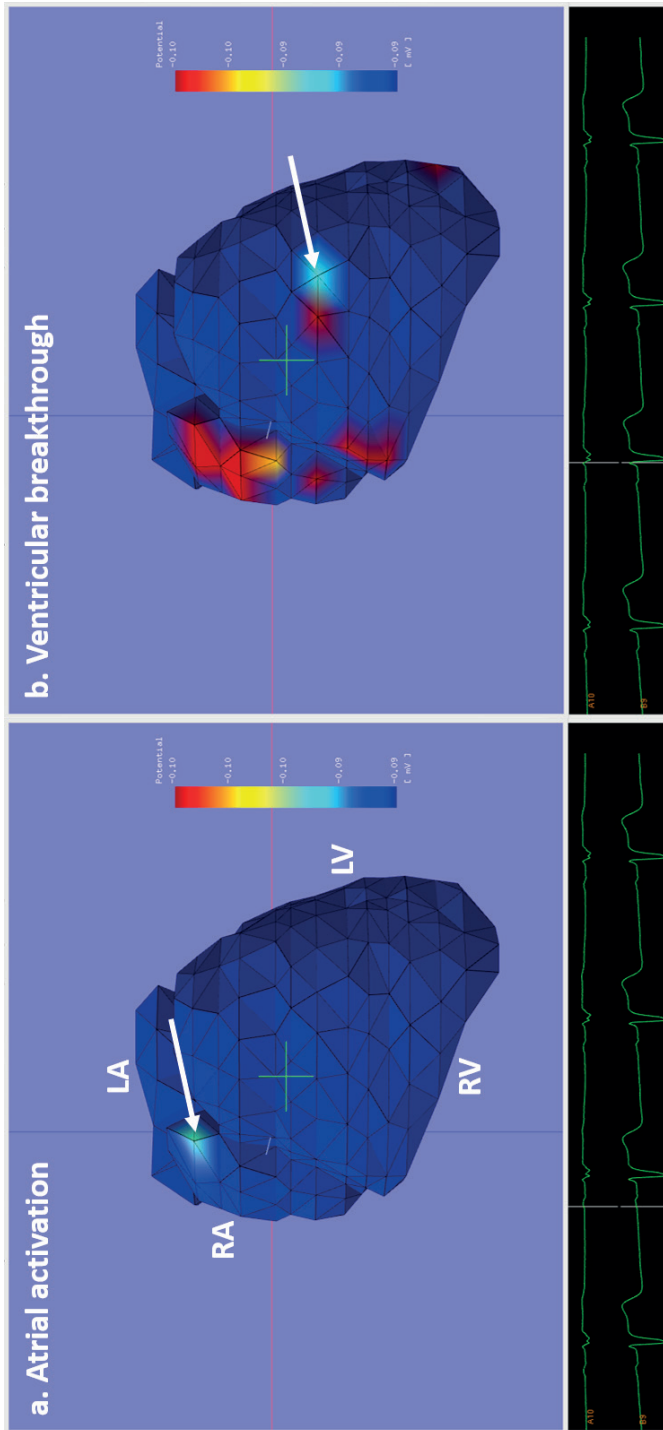


**Figure 1.** IPM in a healthy volunteer during sinus rhythm.

The left panel depicts the IPM at the start of the atrial depolarization (P wave) and the right panel depicts the IPM at the start of the ventricular depolarization (QRS). The Anterior-Posterior (AP) view of the 3D heart model can be observed.

The first point of atrial activation is observed near the entrance of the Superior Vena Cave (white arrow) into the Right Atrium. The first point of ventricular activation is observed at the RV free wall (white arrow) where the moderator band is attached to the ventricular myocardium.

**Table 2.** Comparison of PVC focus identified with IPM and ablation site on EAM.

Case	PVC focus IPM	Ablation site
1	NCC-LCC junction	LCC
2	RVOT-Septal	RVOT-Septal
3	RVOT-Anterior proximal	RVOT-Anterior proximal
4	RVOT-Anterior	RVOT-Anterior
5	RVOT-Septal proximal	RVOT-Septal proximal
6	RVOT-Antero-septal	RVOT-Septal
7	RVOT-Postero-septal	RVOT-Septal
8	NCC	NCC

NCC indicates non-coronary cusp; LCC, left coronary cusp; RCC, right coronary cusp; LVOT, left ventricular outflow tract; RVOT, right ventricular outflow tract.

In all 8 cases, IPM located the ectopic focus in the correct cardiac compartment (**table 2**). IPM identified all RVOT foci in close proximity to the ablation lesion ( $8.4 \pm 3$  mm,  $n=6$ ) defined on the EAM (**figure 2** and **movie 2**). A similar difference was found for the LVOT foci ( $7.9 \pm 1.5$  mm,  $n=2$ ). IPM located one of the LVOT foci (Case 2) at the right-coronary cusp. However, the ablation for this patient was successfully performed in the distal LVOT (**figure 3**). The other LVOT focus was closely approximated to the actual site of ablation.

### Comparison between homogeneous and inhomogeneous volume conductor models

The comparison of PVC focus between the inhomogeneous VCM and EAM demonstrated a localization accuracy of  $8.3 \pm 2.7$  mm (observer 1) and  $8.2 \pm 2.8$  mm (observer 2) with a high inter-observer agreement (ICC=0.812, 95% CI [0.318 to 0.959],  $p=0.004$ ). A similar comparison between the homogeneous VCM and EAM demonstrated an accuracy of  $10.3 \pm 3.1$  mm (observer 1) and  $9.8 \pm 2.9$  mm (observer 2) and also showed a high inter-observer agreement (ICC=0.862, 95% CI [0.399 to 0.975],  $p=0.003$ ).

The focus localization accuracy showed significant differences between the homogeneous and inhomogeneous VCM's. The homogeneous VCM had a significantly higher localization error compared to the inhomogeneous VCM for both observers (**table 3**) ( $p=0.043$ ). In addition, the homogeneous VCM failed to identify the focus in one RVOT case (**figure 4**, case 6) where the inhomogeneous model correctly identified the site of ablation.

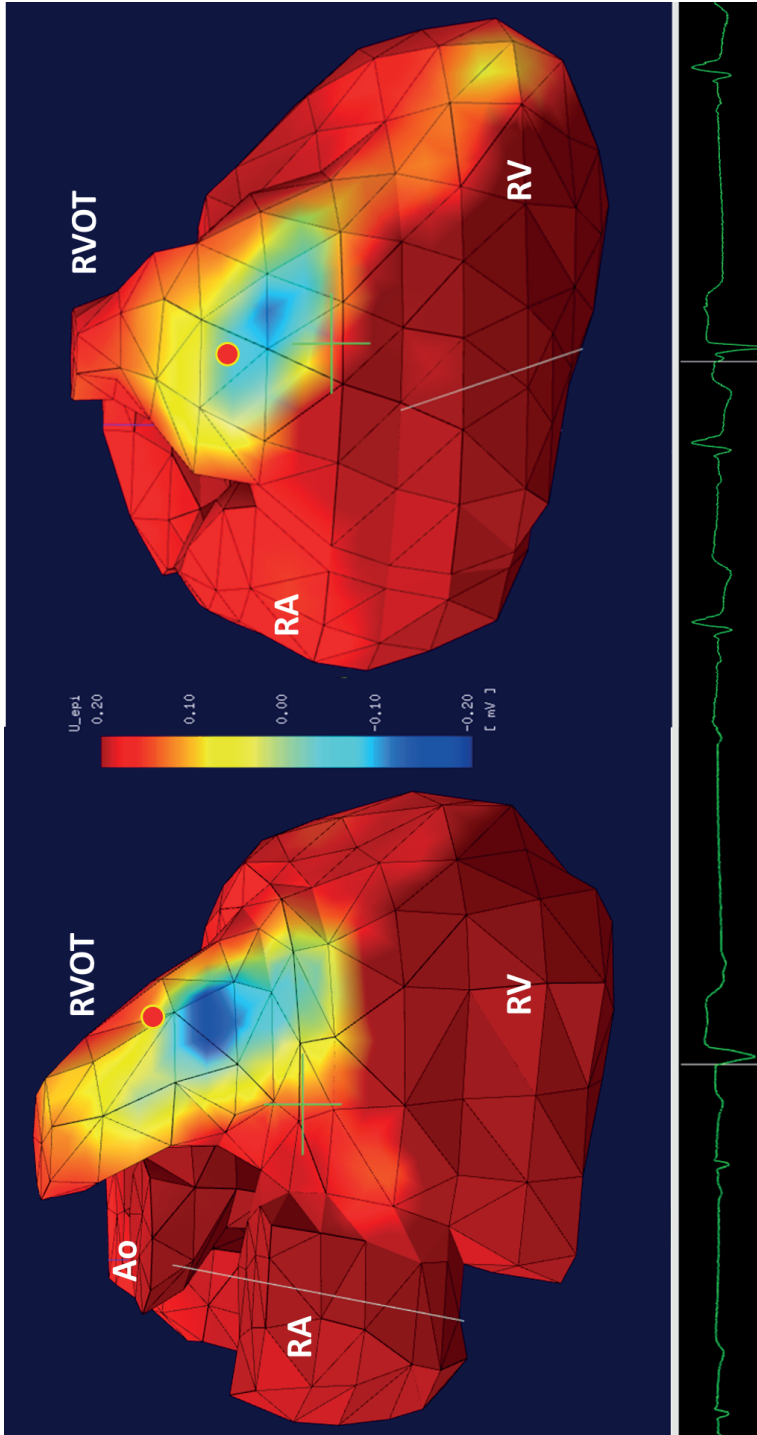


**Figure 2.** Comparison between IPM and EAM for the right ventricle outflow tract PVC patients. Blue indicates the area of epicardial breakthrough. The red dot indicates the site of ablation. ECG is provided underneath each image.



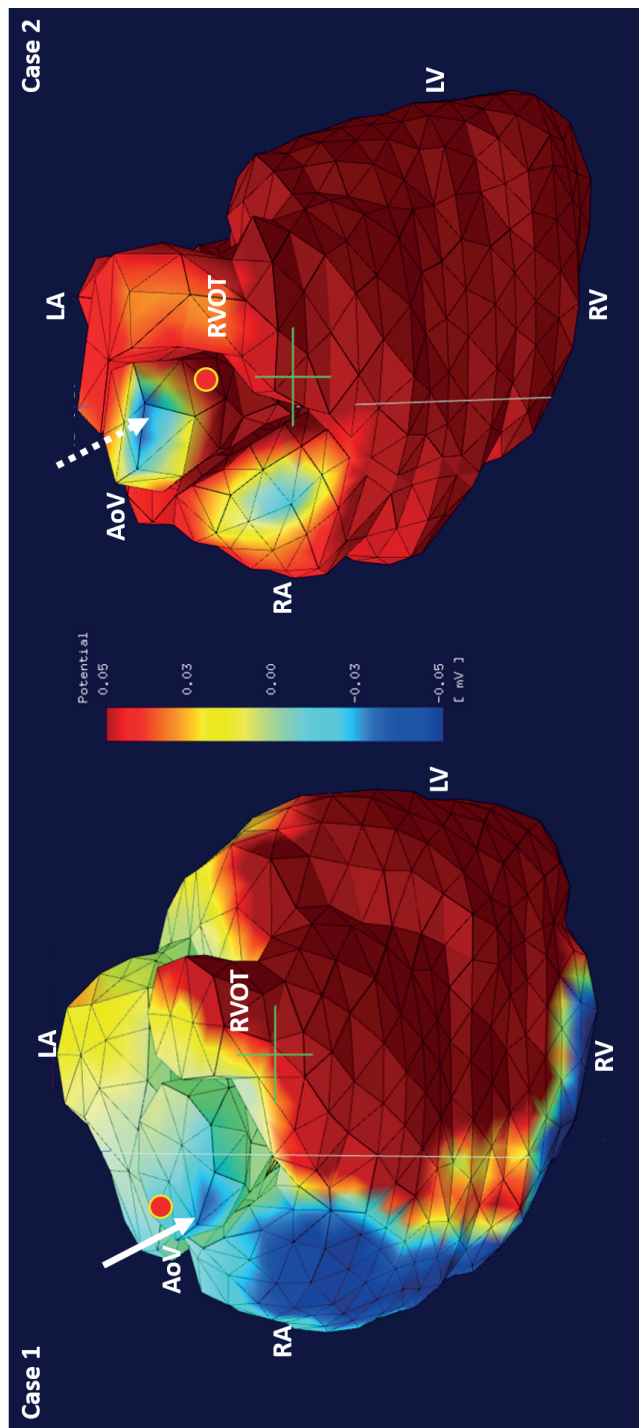


**Figure 3.** Comparison between IPM and EAM for the left ventricle outflow tract PVC patients. Blue indicates the area of epicardial breakthrough (white arrows). The red dot indicates the site of ablation. ECG is provided underneath each image.

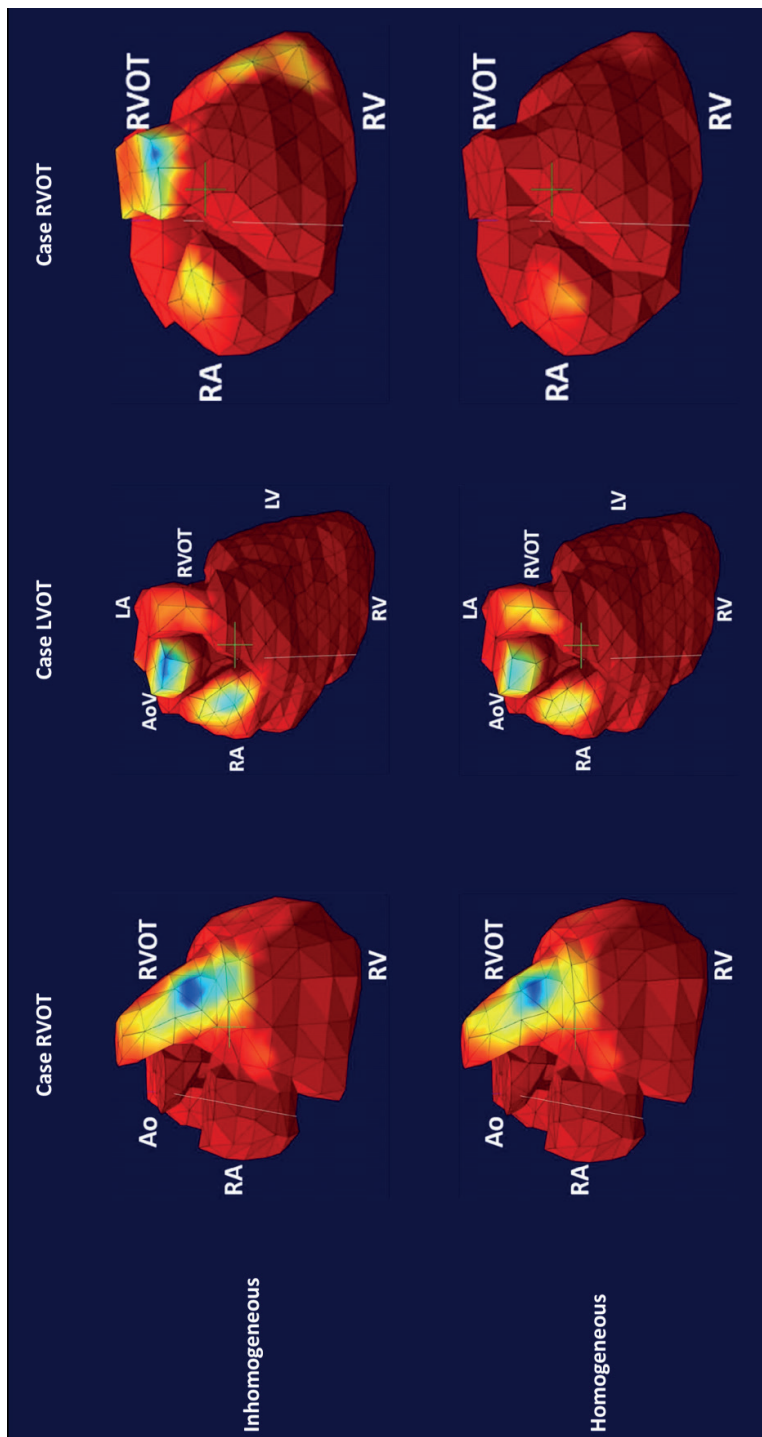


**Figure 4.** Comparison between homogeneous and inhomogeneous VCM. Left column and center columns depict insignificant and subtle differences between homogeneous and inhomogeneous VCM respectively. Right column depicts a clinically significant difference between the two VCM's.



## DISCUSSION

To our knowledge, this is the first study investigating whole-heart IPM using a 62 lead anterior BSP recording and an MRI derived inhomogeneous VCM.

The evaluation of this model was performed in healthy volunteers and patients with idiopathic arrhythmias. Using this MRI based non-invasive method it was possible to estimate the PVC focus location with clinically sufficient accuracy using BSP's of a *single* ectopic beat. In addition, a comparison between two independent observers demonstrated a high reproducibility of the results.

### Evaluation in healthy volunteers

IPM localized the origin of atrial activity near the transition of the superior vena cave (crista terminalis) into the right atrium. This location has been described in the literature as the anatomical location of the sinus node<sup>(11)</sup>. These results suggest that atrial activity may be non-invasively assessed using this combined MRI IPM method.

The first ventricular epicardial breakthrough was located at the RV free wall and corresponded with descriptions in the literature<sup>(1,12)</sup>. Furthermore, it was also possible to visualize abnormal ventricular activation patterns such as a RBBB (Movie 1).

These findings illustrate the potential sensitivity of IPM to detect minute changes in cardiac activation and demonstrate the ease of combining IPM with MRI acquisitions. This offers the prospect to use this method for screening purposes.

### Clinical impact in idiopathic PVC ablation

IPM successfully approximated the ablation site in 8 of 8 patients, a surrogate for the clinical PVC focus. This finding suggests that routine application of this *non-invasive* technique as part of the clinical workup could have multiple benefits such as improved ablation planning due to accurate pre-procedural identification of the PVC focus (target ablation site), and reduction in procedural duration (and accompanying radiation exposure) due to reduced invasive mapping time. This may especially be valid for patients with a low PVC burden and/or multifocal PVC's.

### Volume conductor models

The current, most frequently utilized BSPM technique (ECVUE™) uses a homogeneous torso conductor model. The clinical utility of this method has been demonstrated after extensive investigation<sup>(13,14)</sup>. However, recent research advocates the integration of the various organs with their own specific impedance<sup>(8,15)</sup>. This may especially be the case

in patients with a high body surface area, pulmonary edema or myocardial infarction. These circumstances could substantially influence the BSP's due to altered conductivity and resistivity conditions.

The comparison performed in this study indicated a significant difference between homogeneous and inhomogeneous VCM (**table 3**). These results suggest that although it is possible to perform IPM using a homogeneous VCM, an inhomogeneous VCM provides more accurate results.

**Table 3.** Localization difference between ectopic focus identified using homogeneous and inhomogeneous VCM compared to the ablation site marked on the EAM.

Case	Homogeneous (mm)	Inhomogeneous (mm)	p
1	11.1	9.3	
2	9.1	9.1	
3	6.4	6.4	
4	14.4	12.1	
5	<i>focus not identified</i>	7.6	
6	14.9	11.7	
7	7.8	3.6	
8	8.3	6.4	
Median and IQR	9.1 (IQR: 7.8-14.4)	8.35 (IQR: 6.4-11.1)	p = 0.043

IQR indicates interquartile range.

### Limitations

Several inherent technical limitations may have led to the observed differences between IPM identified ectopic focus and site of ablation defined on the EAM.

Although clinically more practical, the limited number of electrodes used in this study and the electrode positioning on the patient thorax may have affected the accuracy of focus localization. In addition, movement of the ablation catheter may cause spatial displacement of the marked ablation site by approximately 10 mm<sup>(16)</sup>. Furthermore, small and subtle catheter movements can also result in significant shifts within the EAM while using a reference catheter. All these factors could have contributed to the differences in focus location between IPM and EAM.

However, even if these conditions can be optimized, there still remain factors that may cause discrepancies. These include image misregistration due to patient respiration, inaccurate cardiac geometry due to image acquisition during different phases of the cardiac cycle and substantial regional variations in cardiac displacement during contraction and relaxation (ranging between 5-25 mm) <sup>(17, 18)</sup>. Especially the base of the heart moves 20 mm or more towards the apex. This is of particular importance, since all ectopic foci were located at the basal part of the heart. Motion related inaccuracies will probably have less influence on hearts with reduced function (less movement) or when analyzing foci from regions less susceptible to motion. A larger study will be needed to establish the impact of a screening approach prior to routine implementation.

### **Future directions**

This proposed combined IPM and MRI strategy offers the prospect to study the electrical activation in relation to tissue characteristics for complex (supra-)ventricular tachycardia's and scar based arrhythmias with clinically relevant accuracy.

The design of the computational model allows for instantaneous integration of patient-specific characteristics such as tissue properties and its associated conductivity. These tissue properties can be easily obtained using MRI. Integration of these characteristics will enable the operator to provide more patient tailored therapy.

### **CONCLUSION**

This study demonstrates the clinical applicability of an MRI based whole-heart IPM method in patients with idiopathic ventricular foci. There was a high localization accuracy between the focus identified with IPM and the ablation site on the EAM. The inter-observer agreement was high for both VCM's. The IPM accuracy improved significantly when utilizing an inhomogeneous VCM.

The integration of this IPM technique with EAM systems may facilitate patient-specific catheter ablation strategies.

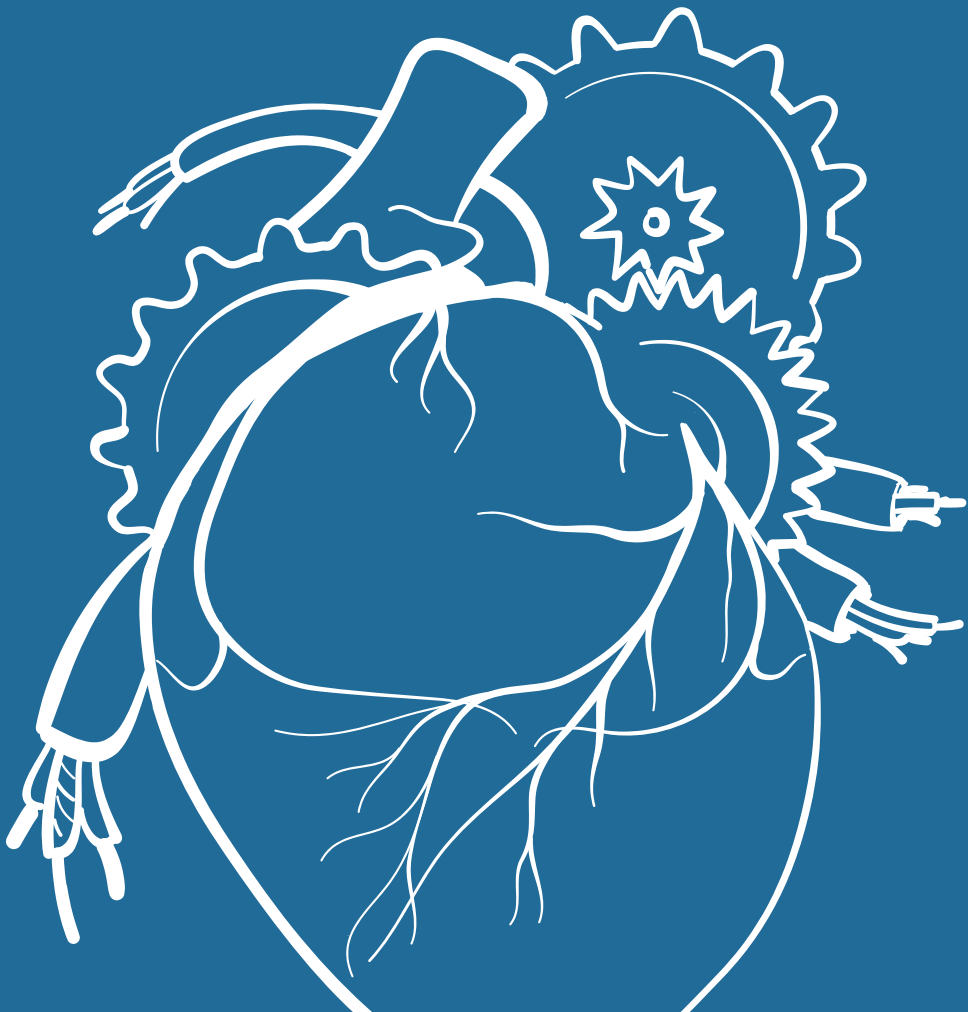
## REFERENCES

- 1 Ramanathan C, Ghanem RN, Jia P, Ryu K, Rudy Y. Noninvasive electrocardiographic imaging for cardiac electrophysiology and arrhythmia. *Nat Med.* 2004;10:422-428.
- 2 Jamil-Copley S, Bokan R, Kojodjojo P, Qureshi N, Koa-Wing M, Hayat S, Kyriacou A, Sandler B, Sohaib A, Wright I, Davies DW, Whinnett Z, Peters S, Kanagaratnam P, Lim PB. Noninvasive electrocardiographic mapping to guide ablation of outflow tract ventricular arrhythmias. *Heart Rhythm.* 2014;11:587-594.
- 3 Erkapic D, Greiss H, Pajitnev D, Zaltsberg S, Deubner N, Berkowitsch A, Mollman S, Sperzel J, Rolf A, Schmitt J, Hamm C, Kuniss M, Neumann T. Clinical impact of a novel three-dimensional electrocardiographic imaging for non-invasive mapping of ventricular arrhythmias-a prospective randomized trial. *Europace.* 2015;17:591-597.
- 4 Roguin A. *CardioPulse.* Radiation in cardiology: can't live without it! : using appropriate shielding, keeping a distance as safely as possible and reducing radiation time are essential principles for radiation reduction. *Eur Heart J.* 2014;35:599-600.
- 5 van Dam PM, Tung R, Shivkumar K, Laks M. Quantitative localization of premature ventricular contractions using myocardial activation ECGI from the standard 12-lead electrocardiogram. *J Electrocardiol.* 2013;46:574-579.
- 6 Cochet H, Dubois R, Sacher F, Derval N, Sermesant M, Hocini M, Montaudon M, Haissaguerre M, Laurent F, Jais P. Cardiac arrhythmias: multimodal assessment integrating body surface ECG mapping into cardiac imaging. *Radiology.* 2014;271:239-247.
- 7 Revishvili AS, Wissner E, Lebedev DS, Lemes C, Deiss S, Metzner A, Kalinin VV, Sopov OV, Labartkava EZ, Kalinin AV, Chmelevsky M, Zubarev SV, Chaykovskaya MK, Tsiklauri MG, Kuck KH. Validation of the mapping accuracy of a novel non-invasive epicardial and endocardial electrophysiology system. *Europace.* 2015. <http://dx.doi.org/10.1093/europace/euu339>
- 8 Bear LR, Cheng LK, LeGrice IJ, Sands GB, Lever NA, Paterson DJ, Smaill BH. The Forward Problem of Electrocardiography: Is it Solved? *Circ Arrhythm Electrophysiol.* 2015;8:677-684.
- 9 Marchandise E, Geuzaine C, Remacle JF. Cardiovascular and lung mesh generation based on centerlines. *Int J Numer Method Biomed Eng.* 2013;29:665-682.
- 10 Oostendorp T, Nenonen J, Korhonen P. Noninvasive determination of the activation sequence of the heart: application to patients with previous myocardial infarctions. *J Electrocardiol.* 2002;35 Suppl:75-80.
- 11 Sanchez-Quintana D, Cabrera JA, Farre J, Climent V, Anderson RH, Ho SY. Sinus node revisited in the era of electroanatomical mapping and catheter ablation. *Heart.* 2005;91:189-194.
- 12 Arisi G, Macchi E, Baruffi S, Spaggiari S, Taccardi B. Potential fields on the ventricular surface of the exposed dog heart during normal excitation. *Circ Res.* 1983;52:706-715.
- 13 Ramanathan C, Rudy Y. Electrocardiographic imaging: I. Effect of torso inhomogeneities on body surface electrocardiographic potentials. *J Cardiovasc Electrophysiol.* 2001;12:229-240.

- 14 Ramanathan C, Rudy Y. Electrocardiographic imaging: II. Effect of torso inhomogeneities on noninvasive reconstruction of epicardial potentials, electrograms, and isochrones. *J Cardiovasc Electrophysiol*. 2001;12:241-252.
- 15 van Oosterom A. A comparison of electrocardiographic imaging based on two source types. *Europace*. 2014;16 Suppl 4:iv120-iv128.
- 16 Andreu D, Berruezo A, Fernandez-Armenta J, Herczku C, Borrás R, Ortiz-Perez JT, Mont L, Brugada J. Displacement of the target ablation site and ventricles during premature ventricular contractions: relevance for radiofrequency catheter ablation. *Heart Rhythm*. 2012;9:1050-1057.
- 17 Zwanenburg JJM, Gotte MJW, Kuijjer JPA, Hofman MBM, Knaapen P, Heethaar RM, van Rossum AC, Marcus JT. Regional timing of myocardial shortening is related to prestretch from atrial contraction: assessment by high temporal resolution MRI tagging in humans. *Am J Physiol Heart Circ Physiol*. 2005;288:H787-H794.
- 18 ter Keurs HE, Rijnsburger WH, van Heuningen R, Nagelsmit MJ. Tension development and sarcomere length in rat cardiac trabeculae. Evidence of length-dependent activation. *Circ Res*. 1980;46:703-714.



# 11



# GENERAL DISCUSSION

---



This thesis was focused on designing novel strategies for the assessment of the arrhythmogenic substrate of atrial fibrillation (AF) and idiopathic ventricular tachycardia. Firstly, the drawbacks of the currently utilized techniques were evaluated. For AF this encompassed the evaluation of the workup strategy using the key non-invasive imaging modalities. In idiopathic ventricular tachycardia both the invasive and non-invasive electrical assessment were compared.

The identified shortcomings were addressed by designing and validating new imaging methods. This chapter will discuss the outcomes of this thesis and provide future research perspectives.

## **IMAGING BASED SUBSTRATE ANALYSIS IN ATRIAL FIBRILLATION**

Various non-invasive imaging modalities, including transthoracic echocardiography, trans-esophageal echocardiography, computed tomography and cardiac magnetic resonance (CMR) are currently employed in the treatment strategy of AF<sup>1-4</sup>. All these techniques have their advantages and limitations, and due to a different gold standard for each step in the workup, a multimodality approach is advocated in the daily practice<sup>1,5</sup>.

An increasing demand for catheter ablation procedures has resulted in electrophysiology centers with high volume practices, necessitating an optimization of the existing work-up. Moreover, ongoing technological developments have increased the capability of the individual techniques and permit a single modality approach that can supply consistent and uniform imaging data, applicable during the workup, guidance and evaluation of ablation procedures<sup>6,7</sup>.

Today, the most promising modality seems to be cardiac magnetic resonance imaging as its ability to visualize anatomy combined with information about tissue characteristics enable a detailed workup to be performed. However, it is the least frequently used due to time constraints and restrictions for some patient groups.

### **Optimized CMR based workflow**

To improve the usability of CMR, a standardized CMR based workflow for patient selection and procedural guidance for AF ablation was designed. The clinical utility and feasibility of this workflow was investigated by evaluating:

- (1) The ability to assess for left atrial appendage thrombus, left atrial (LA) volume and sphericity

- (2) The capability to facilitate procedural guidance by fusion of CMR-derived LA models with the electro-anatomical mapping (EAM) system, and
- (3) The correlation between sites of ablation and scar localization on the LA model.

It was observed that a comprehensive CMR protocol, consisting of commercially available sequences, can be completed in less than 40 minutes ( $36 \pm 3$  minutes) with post-processing of this information requiring  $2.8 \pm 0.8$  minutes. Further analysis of the LA volume and sphericity could be performed using an open source tool without any further post-processing actions. In addition, integration with the EAM could also be performed instantaneously by importing the post-processing results to the EAM system.

The gaps identified using late gadolinium enhanced-CMR (LGE-CMR) demonstrated a high correlation with the invasively measured sites of reconnection. However, not all LGE-CMR gaps showed electrical reconnection. Although previous investigations have mentioned non-conducting gaps,<sup>8,9</sup> no study has yet characterized the temporal electrical course of these gaps.

Certain groups of patients develop AF recurrences after the ablation procedure. Therefore, it may be hypothesized that such electrically dormant gaps may demonstrate reconnection in the long-term. In such case, these gaps should be considered a potential ablation site during the redo-procedure.

### **Tissue characteristics**

The outcome of the previous investigations with regard to scar-maps warrants further study towards the identification of a strategy to differentiate between electrically dormant gaps and gaps associated with the recurrence of AF.

To this extent, all available algorithms for scar analysis needed to be evaluated as it is not clear how they compare or perform relative to one another. Furthermore, algorithms have only been tested on center- and vendor-specific images. The translation of such algorithms into the clinical environment thus remains challenging. Benchmarking frameworks, providing a common dataset and evaluation strategies, are important for clinical translation of these algorithms. A benchmarking framework was constructed to provide thirty datasets, with fifteen datasets in each cohort: patient and porcine. Datasets in the two separate cohorts were acquired using different scanner vendors and field strength (1.5T and 3T), resolutions and acquisition protocols (2D and 3D). The ground truth is often absent in such datasets, and to this end, the framework provides with a powerful expert observers' consensus ground truth. The proposed framework

remains publicly available for accessing the image database, uploading segmentations for evaluation and contributing manual segmentations for improving the consensus ground truth on the datasets.

### **Left atrial geometry**

Preliminary results of left atrial sphericity (LASP) from the previous study showed that all patients undergoing an index procedure had a lower sphericity of  $77 \pm 4$  when compared to  $85 \pm 3$  in patients undergoing a redo ablation. This was associated with a high AF recurrence and was considered indicative of advanced structural remodeling and rate. These findings lead to a study where the impact of LA geometrical remodeling, expressed as sphericity, and maintenance of sinus rhythm after repeat pulmonary vein isolation was investigated.

The results showed a strong relation between the pattern of LA geometrical remodeling and the outcome of a repeat ablation procedure. The post-procedural *change* in the left atrial geometry, calculated as the difference between pre-procedural LASP and post-procedural LASP, was significantly associated with AF recurrence ( $p < 0.001$ ). Patients with AF recurrence following the redo ablation ( $n=14$ ) showed an increase of the LASP (negative remodeling) after the index procedure. Eleven patients had a reduction of LASP (positive remodeling) after the index ablation and were all free from AF recurrence following the repeat ablation.

This association was independent of volumetric remodeling as both pre- and post-index procedural LA volume index demonstrated no correlation with post-procedural AF recurrence. In addition, conventional clinical parameters such as the nature of AF were not correlated with changes in the LASP as both negative and positive geometrical changes were observed in paroxysmal as well as persistent AF patients.

### **Clinical implications**

A single modality, CMR based imaging workflow was proven clinically feasible, and suitable to perform patient selection and procedural guidance of AF ablation. The results indicate that procedural efficacy of repeat ablation procedure may be improved by:

1. Incorporating LA sphericity as a stratification criteria during AF ablation workup
2. A scar-map guided (patient-specific) ablation strategy for targeted gap ablation

A larger prospective study to investigate the cost-efficiency and clinical efficacy of this workup and stratification approach is currently being planned and would support the rationale for routine clinical use.

### **Future perspectives**

Interventional CMR (iCMR) is an emerging technology and is assigned an important role in the field of Electrophysiology (EP) <sup>10</sup>. iCMR allows for integrated use of pre-procedural 3D anatomical scans to help guidance of active tracked catheters, peri-procedural interactive multi-planar visualization of relevant anatomy and visualization of the extent of ablation lesion as well as evaluation of complications. The therapeutic strategy incorporating this information could potentially improve the EP procedure by reducing procedural time and increasing (therapeutic) efficacy, including less redo procedures. An increasing number of iCMR guided EP procedures have been conducted over the past 5 years <sup>11-26</sup>.

So far, the limited number of (safety) studies conducted in humans have been successful and uncomplicated. However, there are still a few major challenges to overcome prior to performing complex ablation procedures in the MRI environment; 1) MRI compatible equipment (12 lead ECG, catheters and ablation systems) with regulatory approval is needed, and 2) emergency strategies especially regarding defibrillation inside the MRI have to be established. The coming years should be targeted at resolving these issues in order to expedite the clinical transition of ablation procedures towards iCMR. Finally, the complete integration of non-invasively obtained anatomical data with tissue characteristics and its electrical behavior will demonstrate the full strength of such an iCMR approach.

## **DESIGN AND VALIDATION OF AN INVERSE POTENTIAL MAPPING METHOD**

Non-invasive imaging of cardiac electrophysiology using inverse potential mapping (IPM) is considered a promising tool to complement conventional (invasive) electrophysiological study, despite challenges such as selecting appropriate source and volume conductor models and a continuing need for validation in humans. The second part of the research was focused on developing and evaluating a clinically applicable whole-heart workflow, integrating IPM and cardiac activation simulations.

The pilot study evaluating the IPM algorithm for reconstructing sinus rhythm, revealed the first point of atrial activation near the crista terminalis of the superior vena cave into the right atrium. The first point of ventricular epicardial breakthrough was located at the right ventricular free wall. These findings corresponded to the anatomically known location of the sinus node and where the moderator band attached to the ventricular myocardium<sup>27</sup>.

The use of MRI is unique and enables visualization and incorporation of tissue-characteristics in computational meshes. In addition, an integrated IPM and simulation based approach facilitates a comprehensive assessment of arrhythmias and underlying substrate. These two factors significantly contribute towards the clinical applicability of this workflow and offer a unique environment for the development and evaluation of patient tailored therapeutic strategies.

Subsequently, using this workflow, a comparison between the boundary element model (BEM) and finite element model (FEM) was performed. Body volume potential computation using the finite element model proved to be efficient if the number of bounding surfaces between organs taken into account was high. In addition, using the FEM rather than the BEM enabled the incorporation of different anisotropies, local tissue characteristics and sigma gradients over different regions. From a computational standpoint, computing a potential field by means of the FEM was not a problem. The computation time of a 240,000 points potential field was approximately 3 minutes. Graphics processors with hundreds of computation units combined with quad core main CPU's are becoming available at consumer prices. Generally available FEM packages are able to benefit from this just by setting some parameters and do not require custom coding. While the performance gains by computing the FEM in parallel may easily be tenfold.

The same workflow was utilized to investigate the optimal positioning of 62 torso electrodes for IPM. Computer simulations were used to gain insight and predict probable image quality of different electrode configurations and demonstrated that an anterior view of the epicardial potentials could be reconstructed at a high resolution using only 62 anterior electrodes with an inter-electrode distance of 20mm.

These findings demonstrate that the proposed FEM based whole-heart computational workflow offers an integrated platform for cardiac electrical assessment using IPM and simulations. The IPM algorithm can accurately reconstruct reliable cardiac activation

sequences from body surface potentials. The simulation model was able to incorporate patient-specific electrical parameters and rapidly perform whole-heart cardiac activation simulations.

Further clinical validation of this workflow was performed in patients undergoing catheter ablation of idiopathic right- and left- ventricular outflow tract (RVOT and LVOT) premature ventricular contractions (PVC). In addition to the validation of the IPM algorithm, the influence of tissue impedance on the results of IPM was studied using two different volume conductor models (VCM). A homogeneous thoracic VCM was compared to an inhomogeneous VCM where, in addition to thoracic impedance, the resistance value of the lungs was included.

In all cases, IPM located the ectopic focus in the correct cardiac compartment and identified all foci in close proximity to the ablation lesion (RVOT  $8.4 \pm 3$  mm,  $n=6$  and LVOT  $7.9 \pm 1.5$  mm,  $n=2$ ). The comparison performed in this study indicated a significant difference between homogeneous and inhomogeneous VCM, with the homogeneous VCM having a significantly higher localization error and failing to identify the focus in one RVOT case.

The current, most frequently utilized BSPM technique (ECVUE™) uses a homogeneous torso conductor model. The clinical utility of this method has been demonstrated after extensive investigation<sup>28,29</sup>. However, recent research advocates the integration of the various organs with their own specific impedance<sup>30,31</sup>. This may especially be the case in patients with a high body surface area, pulmonary edema or myocardial infarction. These circumstances could substantially influence the BSP's due to altered conductivity and resistivity conditions. These results suggested that although it is possible to perform IPM using a homogeneous VCM, an inhomogeneous VCM provides more accurate results.

### **Clinical implications**

This proposed combined IPM and MRI strategy offers the prospect to study the electrical activation in relation to tissue characteristics for complex (supra-)ventricular tachycardia's and scar based arrhythmias with clinically relevant accuracy.

The design of the computational model allows for instantaneous integration of patient-specific characteristics such as tissue properties and its associated conductivity. These tissue properties can be easily obtained using MRI. Integration of these characteristics will enable the operator to provide more patient tailored therapy.

### **Future perspectives**

Inverse potential mapping and simulations of cardiac activation are promising computational techniques for non-invasive assessment of rhythm disorders. Utilizing these tools for guidance of catheter ablation improves the procedural accuracy when compared to ablation using conventional mapping procedures. The computational model designed and investigated in this thesis, has been designed in a way that allows for instantaneous integration of patient-specific characteristics such as tissue properties (obtained using CMR). This integrated model offers the prospect to study the electrical activation in relation to tissue characteristics for complex (supra-)ventricular tachycardia and scar based arrhythmias.

However, despite this drastic improvement in the possibilities to provide patient tailored therapy, there still remain factors that can cause discrepancies in the results of inverse potential mapping. In addition to the spatial displacement related to the movement of the ablation catheter, these include image misregistration due to patient respiration, inaccurate cardiac geometry due to image acquisition during different phases of the cardiac cycle and substantial regional variations in cardiac displacement during contraction and relaxation (ranging between 5-25 mm)<sup>32,33</sup>. Especially the base of the heart moves 20 mm or more towards the apex.

As this proposed model already utilizes CMR for the creation of the volume conductor model, future research should attempt to increase the accuracy of the inverse solution by incorporating movement correction and contractility related parameters derived from CINE images.



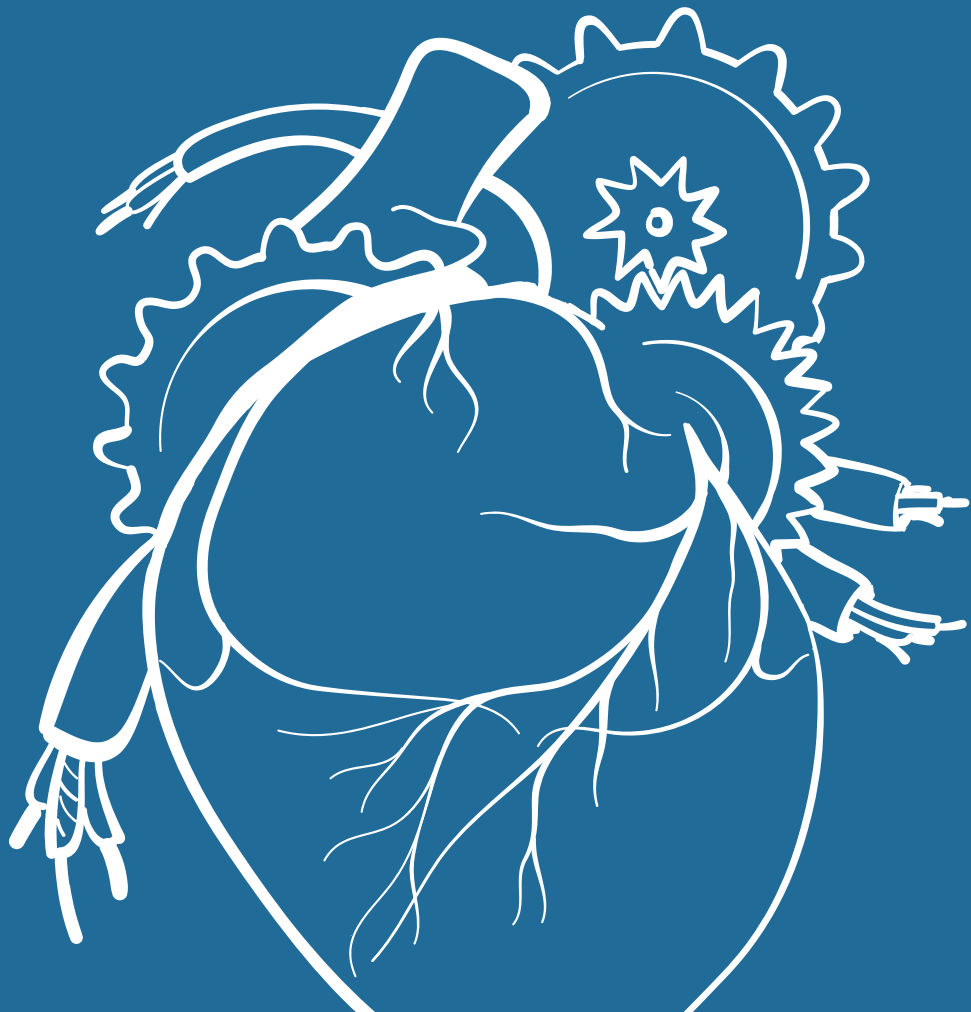
## REFERENCES

- 1 Tops LF, Schalij MJ, Bax JJ. Imaging and atrial fibrillation: the role of multimodality imaging in patient evaluation and management of atrial fibrillation. *Eur Heart J* 2010;31:542-551.
- 2 Blomstrom LC, Auricchio A, Brugada J et al. The use of imaging for electrophysiological and devices procedures: a report from the first European Heart Rhythm Association Policy Conference, jointly organized with the European Association of Cardiovascular Imaging (EACVI), the Council of Cardiovascular Imaging and the European Society of Cardiac Radiology. *Europace* 2013;15:927-936.
- 3 Camm AJ, Kirchhof P, Lip GY et al. Guidelines for the management of atrial fibrillation: the Task Force for the Management of Atrial Fibrillation of the European Society of Cardiology (ESC). *Eur Heart J* 2010;31:2369-2429.
- 4 Fuster V, Ryden LE, Cannom DS et al. 2011 ACCF/AHA/HRS focused updates incorporated into the ACC/AHA/ESC 2006 guidelines for the management of patients with atrial fibrillation: a report of the American College of Cardiology Foundation/American Heart Association Task Force on practice guidelines. *Circulation* 2011;123:e269-e367.
- 5 Calkins H, Kuck KH, Cappato R et al. 2012 HRS/EHRA/ECAS Expert Consensus Statement on Catheter and Surgical Ablation of Atrial Fibrillation: recommendations for patient selection, procedural techniques, patient management and follow-up, definitions, endpoints, and research trial design. *Europace* 2012;14:528-606.
- 6 Della BP, Fassini G, Cireddu M et al. Image integration-guided catheter ablation of atrial fibrillation: a prospective randomized study. *J Cardiovasc Electrophysiol* 2009;20:258-265.
- 7 Bertaglia E, Bella PD, Tondo C et al. Image integration increases efficacy of paroxysmal atrial fibrillation catheter ablation: results from the CartoMerge Italian Registry. *Europace* 2009;11:1004-1010.
- 8 Spragg DD, Khurram I, Zimmerman SL et al. Initial experience with magnetic resonance imaging of atrial scar and co-registration with electroanatomic voltage mapping during atrial fibrillation: success and limitations. *Heart Rhythm* 2012;9:2003-2009.
- 9 Hunter RJ, Jones DA, Boubertakh R et al. Diagnostic accuracy of cardiac magnetic resonance imaging in the detection and characterization of left atrial catheter ablation lesions: a multicenter experience. *J Cardiovasc Electrophysiol* 2013;24:396-403.
- 10 Bhagirath P, van der Graaf M, Karim R et al. Interventional cardiac magnetic resonance imaging in electrophysiology: advances toward clinical translation.
- 11 Nazarian S, Kollandaivelu A, Zviman MM et al. Feasibility of real-time magnetic resonance imaging for catheter guidance in electrophysiology studies. *Circulation* 2008;118:223-229.
- 12 Dukkipati SR, Mallozzi R, Schmidt EJ et al. Electroanatomic mapping of the left ventricle in a porcine model of chronic myocardial infarction with magnetic resonance-based catheter tracking. *Circulation* 2008;118:853-862.

- 13 Schmidt EJ, Mallozzi RP, Thiagalingam A et al. Electroanatomic mapping and radiofrequency ablation of porcine left atria and atrioventricular nodes using magnetic resonance catheter tracking. *Circ Arrhythm Electrophysiol* 2009;2:695-704.
- 14 Nordbeck P, Bauer WR, Fidler F et al. Feasibility of real-time MRI with a novel carbon catheter for interventional electrophysiology. *Circ Arrhythm Electrophysiol* 2009;2:258-267.
- 15 Hoffmann BA, Koops A, Rostock T et al. Interactive real-time mapping and catheter ablation of the cavotricuspid isthmus guided by magnetic resonance imaging in a porcine model. *Eur Heart J* 2010;31:450-456.
- 16 Nordbeck P, Hiller KH, Fidler F et al. Feasibility of contrast-enhanced and nonenhanced MRI for intraprocedural and postprocedural lesion visualization in interventional electrophysiology: animal studies and early delineation of isthmus ablation lesions in patients with typical atrial flutter. *Circ Cardiovasc Imaging* 2011;4:282-294.
- 17 Eitel C, Piorkowski C, Hindricks G, Gutberlet M. Electrophysiology study guided by real-time magnetic resonance imaging. *Eur Heart J* 2012;33:1975.
- 18 Vergara GR, Vijayakumar S, Kholmovski EG et al. Real-time magnetic resonance imaging-guided radiofrequency atrial ablation and visualization of lesion formation at 3 Tesla. *Heart Rhythm* 2011;8:295-303.
- 19 Ranjan R, Kholmovski EG, Blauer J et al. Identification and acute targeting of gaps in atrial ablation lesion sets using a real-time magnetic resonance imaging system. *Circ Arrhythm Electrophysiol* 2012;5:1130-1135.
- 20 Ganesan AN, Selvanayagam JB, Mahajan R et al. Mapping and ablation of the pulmonary veins and cavo-tricuspid isthmus with a magnetic resonance imaging-compatible externally irrigated ablation catheter and integrated electrophysiology system. *Circ Arrhythm Electrophysiol* 2012;5:1136-1142.
- 21 Nordbeck P, Beer M, Kostler H et al. Cardiac catheter ablation under real-time magnetic resonance guidance. *Eur Heart J* 2012;33:1977.
- 22 Sommer P, Grothoff M, Eitel C et al. Feasibility of real-time magnetic resonance imaging-guided electrophysiology studies in humans. *Europace* 2013;15:101-108.
- 23 Nordbeck P, Quick HH, Ladd ME, Ritter O. Real-time magnetic resonance guidance of interventional electrophysiology procedures with passive catheter visualization and tracking. *Heart Rhythm* 2013;10:938-939.
- 24 Gaspar T, Piorkowski C, Gutberlet M, Hindricks G. Three-dimensional real-time MRI-guided intracardiac catheter navigation. *European Heart Journal* 2014;35:589.
- 25 Piorkowski C, Grothoff M, Gaspar T et al. Cavotricuspid isthmus ablation guided by real-time magnetic resonance imaging. *Circ Arrhythm Electrophysiol* 2013;6:e7-10.
- 26 Grothoff M, Piorkowski C, Eitel C et al. MR Imaging-guided Electrophysiological Ablation Studies in Humans with Passive Catheter Tracking: Initial Results. *Radiology* 2014;271:695-702.

- 27 Sanchez-Quintana D, Cabrera JA, Farre J, Climent V, Anderson RH, Ho SY. Sinus node revisited in the era of electroanatomical mapping and catheter ablation. *Heart* 2005;91:189-194.
- 28 Ramanathan C, Rudy Y. Electrocardiographic imaging: I. Effect of torso inhomogeneities on body surface electrocardiographic potentials. *J Cardiovasc Electrophysiol* 2001;12:229-240.
- 29 Ramanathan C, Rudy Y. Electrocardiographic imaging: II. Effect of torso inhomogeneities on noninvasive reconstruction of epicardial potentials, electrograms, and isochrones. *J Cardiovasc Electrophysiol* 2001;12:241-252.
- 30 van Oosterom A. A comparison of electrocardiographic imaging based on two source types. *Europace* 2014;16 Suppl 4:iv120-iv128.
- 31 Bear LR, Cheng LK, LeGrice IJ et al. The Forward Problem of Electrocardiography: Is it Solved? *Circ Arrhythm Electrophysiol* 2015.
- 32 Zwanenburg JJM, Gotte MJW, Kuijjer JPA et al. Regional timing of myocardial shortening is related to prestretch from atrial contraction: assessment by high temporal resolution MRI tagging in humans. *Am J Physiol Heart Circ Physiol* 2005;288:H787-H794.
- 33 ter Keurs HE, Rijnsburger WH, van Heuningen R, Nagelsmit MJ. Tension development and sarcomere length in rat cardiac trabeculae. Evidence of length-dependent activation. *Circ Res* 1980;46:703-714.





# APPENDICES

---

Summary  
Samenvatting  
Dankwoord  
Curriculum vitae  
List of publications



## SUMMARY

In the present thesis, we studied the role of imaging modalities in characterizing arrhythmogenic substrate.

In **Chapter 1** the scope of the thesis and current challenges in electrophysiology are addressed. Recent technological developments have provided new ways to improve our knowledge about the arrhythmogenic substrate.

- Cardiac magnetic resonance (CMR) can provide a comprehensive non-invasive analysis of the cardiac geometry, function and tissue characteristics.
- Inverse potential mapping (IPM) can reconstruct cardiac surface potentials from body surface potentials, allowing for a non-invasive electrophysiological study to be performed in an out-patient setting.

Experiences gained using these techniques can prove critical for developing more effective ablation strategies.

In **Chapter 2** we provided a summary of the application of cardiac imaging for pulmonary vein and left atrial ablation divided in stages. A pre-procedural stage (assessment of left atrial dimensions, left atrial appendage thrombus and pulmonary vein anatomy), peri-procedural stage (integration of anatomical and electrical information) and post-procedural (evaluation of efficacy by assessment of tissue properties) stage. CMR was found to be comparable to the other key imaging modalities, providing all the information during a single examination, in a safe and reproducible manner.

In **Chapter 3** we described a benchmarking evaluation framework for quantifying late gadolinium enhancement images. Six widely-used fixed-thresholding methods and five recently developed algorithms were compared. Results demonstrated that the algorithms have better overlap with the consensus ground truth than most of the fixed-thresholding methods, with the exception of the Full-Width-at-Half-Maximum fixed-thresholding method. As infarct quantification is an important assessment criterion for many cardiac therapies, it is advisable to compare new algorithms using the proposed benchmark prior to clinical implementation.

In **Chapter 4** we investigated the feasibility and clinical applicability of a standardized CMR based workup for atrial fibrillation (AF) ablation. The acquisition using commercially available sequences and post-processing of the CMR images with open-source software was possible in less than 45 minutes. Although not all discontinuous regions of scar showed electrical activity, the majority of the invasively measured electrical gaps

correlated with viable myocardium on the scar-map. These findings suggested that a CMR based workflow is feasible and clinically usable to perform a detailed study of the left atrial (LA) geometrical and structural changes using a single examination. Clinical application of this workflow could significantly improve patient selection and procedural guidance of (redo-) AF ablation.

In **Chapter 5** we studied the effect of LA geometrical changes (sphericity), following the index ablation of AF, on the outcome of redo-ablation procedures. All patients with a reduction of sphericity following the index ablation were free from AF following the redo-ablation, whereas all patients with an increased sphericity, had recurrence of AF. These results suggest that selection for redo-ablation can be improved by including LA sphericity as a stratification factor.

In **Chapter 6** we examined the requirements and clinical feasibility of a dedicated interventional CMR (iCMR) suite for EP procedures. First, the limitations of current EP procedures and ablation strategies are analyzed and the advantages of an iCMR suite were discussed. Second, the clinical feasibility was examined by presenting the current challenges of working in an MRI environment. Safety, imaging and device related aspects were also reviewed. Finally, the requirement for implementing an iCMR suite and the current state of their development was addressed.

In **Chapter 7** we proposed a clinically applicable, integrated whole-heart computational workflow for non-invasive, in-vivo assessment of electrical activation using IPM and cardiac activation simulations. In contrast to currently available methods, the presented work-flow performed an integrated evaluation of inverse potential mapping and cardiac activation simulations, allowing for a comprehensive clinical study of whole-heart electrical interaction. When integrated with tissue characteristics as provided by cardiac MRI, this workflow provided a realistic, patient-specific model for electrical modeling.

In **Chapter 8** the feasibility and relevance of computing body volume potentials (BVP) for IPM was investigated using a rectangular tank filled with an electrolytic conductor and a patient specific 3D model. Efficient generation of high quality volume meshes and computation of BVP with a resolution of 5 mm was found feasible. This allowed incorporation of different anisotropies, local tissue characteristics and sigma gradients over different regions which could improve understanding of the genesis of body surface potentials and sources of local inaccuracies.

In **Chapter 9** we investigated the possibility of deriving information on the epicardial potentials using only 62 torso electrodes without the aid of a-priori models. Various electrode configuration simulations were used to gain insight and predict probable image quality of different electrode configurations. Application of 62 anterior electrodes with an inter-electrode distance of 20mm enabled reconstruction of an anterior view of the epicardial potentials in the absence of an a-priori model. By increasing the total number of recording electrodes, information on the posterior area of the heart can also be reconstructed using this super-concentrated electrode configuration.

In **Chapter 10** the IPM workflow was clinically validated in patients undergoing catheter ablation of idiopathic ventricular tachycardia (VT). It was found that using this MRI based IPM method it was possible to estimate the VT focus location with clinically sufficient accuracy using body surface potentials of a single ectopic beat. In addition, a comparison between two independent observers demonstrated an almost perfect reproducibility of the results. The comparison between the homogeneous and inhomogeneous volume conductor models (VCM) indicated a significant difference in favor of the inhomogeneous VCM.

In **Chapter 11** the main findings of this thesis are summarized and put in clinical perspective.





## SAMENVATTING

In dit proefschrift hebben wij de rol van beeldvormende modaliteiten onderzocht in het karakteriseren van aritmogeen substraat.

In **hoofdstuk 1** wordt de strekking van het proefschrift en de huidige uitdagingen binnen de elektrofysiologie beschreven. Recente technologische ontwikkelingen hebben ons nieuwe manieren verstrekt om onze kennis over het aritmogene substraat te verbeteren.

- Cardiale magnetische resonantie (CMR) kan voorzien in een volledig niet-invasieve analyse van de cardiale geometrie, functie en weefseigenschappen.
- Inverse potential mapping (IPM) kan gebruikt worden om het cardiale oppervlaktepotential te reconstrueren vanuit lichaamsoppervlak potentialen, waardoor een niet-invasief elektrofysiologisch onderzoek kan worden uitgevoerd in een poliklinische omgeving.

Ervaringen die zijn opgedaan met behulp van deze technieken kunnen van belang zijn voor de ontwikkeling van effectievere ablatie strategieën.

In **hoofdstuk 2** wordt een overzicht gegeven van de toepassingen van cardiale beeldvorming voor longvene ablatie verdeeld in 3 fasen. Pre-ablatie (beoordeling van linker atrium dimensies, linker hartoor trombus en anatomie van de pulmonaalvene), peri-procedureel (integratie van anatomische en elektrische informatie) en post-procedureel (beoordeling van weefseigenschappen). CMR bleek vergelijkbaar met de andere beeldvormingsmodaliteiten en was in staat alle benodigde informatie op een veilige en reproduceerbare wijze te verkrijgen met slechts één onderzoek.

In **hoofdstuk 3** werd een benchmarking evaluation framework opgesteld voor het kwantificeren van late gadolinium enhancement beelden. Zes veelgebruikte fixed-thresholding methoden en vijf recent ontwikkelde algoritmen werden vergeleken. Resultaten toonden aan dat, met uitzondering van de Full-Width-at-Half-Maximum fixed-thresholding method, de algoritmen een betere overlap hadden met de consensus ground truth dan de meeste fixed-thresholding methoden. Gezien het belang van scar kwantificatie als een belangrijk beoordelingscriterium voor vele therapieën, is het raadzaam om nieuwe algoritmen voorafgaand aan de klinische implementatie te vergelijken met deze benchmark.



In **hoofdstuk 4** werd de haalbaarheid en klinische toepasbaarheid van een gestandaardiseerde, CMR gebaseerde workup voor atriumfibrilleren (AF) ablatie onderzocht. Acquisitie en post-processing van de CMR-beelden waren mogelijk in minder dan 45 minuten met commercieel verkrijgbare sequenties en open-source software. Hoewel niet alle discontinue littekengebieden elektrische activiteit vertoonden, correleerde de meerderheid van de invasief gemeten elektrische gaps met viabel myocard op de scar-map. Deze bevindingen suggereren dat een CMR gebaseerde workflow klinisch bruikbaar is om een gedetailleerd beeld te krijgen van de geometrie en structurele veranderingen van het linker atrium (LA). Deze workflow kan de patiënten selectie en procedurele begeleiding van (redo-) AF-ablaties aanzienlijk verbeteren.

In **hoofdstuk 5** werd het effect bestudeerd van geometrische veranderingen van het LA (sphericity), na index ablatie van AF, op het resultaat van redo-ablatie procedures. Alle patiënten met een verminderde sphericity na index ablatie waren vrij van AF na de redo-ablatie, terwijl alle patiënten met een verhoogde sphericity een recidief kregen. Deze resultaten suggereren dat selectie voor redo-ablatie kan worden verbeterd door LA sphericity te incorporeren als een stratificatie parameter.

In **hoofdstuk 6** werden de vereisten en klinische haalbaarheid van een speciaal voor EP-procedures bestemde interventie-CMR (iCMR) suite beschreven. Als eerste werden de beperkingen van de huidige EP-procedures en ablatie strategieën geanalyseerd en werden de voordelen van een iCMR suite besproken. Als tweede werd de klinische haalbaarheid onderzocht door de huidige uitdagingen van het werken in een MRI-omgeving in kaart te brengen. Veiligheid, imaging en device gerelateerde aspecten werden ook besproken. Ten slotte werden de vereisten voor de implementatie van een iCMR suite en de huidige stand van ontwikkeling geadresseerd.

In **hoofdstuk 7** werd een klinisch toepasbaar, geïntegreerd whole-heart computational workflow beschreven voor niet-invasieve, in-vivo bepaling van elektrische activatie via IPM en cardiale simulaties. In tegenstelling tot de huidige beschikbare methoden, integreert de voorgestelde work-flow inverse potential mapping en cardiale activatie simulaties waardoor een gedegen onderzoek mogelijk is van de whole-heart elektrische interactie. Wanneer weefsel karakteristieken, bepaald met behulp van cardiale MRI, werden toegevoegd aan deze workflow ontstond een realistisch, patiënt-specifiek model geschikt voor elektrische modellering.

In **hoofdstuk 8** werd de haalbaarheid en klinische relevantie van het berekenen van body volume potentials (BVP) voor IPM onderzocht. Dit werd gedaan met behulp van een rechthoekige tank gevuld met een elektrolytische geleider en een patiënt-

specifiek 3D-model. Het was mogelijk om efficiënt een hoogwaardige volume mesh te genereren en BVP te berekenen met een resolutie van 5 mm. Hierdoor was het mogelijk om verschillende anisotropie waarden, weefsel karakteristieken en sigma gradiënten te integreren die ons begrip over het ontstaan van potentiaal verdelingen op het lichaamsoppervlak en over bronnen van lokale onnauwkeurigheden kunnen verbeteren.

In **hoofdstuk 9** is de mogelijkheid onderzocht tot het verkrijgen van informatie over epicardiale potentialen met alleen 62 torso elektroden en zonder hulp van een a-priori model. Simulaties werden toegepast om inzicht te verkrijgen en de beeldkwaliteit van verschillende elektrodeconfiguraties te voorspellen. Hiermee bleek het mogelijk in afwezigheid van een a-priori model de anterieure epicardiaal potentiaal verdeling te reconstrueren met 62 elektroden (onderlinge elektrodeafstand 20 mm). Door het totaal aantal elektroden te vermeerderen zou ook informatie over het posterieure gedeelte van het hart gereconstrueerd kunnen worden met behulp van deze supergeconcentreerde elektrodeconfiguratie.

In **hoofdstuk 10** werd de klinische validatie verricht van de inverse potential mapping (IPM) workflow bij patiënten die een katheterablatie ondergingen voor idiopathische ventriculaire tachycardie (VT). Gebruik makend van body surface potentials van één ectopische slag kon deze MRI gebaseerde IPM methode de focus van de VT inschatten met een klinisch relevante nauwkeurigheid. Vergelijking tussen twee onafhankelijke waarnemers toonde een bijna perfecte reproduceerbaarheid van de resultaten. Vergelijking tussen de homogene en niet-homogene volume geleidingsmodellen (VCM) wees op een significant verschil ten voordele van de inhomogene VCM.

In **hoofdstuk 11** zijn de belangrijkste bevindingen van deze proefschrift samengevat en in klinisch perspectief geplaatst.





## LIST OF PUBLICATIONS

**Integrated whole-heart computational workflow for inverse potential mapping and personalized simulations.** Bhagirath P, van der Graaf AW, de Hooge J, de Groot NM, Götte MJ. *J Transl Med.* 2016 May 25.

**MR feature tracking in patients with MRI-conditional pacing systems: The impact of pacing.** van der Graaf AW, Bhagirath P, Scheffer MG, de Medina RR, Götte MJ. *J Magn Reson Imaging.* 2016 Mar 17.

**Evaluation of state-of-the-art segmentation algorithms for left ventricle infarct from late Gadolinium enhancement MR images.** Karim R, Bhagirath P, Claus P, Housden RJ, Chen Z, Karimaghaloo Z, Sohn HM, Lara Rodríguez L, Vera S, Albà X, Hennemuth A, Peitgen HO, Arbel T, González Ballester MA, Frangi AF, Götte M, Razavi R, Schaeffter T, Rhode K.. *Med Image Anal.* 2016 May.

**Feasibility and Accuracy of Cardiac Magnetic Resonance Imaging-Based Whole-Heart Inverse Potential Mapping of Sinus Rhythm and Idiopathic Ventricular Foci.** Bhagirath P, van der Graaf M, van Dongen E, de Hooge J, van Driel V, Ramanna H, de Groot N, Götte MJ. *J Am Heart Assoc.* 2015 Oct 14;4(10). pii: e002222. doi: 10.1161/JAHA.115.002222..

**Non-invasive focus localization, right ventricular epicardial potential mapping in patients with an MRI-conditional pacemaker system - a pilot study.** van der Graaf AW, Bhagirath P, de Hooge J, Ramanna H, van Driel VJ, de Groot NM, Götte MJ. *J Interv Card Electrophysiol.* 2015 Dec;44(3):227-34. doi: 10.1007/s10840-015-0054-9. Epub 2015 Sep 14.

**A priori model independent inverse potential mapping: the impact of electrode positioning.** van der Graaf AW, Bhagirath P, de Hooge J, de Groot NM, Götte MJ. *Clin Res Cardiol.* 2015 Jul 28.

**Interventional cardiac magnetic resonance imaging in electrophysiology: advances toward clinical translation.** Bhagirath P, van der Graaf M, Karim R, Rhode K, Piorkowski C, Razavi R, Schwitter J, Götte M.. *Circ Arrhythm Electrophysiol.* 2015 Feb;8(1):203-11. doi: 10.1161/CIRCEP.114.002371.

**Cardiac magnetic resonance imaging: artefacts for clinicians.** van der Graaf AW, Bhagirath P, Ghoerbiën S, Götte MJ. *Neth Heart J.* 2014 Dec;22(12):542-9. doi: 10.1007/s12471-014-0623-z.

**Computing Volume Potentials for Noninvasive Imaging of Cardiac Excitation.** van der Graaf AW, Bhagirath P, van Driel VJ, Ramanna H, de Hooge J, de Groot NM, Götte MJ. *Ann Noninvasive Electrocardiol.* 2014 Jul 17. doi: 10.1111/anec.12183.

**Multimodality imaging for patient evaluation and guidance of catheter ablation for atrial fibrillation - current status and future perspective.** Bhagirath P, van der Graaf AW, Karim R, van Driel VJ, Ramanna H, Rhode KS, de Groot NM, Götte MJ. *Int J Cardiol.* 2014 Aug 20;175(3):400-8. doi: 10.1016/j.ijcard.2014.06.047.

**MRI and cardiac implantable electronic devices; current status and required safety conditions.** van der Graaf AW, Bhagirath P, Götte MJ. *Neth Heart J.* 2014 Apr 15.

**Noninvasive imaging of cardiac excitation: current status and future perspective.** van der Graaf AW, Bhagirath P, Ramanna H, van Driel VJ, de Hooge J, de Groot NM, Götte MJ. *Ann Noninvasive Electrocardiol.* 2014 Mar;19(2):105-13. doi: 10.1111/anec.12140.

**Residual blood processing by centrifugation, cell salvage or ultrafiltration in cardiac surgery: effects on clinical hemostatic and ex-vivo rheological parameters.** Vonk AB, Muntajit W, Bhagirath P, van Barneveld LJ, Romijn JW, de Vroege R, Boer C. *Blood Coagul Fibrinolysis* 2012 Oct;23(7):622-8.

**Etiology and diagnosis of acute biliary pancreatitis.** van Geenen EJ, van der Peet DL, Bhagirath P, Mulder CJ, Bruno MJ. *Nat Rev Gastroenterol Hepatol.* 2010 Sep;7(9):495-502.

## CURRICULUM VITAE

Pranav Bhagirath was born on the 9<sup>th</sup> of November, 1985 in New Delhi, India.

### Qualifications

- 2017 – present    London School of Economics, London – England  
*Executive MSc Health Economics, Outcomes and Management in Cardiovascular Sciences*
- 2013                European Society of Cardiology (ESC), Florence – Italy  
*ESC certification for Cardiac MRI – Competency level 3*
- 2012                Haga Teaching Hospital, The Hague – The Netherlands  
*Good Clinical Practice certification*
- 2004 – 2011        Vrije Universiteit, Amsterdam – The Netherlands  
*Medicine*
- 1998 – 2004        Caland Lyceum, Amsterdam – The Netherlands  
*Higher studies*

### Work experience

- 2017 - present    Nictiz, The Hague – Netherlands  
*Researcher*  
Apprenticeship eHealth with focus 'Economic implications of eHealth and potential clinical models for implementation'. Supervisor: dr. L. van Gennip (director Nictiz).
- 2017 - present    Society for Cardiovascular Magnetic Resonance (SCMR)  
*Member Communication Committee*  
Responsible for effective utilization of the Society's means of communication.
- 2016 - present    Specialization training Cardiology  
*Specialist registrar*  
Internal Medicine in OLVG West (2 years). Chief trainers: dr. C.E.H. Siegert and dr. M.C. Weijmer.  
Extracurricular: Apprenticeship Management, focus 'e-Health' (1 year). Supervisor: dr. M.C. Weijmer.  
Extracurricular: Principal Investigator 'Influence of shunt-flow on cardiac contractility in hemodialysis patients' (1 year).

- 2015 - present Holy Family Hospital, New Delhi – India  
*Consultant Cardiac MRI*  
Responsible for implementing and maintaining a cardiac MRI service in a tertiary cardiac care center.
- 2014 - present Wiki Cardiovascular Magnetic Resonance (Wiki CMR)  
*Founder and President*  
Responsible for conceptualizing and development of an e-learning platform targeted at cardiac MRI. Organizing cardiac MRI training for residents and specialists.
- 2014 - present Society for Cardiovascular Magnetic Resonance (SCMR)  
*Associate editor*  
Responsible for evaluating and reviewing clinical cases.
- 2016 King's College, London – England  
*Clinical lead*  
MICCAI 2016: Left atrial wall thickness challenge.
- 2012–2016 HAGA Teaching Hospital, The Hague – The Netherlands  
*PhD student*  
Reading for a PhD in the Cardiology department. Topic: Design and clinical validation of novel imaging strategies for analysis of arrhythmogenic substrate.
- 2012 HAGA Teaching Hospital, The Hague – The Netherlands  
*Resident*  
Worked in the Cardiology department of a tertiary cardiac care center.
- 2011 - 2012 Medisch Centrum Haaglanden, The Hague – The Netherlands  
*Resident*  
Worked in the departments of Internal Medicine and Cardiology in a tertiary cardiac care center.
- 2008 Vrije Universiteit, Department of Anesthesiology  
*Researcher*  
Researched the reduction in homologous blood transfusions in patients who underwent a CABG operation.
- 2006 - 2008 Vrije Universiteit, Department of Molecular Cellbiology en Immunology  
*Teaching assistant*

## Presentations

- 2017           CMR Dagen (OLVG Amsterdam)  
*Course director*  
 Level 1 CMR cursus for Residents Cardiology.
- 2016           Heart Rhythm Society  
*Poster presentation*  
 1. Relation between Left Ventricular Tissue Characteristics and Electrical Heterogeneity.  
 2. Electrophysiological Characteristics of Myocardial Sleeves in the Right Ventricular Outflow Tract - a High-Resolution Epicardial Mapping Study.
- 2015           Cardiac MRI Symposium (The Hague)  
*Oral presentation*  
 Case reading and protocol design.
- 2015           Nederlands Vereniging voor Cardiologie (NVVC)  
*Oral presentation*  
 Improving patient selection for AF ablation based on sphericity and strain.
- 2015           Netherlands Heart Rhythm Association (NHRA)  
*Oral presentation*  
 Left atrial geometry and volumetry - predictors of redo pulmonary vein isolation outcome.
- 2015           EHRA Europace-Cardiostim  
*Oral presentation*  
 MRI based inverse potential mapping of premature ventricular contractions.
- 2015           Society for Cardiovascular Magnetic Resonance (SCMR)  
*Poster presentation*  
 Cost and efficiency benefits of a single modality imaging strategy for pre-procedural workup of Atrial Fibrillation catheter ablation.
- 2014           Cardiac MRI Symposium (The Hague)  
*Oral presentation*  
 Evolution of Cardiac MRI for RV evaluation.

- 2014 Cardiovascular Research School Erasmus University Rotterdam (COEUR)  
*Oral presentation*  
Cardiac MRI and Body Surface Mapping to guide catheter ablation procedures.
- 2014 Asia Pacific Heart Rhythm Association (APHRs)  
*Oral presentation*  
Contrast enhanced MRI of the left atrium to identify electrical gaps - initial experience.
- 2014 AF Symposium (Boston-AF)  
*Poster presentation*  
Contrast enhanced MRI of the left atrium to identify electrical gaps - initial experience.
- 2013 Cardiac MRI Symposium (The Hague)  
*Oral presentation*  
Multimodality imaging – still a pre-requisite for ablation of Atrial Fibrillation?
- 2013 Netherlands Heart Rhythm Association (NHRA)  
*Oral presentation*  
Cardiac MRI guided redo catheter ablation of Atrial Fibrillation.

## DANKWOORD

Vanaf mijn tijd als geneeskunde student was het voor mij al duidelijk dat ik wetenschappelijk onderzoek wilde doen. Er was een drang om mijzelf te bewijzen en mijn kennis te verbreden. Na 2 onderzoekstrajecten waar ik als student-onderzoeker bij betrokken was, leek het krijgen van een promotie c.q. onderzoeksplek onmogelijk gezien mijn tekort aan 'klinische ervaring'.

Om deze lacunes te vullen begon ik in 2011 als ANIOS Cardiologie in het MCH Westeinde waar mijn interesse werd gewekt voor cardiale beeldvorming, in het bijzonder voor Cardiale MRI. Een half jaar later werd mij aangeraden door dr. Hemanth Ramanna om mijn zoektocht voor een onderzoekersplek voort te zetten bij de afdeling Cardiologie van het HAGA Ziekenhuis. Hier was dr. Marco Götte, een beeldvormend cardioloog met expertise in Cardiale MRI, bezig om een nieuwe onderzoekslijn op te zetten en was op zoek naar iemand met zowel klinische kennis als ervaring met programmeren en software ontwikkeling. Onze kennismakingsgesprek resulteerde in een aanbod vanuit hem om als promovendus aan de slag te gaan in een perifeer opleidingskliniek. Het resultaat hiervan is dit proefschrift.

Het was vanaf het begin duidelijk dat deze tijd een belangrijke bijdrage ging leveren aan mijn ontwikkeling als onderzoeker en clinicus. Ik had het niet voor mogelijk gehouden hoe dit mij als mens zou beïnvloeden, en ik heb getracht de opgedane ervaringen hieronder te beschrijven.



Geachte Prof. Dr. Zijlstra, beste Felix, wij hebben elkaar niet veel gesproken maar de keren dat ik tegenover je zat, heb ik veel geleerd waarvoor mijn dank.

Beste Marco, 'kompas en kapmes'. Dat waren de woorden die mij het meest bijbleven na onze eerste gesprek. Dat waren volgens jou de hulpmiddelen waar elke onderzoeker het mee moest doen. Gezien alle tijd die ik in en nabij de scanner heb doorbracht, ben ik blij dat dit een 'figure of speech' was anders was de term 'projectile effect' waarschijnlijk iets wat ik niet alleen van de boeken zou kennen. Mede door jouw coaching en vertrouwen in mijn capaciteiten heb ik mijzelf kunnen ontwikkelen tot zowel onderzoeker als klinisch beeldvormer. Bedankt voor al jouw steun en ik kijk er naar uit om onze samenwerking voort te zetten.

Beste Natasja, voor onze samenwerking was ik voornamelijk bezig geweest met non-invasieve technieken en het werken aan de epicardiale ventriculaire high-resolution mapping. Onder jouw leiding werd een nieuwe mijlpaal bereikt in mijn carrière als onderzoeker. Het ontwikkelen van onze eigen mapping scheme, interpretatie van de ventriculaire potentialen en uiteraard het schrijven van 3 abstracts voor het HRS in één dag (waarvan slechts 2 geaccepteerd waren) hebben mij ontzettend doen groeien. Vanwege het doorstromen naar de opleiding Cardiologie ben ik helaas maar kort in het Erasmus geweest, maar desondanks heb ik in deze korte tijd veel van jou geleerd, waarvoor ontzettend bedankt.

De leden van de beoordelingscommissie, prof. Ad Bogers (secretaris), prof. Frank Rademakers en dr. Cor Allaart ben ik erkentelijk voor het beoordelen van dit proefschrift.

Beste Maurits, 4 mooie jaren samen gewerkt aan het opzetten en uitvoeren van dit onderzoek, ons avontuur is bijna niet samen te vatten. Dankzij alle verhuizingen, van de oude echokamer waar wij af en toe plaats moesten maken voor dr. Delemarre tot onze kraak-hok in het tijdelijk gebouw, hebben wij het Haga ziekenhuis en elkaar goed leren kennen. Onze ambities sloten nauw op elkaar aan, onder andere af te leiden van de zoveelste scanzondag waarop wij (zoals gewoonlijk) teveel patiënten hadden gepland en weer eens de research programma deden uitlopen. Uit onze gezamenlijke passie en leergierigheid voor Cardiale MRI is een mooi initiatief voortgekomen in de vorm van de AIOS en Advanced cursussen en dit gaan wij de komende jaren verder opbouwen.

Beste Suresh, onze samenwerking was voor mij ontzettend leerzaam. Ik bewonder jou voor de energie en inspanning waarmee je, na een volle werkdag, nog research scans maakte tot middernacht en ik wil je bedanken voor alle tijd die je hebt geïnvesteerd om mijn MRI-kennis te verbeteren. Ik wil ook jouw familie bedanken voor de gastvrijheid

tijdens mijn zoveelste bezoek bij jou thuis om de scanprotocollen en mijn presentaties te bespreken. Jouw feedback op mijn manuscripten was ook erg leerzaam, al werd het op den duur enigszins verdacht hoe snel ik het stempel 'volledig en technisch correct' kreeg. Op onze trip naar New Orleans (SCMR) heb ik ontzettend veel geleerd van jou expertise op MRI en een aantal andere vakgebieden die buiten de scope gaan om hier te bespreken.

Beste Jacques, zonder jou was dit simpelweg niet gelukt. Waar ik meende te starten met een klinisch onderzoekstraject werd sinds jouw komst in onze team dit aangevuld met behoorlijke verdieping in de hogere wiskunde en natuurkunde. Gelukkig was je altijd beschikbaar voor een overleg ter verduidelijking van deze complexe materie. In combinatie met de blauwe-bak experimenten was het workflow artikel fundamenteel voor mijn begrip van de 'niet-klinische materie' en heeft de basis gevormd voor mijn begrip van de inverse methode. Naast de opgedane technische kennis ben ik ook blij te hebben genoten van de groovy jazz-tunes die je op je keyboard speelde om even een break te nemen van het segmenteren en troubleshooten.

De electrofysiologen van het HAGA Ziekenhuis, dr. Vincent van Driel en dr. Hemanth Ramanna. Ondanks de drukte op de HCK en de complexiteit van de ablatie procedures hebben jullie altijd de rust gehad en ervoor gezorgd dat mijn 'research wensen' zo goed als mogelijk werden gehonoreerd. Inclusie van poli patiënten, de uitgebreide 3D mapping en de extra pacing locaties maar ook überhaupt het ableren van een patiënt die met 65 radiopaque elektrodes op tafel lag was vaak een grote uitdaging en tijdsintensief. Jullie hebben mijn interesse voor EP doen oplaaien en ik ben vereerd om met zulke ervaren electrofysiologen te hebben mogen werken. Harry, Alex, ook jullie bedankt voor alle begeleiding achter de schermen op de HCK. De wonderere wereld van cardiale signalen is iets toegankelijker geworden met jullie uitleg en Fogoros. Ik hoop ooit samen met jullie op de HCK te staan en mijn kennis verder op te bouwen.

In de tweede fase van het onderzoek is er epicardiale mapping gedaan op de OK waarvoor ik onze cardio-thoracale chirurgen, dr. Arya Yazdanbakhsh en dr. Gerard Hoohekerk, wil bedanken voor het faciliteren hiervan en het enthousiasme waarmee de acquisities zijn verricht. Arya, vooral jou werkstijl en manier van omgang op OK is iets wat ik zou willen overnemen in mijn toekomstige carrière als medisch specialist.

Beste Annemiek, onze eerste gezamenlijk studie patiënt op de HCK was een WPW ablatie en jouw aanbod om eerder te komen en te helpen met de voorbereidingen werd zeer gewaardeerd. Alleen om 07:15 al te beginnen met allerlei vragen over het mapping apparaat en de procedure was toch iets aan de vroege kant. Achteraf gezien

had ik de cafeïne eerst zijn werk moeten laten doen. Dat moment heeft uiteindelijk wel geresulteerd in een leuke anekdote en een mooi samenwerkingsverband die wij hopelijk bij mijn terugkomst naar de Cardiologie weer kunnen oppakken.

I would like to thank my colleagues from Kings College, Kawal and Rashed, for all their support surrounding the post-processing and analysis of the LA LGE images. I am glad that despite your busy schedules you were always able to make time for discussing my results and giving feedback on my papers. The time spent in London has contributed significantly to this thesis and towards my personal development. I look forward to continuing our collaboration in the years to come.

Lieve MRI Laboranten van het Haga, Annet – Newton – Ram en in het bijzonder Visnja. Ik besef heel goed dat het op bepaalde momenten ongetwijfeld vermoeiend geweest zal zijn om weer eens een extra sequentie uit te voeren, de zoveelste zondag te scannen en alle onderbrekingen vanwege de wachttijd bij alle 'plakwerk'. Jullie inzet hierbij is altijd zeer gewaardeerd. Ik heb met veel plezier samengewerkt met jullie en de radiologen, Jan-Kees en Rogier.

Collega promovendi EMC, Christophe, Eva, Ilse, Lisette, Paul, Tanwir en Ameeta, bedankt voor de prettige samenwerking en de gezellige werksfeer op het lab. Vooral de hulp van Christophe en Lisette heeft een belangrijke rol gespeeld in de vormgeving van de ventriculaire high-resolution mapping. Ameeta en Tanwir gefeliciteerd met jullie mooie boekjes en voor de rest, jullie werk belooft mooie boekjes en ik kijk uit om bij jullie promoties aanwezig te zijn.

Mijn opleiders in het OLVG, dr. Carl Siegert en dr. Marcel Weijmer, wil ik bedanken voor de tijd die zij beschikbaar hebben gesteld zodat ik naast het opdoen van klinische vaardigheden ook tijd beschikbaar had voor het afronden van mijn promotie en het opzetten van een nieuw onderzoekslijn bij de Hemodialyse. Marcel, ik wil jou ook bedanken voor de kritische feedback op het onderzoeksprotocol en de stageplan Beleid en Management. Met name door jouw eerste vraag bij elk nieuw project waarmee ik aankwam ('wat is nou je doel?') is mijn kennis en kunde ontzettend gegroeid. Ik ben jou ook ontzettend dankbaar voor het mogelijk maken van mijn executive MSc aan de London School of Economics. Het belooft een mooi traject te worden en ik hoop in de komende jaren dit verder uit te bouwen binnen het OLVG.

Dear dr. Mohan Nair, thanks to you I was given the opportunity to set up and maintain a Cardiac MRI service in Holy Family Hospital. I have learned a great deal during my visits in the past 2 years and I hope this continues in the years to come. I would also

like to express my sincere gratitude to Father George and dr. Sumbul Warsi for their continued support in making this happen. In addition, I would like to thank dr. Amitabh Yaduvanshi and dr. Vikas Kataria for the enthusiasm with which they participate and promote this project. A word of appreciation also goes out to the administrative staff, Jenny and Deepak.

Beste collega assistenten Cardiologie HAGA en Interne Geneeskunde OLVG, Matthijs Kuiper, Roel Slenter en Thomas Rohde, bedankt voor jullie 'vrijwillige' bijdrage aan de studie. Ik ben ontzettend dankbaar dat jullie aansluitend aan een drukke nachtdienst toch bereid waren om onder geplakt met ECG elektrodes een MRI te ondergaan. Dit heeft een belangrijke bijdrage geleverd aan de validatie van onze methode.

Lieve Maya, bedankt voor alle (administratieve) ondersteuning.



## Familie

Lieve Papa en Mama, sinds dat ik het mij kan herinneren, heb ik jullie altijd hard zien werken. Dubbele diensten en lange dagen zonder ook maar ooit te klagen. Van jullie heb ik nog nooit één woord over hoge werkdruk of stress gehoord. Ondanks jullie drukke en ambitieuze levens, hebben jullie mij altijd alle tijd gegeven. Van dingen zoals ritmestoornissen of MRI hadden jullie geen verstand, maar er was iets belangrijker wat ik heb geleerd van onze band. Jullie zijn een voorbeeld voor mij en de lessen die ik van jullie heb geleerd blijven heel mijn leven bij. Ik hou van jullie.

Rajan Mamu, although we are unable to meet up that often, you have always been there with us, both in times of celebration and during times of need. To this extent, I would like to thank you for your presence in our lives and for all the support and love that I have received.

Sheena, inmiddels ben jij al klaar met je Bachelor geneeskunde en ga je snel een doorstart maken met een onderzoek op de hemodialyse afdeling in het OLVG. Uiteraard ligt ook jouw hart bij de cardiologie, dus was het vanzelfsprekend dat dit een cardiologisch georiënteerd onderzoek werd. Mede door deze recente ontwikkelingen hoor je vaak genoeg dat het vervolg voor jou allemaal veel makkelijker is aangezien je broer al in het vak zit. Je weet ook wat ik van deze nonsens vind! Ik zeg het nooit hardop maar ik ben trots op jouw prestaties tot nu toe. Ik kan mij voorstellen dat het continue pushen vanuit mij soms teveel voor je is. Ik doe het alleen omdat ik weet wat je potentie is en dat ik deze ook effectief benut wil zien worden. Bedankt voor al jouw hulp vanuit de zijlijn de afgelopen jaren en ik kijk er naar uit om jouw onderzoek te gaan begeleiden. Zodra jij de 'research bug' te pakken hebt, ben ik er van overtuigd dat dit zal leiden tot een succesvol promotietraject.

Siddha, mijn lieve zoon, het is onbeschrijfelijk wat jou komst met Papa's leven heeft gedaan. Met elke mijlpaal die je de afgelopen jaren hebt behaald, word ik trotser. Tegelijkertijd ga je zo hard, gisteren nog een kleine baby en binnenkort al naar de basisschool. Vanaf het moment dat ik naar werk vertrek tot ik weer het huis binnenstap, kan ik niet wachten om bij je te zijn en leuke dingen met je te doen. Papa is trots op jou en al onze momenten samen

Yumiko, if only words could express what is in my heart. Jij bent mijn drijvende kracht, steun en toeverlaat, en ik ben zo blij dat ik dit leven met jou kan delen. Jij slaagde er altijd in om bij mij de rust te doen wederkeren zoals het onder andere nodig was voor het MRI examen in Florence. Wat dat betreft sluiten onze persoonlijkheden naadloos aan op elkaar, you are the yin to my yang! Het is onvoorstelbaar hoe je elke keer, ondanks je

eigen drukke opleiding, vol enthousiasme hebt meegeluisterd naar mijn oefensessies voor alle cursus- en congrespresentaties. Ik hoop dat ik je niet te pletter heb verveeld met de eindeloze 'spannende' verhalen over cardiale MRI en elektrofysiologie. De afgelopen jaren zijn druk geweest met mijn promotie, jouw opleiding en natuurlijk onze koekie Siddha. Gelukkig hebben wij een aantal congres reizen samen kunnen doen (Milaan, Londen en Orlando waren lang niet zo leuk geweest als jij niet mee was!). Deze hectiek zal ons voorlopig bezig houden omdat ook voor jou het vervolg er aankomt. Voordat het zover is gaan wij snel onze salsa avonden weer oppakken!



Financial support for the publication of this thesis was provided by:

Erasmus Universiteit Rotterdam, Afdeling Cardiologie van het Erasmus Medisch Centrum Rotterdam, Biosemi B.V., Biotronik Nederland B.V., Chipsoft, Guerbet Nederland B.V., Haga Teaching Hospital, Servier Nederland Farma B.V. and Stichting Cardiovascular.

In addition, I would like to thank the following friends and relatives: The Tours Guru, Athena Travels, Rajan Dhar, Harneet Grewal, Anita Sharma, Yogesh Sachdeva & Family, dr. Anil Sharma & Family, Atul Ahuja & Family, Ish & Kavita Kapoor, Rajiv Nath, Om Prakash Yadav & Family, Baldev Singh, Cafeteria Vikas, Family Jammu, Family Kaul, Gurdeep Singh (ANC), India Bazaar, Jaspal Singh, Lt. Sh. Jogindera Devi, Manu Asian Food Store, Phi Promotions BV, Raj Consult BV and Sehgal Jewellers.